

On the Transformation of Amorphous Calcium Carbonate into Calcite

by

Christopher James Stephens

Submitted in accordance with the requirements for the
degree of Doctor of Philosophy

The University of Leeds
Faculty of Mathematics and Physical Sciences
School of Physics and Astronomy

August 2010

The candidate confirms that the work submitted is his own, except where work which has formed part of jointly-authored publications has been included. The contribution of the candidate and the other authors to this work has been explicitly indicated overleaf. The candidate confirms that appropriate credit has been given within the thesis where reference has been made to the work of others. This copy has been supplied on the understanding that it is copyright material and that no quotation from the thesis may be published without proper acknowledgement.

One flew east, one flew west...

Abstract

The work presented in this thesis considers the formation mechanisms of the mineral CaCO_3 . The role of amorphous calcium carbonate (ACC) as a precursor to calcite, the most thermodynamically stable CaCO_3 polymorph, is investigated in several systems. Precipitation of CaCO_3 in bulk solution proceeds via ACC, identified using Raman spectroscopy, SEM, TEM and spectrophotometry characterisation techniques. The formation rate and stability of ACC was shown to be dependent on the initial solution concentration in the range of $[\text{Ca}^{2+}] = 2\text{-}10$ mM.

The amorphous phase of CaCO_3 is stabilised under moderate degrees of confinement. Precipitation of CaCO_3 within an annular wedge, formed around the region of contact of crossed cylinders, resulted in different crystal morphologies dependent upon the surface separation. Single calcite rhombohedra formed at surface separations greater than $5\ \mu\text{m}$, identical to those observed on equivalent surfaces in bulk solution. Irregular, multifaceted calcite particles formed at intermediate surface separations, whereas only ACC particles were observed at separations below $1\ \mu\text{m}$. There was a rapid transition from ACC into calcite upon the removal of the confining surface and subsequent incubation in depleted solution. Furthermore, heating of an amorphous particle after separation resulted in the transformation into calcite. The stabilisation of the amorphous phase was attributed to kinetic factors, since it was shown that ACC would be thermodynamically preferable to calcite at only sub-nanometre surface separations, at least three orders of magnitude smaller than observed here.

The precipitation of CaCO_3 is influenced by the substrate properties, which afford control over number density, polymorphism and crystallographic orientation. On homogeneous functionalised self-assembled monolayers (SAMs) of mercaptohexadecanoic acid (MHA) on gold, face selective growth of calcite parallel to the (012) and (015) growth planes was observed, ascribed to favourable interactions between the inorganic CaCO_3 and the organic monolayer. Using patterned SAMs,

formed using the deep-UV photo-lithography method, crystallisation at carboxyl-terminated regions resulted in localised undersaturation at polar-terminated regions, demonstrating that crystallisation is dependent upon concentration gradients. CaCO_3 crystallisation on weathered mica substrates yielded epitaxial growth of calcite in a (001) orientation, parallel to the mica basal cleavage plane. Despite a close lattice match between the Ca-Ca spacing parallel to the (001) plane (0.499 nm) and the adjacent K^+ site spacing on the basal cleavage plane (0.512 nm), epitaxial overgrowth did not occur on freshly cleaved mica surfaces. It is proposed that the presence of naturally formed surface crystallites of K_2CO_3 are a necessary intermediary for the occurrence of epitaxial calcite. Amorphous-type particles, morphologically similar to those characterised in bulk solution, were observed during the first 60 s after nucleation on both these substrates, before transformation into the crystalline state.

Crystallisation of CaCO_3 within arrays of sub-picolitre droplets supported on patterned SAMs was affected by the limited solution volume. Calcite crystals formed almost exclusively in a tetrahedral configuration, in contrast to the rhombohedral particles observed during precipitation from bulk solution. Multiple occupancy of droplets was rare after a 24 h growth period, attributed to concentration depletion. As in the other studied systems, sub-micron amorphous-type particles were present after short growth times, presenting further evidence for the crystallisation of CaCO_3 through an amorphous precursor phase.

Acknowledgements

First and foremost I would like to thank my supervisor, Dr Hugo Christenson for the guidance and support he provided throughout the last four years. Without his knowledge, patience and understanding this thesis would not have been written. I also thank Prof. Fiona Meldrum, who's clear enthusiasm and depth of knowledge has been a source of inspiration. Prof. Steve Evans granted me access to many instruments, providing a substantial part of the results presented in this thesis. I had the privilege of discussing many aspects of my research with Prof. Dima Kashchiev throughout his year in Leeds, for which I will be forever grateful.

Dr. Ray Lam gave me an excellent crash course into working in a chemistry lab all those years ago. Dr Yi-Yeoun Kim deserves many thanks for her assistance and advice, as well as her tolerance of my sometimes erratic laboratory practices. I acknowledge Beth Noel for her help with the Raman microscope and Bram Cantaert for his assistance with those tricky TEM diffraction patterns. Panida 'Nim' Prompinit, Alex Walton and Jonathan Bramble all assisted me at various times in the laboratory. Dr Aidan Hindmarch was always at hand during the inevitable high vacuum/sputter head failures. I have been assisted by many others along the way, including Dr. Manon Ali, Bob Turner, Kevin Critchley, and Dr Alex Kulak. In LEMAS: John Harrington, Dr Rich Walshaw and Dr Mike Ward. In the workshop, Trev, Brian, Lee and Mark were always friendly and Brian Chesworth was always able to help during the frequent mix-ups in purchasing. I have worked with four final year project students during my PhD, Michael Chisholm, Youmna Mouhamad, Harriet Stibbard and Jenny Evans and I value the commitment and contributions of each.

On a personal level I would like to thank all those past and present who have made the MNP group such a great place to work. In no particular order; James Kendall, Dan Lund, Jono McKendry (keep practicing), John Blockley, Pete Allen, Jo Galloway, James Towey, Sophie Weiss, Marcin Gorzny, Matthew Cheetham and Dan Billingsley amongst others. I am indebted to the condensed matter footballers, for providing a welcome distraction when times were tough. I thank George Penn and Maxim Lewis for putting me up during the past six months.

I thank Dr. Dominika Nowak, who's friendship and kindness I value and Simone Stuart-Cole, for far too many reasons to articulate here.

Finally, I thank my family, not least for tolerating me during the writing of this thesis, but also for the encouragement and unconditional support down the years.

Contents

Publications	i
Abstract	iii
Acknowledgements	v
List of Figures	x
List of Tables	xvi
Abbreviations	xvii
1 Background and Theory	1
1.1 Introduction	1
1.2 Crystal Formation	5
1.2.1 Supersaturation and the Metastable Zone	5
1.2.2 Nucleation	8
1.2.2.1 Homogeneous Nucleation	8
1.2.2.2 Heterogeneous Nucleation	14
1.2.2.3 Non-classical Nucleation Theory	16
1.2.3 Growth	17
1.2.4 The Growth Surface	20
1.3 Crystal Classification	21
1.3.1 Crystallographic Systems	23
1.3.2 Indexing Faces	25
1.4 Calcium Carbonate	26
1.4.1 Calcite	26
1.4.2 Aragonite	28
1.4.3 Vaterite	29
2 Experimental Methods	30
2.1 Experimental Preparation	30

2.2	Substrate Preparation	31
2.2.1	Muscovite Mica	31
2.2.2	Self Assembled Monolayers	32
2.3	Crystal Growth	33
2.4	Characterisation Techniques	35
2.4.1	Contact Angle Measurements	35
2.4.2	XPS	36
2.4.3	Optical Microscopy	37
2.4.4	Electron Microscopy	37
2.4.4.1	Transmission Electron Microscopy	37
2.4.4.2	Scanning Electron Microscopy	38
2.4.5	X-Ray Diffraction	42
2.4.6	Raman Spectroscopy	42
2.4.7	UV-VIS Spectrophotometry	43
2.5	Analytical Software	43
3	Epitaxial Growth of Calcite on Mica	45
3.1	Introduction	45
3.2	Results	50
3.2.1	Freshly Cleaved Mica	50
3.2.2	Weathered Mica	50
3.2.3	Ion Exchanged Mica	57
3.2.4	Early Growth Stages on Mica	62
3.3	Discussion	70
3.4	Conclusions	75
4	Crystallisation on Self-Assembled Monolayers	76
4.1	Introduction	77
4.2	Structure and Formation of SAMs	77
4.2.1	Patterning of SAMs Using Deep-UV Photolithography	82
4.3	Results	83
4.3.1	Characterisation of SAMs	83
4.3.2	Crystallisation on Homogeneous SAMs	86
4.3.3	Growth on Patterned SAMs	92
4.3.4	Early Growth Stages on SAMs	97
4.4	Discussion	107
4.5	Conclusions	109
5	Crystallisation in Confinement	110
5.1	Introduction	111
5.2	Experimental Methods	113
5.3	Results	118
5.3.1	SEM Analysis	118
5.3.2	Raman Microscopy Analysis	128
5.4	Discussion	132

5.5	Focused Ion-Beam Section Analysis	137
5.6	Conclusions	147
6	Precipitation of Calcium Carbonate in Bulk Solution	149
6.1	Introduction	149
6.2	Experimental Methods	154
6.3	Results	156
6.3.1	Spectrophotometry Analysis	156
6.3.1.1	Precipitation of Calcium Carbonate Without Additives	156
6.3.1.2	Precipitation of Additive-Stabilised ACC	157
6.3.2	Electrode Measurements	161
6.3.3	Raman Spectroscopy Measurements	161
6.3.4	EM analysis	169
6.4	Discussion	181
6.5	Conclusions	183
7	Crystallisation in Arrays of Picolitre Droplets	185
7.1	Introduction	186
7.2	Experimental Methods	189
7.3	Results	191
7.3.1	Determination of Droplet Volumes	191
7.3.2	Droplet Size Dependency	192
7.3.3	Particle Morphology	198
7.3.4	Growth Time Dependency	198
7.4	Discussion	204
7.5	Conclusions	206
8	Conclusions	207
9	Future Work	209
A	Appendix A	211
	Bibliography	213

List of Figures

1.1	Comparison of single crystal calcite.	3
1.2	The solution state as a function of solute concentration and temperature.	7
1.3	The formation of a crystalline embryo (blue atoms) within a metastable bulk phase (grey atoms) is determined by the aggregation and desorption events shown.	9
1.4	Plot of ΔG as function of r for an embryonic phase within a bulk phase.	13
1.5	Heterogeneous (left) and homogeneous (right) critical nuclei, both of radius r	14
1.6	The three lattice sites as proposed by Kossel.	18
1.7	Growth rate as a function of supersaturation.	20
1.8	The progression of a screw dislocation in accordance to the BCF model	21
1.9	Crystal growth rate as a function of fluid flow rate.	22
1.10	The basis vectors a , b , c and the inter-axial angles α , β and γ defining the crystallographic reference system	22
1.11	6-fold and 3-fold symmetry axes.	24
1.12	SEM micrographs of the anhydrous polymorphic forms of calcium carbonate, from left to right calcite, aragonite and vaterite	27
1.13	The crystal structure of calcite.	28
1.14	The crystal structures of a aragonite and b vaterite.	29
2.1	Substrate-water contact angle for a hydrophilic surface (left) and a hydrophobic surface (right). The subscripts LV, LS and SV define the liquid-vapour, liquid-substrate and substrate-vapour interfaces respectively.	36
2.2	Schematic diagram showing the components of an TEM column	39
2.3	Schematic diagram showing the components of an SEM column.	41
2.4	ImageJ particle size analysis procedure	44
3.1	The atomic structure of muscovite mica	47
3.2	TEM and AFM evidence for K_2CO_3 crystallites	49
3.3	$CaCO_3$ crystallisation on freshly cleaved mica	51
3.4	$CaCO_3$ growth on weathered mica	52
3.5	Simulated and actual epitaxial calcite crystals	53
3.6	The 60° increment in rotation of the epitaxial calcite crystal	53

3.7	2θ XRD plot of epitaxial calcite crystals on mica	55
3.8	Rhombohedral, intermediate and tetrahedral calcite configurations .	56
3.9	CaCO_3 crystal growth as a function of weathering period	58
3.10	CaCO_3 growth on ion exchanged mica substrates	59
3.11	CaCO_3 growth on mica surfaces under different weathering conditions	60
3.12	Precipitation of CaCO_3 on weathered mica after a 30 s growth period	64
3.13	Precipitation of CaCO_3 on weathered mica after a 2 minute growth period	65
3.14	High magnification SEM images for the precipitation of CaCO_3 on weathered mica after a 2 minute growth period	66
3.15	Precipitation of CaCO_3 on weathered mica after a 4 minute growth period	67
3.16	Precipitation of CaCO_3 on weathered mica after a 6 minute growth period	68
3.17	[Precipitation of CaCO_3 on weathered mica after an 8 minute growth period	69
3.18	AFM images of early stage CaCO_3 growth on a mica surface	74
3.19	Schematic model representing the proposed early stage CaCO_3 growth on a mica surface.	74
4.1	Schematic diagram of the components of a mercaptohexadecanoic acid SAM	78
4.2	Schematic diagram showing the geometry of a SAM, dependent on the chain tilt angle α and the chain twist angle β	80
4.3	Advancing (black squares) and receding (red circles) contact angles as a function of immersion time for ODT SAMs in 0.1 mM MHA & ethanol solution.	84
4.4	Relative elemental surface compositions of SAMs at each stage of the deep-UV photo-patterning process.	86
4.5	Calcite growth on carboxyl-terminated SAMs.	88
4.6	CaCO_3 on homogeneous DCM SAMs as a function of precipitation method.	89
4.7	CaCO_3 on homogeneous ethanol with acetic acid SAMs as a function of precipitation method.	90
4.8	CaCO_3 on 20 μm diameter patterned SAMs.	94
4.9	CaCO_3 on 10 μm diameter patterned SAMs.	95
4.10	CaCO_3 on 20 μm diameter patterned SAMs as a function of distance from the air-solution interface.	96
4.11	CaCO_3 precipitates on MHA SAMs after a 30 s growth period . . .	100
4.12	CaCO_3 precipitates on MHA SAMs after a 30 s growth period as a function of concentration	101
4.13	CaCO_3 precipitates on MHA SAMs after a 1 min growth period . .	102
4.14	CaCO_3 precipitates on MHA SAMs after a 1 minute growth period as a function of concentration	103
4.15	CaCO_3 precipitates on MHA SAMs after a 2 min growth period . .	104

4.16	CaCO ₃ precipitates on MHA SAMs after a 5 min growth period . . .	105
4.17	CaCO ₃ precipitates on MHA SAMs after a 10 min growth period . . .	106
5.1	Schematic diagram for the crossed-cylinder configuration.	115
5.2	Surface separation as a function of distance from the contact region, according to equation 5.1.	116
5.3	SEM overview of the region of contact.	116
5.4	HR-SEM image of a typical region of contact	117
5.5	SEM images for CaCO ₃ growth on MHA SAMs using the gas dif- fusion method on a isolated control surfaces and b crossed cylinder surfaces at millimeter surfaces	120
5.6	SEM images for CaCO ₃ growth on MHA SAMs at millimeter sep- arations.	121
5.7	SEM images for CaCO ₃ growth on MHA SAMs using the gas diffu- sion method ([Ca ²⁺]= 8 mM, for 24 h) at an intermediate surface separation of ~5 μm. a Overview image, with fully faceted calcite crystals towards the top right of the image. b medium magnifi- cation, showing multifaceted, irregular calcite crystals orientation.	122
5.8	SEM images for CaCO ₃ growth on MHA SAMs at an intermediate surface separation of ~3 μm	123
5.9	SEM images for CaCO ₃ growth on MHA SAMs using the gas dif- fusion method ([Ca ²⁺]= 8 mM, 24 h) at surface separations of a 2 μm and b ~0.5 μm.	124
5.10	SEM images for CaCO ₃ growth on MHA SAMs at intermediate surface separations of ~3 μm as a function of solution concentration.	125
5.11	HR-SEM images of CaCO ₃ precipitates supported on MHA SAMs at a sub-micron surface separation	126
5.12	SEM images for CaCO ₃ growth on MHA SAMs using the gas dif- fusion method at an sub-micron surface separation.	127
5.13	Normalised Raman spectra for synthetic samples of a calcite, b aragonite, c vaterite and d synthetic ACC, taken over a range of 180-1200 cm ⁻¹	129
5.14	Normalised Raman spectra of CaCO ₃ particles precipitated at sur- face separations of a ~5 mm b ~ 5 μm, c ~ and 0.5 μm. d The Raman spectrum for synthetic ACC is included for comparison.	130
5.15	Normalised Raman spectra of the same CaCO ₃ particle precipitated a after heating for 1 h at 180° b before heating. Double decompo- sition growth method, [Ca ²⁺]=5mM, 24 h.	131
5.16	Schematic diagram showing the approximation of ACC as a disc of radius <i>r</i> and height <i>d</i> . The ACC particle is located near to the region of contact (top surface not shown).	134
5.17	Geometric configuration of single crystal electron diffraction.	139
5.18	SEM micrographs showing the various stages of the FIB milling process.	140

5.19	SEM micrographs of the CaCO_3 precipitates prior to FIB milling, supported on MHA gold on mica substrates. 5 mM double decomposition growth method, 24 h growth. a single calcite, precipitated at a large surface separations ($\sim 5\text{mm}$), b polycrystalline calcite precipitated at intermediate surface separations ($\sim 5\ \mu\text{m}$).	141
5.20	TEM micrographs of FIB sections for CaCO_3 precipitated at a large surface separations (5 mm) and b intermediate surface separations ($\sim 5\ \mu\text{m}$).	142
5.21	High resolution TEM image of a single crystal calcite FIB cross section. a Original image, b Fourier enhanced image.	143
5.22	TEM overview of a CaCO_3 particle precipitated at an intermediate surface separation showing a the crystal-substrate interface for and b the presence of grain boundaries.	144
5.23	High magnification TEM images of CaCO_3 precipitated at intermediate surface separations.	145
5.24	TEM electron diffraction patterns of CaCO_3	146
6.1	Chronological photographs showing a 5mM supersaturated CaCO_3 solution in a 100 ml vessel after a 30 s, b 2 min, c 4 min, d 6 min, e 8 min and f 10 minutes.	151
6.2	Schematic diagram showing the spectrophotometry cuvette.	152
6.3	UV-Vis absorption over 200-700 nm, measured for a $[\text{Ca}^{2+}]$ 5 mM solution 30 s after mixing. A wavelength of $\lambda=500\ \text{nm}$ was used for the spectrophotometry measurements	155
6.4	In situ spectrophotometry measurements of the transmitted intensity, I/I_0 , as a function of time. $[\text{Ca}^{2+}] = \text{a-g } 2, 4, 4.5, 5, 6, 8$ and 10 mM respectively.	158
6.5	In situ spectrophotometry measurements of CO_2 equilibrated and fresh CaCO_3 solutions.	159
6.6	In situ spectrophotometry measurements for the precipitation of CaCO_3 from 10 mM aqueous solutions under different conditions.	160
6.7	In situ spectrophotometry measurements for the precipitation of CaCO_3 from $[\text{Ca}^{2+}] = 10\ \text{mM}$ solutions, in presence of Mg^{2+} salts. The $[\text{Mg}^{2+}]$ concentrations are listed, in the range of $[\text{Ca}^{2+}] = 0\text{-}10\ \text{mM}$	162
6.8	pH (right axis, blue line) and turbidity (left axis, black line) as a function of time, for CaCO_3 solution concentrations of 2.5 mM (top) and 5 mM (bottom).	163
6.9	Raman spectra of CaCO_3 precipitates as a function of growth time, 2.5 mM CaCO_3 solution concentration. Top Absolute intensity scale, Bottom relative intensity scale. Baselines are displaced for different spectra.	165
6.10	Raman spectra of CaCO_3 precipitates as a function of growth time, 5 mM CaCO_3 solution concentration. Top Absolute intensity scale, Bottom relative intensity scale. Baselines are displaced for different spectra.	166

6.11 Raman spectra of CaCO_3 precipitates as a function of growth time, 10 mM CaCO_3 solution concentration. Top Absolute intensity scale, Bottom relative intensity scale. Baselines are displaced for different spectra.	167
6.12 SEM overview of CaCO_3 precipitates on Formvar TEM grids.	171
6.13 High resolution SEM images of CaCO_3 precipitates on Formvar TEM grids, 2.5 mM concentration. a 15 s growth period, b 5 minutes growth period. The depletion region surrounding the calcite crystals can clearly be seen.	172
6.14 High resolution SEM images of CaCO_3 precipitates on Formvar TEM grids, 5 mM solution concentration. a 15 s and b 1 min growth periods, showing aggregation of sub-micron particles.	173
6.15 TEM micrographs of CaCO_3 precipitates on a Formvar TEM grid, for a 15 s growth period and a 5 mM solution concentration. a Aggregates of 2 or more particles tended to form, even after short growth periods. b A region of single CaCO_3 particles, showing a uniform distribution of 50-80 nm particles, consistent with ACC.	174
6.16 TEM diffraction patterns for CaCO_3 precipitates on a Formvar TEM grid, for a 1 minute growth period and a 5 mM solution concentration. a b	175
6.17 TEM diffraction patterns for CaCO_3 precipitates on a Formvar TEM grid, for a 1 minute growth period and a 5 mM solution concentration.	176
6.18 a, b: TEM micrographs of CaCO_3 precipitates on a Formvar TEM grid, for a 1 minute growth period and a 5 mM solution concentration.	177
6.19 a, b: TEM micrographs of CaCO_3 precipitates on a Formvar TEM grid, for a 5 minute growth period and a 5 mM solution concentration.	178
6.20 CaCO_3 particle diameters after a 15 second growth period, $[\text{Ca}^{2+}] = 5$ mM concentration.	179
6.21 CaCO_3 particle diameters after a 1 minute growth period, $[\text{Ca}^{2+}] = 5$ mM concentration.	179
6.22 CaCO_3 particle diameters after a 5 minute growth period, $[\text{Ca}^{2+}] = 5$ mM concentration.	180
7.1 Optical image showing an array of supersaturated CaCO_3 droplets .	186
7.2 Schematic diagram showing crystallisation within a single droplet of droplet-substrate radius r and droplet-substrate contact angle θ . .	187
7.3 Schematic diagram of the spherical cap model, showing droplet volume as a function of droplet radius a , droplet-substrate interfacial radius r and cap height, h	188
7.4 Schematic diagram defining the photomask spacings a_{centre} , a_{edge} and radius r	189
7.5 400 \times optical image showing 4 photomask geometries. Radii; a 10 μm , b 5 μm , c 4 μm and d 2 μm	190

7.6	Optical images showing arrays of 10 μm radius droplets of supersaturated CaCO_3 solutions supported on patterned SAMs at two magnifications a , b	192
7.7	Side profile of 3 different $[\text{Ca}^{2+}] = 5 \text{ M}$ droplets, 10 μm radius.	192
7.8	Low-Res SEM overview showing CaCO_3 particles as a function of droplet radius. a 10 μm , b 5 μm , c 4 μm and d 2 μm . $[\text{Ca}^{2+}] = 5 \text{ mM}$ CaCO_3 droplet concentration, 24 h growth period.	193
7.9	FEG SEM images of CaCO_3 particles precipitated from 2 μm radii droplets	194
7.10	Low-resolution SEM images showing the CaCO_3 particle location, $[\text{Ca}^{2+}] = 5 \text{ mM}$, 24 h growth period. a 10 μm radii droplets where $74 \pm 4\%$ of the particles were within 2 μm of the droplet boundary. b 4 μm radii droplets, where $78 \pm 6\%$ of particles were located within 1 μm of the droplet boundary.	195
7.11	Size distribution of CaCO_3 particles precipitated from 10 μm radius droplets, 24 h growth period, $[\text{Ca}^{2+}] = 5 \text{ mM}$. 200 μm bin size.	196
7.12	Size distribution of CaCO_3 particles precipitated from 5 μm radius droplets, 24 h growth period, $[\text{Ca}^{2+}] = 5 \text{ mM}$. 100 μm bin size.	196
7.13	Size distribution of CaCO_3 particles precipitated from 4 μm radius droplets, 24 h growth period, $[\text{Ca}^{2+}] = 5 \text{ mM}$. 100 μm bin size.	197
7.14	top HR-SEM images of individual face selective calcite tetrahedra, observed within 10 μm radius, 2.5 mM droplets after a 24 h growth period. a 44% of calcite particles were in a (012) orientation, b 33% of calcite particles were in a (015) orientation. The remaining 23% of calcite particles were in a variety of orientations, of which c (113) and d (122) were the most frequent. bottom SHAPE simulated calcite tetrahedra in corresponding orientations.	197
7.15	SEM overview of CaCO_3 precipitates from 5 mM solutions.	200
7.16	SEM images of the precipitation of CaCO_3 within 10 μm radii droplets after 24 hours	201
7.17	CaCO_3 particles in 10 μm radius droplets as a function of growth period.	202
7.18	High magnification SEM images of individual irregular CaCO_3 particles.	203

List of Tables

1.1	The seven crystallographic systems, defined in terms of the symmetry elements present and the axial restrictions.	25
1.2	The CaCO_3 unit cell parameters for the CaCO_3 polymorphs calcite, aragonite and vaterite.	27
3.1	The effect of mica weathering conditions on the CaCO_3 nucleation density, polymorphism and percentage of epitaxial calcite crystals.	61
4.1	Advancing and receding water contact angles for MHA and ODT SAMs prepared in DCM and EtOH with acetic acid solvents respectively. The advancing and receding contact angle of pure gold surfaces are included	83
4.2	Percentage orientation of calcite crystals on MHA SAMs formed in 0.1 mM EtOH & acetic acid and DCM solvent. Crystals formed by double decomposition (DD) and gas diffusion (GD) methods at 5 mM, 12 h growth period	87
4.3	Nucleation density, particle size and polymorphism for CaCO_3 particles on glass, gold and MHA SAM substrates for both precipitation methods. 8 mM solution concentration, 24 growth period.	91
4.4	CaCO_3 polymorphism and size as a function of growth time for precipitation from 5 mM solutions on MHA SAMs.	98
5.1	The internal Raman active vibrational modes for calcite, aragonite and vaterite.	129
6.1	The intensity (left of forward slash, arbitrary units) and full-width, half-max (FWHM) (right of forward slash, cm^{-1}) of the 1085 cm^{-1} carbonate mode as a function of growth time, for initial concentrations of $[\text{Ca}^{2+}] = 2.5, 5$ and 10 mM	168
7.1	Photomask spacings x_{centre} and x_{edge} as a function of radius r	189
7.2	Droplet-substrate interfacial area (A_{ds}) and droplet volumes for contact angles of 43° (V_{43}) and 90° (V_{90}), as a function of droplet-substrate interfacial radius r , calculated using equations 7.1 and 7.2 respectively.	192
7.3	Droplet occupancy, multiple occupancy and average CaCO_3 particle size as a function of droplet radius. $[\text{Ca}^{2+}] = 5 \text{ mM}$ CaCO_3 droplet concentration, 24 h growth period.	193

Abbreviations

ACC	Amorphous Calcium Carbonate
AFM	Atomic Force Microscopy
BCF	Burton Cabrera Frank
CNT	Classical Nucleation Theory
DFT	Density Functional Theory
FIB	Focused Ion-Beam
MHA	Mercapto Hexadecane Acid
ODT	Octa Decane Thiol
PDT	Perfluoro Decane Thiol
SEM	Scanning Electron Microscopy
SAM	Self Assembled-Monolayer
TEM	Transmission Electron Microscopy
UHV	Ultra-High-Vacuum
XPS	X-ray Photoelectron Spectroscopy

Chapter 1

Background and Theory

1.1 Introduction

The field of crystallisation traverses many disciplines, including chemistry, physics, materials science and biology. Control over the orientation, size, morphology, organisation and hierarchical assembly has been the focus of significant interest for the potential design of new materials across a wide range of fields, including pharmaceuticals [1, 2], electronics [3–5], food stuffs [6, 7], ceramics [8, 9] and medicine [10]. Amongst recent examples, the properties of ceramic films [11], metal nanocrystals [12–15] and semiconductor nanocrystals [16–18] are dependent on the degree of space control and structural specialty [19, 20].

Current synthesis techniques afford only limited control over the crystallisation process and often require high pressures and temperatures or the use of expensive screening processes. It remains a technical challenge to control the morphology and surface features of these materials. Emerging strategies for the synthesis of inorganic materials with controlled morphologies include the use of organic additives, functionalised templates and self-assembling organic superstructures. In addition, there is significant interest in the directed self-assembly of organic/inorganic hybrid nanostructures [19]. These biomimetic approaches are inspired by nature, aiming to develop new synthesis techniques through the study of biomineralisation mechanisms.

Biom mineralisation is a widespread natural phenomena, signified by the formation of solid inorganic structures, including bones, teeth and shells by living organisms [19]. The mechanisms by which the organisms selectively extract and uptake elements into the functional structures are receiving significant interest, since these biominerals often exhibit remarkable morphologies, with intricate features vastly more sophisticated than their synthetic counterparts. Biominerals can be characterised by well defined structures, often leading to a higher order hierarchical assembly at the nano, micro, and meso levels [21]. Biom mineralisation offers outstanding control over the composition, morphology, crystallinity, and material properties at physiological temperature, pressure, and pH ranges [22]. In addition, these materials have been shown to exhibit repair mechanisms, providing a unique guide for the fabrication of future materials.

Mineralised deposits are not present in the majority of organisms, yet the biom mineralisation phenomenon is still extremely widespread, occurring in all five kingdoms and distributed across some 55 phyla [23]. Exoskeletons in protozoa, skeletal plates of echinoderms, mammalian bone and teeth, eggshells and stratoliths, are well known examples of this process. Calcium cations are present in around 50% of known biominerals, including calcium phosphate, calcium oxalate and calcium carbonate. This is unlikely to be coincidental, since calcium ions are fundamental in many cellular functions [24]. Other known cations observed in biominerals include magnesium, iron, barium and zinc [25].

Biominerals have been loosely classified into three categories; amorphous, polycrystalline and single crystal [26]. Amorphous minerals have no regular internal atomic structure and constitute less than a quarter of known biominerals [23]. These minerals are usually metastable with respect to their polycrystalline and crystalline counterparts in an absence of biological control. However, when formed with biological control, amorphous minerals are reportedly stable for the life span of the organism [27]. Since there is no preferred form of the amorphous mineral, it can be readily moulded into a desired shape by the organism [28, 29]. Polycrystalline biominerals exhibit a wide range of morphologies, with complex forms assembling from small crystalline components [30]. Single-crystal biominerals often display no relation to their internal crystal structure, contradicting the classical definition of a single crystal being bounded by smooth, planar faces parallel to the unit cell.

Figure 1.1 shows two examples of single crystal calcite (CaCO_3), firstly for a skeletal plates of an echinoderm displaying a sponge-like morphology, and secondly for a synthetic calcite crystal with planar faces parallel to the unit cell. The elaborate structure of the biomineral contrasts with the non-complex structure of synthetic calcite.

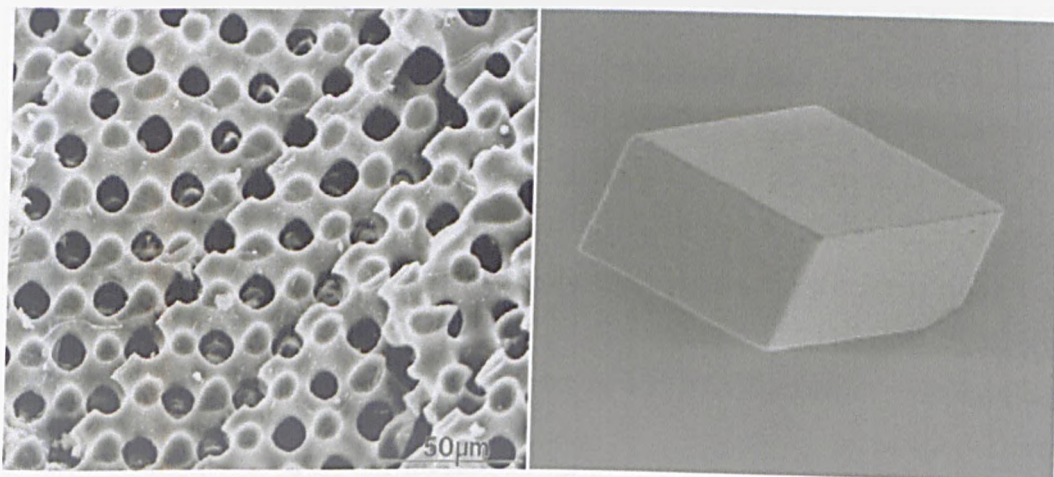


Figure 1.1: Comparison of single crystal calcite. **left** Stereom of the biomineral echinoderm, with a higher order hierarchical assembly (taken from reference [31]) and **right** synthetic calcite, morphologically similar to the calcite unit cell (image size $20 \times 20 \mu\text{m}$).

The work in this thesis is based on the transformation of CaCO_3 from an amorphous phase into a crystalline state. CaCO_3 exists in three anhydrous polymorphs, which in order of decreasing stability are calcite, aragonite and vaterite. A detailed description of each is presented in section 1.4. In addition there are two hydrated polymorphs, calcium carbonate monohydrate and calcium carbonate hexahydrate [32]. CaCO_3 also exists as a highly unstable amorphous phase, amorphous calcium carbonate (ACC), known to act as a precursor phase during biomineralisation. CaCO_3 was used as a model biomineral due to the relative ease of precipitation, the known occurrence of an amorphous precursor phase (ACC) under certain precipitation conditions and the wealth of available knowledge, since CaCO_3 is the most abundant carbonate in nature. CaCO_3 is attracting great interest in the context of controlling crystallisation [33–37]. Recent studies demonstrated control over the polymorphism, nucleation site, crystal morphology and hierarchical structure of this mineral. Furthermore, CaCO_3 has many industrial applications, and is used in the manufacturing of plastics, cements, adhesives, medicines and paper.

Amorphous calcium carbonate was first reported over 100 years ago, when it was observed that particular calcium carbonate deposits were isotropic when viewed between crossed polarised lenses [38, 39]. It was later shown that these deposits did not diffract X-rays, an important characteristic of a crystalline material [40]. Amorphous calcium carbonate is widespread amongst the *Crustacean* taxon with reported functions including as a temporary storage mineral, to provide mechanical support and as a precursor phase to the crystalline CaCO_3 polymorphs [39]. Biogenic ACC often contains considerable quantities of magnesium or phosphorous additives, and is reportedly heavily hydrated, with one mole of water per mole of calcium carbonate [41]. Synthetic ACC, formed in the absence of additives, consists of spherical microparticles, shown using thermogravimetric analysis to contain less than one third of a molecule of water per unit cell [41]. Synthetic ACC is reportedly stabilised indefinitely using additives, including polyphosphonates and amino acids. In high pH solutions, ACC reportedly forms as ~ 50 nm diameter particles, with the dehydration of the ACC occurring more easily with decreasing pH [42]. Similarly, Donners *et al.* precipitated stable ACC by coating the particles with hydrophobic surfactants, preventing the expulsion of water [43].

The stabilisation of ACC is often attributed to kinetic factors, although the formation mechanism is not fully understood. The aim of the work presented here is to gain greater insight into these processes. The biological mechanisms involved in the formation of biogenic ACC result in the formation of elaborate, defined structures and are presumably dependent on many complex interactions. The work of this thesis investigates several control parameters independently. The nucleation pathways of CaCO_3 on weathered mica and homogeneous SAMs are considered in chapters 3 and 4 respectively. Both these surfaces are shown to promote the heterogeneous nucleation of CaCO_3 , and ACC is identified during the early growth stages on both these surfaces. The effects of a physical confinement on the stabilisation of an amorphous phase is investigated in chapter 5, with the stabilisation mechanism attributed to a hindrance of water expulsion within the confined systems. The nucleation pathways of CaCO_3 within bulk solution are examined in chapter 6, with transiently present ACC identified using Raman spectroscopy and transmission electron microscopy (TEM). Finally, ACC is reported during precipitation within sub-picolitre droplets in chapter 7. The results presented in the first

part of chapter 3 do not strictly concern the ACC formation mechanisms, but are included as a novel finding, demonstrating that the exact condition of a mica surface is an important consideration for the epitaxial growth of CaCO_3 .

The chapter presents an overview of nucleation and growth. Section 1.3.1 describes the crystal classification used in this thesis, with the structures of the anhydrous CaCO_3 polymorphs, calcite, aragonite and vaterite presented in section 1.4. The general experimental methods used throughout the experiments presented in this thesis are described in chapter 2.

1.2 Crystal Formation

The onset of crystallisation is the result of three distinct processes, supersaturation, nucleation and growth. A quantitative theoretical outline of each is presented here.

1.2.1 Supersaturation and the Metastable Zone

The driving force for crystallisation is supersaturation, which occurs when the amount of dissolved material exceeds the solubility limit of a given substance. First described by Lowitz in 1795 [44], supersaturation results from a physical change to the solution, most commonly in temperature, pressure or chemical composition (additives, evaporation etc.) [45, 46], but can also be induced by acoustic waves and electromagnetic fields. Gibbs stated that for supersaturated solutions, the free energy of the initial solution is greater than that of the crystalline phase plus the final solution phase [47–49]. Supersaturation is therefore a prerequisite to crystallisation. In systems where a single compound crystallises, it is often convenient to express the supersaturation in terms of a change in chemical potential, $\Delta\mu$, since this is a measure of change in free energy upon the phase transformation.

$$\Delta\mu = -k_B T \ln \frac{AP}{K_{sp}} \quad (1.1)$$

where k_B denotes the Boltzmann constant and T is the absolute temperature. AP is the activity product of the reactants, which, for supersaturated solutions exceeds the equilibrium activity product, K_{sp} . AP/K_{sp} is a measure of the relative supersaturation, σ . Relative supersaturation is an important concept in crystal growth as it is directly proportional to the difference in Gibbs free energy between the bulk phase and the nucleating phase.

$$\sigma = \frac{AP}{K_{sp}} \quad (1.2)$$

Writing σ in terms of $\Delta\mu$

$$\Delta\mu = -k_B T \ln \sigma \quad (1.3)$$

For dilute solutions, it is more useful to define σ in terms of the saturation concentration, c_{sat} , and the reactant concentration, c .

$$\rho = \frac{c}{c_{sat}} \quad (1.4)$$

For a supersaturated vapour, equation 1.4 can be written

$$\rho = \frac{P}{P_{sat}} \quad (1.5)$$

where P and P_{sat} define the saturation vapour pressure and the actual vapour pressure respectively.

First stated by De Coppet, there is a finite region of supersaturation within which crystallisation proceeds spontaneously via nucleation and growth [50]. This metastable zone is commonly referred to as the Ostwald-Miers region with its size specific to each solution [51]. Ostwald observed a sharp upper boundary, or supersolubility curve, to this region approximately parallel to the solubility curve, thus defining three distinct solution states; stable, metastable and unstable (Figure 1.2). Within unstable solutions, phase separation proceeds by a non-activated

process known as *spinodal decomposition* without having to overcome a thermodynamic barrier [52]. Spinodal decomposition is resultant solely upon diffusion with two distinct new phases propagating evenly through the bulk phase. In practice, however, the onset of spinodal decomposition is extremely rare in nature since the metastable zone is almost always limited by the onset of heterogeneous nucleation.

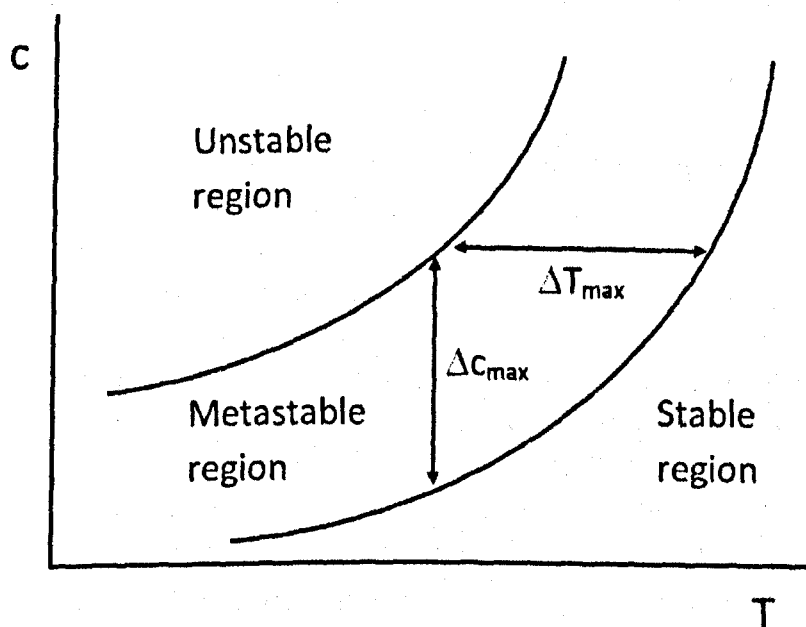


Figure 1.2: The solution state as a function of solute concentration and temperature. Below the solubility curve the solution is stable and above the supersolubility curve the solution is unstable. Between the two curves the solution is metastable with phase separation occurring via an activated process known as nucleation.

The metastable zone width has important consequences for the onset of nucleation and the resultant crystal form, since polymorphism, size distribution, defect density, and morphology are all parameters dependent upon the degree of metastability. Impurities, vessel topography, solution agitation rate, bubble formation and the rate of cooling are common factors known to influence the metastable zone width [53]. Experimentally, the zone width can be readily determined using either an isothermal or a polythermal method [50]. For the isothermal method supersaturation is generated by evaporation at a constant rate and at a fixed temperature, whereas for the polythermal method supersaturation is achieved by supercooling at a fixed concentration. These methods yield the maximum achievable supersaturation, ΔC_{max} , and supercooling, ΔT_{max} , values respectively and define the boundaries of the metastable zone shown in Figure 1.2

Numerous theoretical studies have attempted to predict the metastable zone width from nucleation kinetics, with success limited to specific systems. Important works include those by Kaschiev *et al.* [54] who related the metastable zone width to the nucleation induction time, independent from the number of nuclei and Nyvlt, who obtained the zone width from a semi-empirical calculation of the order of nucleation based upon the rate of cooling and maximum range of supercooling [55]. However there remains no universal theoretical model for the prediction of metastable zone width general to all conditions, a consequence of which is the relatively low level of control achievable in synthetic crystallisation.

1.2.2 Nucleation

Metastable solutions have a tendency to relax into two or more distinct, stable phases. The initial part of this process is nucleation, an activated process in which a free energy barrier must be exceeded in order to form embryos of a critical size [56–58]. Once the embryos attain the size of the critical nucleus, growth occurs spontaneously following several mechanisms (section 1.2.3). In the absence of impurities, solid surfaces or other preferential nucleation sites, nucleation occurs within bulk solution by a process known as *homogeneous nucleation*. Practically, however, the presence of dissolved impurities and solid surfaces (vessel walls etc.) act as preferential nucleation sites, lowering the free energy nucleation barrier in a process known as *heterogeneous nucleation*. Both nucleation processes are described by the *classical nucleation theory* (CNT), which originates from the works of Volmer and Webber in 1926 [59]. An outline of each is presented here.

1.2.2.1 Homogeneous Nucleation

Homogeneous nucleation begins with the association of atoms or molecules due to statistical density fluctuations [60] and is a highly localised process. An interface is formed as a result of this phase change, between the small embryos of the new phase and the surrounding metastable bulk phase. On an atomic scale there are frequent collisions between the embryo and the neighboring bulk phase, with the resultant energy dissipating principally amid the translational, vibrational and

rotational modes of the embryo [61]. Occasionally, the nature of the collision is such that a molecule leaves the embryo due to a fission event, or attaches to the embryo due to an inelastic collision (Figure 1.3). These competing events occur in a stochastic nature with fission generally more likely than aggregation, and only occasionally will an embryo reach the size of the critical nucleus. The size of the critical nucleus is determined by several factors, primarily temperature, relative supersaturation, molecular volume and interfacial energy [62]. Classical homogeneous nucleation theory defines the rate of nucleation, J , the net time for embryos to reach the critical size. J is defined as the number of nuclei forming per unit time per unit volume. Volmer and Weber and later Becker [63] proposed that it took the form

$$J = K e^{-\frac{G^*+q}{kT}} \quad (1.6)$$

where G^* denotes the maximum free energy required for the formation of a critical nucleus, q relates to the energy of diffusion across the interface, k_B is the Boltzmann constant and T is the absolute temperature. J is a decreasing function of supersaturation, leading to an increased rate of nucleation with increased undercooling. K is an indeterminate kinetic constant.

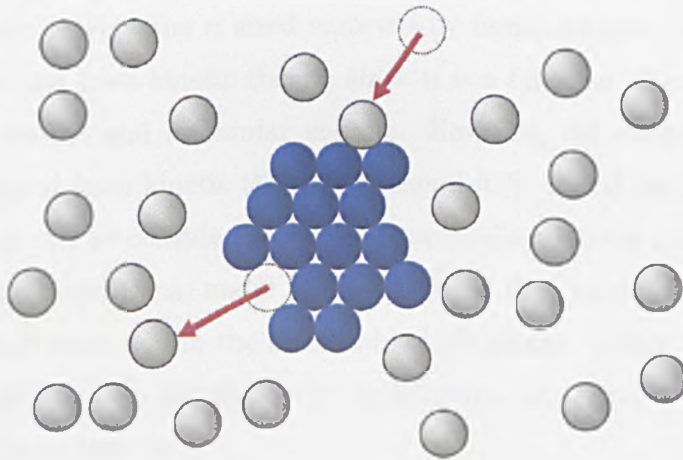


Figure 1.3: The formation of a crystalline embryo (blue atoms) within a metastable bulk phase (grey atoms) is determined by the aggregation and desorption events shown.

The minimum work required for the formation of a new phase, W_{min} can be determined from CNT. The following derivations are adapted from the formation a liquid droplet phase within a supercooled vapour at constant pressure and temperature, following the description given by Debenedetti [60]. This is a somewhat simpler calculation than for the formation of a crystalline embryo within a metastable liquid, but the underlying principles remain the same. The density of embryos is assumed to be sufficiently low that each can be considered in isolation.

Each embryo changes size due to single-molecule events, by the fission and adsorption events described previously (Figure 1.3). Considering an embryo containing n molecules, $D(n)$ denotes the rate at which the embryos changes size. The embryos grow with each single molecular addition onto an embryo containing $(n - 1)$ molecules, whilst simultaneously contracting with each single molecular desorption from a n sized embryo.

$$D(n) = f(n - 1)A(n - 1)\beta(n - 1) - f(n)A(n)\alpha(n) \quad (1.7)$$

where f denotes the concentration of the respective embryos and A their relative surface areas. $\beta(n - 1)$ is the flux of single molecules adsorbing at the interface of a $(n - 1)$ sized embryo. $\alpha(n)$ is the dissociation coefficient, defining the flux of the molecules leaving the n sized embryos by fission events. $\beta(n - 1)$ can be readily determined from kinetic theory, since it is a function of known quantities such as temperature and molecular volume. However, the coefficient $\alpha(n)$ cannot be determined from kinetic theory in general [60]. It will be shown that this kinetic problem can be considered thermodynamically with the imposition of embryo equilibrium conditions, under the assumption that an equilibrium between embryo sizes will exist within the metastable bulk phase. Under the assumption that these coefficients do not change at equilibrium, i.e. $D(n) = 0$, equation 1.7 can therefore be written as

$$N(n - 1)A(n - 1)\beta(n - 1) = N(n)A(n)\alpha(n) \quad (1.8)$$

due to the macroscopic reversibility at equilibrium. In this case, $N(n-1)$ and $N(n)$ denote the respective embryo concentrations.

It can be seen from 1.7 that

$$\frac{\partial f(n,t)}{\partial t} = D(n) - D(n+1) \quad (1.9)$$

such that $D(n)$ defines the rate of n sized embryos formation due to a single molecular addition to $(n-1)$ sized embryos in addition to the single molecular subtraction from $(n+1)$ sized embryos. $D(n+1)$ defines the rate at which n sized embryos vanish due to the addition and subtraction of single molecules. Consequently, the embryo populations do not vary with time when A is independent of n . Using 1.8 to solve for α and substituting into 1.7 it can be shown

$$\frac{D}{\beta A(n-1)N(n-1)} = \frac{f(n-1)}{N(n-1)} - \frac{f(n)}{N(n)} \quad (1.10)$$

when D is independent of n . By summing over all embryo sizes in the range $n = 2$ to $n = \Lambda$, where Λ is a large, indeterminate number, 1.10 becomes

$$D = \frac{\frac{f(1)}{N(1)} - \frac{f(\Lambda+1)}{N(\Lambda+1)}}{\sum_{n=1}^{\Lambda} \frac{1}{\beta A(n)N(n)}} \quad (1.11)$$

Therefore the nucleation rate D is determined only by the adsorption coefficient, β , the equilibrium embryo distribution $N(n)$ and the ratio of single molecules to large sized molecules at equilibrium. The bulk metastable phase consists almost entirely of single molecules, consequently the equilibrium and actual droplet concentrations are indistinguishable. Over the timescale of the phase transition, $f(n)$ must disappear for large n otherwise the system would comprise primarily of the liquid phase. $N(n)$ does not vanish for large n , therefore equation 1.11 becomes

$$D = \frac{1}{\sum_{n=1}^{\Lambda} \frac{1}{\beta A(n)N(n)}} \quad (1.12)$$

It is therefore shown that the kinetic problem arising from the difficulty in calculating α can be solved by the thermodynamic consideration equilibrium embryo concentrations. The minimum work required to form a cluster of n molecules is dependent upon surface and bulk contributions

$$W_{min} = \sigma A + (P - P')V' + n[\mu'(T, P') - \mu(T, P)] \quad (1.13)$$

where σ represents the embryonic surface tension, A is the interfacial area, P and P' are the respective pressures of the bulk phase and the embryo and V' is the embryonic volume. μ and μ' are the respective chemical potentials in the embryo and bulk phases. For a metastable liquid away from the critical radius the embryo can be assumed as incompressible, for which the difference between bulk and embryo pressures can be written as

$$\mu'(T, P') - \mu(T, P) = \nu'(P' - P) \quad (1.14)$$

where ν' is the embryonic molecular volume. Equation 1.13 becomes

$$W_{min} = \sigma A + n[\mu'(T, P') - \mu(T, P)] = \sigma A + n\Delta\mu \quad (1.15)$$

whereby $\Delta\mu$ denotes the change in chemical potentials between the stable and metastable bulk phases. Since the embryonic volume is a measure of n , it follows from basic geometry that

$$A \propto n^{2/3} \quad (1.16)$$

Equation 1.15 is of the form

$$W_{min} = an^{2/3} - bn = 2cr^2 - dr^3 \quad (1.17)$$

where a , b , c and d are positive constants and r is the embryo radius. It follows that n is proportional to r^3 . The work is maximized for a particular value of n ,

i.e. $W_{min}/n = 0$. This is an unstable equilibrium, embryos containing fewer than n^* molecules will dissolve spontaneously, whereas larger embryos ($r > r^*$) are energetically favourable, as the addition of a single molecule results in a lower free energy. Figure 1.4 shows a plot for W_{min} as a function of r , giving the total energy for embryo formation as a function of surface and bulk free energy terms.

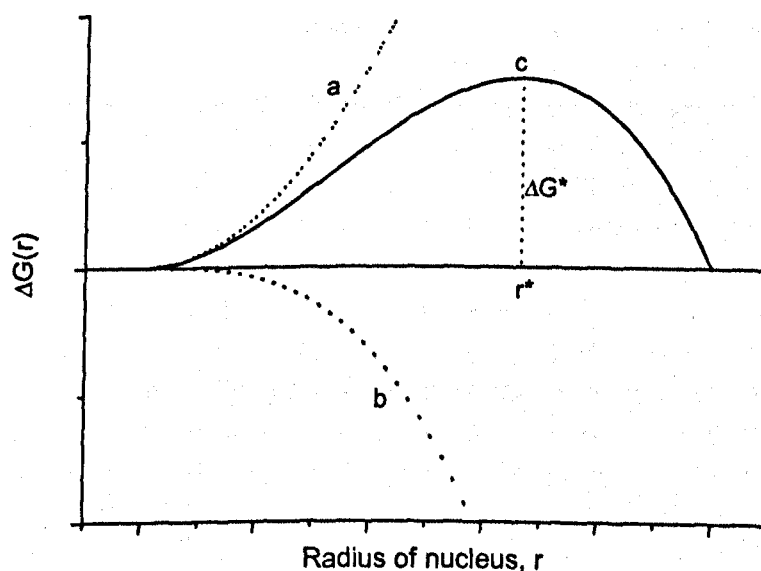


Figure 1.4: Plot of ΔG as function of r for an embryonic phase within a bulk phase. ΔG is dependent on surface (a) and bulk (b) terms, with the critical radius, r^* , at $\delta\Delta G/\delta r = 0$.

The minimum work required for the formation of an embryo has a maximum value at r^* , where $\partial G/\partial r = 0$. A nucleus of radius r^* (containing n^* molecules) is defined as a critical nucleus. For a spherical embryo, n^* , is given by

$$n^* = \frac{32\pi}{3} \left[\frac{\nu' \sigma'^2/3}{(-\Delta\mu)} \right]^3 \quad (1.18)$$

and the critical radius, r^* , is

$$r^* = \frac{2\sigma\nu'}{(-\Delta\mu)} \quad (1.19)$$

The minimum reversible work required to form a critical embryo is

$$W_{min} = \frac{4a^3}{27b^2} = \frac{16\pi}{3} \left[\frac{\nu' \sigma^{3/2}}{(-\Delta\mu)} \right]^2 \quad (1.20)$$

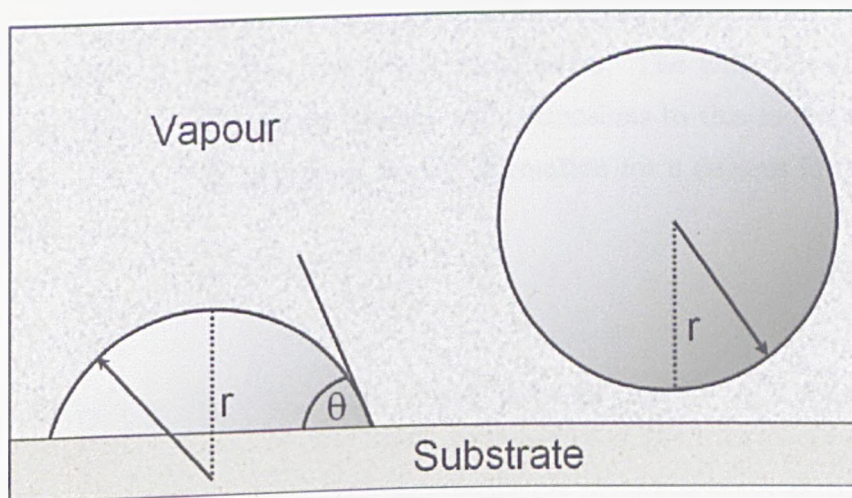


Figure 1.5: Heterogeneous (left) and homogeneous (right) critical nuclei, both of radius r . The heterogeneous nucleus is approximated as a truncated homogeneous nucleus, at internal angle θ to the substrate.

The critical nucleus is at unstable equilibrium. Embryos containing fewer than n^* molecules will spontaneously reduce in size, since each fission process results in a lower overall free energy whereas embryos containing more than n^* molecules will spontaneously increase in size, since each adsorption process lowers the overall free energy. This theory assumes the validity of macroscopic thermodynamics for very small droplets, such that the surface tension for an embryo containing 10-100 molecules is identical to that in flat plane bulk surface tension [64–66]. The validity of this so called capillarity approximation and additional shortcomings of CNT are treated in section 1.2.2.3

1.2.2.2 Heterogeneous Nucleation

In practice, the existence of solids other than the nucleating phase substantially reduces the nucleation barrier for embryo formation, resulting in an increased rate of nucleation [67]. In the case of the formation of a crystalline phase within a melt, foreign surfaces reduce the surface contribution to the overall free energy since the bonds between the molecules in the crystalline phase and the substrate are often stronger than the bonds of solvation [49]. In the case of the formation of the liquid

droplet phase from supercooled vapour, the embryo-substrate interfacial energy is almost always lower than the embryo-bulk phase interfacial energy, reducing the value of ΔW . The embryo will therefore 'wet' the substrate, with a larger degree of wetting corresponding to a lower nucleation barrier. In addition, the developing embryo is distorted, affecting the inter-atomic forces. The following description describes classical heterogeneous theory, with extensions to this model discussed in section (1.2.2.3). The minimum work of formation for a nucleus forming on a substrate is given by

$$W_{min} = \Sigma_{bc}A_{bc} + (\Sigma_{bs} - \Sigma_{cs})F_{bs} + (P - P')V' + [\mu'(T, P') - \mu(T, P)]n \quad (1.21)$$

where A again denotes the interfacial area and Σ now represents the surface tensions of the respective interfaces. The subscripts denote the various interfaces between the bulk phase, b , the crystalline phase, c and the substrate, s . The primed and unprimed quantities refer to embryo and bulk quantities respectively. n denotes the number of molecules in the embryo. At equilibrium this truncated sphere geometry is analogous to that for a water droplet on a surface, a system described by Young's equation [68]. In the case of a crystal nucleus on a substrate (Figure 1.5), the following must hold

$$\sigma_{cs} + \sigma_{bc} \cos \theta = \sigma_{bs} \quad (1.22)$$

Where θ is the substrate-crystalline contact angle, such that an angle of ($\theta = 0$) corresponds to a complete wetting of the substrate and a contact angle of ($\theta = \pi$) corresponds to non-wetting surface and describes homogeneous nucleation. The surface contribution to heterogeneous nucleation can therefore be written as

$$\sigma_{bc}A_{bc} + (\sigma_{bs} - \sigma_{cs})A_{bs} = \pi R^2 \sigma_{cb} [2(1 + \cos(\pi - \theta)) + \sin^2(\pi - \theta) \cos(\pi - \theta)] \quad (1.23)$$

The minimum work required to overcome the nucleation barrier is

$$W_{min} = \frac{16\pi\sigma^3}{3(P' - P)^2} \frac{(1 + \cos(\pi - \theta))^2(2 - \cos(\pi - \theta))}{4} \quad (1.24)$$

This expression is of the same form as equation 1.20 with an additional correction factor dependent on the substrate-crystalline contact angle.

1.2.2.3 Non-classical Nucleation Theory

There are many shortcomings associated with classical nucleation theory. Experimentally, CNT has been found to predict nucleation rates which are too low at small temperatures and too high at large temperatures [69]. Central to CNT is the capillarity approximation, such that the surface tension for an atomic scale curved interface is identical to that for a planar interface in bulk solution. The capillarity approximation also assumes that atoms in the centre of the embryo behave like those within a bulk crystal [70]. These assumptions have been shown to be incorrect in several studies where the critical nucleus contains in the region of 10-50 atoms. Classical theories describing the onset the crystallisation are further complicated by the fact that there is a change in local periodic structure in addition to the change in density. The order in which these processes occur varies with different substances. For metastable liquids composed of small molecules a change in density succeeds crystallisation, whereas for metastable liquids comprising of large molecules, a localised change in density followed by an atomic rearrangement, resulting in a long range periodic structure.

Several studies have adapted density functional theory (DFT) to describe this behaviour, as part of a so called *non-classical nucleation theory*[70-72]. Here the free energy is dependent not only on a single function (embryo radius, R) but on an average spherical density profile $\rho(R)$. DFT treats the embryo phase as an inhomogeneous fluid [69, 70], whereby $\rho(r)$ is expressed in terms of the reciprocal lattice vectors k_i

$$\rho(r) = \rho_0 + \rho_c \sum_i m_i \exp^{iK_i \cdot r} \quad (1.25)$$

where ρ_0 denotes the average density of the metastable bulk phase and ρ_c is the density of the crystalline phase. m_i are structural order parameters describing the periodic structure of the crystalline phase. In the bulk metastable phase, m_i is zero since there is no structural order. Nucleation is therefore characterised by an infinite set of spatially dependent order parameters m_i , in contrast to the single density parameter characteristic of the vapour-liquid phase transition.

As in the CNT model, the DFT theory describes a small embryo is surrounded by the bulk metastable liquid. In this case, however, the order parameters, m_i are dependent on the distance, r , from the centre of the nucleus. The critical nucleus is now described as the saddle point of the space function, yielding a set of coupled equations describing the structure and free energy of the critical nucleus. The saddle point is conventionally found by minimising the grand canonical potential function, Ω , with respect to $\rho(r)$ [69]. By approximating the densities as a sum of Gaussians, centred about the crystal lattice sites, the crystal structure can be assumed to be harmonic such that all higher order structural parameters, μ_i , are related to the first order, μ_1 . This Gaussian approximation yields two ordinary differential equations for the average density change, μ_0 and the structural parameter μ_1 .

$$\frac{\partial \Omega}{\partial \rho_0(r)} = 0 \quad (1.26)$$

$$\frac{\partial \Omega}{\partial m_0(r)} = 0 \quad (1.27)$$

These equations can then be solved for a series of Lennard-Jones atoms. The first stage of crystallisation results in structuring, whereby μ_1 changes at a fixed density. After this density change, there is a resultant change in the average density.

1.2.3 Growth

Growth can be defined as the advances at the liquid-solid or vapour-liquid interfaces due to condensation from a supersaturated phase. In the case of a molecular

crystal within a bulk metastable solution, the solution-crystal interface will grow and dissociate according to similar principles as for heterogeneous nucleation. Indeed, under certain circumstances, crystal growth can be considered as a special case of heterogeneous nucleation for which the interfacial energy of the crystal-solution interface is approximately zero [67]. In this model, growth proceeds by a secondary surface nucleation with the continual addition and incorporation of ions into lattice sites at the advancing interface.

Since this is an activated process, the geometry of the lattice site and the bulk-phase supersaturation strongly affect the surface growth rate. Kossel proposed three types of lattice sites on the crystal surface, kink, step and surface, each with a different interfacial energy (Figure 1.6) [73, 74]. Kink and step sites have three and four *faces* exposed to the bulk phase respectively and are therefore energetically favourable, due to the large number of incomplete bonds within the crystal [75]. Surface sites occur on new layers such that only one 'face' of an adsorbed ion is in contact with the growth face, resulting in a lower binding energy. Surfaces with a large number of step and kink sites will grow at a faster rate or conversely at a lower supersaturation, since these sites propagate with the addition of each ion.

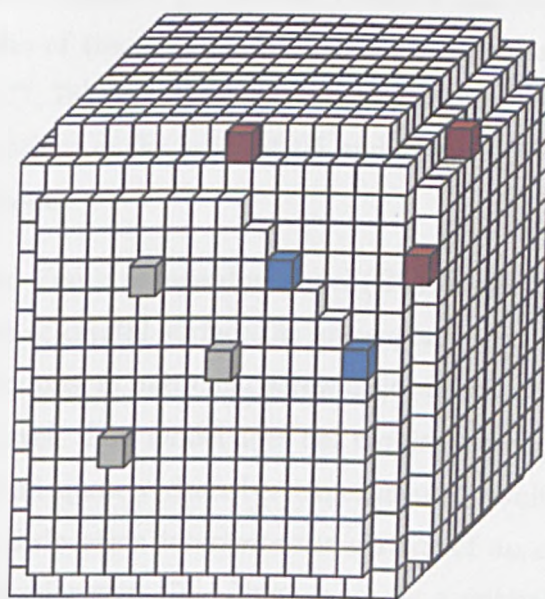


Figure 1.6: The three lattice sites as proposed by Kossel. Surface (grey), edge (red) and kink (blue) sites with 5, 4 and 3 exposed faces respectively

Frank and van der Merve [76] proposed a layer-by-layer growth mechanism describing the surface growth in terms of surface diffusion and step and kink site density. Following their deposition from bulk solution, ions diffuse firstly in two dimensions across the surface, until reaching a step site and then in one dimension across the step site before adsorption at a kink site. This process results in a unit-by-unit growth across the step, until the kink works its way to the surface edge to complete a new step. The next steps propagate in the same manner, until the layer is complete. Although there is an associated energy cost with the adsorption of the first ion on a new step (due to an absence of kink sites), this is small compared with the energy cost of forming a new layer. Indeed, it is the formation of the new layer which leads to the breakdown of the layer-by-layer mechanism.

Once the high index surfaces disappear (those with a high density of steps and kinks), growth proceeds with the two-dimensional nucleation of new molecular layers on low index surfaces (those containing only surface sites) [77]. This is an activated process and is therefore sensitive to the bulk phase supersaturation, with the probability of adsorption negligible below a specific critical supersaturation. This means that an insignificant growth rate arises at a well defined supersaturation ratio (Figure 1.7). Burton, Cabrera and Frank calculated that a supersaturation ratio of the order of 50% would be necessary for nucleation on saturated surfaces [77, 78]. However, experimental observations showed growth to occur at supersaturations of the order of 1% and lower, against the predictions of the layer-by-layer model.

Burton, Cabrera and Frank proposed a model (BCF model), which satisfactorily describes the growth of crystal surfaces at low supersaturations. They suggested that surface imperfections, in particular screw dislocations, act as step sites for the formation of a new layer. This model does not require two-dimensional nucleation at surface sites and adequately describes experimental results at low supersaturations. The screw dislocation intersects the surface of an otherwise flat plane, creating a monomolecular step [79]. Upon reaching a critical size, this step will propagate along the surface, in a self-perpetuating rotary manner (Figure 1.8).

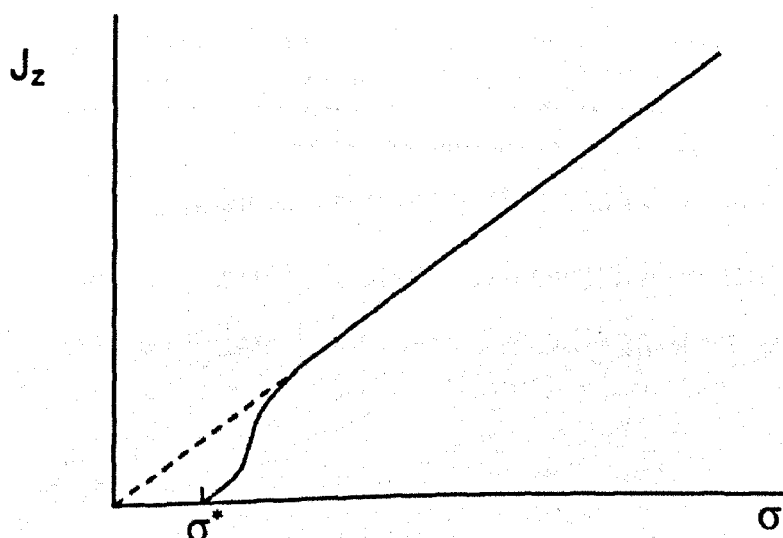


Figure 1.7: Growth rate as a function of supersaturation. According to the layer-by-layer model there should be a critical supersaturation, σ^* below which growth cannot occur, whereas growth has been observed at relative supersaturations below 1% (dashed line)

1.2.4 The Growth Surface

When plotted as a function of fluid flow rate to the surface, the growth rate generally falls into two regimes, transport and kinetic limited. An idealised growth rate versus fluid flow rate is shown in figure 1.9. At a high flow rate, far from equilibrium, the growth is governed by the rate at which the surface can grow given an essentially infinite supply of reactants and is therefore surface, or kinetic limited. At a low flow rate, growth is determined by the addition of reactants to the growth interface, and is thus transport dependent. Despite the continuous motion of the particles at the solid-fluid interface, the supersaturation may be reduced by the formation of a boundary layer at a different concentration to the bulk, due to a hydrodynamic flow rate gradient.

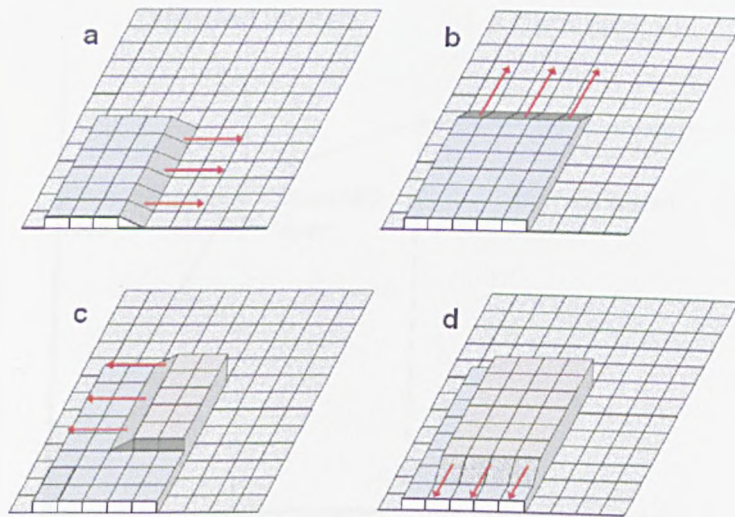


Figure 1.8: **a-d** The progression of a screw dislocation in accordance to the BCF model, accounting for growth as supersaturations below 1%. The screw dislocation progresses in an anti-clockwise manner.

1.3 Crystal Classification

Crystal classification assumes an ideal crystal, containing an infinite, rigid arrangement of uniform atomic unit cells [80]. This can be an unsafe assumption since, all crystals will exhibit certain defects, including irregular occupation of the lattice sites, imperfections in the lattice structure, grain boundaries and edge molecules [81, 82]. The presence of impurities can influence the bulk properties of the crystal including density [83], carrier mobility [84], melting temperature [85] and periodic arrangement. However, these effects are neglected in the following descriptions of the crystal state.

The periodic structures of crystals can be described by the arrangements of atoms and interatomic forces within the smallest possible unit for which it is possible to recreate the crystal by repetition. Such a unit is defined as the *unit cell*, the smallest arrangement of atoms or molecules which can generate the crystal through translation operations alone. The unit cell takes the form of a parallelepiped enclosed by three sets of parallel surfaces. Taking one corner as the origin, it is possible to define the crystallographic reference system. The edges of the parallelepiped define the basis vectors a , b and c , which, along with the angles

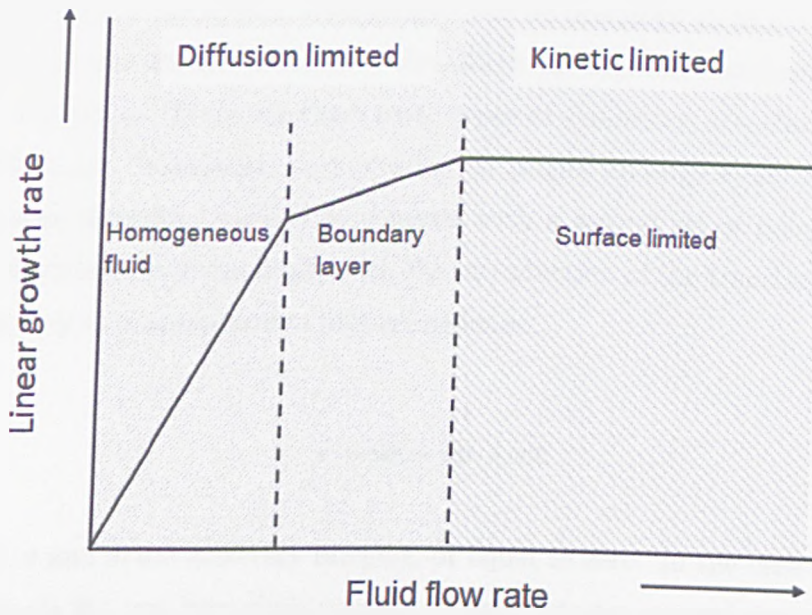


Figure 1.9: Crystal growth rate as a function of fluid flow rate. The system falls into two domains, diffusion and kinetic limited growth.

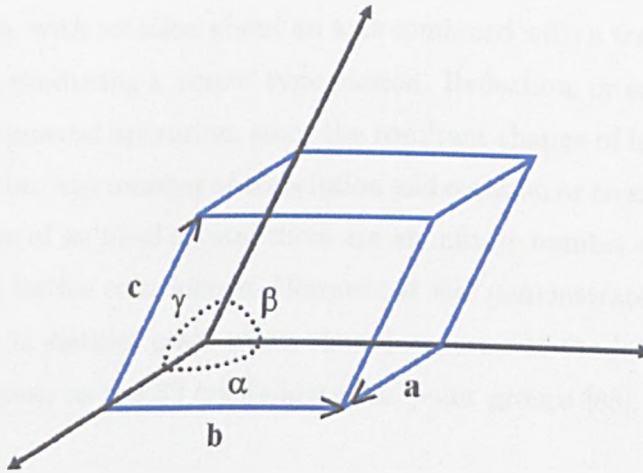


Figure 1.10: The basis vectors a , b , c and the inter-axial angles α , β and γ defining the crystallographic reference system

between these vectors α , β and γ delineate the metric of the cell, and thus the crystallographic reference system (Figure 1.10). Since the positions of the atoms within the unit cell remains constant upon each propagation, there exists an array of identical points throughout the crystal. These points represents the crystal lattice, such that the surroundings of one point are identical to those of all others [86].

The regularity of the atomic arrangement can be described in terms of symmetry elements, an operation which leaves the atomic arrangement unchanged upon arbitrary repetition. There are three basic types of symmetry; translation, rotation and reflection. Translation occurs when all points undergo equal displacement in the same direction, such as to coincide with a second set of points. Translation is described mathematically with the introduction of the translation vector \mathbf{r} , bringing any two lattice points into coincidence.

$$\mathbf{r} = u\mathbf{a} + v\mathbf{b} + w\mathbf{c} \quad (1.28)$$

where u , v and w are arbitrary integers, or equal to zero. In the case of rotation, all points on the axis keep their position. The points are rotated through angle θ , until all points coincide with a second set. The multiplicity of an axis defines the number of times the points will coincide with a different set upon rotation through 2θ (Figure 1.11). A combination of translation and rotation operations results in rototranslation, with rotation about an axis combined with a translation along the axial direction producing a 'screw' type motion. Reflection, or mirror symmetry, is the third fundamental operation, since the resultant change of lattice co-ordinates cannot occur from any number of translation and rotation or translation operations [87]. In the case of an ideal crystal there are an infinite number of such operations which result in lattice coincidence. However, it was demonstrated by Hessel, that there are only 32 distinct cases when viewed in terms of the lattice translational symmetries, known as the 32 crystallographic point groups [88].

1.3.1 Crystallographic Systems

There are seven distinguishable crystallographic symmetry classes, defined by both the symmetry axes and the cell vectors (Table 1.1) [89]. The *cubic* system has the highest symmetry conditions, with the interaxial angles orthogonal and the cell vectors identical. The *tetragonal* system is the result of stretching the cubic system along one of its axes, thus losing the four three-fold symmetry axes associated with the cubic system. This forces a and b to be the same length, with c free to be any length, with the interaxial angles again orthogonal. Similarly, the

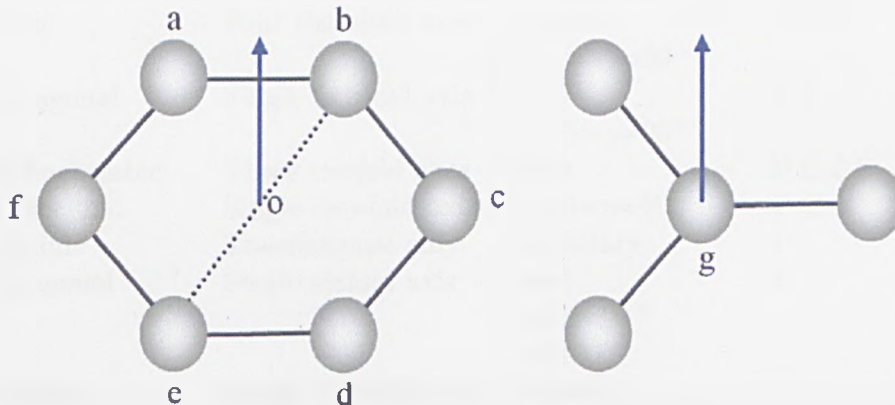


Figure 1.11: 6-fold (left) and 3-fold (right) symmetry axes. $O-Z$ can be rotated through 6 indistinguishable positions through 2π , whereas there are only 3 indistinguishable positions upon rotation through 2π about the $g-Z$ axis. These are two cases for the same lattice

orthorhombic group arises with the unequal stretching of the cubic lattice along two axes, yielding 3 twofold axes. In the *monoclinic* system there are no axial restrictions, with the only criteria being that two of the interaxial angles must be 90° , ensuing in a single twofold rotation axis. The *triclinic* system imposes the fewest symmetry conditions, with no restrictions on axial lengths or angles, resulting in only translational symmetry. The *hexagonal* system occurs in cases where a and b are identical, set at 120° to each other and perpendicular to c . Similar constraints are placed on the *trigonal* (or *rhombic*) system although in this case c is identical to both a and b yielding a single three-fold axis. In the context of this thesis, the rhombohedral, orthorhombic, hexagonal and monoclinic systems are of significance as they correspond to the unit cells of calcite, aragonite, vaterite and mica respectively.

Each of the seven crystallographic systems are associated with a primitive unit cell, denoted P. In addition, there are seven non-primitive unique lattice arrangements associated with the various crystallographic systems. These are body centred (I) with an additional lattice point at the centre of the cell, face centred with an additional lattice point at the centre of each face (F) and on individual faces (A), (B) or (C). For example, a face centred lattice can have a symmetry in accordance

Crystal system	Symmetry elements	Axial restrictions	Lattice types
Cubic	Four threefold axes	$a=b=c$ $\alpha=\beta=\gamma=90^\circ$	P I F
Tetragonal	Single fourfold axis	$a=b$ $\alpha=\beta=\gamma=90^\circ$	P I
Orthorhombic	Three twofold axes	$a=b$	P C I F
Monoclinic	Single two-fold axis	$\alpha=\beta=\gamma=90$	P C
Triclinic	Translational only	Arbitrary	P
Hexagonal	Single sixfold axis	$a=b$ $\alpha=\beta=90^\circ$ $\gamma=120$	P
Trigonal (Rhombohedral)	Single threefold axis	$a=b=c$ $\alpha=\beta=\gamma\neq 90$	P

Table 1.1: The seven crystallographic systems, defined in terms of the symmetry elements present and the axial restrictions. The 14 Bravais lattice arrangements include primitive (P), body centred (I) and face centred on all (F), or individual (A), (B) and (C) faces.

with the orthorhombic system whereas a body centred lattice could fall into either cubic or tetragonal systems. Together, these 14 unique lattice arrangements make up the Bravais lattice, first determined by August Bravais in 1850 [90, 91]

There are exactly 230 possible combinations of symmetry operations (32 point groups plus glide and screw planes) with the Bravais translations known as crystallographic space groups. These are conventionally described using Hermann-Mauguin (international) notation, and are listed fully in reference [92].

1.3.2 Indexing Faces

A freely growing crystal consists of a small number of flat surface elements governed by the thermodynamic conditions of growth (section 1.2.4). The perpendiculars to these faces possess a characteristic set of normal angles in accordance to the law of angular consistency. The rate at which a face grows is determined by the microscopic topography (section 1.2.3) whereby faces with a high density of step and kink sites tend towards a faster growth rate than those without these sites. Since fast growing faces, soon disappear, the resultant morphology is dominated by the slow growth faces. Thus, in most cases, the resultant crystal form is in fact a macroscopic version of the unit cell.

Miller indices are conventionally used for indexing crystal faces, with a family of lattice planes defined by vectors l , m and n . More formally, Miller indices are the reciprocals of the fractional intercepts which the plane makes with the crystallographic axes [93]. The notation $\{l,m,n\}$ denotes a family of planes equivalent to the lattice symmetry, whereas the notation $[l,m,n]$ denotes a lattice vector, (loosely) equivalent to a single plane bisecting points on the crystal lattice. Examples in this thesis include the (001) muscovite mica basal cleavage plane and the $\{104\}$ calcite unit cell.

1.4 Calcium Carbonate

In the context of the work presented in this thesis, it is worth considering the crystalline properties of a particular kind of mineral; carbonates. Carbonates, salts containing CO_3^{2-} groups, are of enormous significance in the context of biomineralisation, geology and synthetic crystal growth. Dolomite ($\text{CaMg}(\text{CO}_3)_2$) is amongst the most abundant of the rock-forming carbonates [94, 95], with applications as a flux in industrial processes and in horticulture to neutralise soil acidity. Other important carbonates include magnesium carbonate (MgCO_3) and potassium carbonate (K_2CO_3), widely used in industrial processes. Iron carbonate (FeCO_3) is used as a ceramic pigment and occasionally as an ore during the production of iron. Strontium carbonate (SrCO_3) is commonly used to make glazes and as a colourant in chemical reactions [96] whereas barium carbonate (BaCO_3) is used in ceramics and as a poison. Two important categories of carbonates are the calcite-type structures, including MgCO_3 and FeCO_3 and the aragonite-type structures including SrCO_3 and BaCO_3 . Calcite and aragonite are in fact the two most stable polymorphs of calcium carbonate (CaCO_3), each described in further detail below.

1.4.1 Calcite

The structure of calcite can be loosely considered as a modified version of the primitive sodium chloride (NaCl) unit cell [94]. For a face centered cubic (NaCl) structure, the primitive unit cell takes the form of a rhombohedron in which the

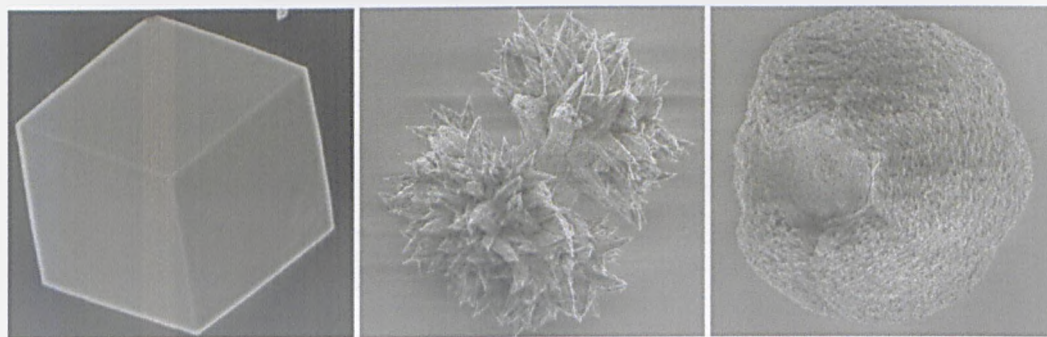


Figure 1.12: SEM micrographs of the anhydrous polymorphic forms of calcium carbonate, from left to right calcite, aragonite and vaterite. Image sizes $5 \times 5 \mu\text{m}$.

	Calcite	Aragonite	Vaterite
Crystal System	Hexagonal	Orthorhombic	Hexagonal
Space group	R3c (167)	mmm (62)	P63 (194)
Cell parameters			
$a(\text{\AA})$	4.99	4.96	7.135
$b(\text{\AA})$		7.97	
$c(\text{\AA})$	17.06	5.74	16.98
$V(\text{\AA}^3)$	121.96	227.08	748.61

Table 1.2: The CaCO_3 unit cell parameters for the CaCO_3 polymorphs calcite, aragonite and vaterite.

body diagonal coincides with the 3-fold axis of symmetry of the cubic unit cell. Substituting the Na^+ ions with Ca^{2+} and the Cl^- ions with CO_3^{2-} results in a stretch along the c -axis to accommodate the carbonate ions, such that the angles of the translational vectors form angles of approximately 46° [97]. This results in a series of alternating Ca^{2+} and CO_3^{2-} layers along the c -axis, with the carbonate ions taking the form of equilateral triangles lying parallel to the (111) plane. The carbonate ions lie in identical orientations within each layer, with a 60° rotation between successive layers (Figure 1.13). Important crystal planes in the context of the results presented in this thesis are included in the figure.

There are some obvious shortcomings with this analogy, since the Cl atoms are centers of symmetry of the NaCl structure, whereas the carbonate ions have alternating orientations in the calcite structure [94]. The formal description of calcite is that of a hexagonal, rhombohedrally-centered unit cell belonging to space group $R\bar{3}c$, for which the cell parameters are listed in table 1.2.

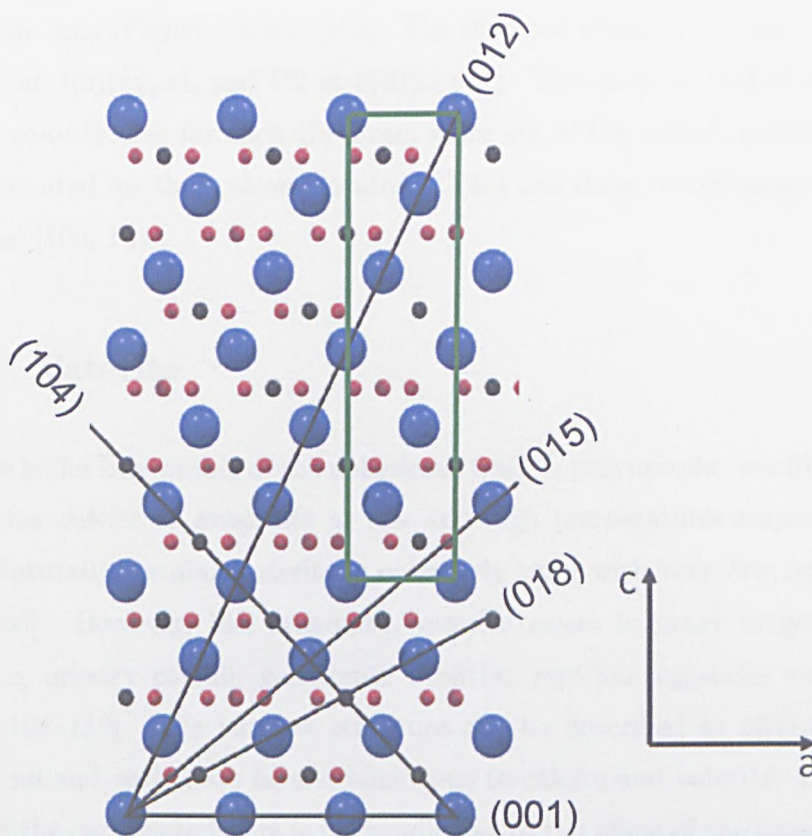


Figure 1.13: The crystal structure of calcite, showing the relative atomic positions of calcium (blue), oxygen (red) and carbon (black) viewed perpendicular to the c -axis. An alternating layered structure is apparent. A single unit cell is shown, (green lines) and several important crystallographic planes are indicated.

1.4.2 Aragonite

Aragonite is both the second most common and stable form of CaCO_3 . Under most conditions, aragonite is metastable with respect to calcite, forming within a narrower range of chemical and physical conditions. However, aragonite has a greater density and hardness in comparison to calcite. Along with calcite, aragonite is an important biomineral with a widespread occurrence in nature [23, 98], despite its relative thermodynamic instability.

The structure of aragonite was first determined by Bragg (1924) and Wyckoff (1925) [99–101]. Aragonite has an orthorhombic symmetry (space group No. 62), with the calcium ions arranged in a pseudo-hexagonal lattice arrangement parallel to the (001) plane. The CO_3 group is almost indistinguishable from that in calcite, although unlike calcite the calcium ions are separated by two distinct layers of

carbonate ions (Figure 1.14a). [102]. The reported atomic co-ordinates are Ca, C and O1 at $4(c)(\frac{1}{4}y, z)$, and O2 at $8(d)(x, y, z)$. This gives a total of nine possible atomic co-ordinates for each Ca atom, since six of the atomic coordinates could be substituted for three atoms located at $(4c)$ and three co-ordinates for O2 at $8d$ positions [103, 104].

1.4.3 Vaterite

Vaterite is the least stable of the anhydrous CaCO_3 polymorphs, readily converting into either calcite or aragonite at low and high temperatures respectively [105–107]. Naturally forming vaterite is extremely rare, with very few reported cases [105, 106]. However, like aragonite, vaterite exists in many biogenic systems, including urinary calculi, gallstones, otoliths, reptilian eggshells and lacklustre pearls [108–110]. The vaterite structure can be described as alternating layers of calcium and carbonate layers, analogous to calcite and vaterite. However, the plane of the carbonate layers is perpendicular to the plane of the layers, with each calcium ion coordinated by 6 carbonate molecules, with three from each adjacent layer (Figure 1.14b) [111].

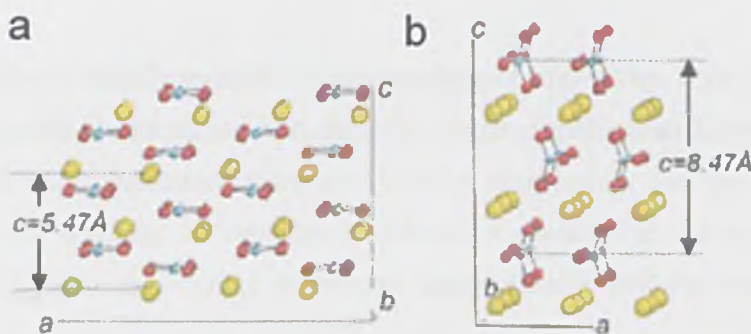


Figure 1.14: The crystal structures of **a** aragonite and **b** vaterite, showing the relative atomic positions of calcium (yellow), oxygen (red) and carbon (blue) viewed perpendicular to the a -axes (adapted from reference [111]).

Chapter 2

Experimental Methods

This section describes the general methods used for the preparation of substrates and the precipitation of CaCO_3 in addition to the techniques used for the characterisation of substrates and precipitates. The crystal simulation programs are also described.

2.1 Experimental Preparation

Crystallisation is highly sensitive to the presence of impurities, with trace amounts of contaminants (surfactants, dust particles, organic molecules) known to dramatically effect both nucleation rates and crystal morphology (section 1.3). A Reduction in the quantity of impurities is therefore essential in the reproduction of results, with rigorous cleaning procedures undertaken before each experiment.

Preparatory tools (tweezers, scissors, scalpels etc.) were rinsed with ethanol prior to use. Preparatory glassware was soaked in a 10% wt/v solution of NaOH for two hours in an ultrasonic bath, resulting in a gradual etching of the glass surface and the removal of organic contaminants [112]. The sonication provided an additional mechanical cleaning and was useful in the removal of larger contaminants. Next the glassware was sonicated in milli-Q deionized water (resistively $18.2 \text{ M}\Omega\text{cm}^{-1}$) for 15 minutes to remove any residue. Glass substrates were further cleaned with a 5 min immersion in 'Piranha' solution, consisting of sulfuric acid (H_2SO_4) and hydrogen

peroxide (H_2O_2) in a 3:1 ratio. All remaining organic particles are removed during this violent oxidative reaction [113],



The curved glass substrates used for the crossed cylinder experiments were unable to withstand the high temperatures generated during the piranha reaction ($> 100^\circ\text{C}$). As an alternative, the half cylinders were cleaned in a Plasma-Preen argon plasma cleaner for 10 minutes at 40% power, after the usual NaOH cleaning protocol.

2.2 Substrate Preparation

A large proportion of the work presented in this thesis involves the heterogeneous crystal growth on substrates. Glass slides, muscovite mica, and functionalised self assembled monolayers (SAMs) were all used as substrates. Glass microscope slides (75 x 25 x 2 mm) were cut in half with a diamond tipped scribe, before cleaning using the procedures outlined in section 2.1. The preparation of the mica and SAM substrates involved more complex procedures and is described in detail below.

2.2.1 Muscovite Mica

Microscope-slide sized pieces of muscovite mica (S&J Trading, New York, or Watanabe Co. Japan) were cut from large sheets in a laminar flow cabinet (OS class) to prevent contamination. Using a scalpel knife and fine point tweezers, the mica was cleaved from both sides to an approximate thickness of 20-50 μm at room temperature. The exact treatment of the mica after cleaving is of critical importance, since this can affect the adsorption properties and the occurrence of epitaxial crystal growth (section 3.1). This conditions to which the mica was exposed after cleaving are referred to hereafter as the *weathering conditions*. Mica

weathered at laboratory humidity was left to stand in the laminar flow cabinet, with the temperature and humidity monitored using a Testo 450 hygrometer. Mica weathered at low humidity (<10%) was left in a dessicator containing ~20 g calcium hydride (Sigma Aldrich), whereas mica weathered at 100% humidity was placed in a dessicator equilibrated with water overnight. Aqueous lithium chloride (Sigma Aldrich) solutions were used when an exact humidity was required, with the variation in partial vapour pressure with solution concentration taken from reference [114].

2.2.2 Self Assembled Monolayers

The first stage in the formation of SAMs involves the deposition of a gold substrate. The crystalline quality of the gold surface is an important factor for consideration, since this directly affects the close packing of the SAM [115]. Au surfaces predominantly exhibit (111)-oriented terraces, the lowest energy configuration for this metal [116]. The number of non (111)-oriented terraces, in addition to the general density of defects, is dependent upon the growth conditions of the metal film. Gold films were deposited on either freshly cleaved mica or glass substrates cleaned in accordance to section 2.1. The deposition took place in an all metal Cressington 308-R vacuum chamber at a nominal pressure of approximately 10^{-6} mbar, adapted from the process described by Critchley [117]. Chromium was sputtered to a thickness of 2 nm from a 3.2 mm target (Cressington DC 100 Dual Output HT Plasma Supply) at a rate not exceeding 1 \AA s^{-1} to promote adhesion and increase mechanical stability. A 50-150 nm gold layer (Goodfellow 99.99%) was thermally evaporated from a resistively heated tungsten boat at the same rate of 1 \AA s^{-1} ensuring sample uniformity and a high quality substrate. The substrates were then rinsed using copious amounts of Milli-Q water, before drying under a nitrogen stream.

SAMs were formed by immersing the gold substrates in 0.1-1 mM solutions of commercial reagent grade thiols (Sigma-Aldrich) in either ethanol (absolute grade) and acetic acid (Sigma-Aldrich HPLC grade) mixed in a ratio of 9:1, or dichloromethane (DCM) (Fisher Scientific, HPLC grade) solvent, maintained at 4°C. Immersion

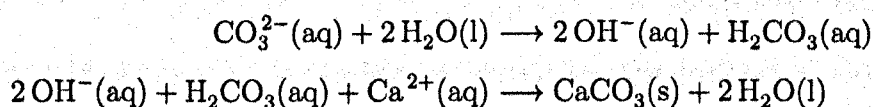
times were varied between 1 and 24 hours and the SAMs were characterised using XPS and contact angle measurements. Hydrophilic SAMs were formed from solutions of mercaptohexadecanoic acid (MHA), whereas hydrophobic SAMs were formed from solutions of either octadecane thiol (ODT) or perfluorodecane thiol (PDT).

The functional group of the alkylthiol determines the wetting properties and degree of heterogeneous nucleation on the SAMs (section 4.1). The work presented in sections 4.3.3 and 7.1 involves crystal growth on patterned SAMs, where the surfaces are functionalised to produce specified nucleation regions. The SAMs were patterned using a deep UV photolithography method adapted from others [118, 119]. A hydrophobic SAM, prepared as described previously, was placed on a patterned quartz photomask at a distance of 2 cm from a $\lambda = 254$ nm wavelength UV penlight. The photomask included three geometric shapes (circles, squares and stripes) each with six possible sizes (range 5-50 μm). Irradiation times were varied between 15 and 120 minutes, after which the samples were thoroughly rinsed with ethanol to remove any partially cleaved molecules and other impurities, before rinsing with Milli-Q water and drying under a nitrogen stream. The samples were subsequently backfilled in MHA for one hour at 4°C before rinsing with Milli-Q water. Growth experiments were typically carried out within 10 minutes of removing from solution, since these high-energy surfaces tended to adsorb material quickly.

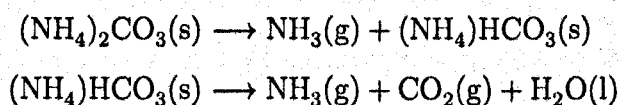
2.3 Crystal Growth

CaCO_3 was precipitated from aqueous solutions using either double-decomposition or gas-diffusion methods. For the double decomposition method, equimolar solutions of CaCl_2 (Sigma-Aldrich) and Na_2CO_3 (Sigma-Aldrich) in Milli-Q water were combined in equal volumes, following the method described by Lam [120]. The majority of experiments were in a concentration range of 1-10 mM, with growth periods between five seconds and several days. In most cases, crystal growth was

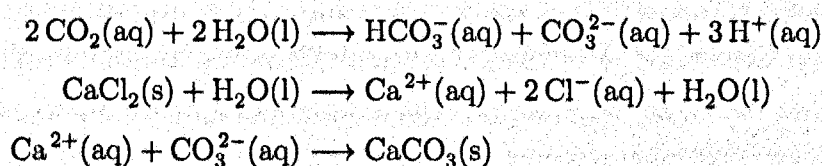
terminated by removing the substrate from solution and rinsing with Milli-Q water and drying under a nitrogen stream. Precipitation occurred by the following pathway,



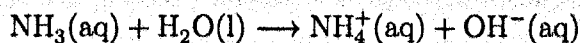
For the gas-diffusion method, aqueous solutions of CaCl_2 (Sigma-Aldrich) were exposed to CO_2 generated upon the decomposition of $(\text{NH}_4)_2\text{CO}_3$ within a sealed dessicator by the following process [121]



CO_2 dissolves into the aqueous CaCl_2 solution, maintaining supersaturation. CaCO_3 precipitates via the following pathway,



The NH_3 gas is a base and acts as a proton acceptor, maintaining the pH of the solution.



The termination of gas diffusion growth was the same as described for double decomposition growth.

2.4 Characterisation Techniques

The substrates and CaCO_3 precipitates were characterised using a variety of techniques. SAM-on-gold substrates were characterised using contact angle measurements and X-ray photoelectron spectroscopy (XPS). CaCO_3 images were obtained using optical and electron microscopy, in scanning (SEM) and transmission (TEM) modes. Raman spectroscopy was used for polymorphic analysis, whereas calcite orientations were verified using X-Ray diffraction. Amorphous lifetimes were determined using UV-Vis spectrophotometry. An brief overview of each is presented here.

2.4.1 Contact Angle Measurements

Water contact angle measurements were recorded for the liquid-vapour interfacial angle with the solid substrate. This was used for the characterisation of SAMs in section 4.3.1. Surface wetting is governed by Young's equation,

$$\gamma_{LV}\cos\theta = \gamma_{SV} - \gamma_{SL} \quad (2.2)$$

where γ denotes the surface tensions of the liquid-vapour, solid-vapour and solid-liquid interfaces respectively. In cases where γ_{SL} is greater than γ_{SV} the cosine term is negative, resulting in a contact angle greater than 90° . In these cases the surface is said to be hydrophobic. Conversely, for hydrophilic surfaces, γ_{SL} is less than γ_{SV} , and the liquid wets the surface. Both advancing and receding contact angles were recorded from the point at which the droplet began to move across the surface. These values defined the maximum range of angles, since all real surfaces display hysteresis, attributed to surface roughness, surfactants and energy dissipation during adsorption of liquid molecules [62].

Contact angles were determined experimentally using an automated FTA 4000 microdrop system, with a 10 picolitre resolution in droplet volume. Advancing and receding angles were obtained for each sample, each from a minimum of 20 images under ambient conditions. Each reading was repeated a minimum of three times.

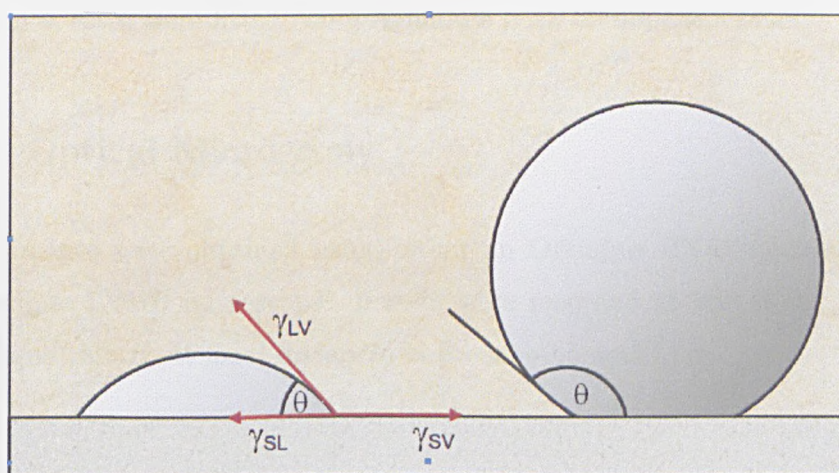


Figure 2.1: Substrate-water contact angle for a hydrophilic surface (left) and a hydrophobic surface (right). The subscripts LV, LS and SV define the liquid-vapour, liquid-substrate and substrate-vapour interfaces respectively.

2.4.2 XPS

The deep-UV photo-patterning of SAMs was characterised using XPS, an analytical surface spectroscopy, giving quantitative information of the top 1-10 nm of a surface, including chemical state, empirical formula and elemental composition. The sample is excited with monochromatic X-ray radiation with the energy of the incident photon imparted on the core electrons within an atom. The electrons exit the atom if the energy of the incident photon, $h\nu$, is greater than the binding energy. By conservation of energy,

$$\text{Binding energy} = h\nu - \text{kinetic energy}$$

Each element possesses a unique set of XPS peaks when plotting intensity as a function of binding energy. From this, the elemental surface composition can be determined.

Experimentally, spectra were obtained using a Thermo Electron Corporation ESCA Lab 250 system in accordance with the procedure listed by Shimoda *et al.* [117]. X-rays were emitted from a monochromatic Al K α source (15kV 150 W) with a spot diameter of 0.5 mm, at a base pressure of 10⁻⁹ mbar. Pass energies of 150 eV were used for large area surface scanning and 20 eV for detailed scans. High resolution spectra were fitted using Avantage peak fitting algorithms.

2.4.3 Optical Microscopy

Optical images were obtained using either an Olympus BX41 microscope or a Nikon eclipse LV100 microscope. Images were recorded at 50x, 100x, 200x and 500x magnifications at focal distances between ~0.5 and 1 cm.

2.4.4 Electron Microscopy

Electron microscopy was widely used for a large part of the results presented in this thesis, operating in two principle modes, transmission electron microscopy (TEM) and scanning electron microscopy (SEM). A brief overview of each is presented here.

2.4.4.1 Transmission Electron Microscopy

The wavelength of an electron, λ , is given by the de Broglie equation.

$$\lambda = \frac{h}{p} \quad (2.3)$$

where h is Planck's constant and p is the relativistic momentum of the electron. The electrons are accelerated in an electric field to velocity v ;

$$v = \sqrt{\frac{2eU}{m_0}} \quad (2.4)$$

where m_0 is the mass of an electron and e is the charge of an electron. A TEM operating at a 200 kV potential will accelerate the electrons to approximately 70% of the speed of light, with relativistic effects therefore needed to be taken into consideration. The electron wavelength is given by

$$\lambda = \frac{h}{\sqrt{2m_0eU}} \frac{1}{\sqrt{1 + \frac{eU}{2m_0c^2}}} \quad (2.5)$$

where the first term is a non-relativistic expression and the second term is a relativistic correction factor. It follows that the wavelength of electrons accelerated at 200 kV is 2.5×10^{12} nm. This suggests a theoretical TEM resolution five orders of magnitude greater than for optical microscopy [122]. However, diffraction artefacts and spherical and chromatic aberrations prevent the theoretical limit from being obtained. Electrons are generated from a thermionic or field emission source, with the field emission source used in high resolution (HR) systems. Whereas light microscopy utilizes glass lenses to bend a light beam, electron microscopy uses electromagnetic lenses to bend an electron beam. The electromagnetic lenses are modified solenoids, with the focal length governed by the accelerating voltage of the electron beam and the lens field strength. The basic setup of a TEM is shown in figure 2.2 adapted from reference [123].

Experimentally, TEM images were obtained using a Phillips CM 200 FEGTEM at 200 kV gun voltage, exposure time 3-10 s. Samples were deposited onto 100×100 Cu grids (Agar Scientific) and dried under N_2 .

2.4.4.2 Scanning Electron Microscopy

The lens construction of SEM is similar to that of TEM. However, unlike in TEM and optical microscopy, the image is not formed by conventional optical principles [124]. In this case, a demagnified spot of electrons is scanned across the surface of an electrically conductive specimen. It is therefore often necessary to deposit a conductive layer onto the surface before imaging.

A schematic diagram of a basic SEM instrument is shown in figure 2.3. The electrons are produced using field emission or thermionic sources under high vacuum

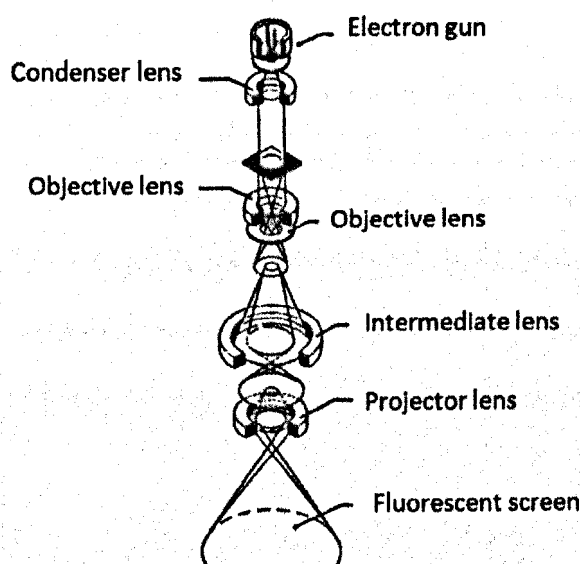


Figure 2.2: Schematic diagram showing the components of an TEM column, adapted from figure 2.2 in reference [123].

column. A series of two or three condenser lenses then demagnify the spot size down to 2 nm. The electron spot is rastered along the surface by a pair of deflector coils. The electrons interact with the specimen up to a depth of 1 μm , generating the electrons which form the image [125]. Different sources of electrons are produced when the electron beam interacts with the surface, with secondary electrons and back scattered electrons most commonly used for imaging. The SEM images presented in this thesis were exclusively obtained in secondary electron mode. A complete description of this detector is presented in reference [124]. Secondary electrons were collected by a Everhart-Thornley (E-T) detector, located behind a positively charged collector screen. Contrast in the image arose due to a change in signal intensity at different surface locations.

Experimentally, high resolution SEM images were acquired using a LEO 1530 FEG-SEM, at a 3 kV operating potential and a 3 mm typical working distance. Low resolution SEM images were obtained using either a Phillips XL-30 ESEM or a JEOL Neoscope benchtop SEM at a 5-30 kV operating potential and a 5-10 mm typical working distance. Both techniques operated at a mid-range chamber vacuum ($\sim 10^{-3}$ mbar). In all cases, samples were coated with a layer of 5-10 nm Pt to prevent charge accumulation.

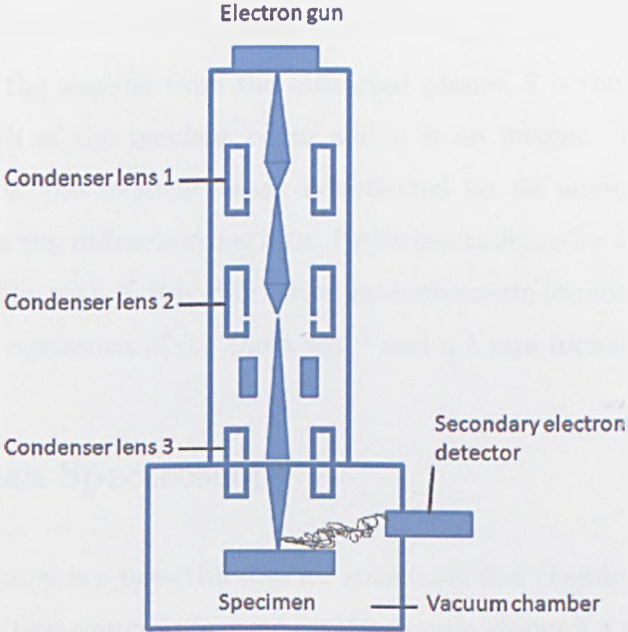


Figure 2.3: Schematic diagram showing the components of an SEM column.

2.4.5 X-Ray Diffraction

X-Ray diffraction was used to verify SEM orientational analysis of epitaxial calcite crystals on mica in section 3.2.2. XRD is non-destructive technique, measuring the scattering of X-rays from atoms in the crystal lattice. Destructive interference from an array of regular scattering centres (crystal lattice) occurs at most incident angles. The incident angles at which constructive interference occurs are defined by Bragg's law[126].

$$2d \sin \theta = n\lambda \quad (2.6)$$

where d defines the spacing from the diffracted planes, θ is the incident angle, λ is the wavelength of the incident beam and n is an integer. In cases of Bragg reflection, part of the incident beam is deflected by an angle 2θ , producing a reflection spot in the diffraction pattern. Experimentally, $\sim 2 \times 2$ cm samples were mounted vertically, with X-Ray diffraction measurements obtained using a Bruker 100 system at a resolution of 0.1 theta sec^{-1} and a 1 min incremental scan rate.

2.4.6 Raman Spectroscopy

Raman spectroscopy is a powerful tool for structural and chemical analysis, where the light from a laser source is focused on the sample through a microscope objective (typically $50\times$) and the scattered light is collected through the same lens. The collected light passes through various gratings and notch filters leaving only the Raman, or inelastically scattered, light. The origin the Raman scattering lies in the interaction of vibrational or rotational motions of molecules with electromagnetic radiation. It should be noted that there is another type of inelastic scattering, Brillouin scattering, originating in the translational motion molecules, however the frequency shift is minimal and is not applicable here [127]. The intensity of the Raman scattered light as a function of incident wavelength is dependent on the various vibrational and rotational modes present within a molecule and the Raman spectrum is therefore unique to each substance. Through a detailed comparison

with reference databases, substance identification over sub-micron areas is possible. Raman spectroscopy was used for CaCO_3 polymorph analysis throughout chapters 4 & 5 and a discussion of the Raman active CaCO_3 modes is presented in section 5.3.2

Experimentally, Raman spectra were acquired using a Renishaw inVia microscope equipped with a 785-nm high-performance near-IR (HP-NIR) diode laser with a $1\ \mu\text{m}$ spot size, using a $50\times$ objective lens.

2.4.7 UV-VIS Spectrophotometry

Turbidity of ACC suspensions were measured using UV-VIS Spectrophotometry in section 6.3.1. Time-driven spectrophotometry measurements were obtained using a Perker-Elkin UV-Vis spectroscopy at a 500 nm wavelength in transmission mode, for a time period of 1200 s. All measurements were taken for 1 ml of solution unless otherwise stated, using disposable plastic cuvettes (Fisherbrand). Various experimental parameters were investigated and are described in detail in section 6.3.1.

2.5 Analytical Software

Calcite orientations were determined in accordance to the method outlined by Archibald *et al.* [128] by measuring the interfacial angles around the three-fold axis and comparing to simulated crystals in known orientations using the SHAPE program, version 7.0 (sections 3.1 and 4.3.2). Side profiles of calcite crystals were also calculated in section 3.2.2 in order to show changes in (001) conformations as a function of ACC contact angle.

Atomic structures were calculated for muscovite mica using Powdercell (version 2.4), with cell refinement data taken from the RRUFF database (section 3.1). Images were rendered using POV-RAY (version 3.6).

Crystal size distributions were determined using imageJ (version 1.42), with the procedure shown in figure 2.4. Firstly the image scale was set before adjusting

the threshold level and switching to a binary image such that only the CaCO_3 particles were visible. The particle size distribution tool gave the number and sizes of the particles, which were compared with the original image for verification (Figure 2.4).

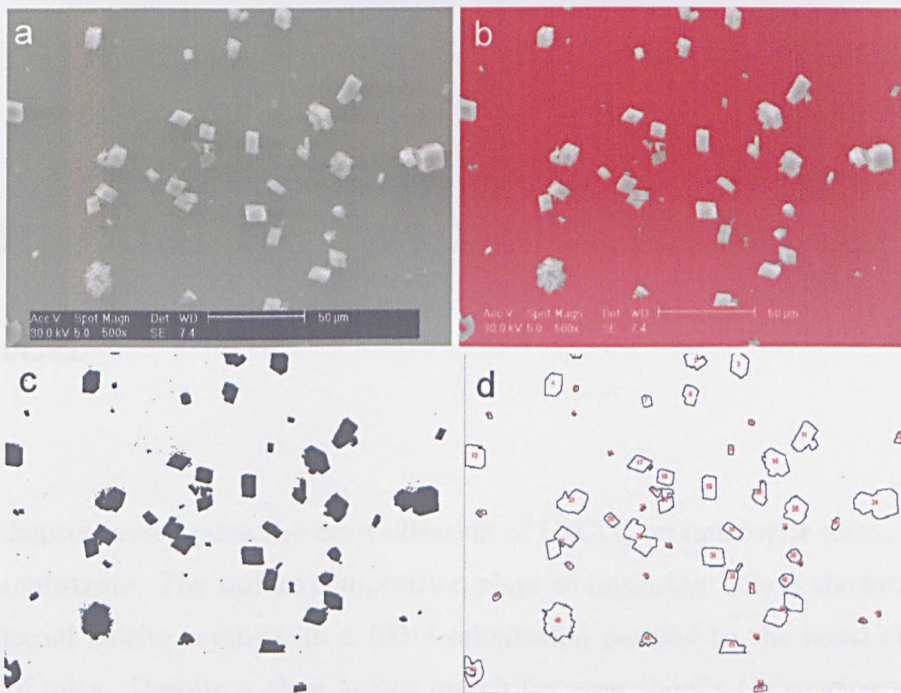


Figure 2.4: The ImageJ particle size analysis procedure. **a** Setting the scale, **b** adjusting the threshold, **c** switching to binary mode and **d** analysis of particles.

Chapter 3

Epitaxial Growth of Calcite on Mica

This chapter investigates the crystallisation of CaCO_3 on muscovite mica, a crystalline substrate. The surface composition plays an important role in the formation of epitaxial calcite crystals, in a (001) orientation parallel to the basal cleavage plane of mica. Despite a close lattice match between the Ca-Ca spacing parallel to the (001) plane (0.499 nm) and the adjacent K^+ site spacing of the mica basal cleavage plane (0.512 nm), epitaxial overgrowth does not occur on freshly cleaved mica surfaces. However, mica surfaces weathered at ambient (35-40 %) humidity for a time period of 30 minutes or greater will support the epitaxial overgrowth of calcite. Nanometer sized K_2CO_3 crystallites are known to form on weathered mica surfaces, and it is shown through a variety of ion exchange processes that these crystallites are necessary for the epitaxial growth of calcite. Calcium ions do not readily adsorb to mica surfaces at the concentrations used here, and it is proposed that the K_2CO_3 crystallites act as specified nucleation sites, where the localised concentration of Ca^{2+} and CO_3^{2-} ions is sufficiently high to promote epitaxy.

3.1 Introduction

Mica substrates have long been used to promote the ordered overgrowth of alkali and ammonium halides. The first systematic studies of epitaxy were performed

over 80 years ago by Royer, who demonstrated the epitaxial growth of RbI, KBr and KCl on mica from aqueous solution [129, 130]. Using the same system, Schulz subsequently obtained the same results for epitaxial growth of RbI, KFl and LiCl from both the vapour phase and from solution precipitation [131, 132]. It was Schultz, along with Lisgarten, who first attributed the epitaxy to a lattice match between the (111) plane of alkali halides and the (001) basal mica cleavage plane [133].

The face-selective templated growth of calcite (CaCO_3) has been reported on numerous modified substrates including alkanethiols [134–136], Langmuir monolayers [137] and functionalised polymer surfaces [138]. It is a source of ongoing debate as to what extent this growth can be considered epitaxial, since the face-selectivity arises from favourable chemical interactions between the substrate and a particular crystalline growth plane as opposed to a direct lattice match between the substrate and crystal phase. Examples of true CaCO_3 epitaxy are less common, with lithium niobate [139], dolomite [140] and zabuyelite [141] being notable substrates. The results presented in this chapter are the first systematic study of the epitaxial overgrowth of calcite on mica. It is shown that epitaxy is dependent on more than a simple lattice match between calcite and mica, and is partly governed by a reconfiguration of a mica surface which occurs naturally upon cleaving. It is worth first considering the structure of mica, and the nature of this surface reconfiguration.

Muscovite mica is often used as a substrate for adsorption of entities ranging from small biomolecules to bacteria and cells [142], and it is also a useful model surface for a variety of surface techniques, including X-Ray reflectivity, atomic force microscopy (AFM), shear force microscopy and surface force measurements [143]. This is due to the ease of cleavage along the (001) basal plane to yield an atomically smooth surface, free of steps across areas of tens of centimetres squared.

Muscovite mica, ideal formula $\text{KA}_1\text{Al}_2(\text{AlSi}_3)\text{O}_{10}(\text{OH})_2$, has a layered pseudo-hexagonal structure (Figure 3.1). Each monoclinic unit cell consists of two silicon layers and an aluminium layer, tetrahedrally and octahedrally coordinated with oxygen respectively. On average a quarter of the Si^{4+} ions are substituted with Al^{3+} cations, leading to one negative charge per surface unit cell. Charge neutrality is satisfied

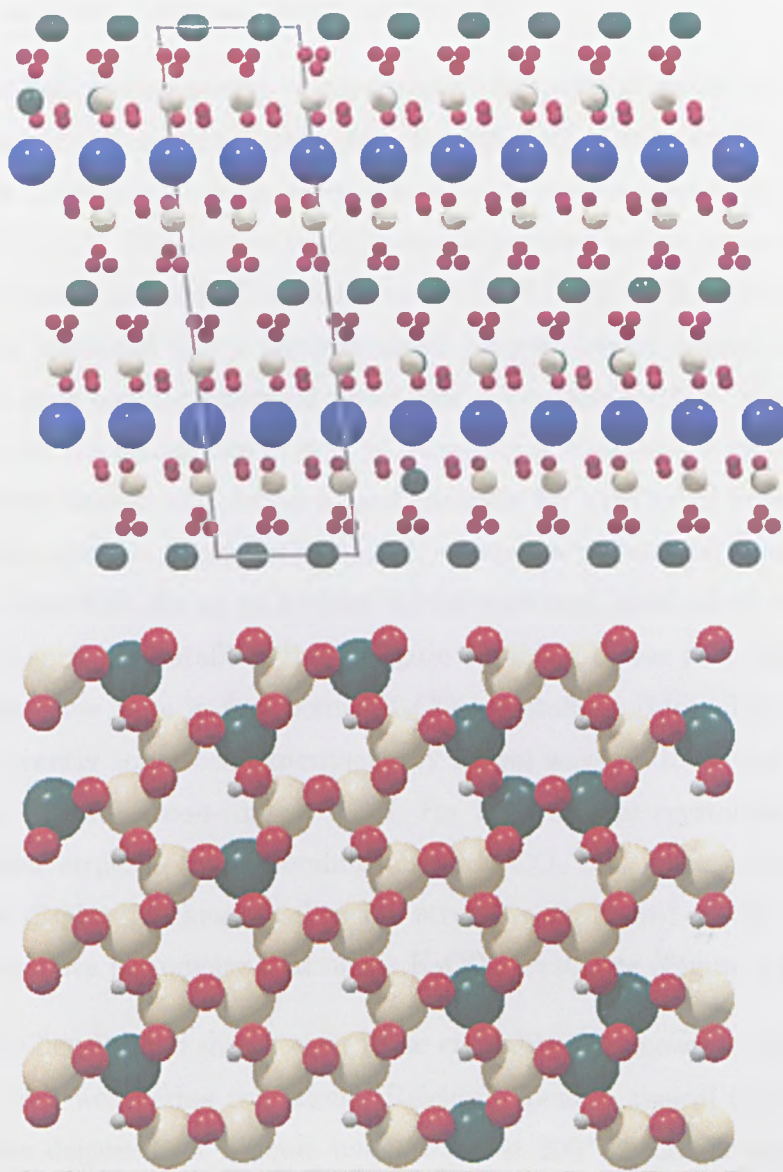


Figure 3.1: The atomic structure of muscovite mica. **Top**; Viewed in a (100) orientation perpendicular to the basal cleavage plane, showing the layered aluminosilicate layers (aluminium - green, silicon - cream and oxygen - red) bound by potassium ions (blue). The gray outline represents the true unit cell. **Bottom**; an aluminosilicate layer viewed in a (001) orientation, showing the 6-fold symmetry axis associated with the K^+ lattice sites.

by a layer of potassium ions occupying hexagonal sites on the surface of the unit cell, electrostatically binding adjacent aluminosilicate layers. The low relative strength of the ionic bonds between these layers results in a regular cleavage parallel to the (001) plane, with the potassium ions dispersed evenly but randomly between the new layers upon separation [144]. Saturation of the oxygen bonds

results in an inert, chemically stable surface [145].

Due to the high surface energy of mica, rapid adsorption of water from the atmospheric vapour occurs immediately after cleavage [146]. Consequently, the work of cleavage in laboratory air is an order of magnitude smaller than in ultra-high vacuum (UHV) [147]. The surface bound water is reported not to completely desorb even at temperatures as high as 560 K under UHV [147]. Of a particular interest to the work presented here is the interaction between bound potassium ions, carbonaceous gases and the adsorbed water film at the mica surface. Several studies have reported the fractal like growth of nanoscale crystallites on *weathered* mica, that is freshly cleaved mica left at a fixed humidity for a period of time. By taking transmission electron micrographs (TEM) of carbon replicas of weathered mica dried for under P_2O_5 for up to 2 weeks, Christenson and Isrealachvili reported the presence of surface crystallites [148] (Figure 3.2 a-b). It was proposed by Christenson that these were in fact bound K_2CO_3 crystallites [146]. This hypothesis has been recently confirmed experimentally in two ways by Reichling *et al.* [149] using high resolution non-contact AFM. For large surface crystallites there was a rectangular structure corresponding to the K_2CO_3 bulk values, whereas small crystallites displayed a hexagonal moiré structure attributed to the interference between the mica periodicity that of the K_2CO_3 crystallite (Figure 3.2 c-d).

The surface density and diameter of these crystallites is known to be dependent upon the mica weathering conditions. Reichling found a typical thickness of 1-5 nm for mica degassed for 2 hours under UHV at 200° C. Larger crystallites up to 1 μm in diameter form after prolonged drying at very low humidity (<20 %) for a period of days, attributed to an Ostwald ripening process [148]. At higher humidity (>50-60%), the K_2CO_3 crystallites do not appear, coinciding with the high solubility of K_2CO_3 in water (~ 8 M). If the cleaved mica is dipped in a weakly acidic solution (pH = 3) there is an exchange between H^+ and K^+ ions, meaning only hydrogen ions are present on the surface preventing the formation of crystalline material.

The work here considers for the first time the effect of K_2CO_3 crystallites on epitaxial growth. Since the size and concentration of the crystallites is dependent upon the weathering conditions, namely the humidity, exposure time and the

drying period, a systematic study of the degree of epitaxy as a function of these conditions was undertaken.

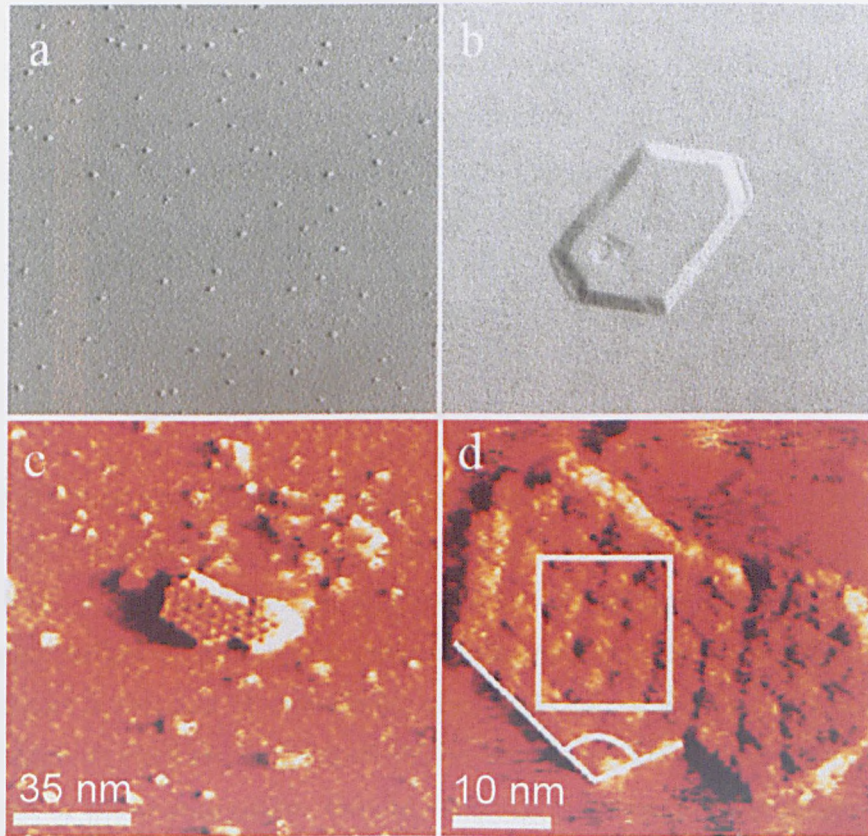


Figure 3.2: **a,b** $1\ \mu\text{m} \times 1\ \mu\text{m}$ transmission electron micrographs for carbon replicas of mica surfaces taken from reference [148]. **a** Weathered at 100% humidity before drying over P_2O_5 for 2 days, revealing a large number of surface K_2CO_3 crystallites **b** A single, larger K_2CO_3 crystallite weathered at 50% humidity for 1 h before drying over P_2O_5 for 2 weeks. **c,d** High resolution non-contact AFM images of K_2CO_3 crystallites, showing the hexagonal structure (marked angle is $117 \pm 5^\circ$). Taken from reference [149]

3.2 Results

CaCO_3 was precipitated on muscovite mica surfaces systematically weathered under a variety of conditions. Changes in the polymorphism, morphology, orientation and nucleation density were observed as a function of the precise weathering conditions. CaCO_3 was precipitated using the double-decomposition method (section 2.3) in all cases, for a 2 h growth period at a $[\text{Ca}^{2+}] = 5 \text{ mM}$ concentration, unless otherwise stated.

3.2.1 Freshly Cleaved Mica

No epitaxy was observed upon the precipitation of CaCO_3 from solution onto freshly cleaved mica (Figure 3.3). For a 2 h growth period at a solution concentration of $[\text{Ca}^{2+}] = 5 \text{ mM}$ there was an increase in the percentage of vaterite, accounting for approximately 20 % of the crystals, in comparison to solution crystallisation on glass control substrates. The majority of crystals appeared in a (104) orientation coinciding with the bounding planes of the calcite unit cell, albeit with no lateral alignment of the crystal edges. Finally, there was a low nucleation density of only (31 ± 20) crystals per mm^2 , significantly lower than the number observed on glass control surfaces, and on weathered mica (section 3.2.2).

Variations in the growth time and solute concentration did not result in epitaxial growth on freshly cleaved mica. There was no significant increase in the crystal number density after a 24 hour growth period (at a $[\text{Ca}^{2+}] = 5 \text{ mM}$ solute concentration) although in this case less than 1% of the CaCO_3 crystals were identified as vaterite.

3.2.2 Weathered Mica

The number density and orientation of CaCO_3 particles precipitated on mica surfaces weathered at ambient humidity were markedly different to those on freshly cleaved mica. Figure 3.4 shows crystals precipitated on mica weathered for one hour at ambient humidity (36-39%) under the same growth conditions as for figure 3.3. A two orders of magnitude increase in the crystal number density was

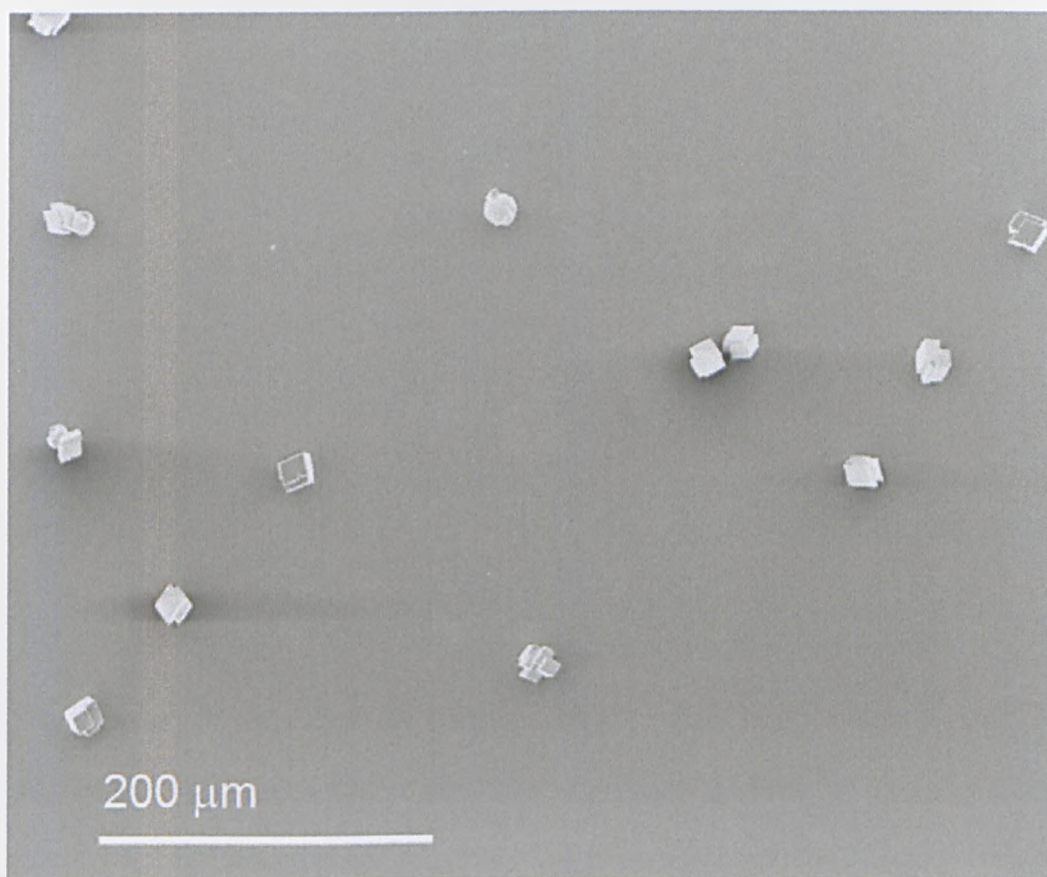


Figure 3.3: SEM image of CaCO_3 crystal growth on freshly cleaved mica (2 h growth period, $[\text{Ca}^{2+}] = 5 \text{ mM}$). There is a low crystal number density (31 ± 20 per mm^2), with no epitaxial calcite crystals. Approximately 20% of the CaCO_3 was in the form of vaterite.

observed, with (4200 ± 300) crystals/ mm^2 in comparison to the value for freshly cleaved mica. In addition, the CaCO_3 precipitated almost uniquely ($> 99\%$) as calcite, predominantly in a (001) orientation, with the projected interfacial angles around the 3-fold c -axis all equal to 120° (Figure 3.5). Lateral alignment of the interfacial angles was observed over distances spanning the length of the sample (maximum recorded length = 8 cm), correlating to the absence of grain boundaries at the (001) basal cleavage plane. A 2 h growth period at 5 mM resulted in a high surface coverage of single-faceted calcite crystals (as shown in figures 3.4, 3.6 and 3.8) and these are the growth conditions used for all subsequent weathering experiments unless otherwise stated.

The orientations of the epitaxial calcite rhombohedra corresponded to a 60° increment in rotation, a consequence of the pseudo-hexagonal structure of the mica

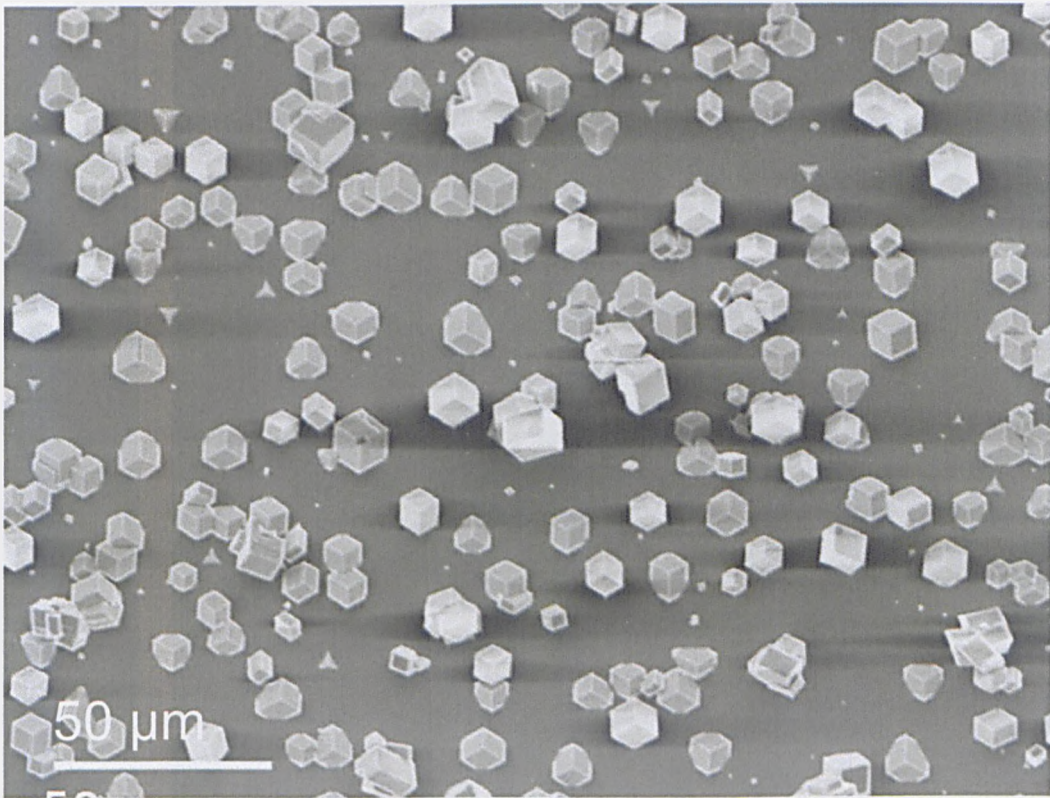


Figure 3.4: SEM image of CaCO_3 growth on mica weathered for 24 hours at room humidity 36-39% (2 h growth period, $[\text{Ca}^{2+}] = 5 \text{ mM}$). There is a large calcite number density ($4200 \pm 300 \text{ per mm}^2$), with $93 \pm 2\%$ of the calcite crystals observed in a (001) orientation.

surface. Since there is alignment of the three-fold calcite c -axis and the six-fold mica surface, only two unique orientations of calcite are possible, with these directors denoted *upwards* and *downwards* here on (Figure 3.6). Whilst no preference between upwards and downwards was observed for any sample, there was a narrow distribution of the calcite edge angles, with a study of 30 epitaxial crystals found to have a range of 6° . In addition, three configurations of epitaxial calcite crystals were observed, relating to the point at which the (001) plane intersected the $\{104\}$ calcite crystal. They were *tetrahedral*, *rhombohedral* and *intermediate* configurations with 3, 6 and 9 edges visible respectively. The configuration distribution was independent of growth time, and concentration (within a 2-10 mM range). Calcite configurations as a function of mica weathering conditions were not systematically studied.

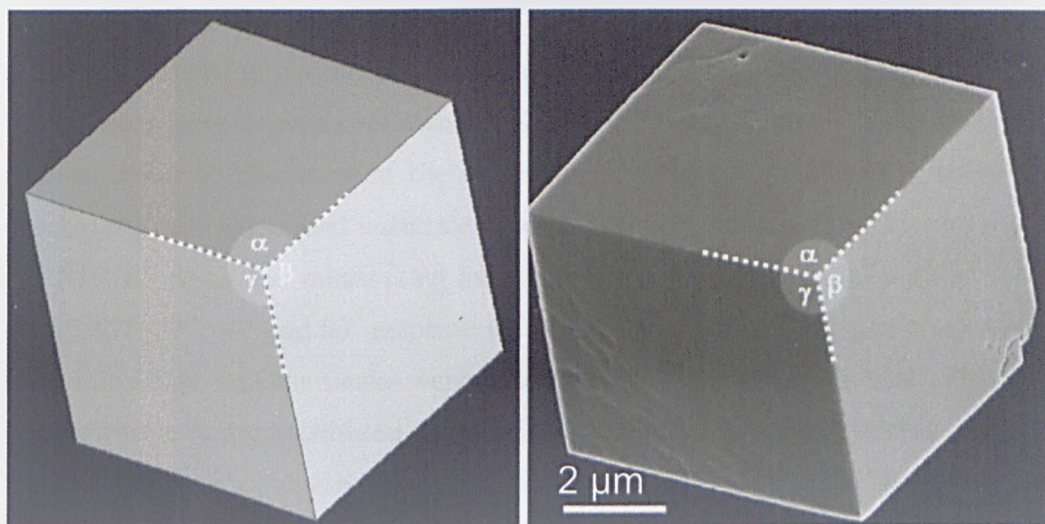


Figure 3.5: **Left** A SHAPE simulated 104 calcite crystal in a (001) orientation, whereby the projected calcite angles $\alpha = \beta = \gamma = 120^\circ$. **Right** A corresponding SEM image of an epitaxial calcite crystal on weathered mica (2 h growth period, $\text{Ca}^{2+} = 5 \text{ mM}$).

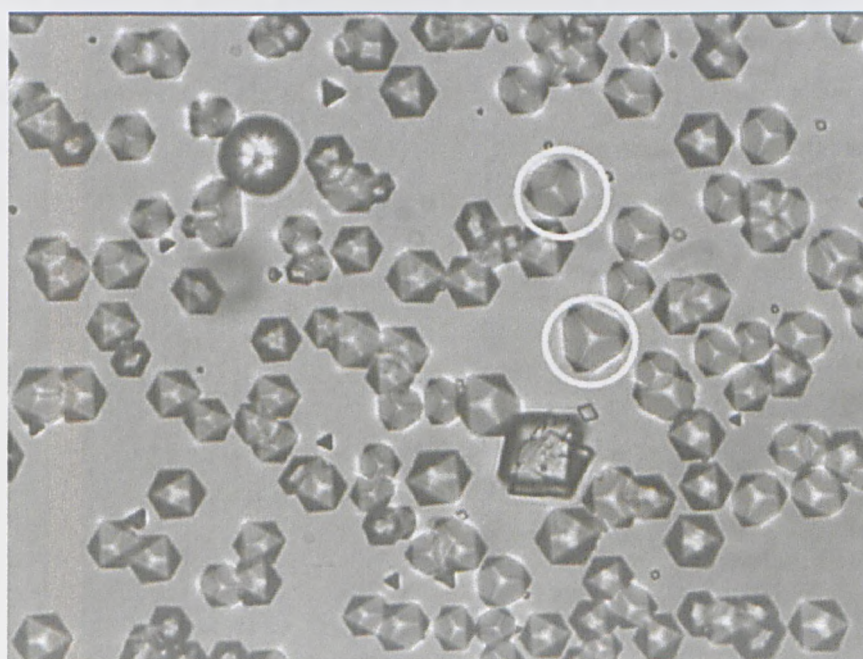


Figure 3.6: 500x optical image showing the 60° increment in rotation of the epitaxial calcite crystal. *Upward* and *downward* configurations are circled.

XRD measurements confirmed the epitaxial overgrowth of calcite in a (001) orientation, following the procedure outlined in section 2.4.5. The sample used was for a 1 hour weathering period and a 2 h growth time, $[\text{Ca}^{2+}] = 5 \text{ mM}$ concentration. There was a large background associated with the crystalline substrate, which was perpendicular to the plane of the incident and reflected X-ray beam. Five fundamental peaks associated with mica could be clearly identified, corresponding to the RRUFF database values [150] for the powder diffraction pattern at 2θ values of 17° , 27° , 37° , 46° and 55° respectively [151]. In addition to the peaks associated with mica, two smaller peaks were observed when the intensity was plotted on a logarithmic scale, attributed to the (006) and (104) planes of calcite using the powder diffraction pattern from reference [151]. The intensity of the (006) peak relative to the (104) peak was over 200 times of that observed in a powder diffraction pattern. The (001) peak cannot be measured directly using XRD operating in a standard configuration. The calcite unit cell comprises of six layers of calcium ions alternating with six layers of carbonate ions, perpendicular to the c -axis. The (006) peak corresponds to scattering from successive carbonate or calcite planes, and the (0012) peak corresponding to scattering between adjacent calcium and carbonate planes. A (001) peak requires scattering between every sixth calcium or carbonate layer, and is therefore more difficult to detect. Since both the (006) and (0012) crystallographic planes are parallel to the (001) plane, either could be used for identification. However, the (006) peak was chosen due to considerable overlapping between the (0012) calcite and the (0014) mica peaks.

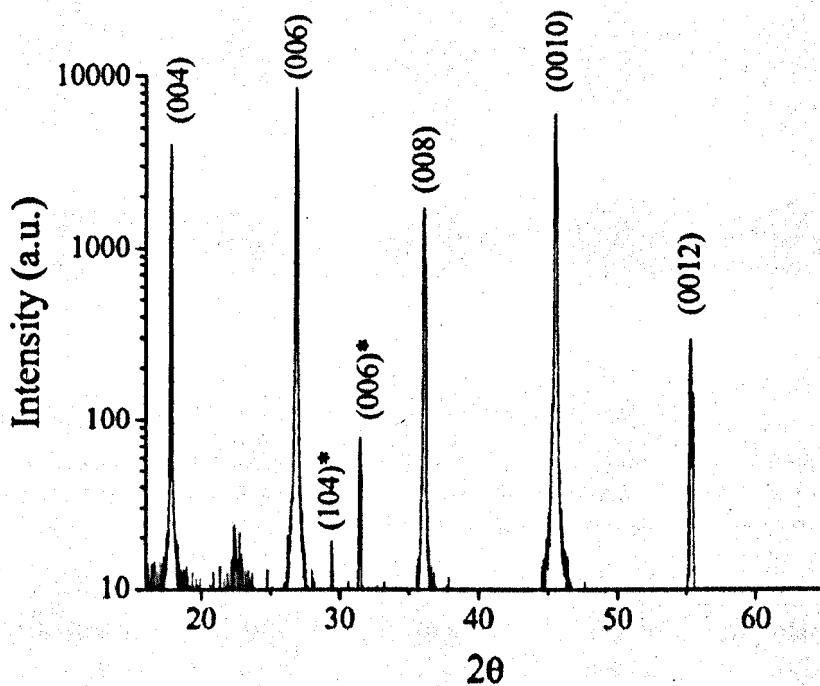
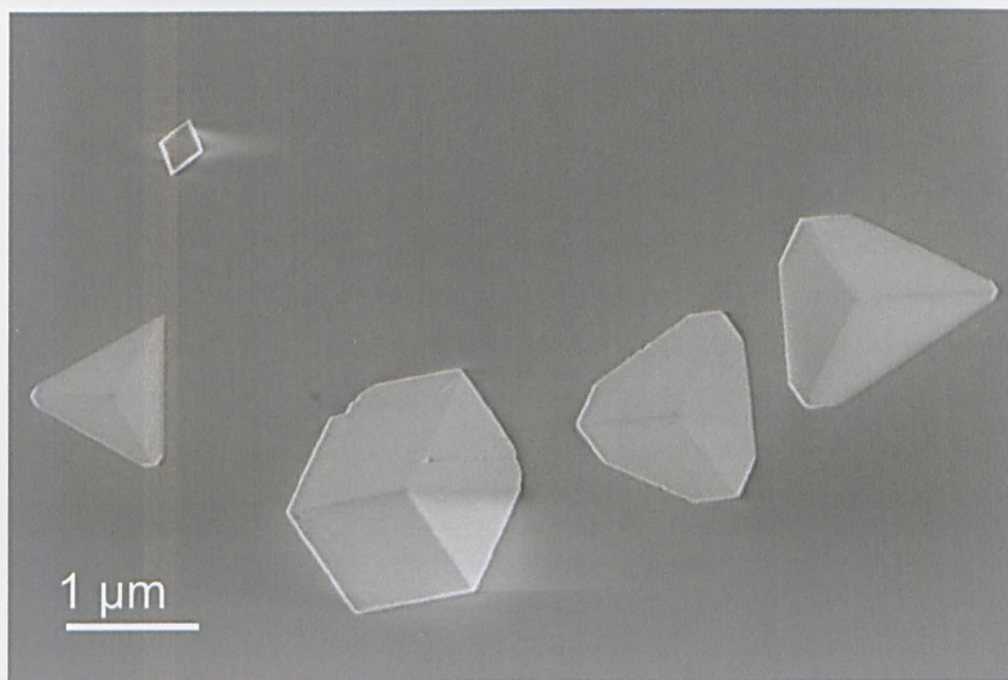


Figure 3.7: 2θ XRD spectrum of orientated calcite crystals on mica (2 h growth period, $[\text{Ca}^{2+}] = 5 \text{ mM}$). The mica sheet is perpendicular to the plane of the incident and reflected X-ray beam and shows only reflections from layers parallel to the basal cleavage plane (no asterisks). Calcite peaks are denoted by asterisks, at 2θ values of 29° and 32° .



Rhombohedral

Intermediate

Tetrahedral

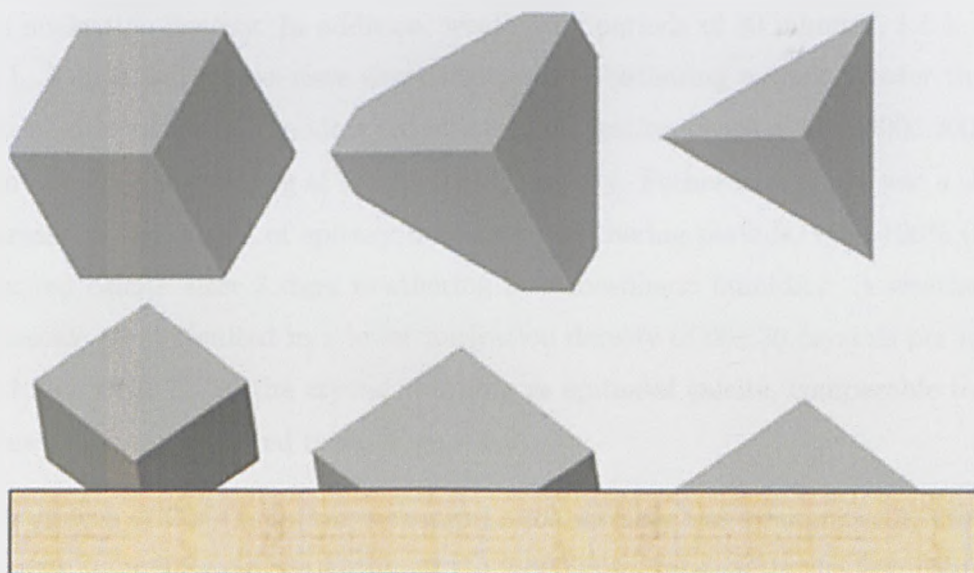


Figure 3.8: **Top** Representative HR-SEM image for the epitaxial growth of calcite in a (001) orientation on mica. Three distinct configurations can be seen, corresponding to rhombohedral, intermediate and tetrahedral configurations respectively. **Bottom** Schematic representation of the 3 conformations viewed top down and sideways on.

3.2.3 Ion Exchanged Mica

The mica was weathered under a variety of conditions, influencing the formation of K_2CO_3 crystallites and the relative degree of epitaxy. Firstly, the relative humidity of the weathering process was considered. Freshly cleaved mica was weathered at < 5% humidity by placing in a dessicator containing CaH_2 for 1 hour and 24 hours. A total absence of epitaxy was observed in these cases, with a large reduction in the number density of crystals in comparison to the weathering at atmospheric humidity. Secondly, samples were weathered at 100% humidity in a glove box equilibrated with water vapour for 1.5 hours. Again, no epitaxial calcite crystals were observed, although in this case the nucleation density of 350 ± 160 per mm^2 was an order of magnitude higher than that observed on freshly cleaved mica (31 ± 20 per mm^2).

At atmospheric humidity, the degree of epitaxy was dependent upon the weathering period. Freshly cleaved mica resulted in no epitaxy and a low nucleation density (section 3.2.1), whereas a 1 hour weathering period at atmospheric humidity yielded epitaxial calcite crystals with a two order of magnitude increase in the nucleation density. In addition, weathering periods of 30 minutes, 1.5 h, 2 h, 24 h, 3 days and 5 days were also considered. Weathering periods greater than 1 h tended to result in a modest reduction in nucleation density, with 900 ± 200 per mm^2 after 3 d weathering at atmospheric humidity. Futhermore, there was a slight increase in the degree of epitaxy for longer weathering periods, with 100% (001) oriented calcite after 3 days weathering at atmospheric humidity. A weathering timescale 30 m resulted in a lower nucleation density of 60 ± 30 crystals per mm^2 , with less than 7% of the crystals forming as epitaxial calcite, comparable to the values for freshly cleaved mica (Figure 3.9).

The growth of $CaCO_3$ on ion exchanged mica surfaces was systematically studied in order to understand the nature of the weathering process. In the first case, K^+ surface ions were exchanged with H^+ ions by by immersing the freshly cleaved mica in milli-Q water for 5 minutes before weathering at atmospheric humidity (35-40%) for 1 hour, 3 days and 5 days, with the control samples for each case weathered without prior rinsing. The water treatment of the mica surface inhibited the formation of epitaxial calcite crystals, increased the relative amount of vaterite

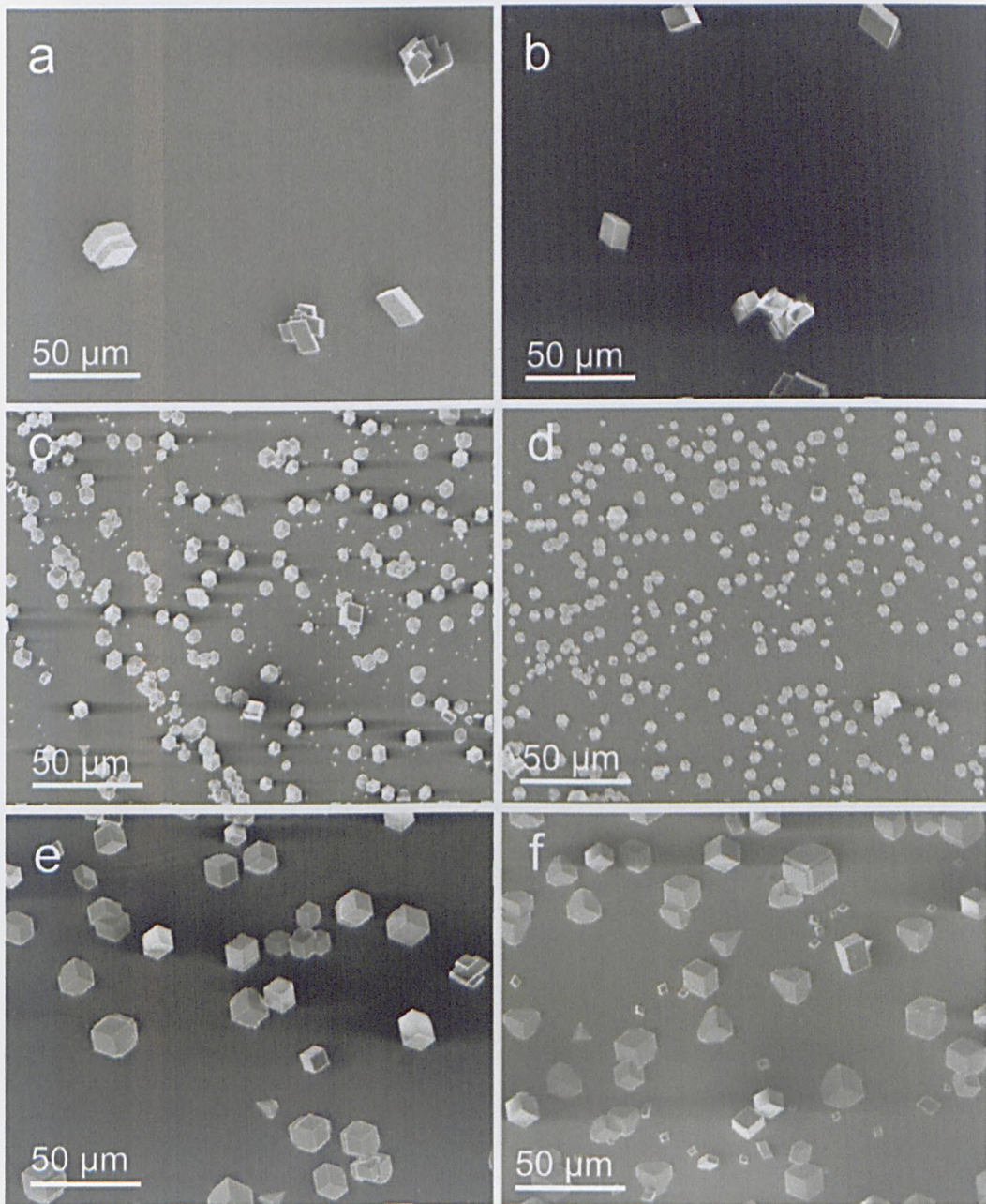


Figure 3.9: SEM micrographs of CaCO_3 precipitates (2 h growth period, $[\text{Ca}^{2+}] = 5 \text{ mM}$) on mica surfaces weathered at 35 - 40% humidity for a period of a 0 min (freshly cleaved), b 30 min, c 1.5 h, d 2h, e 24 h and f 3 d.

and resulted in an overall reduction in the nucleation density (Figure 3.11). For water treated mica, weathered for 1 h at 35-40% humidity, the number density of CaCO_3 crystals was comparable to that on freshly cleaved mica with 50 ± 20 per mm^2 . For the second case, the mica substrates were immersed in Milli-Q water for five minutes *after* weathering at 35-40% humidity for periods of 1 hour and 3

days. This treatment also inhibited epitaxial calcite growth and resulted in a low number density of CaCO_3 particles (66 ± 17 per mm^2). For a final ion exchange experiment, surfaces were immersed in solutions of HCl (pH=3.0) for 5 minutes before weathering for 1 hour at atmospheric humidity. This again inhibited calcite epitaxy and resulted in low CaCO_3 particle number density and a greater occurrence of vaterite ($13 \pm 4\%$) (Figure 3.10).

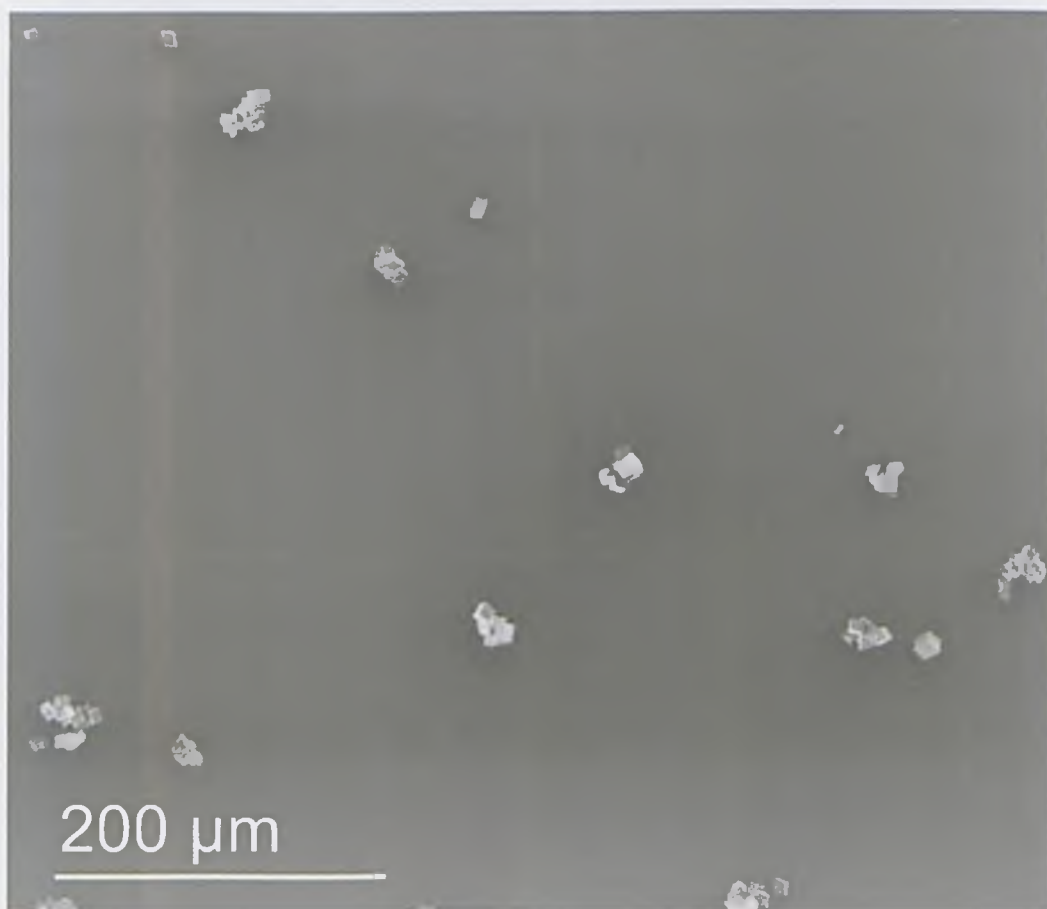


Figure 3.10: SEM image of CaCO_3 growth on H^+ ion exchanged mica substrates, weathered for 1 hour at room humidity (36-39%). There is a low CaCO_3 particle number density, with no epitaxial calcite growth (2 h growth period, $[\text{Ca}^{2+}] = 5$ mM).

The humidity of the weathering process was found to strongly effect the relative degree of epitaxial calcite growth. Firstly, mica was weathered at $<5\%$ humidity by placing in a dessicator containing CaH_2 for periods of 1 and 24 h. No epitaxial calcite was observed in these cases and there was a large reduction in the number density of crystals in comparison to mica weathered at atmospheric humidity. Secondly, mica was weathered at 100 % humidity in a glove box equilibrated with

water vapour for 1.5 hours. Again, no epitaxial calcite crystals were witnessed, although in this case the nucleation density of 350 ± 160 per mm^2 was an order of magnitude higher than that observed on freshly cleaved mica. Subsequent experiments found the optimal weathering conditions to occur upon exposure to a 65-70 % humidity environment for 1 hour before leaving overnight in a dry environment (<15%). The 65-70% environment was created within a dessicator containing aqueous solutions of LiCl at concentrations corresponding to the relative vapour pressures in reference [114].

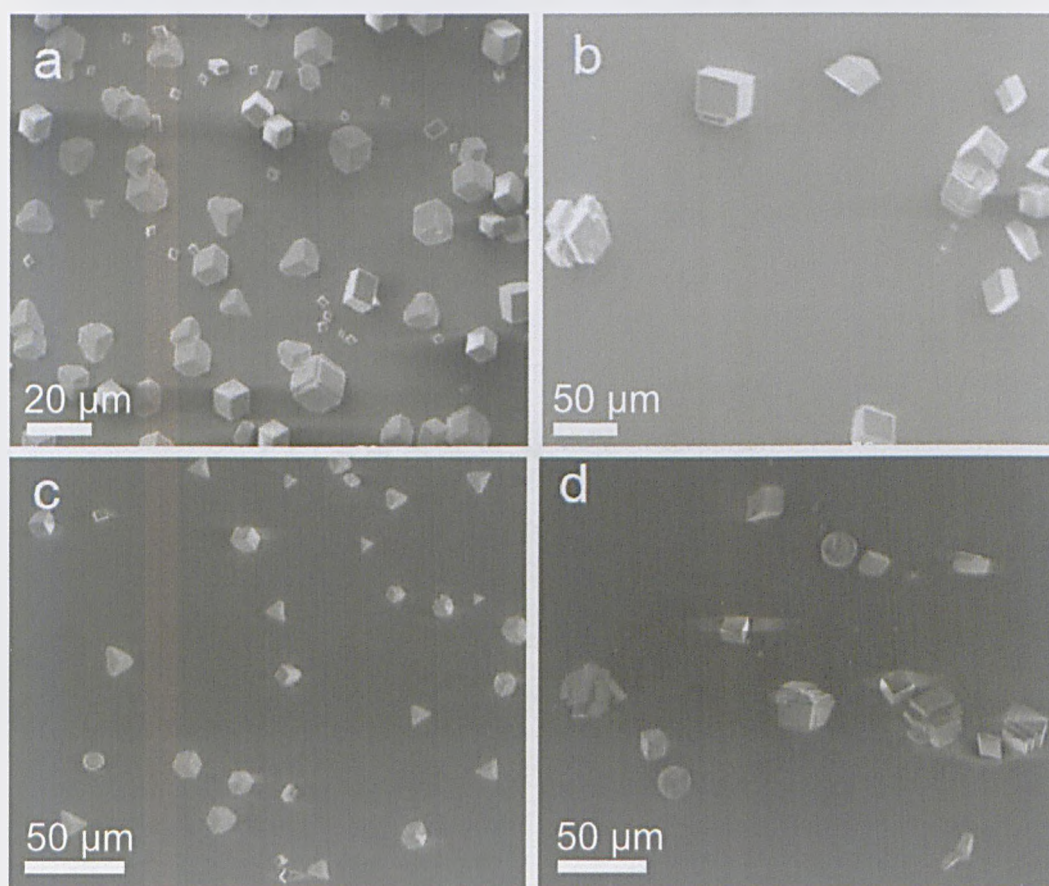


Figure 3.11: SEM images of CaCO_3 crystallisation (1 h growth period, $[\text{Ca}^{2+}] = 5$ mM) on mica surfaces weathered under different conditions. **a** 5 days at 35-40 % humidity, **b** 5 days at 35-40 % humidity followed by 5 min immersion in Milli-Q water **c** 3 days at 35-40 % humidity and **d** 5 minutes immersion in Milli-Q water prior to 3 days weathering at 35-40 % humidity.

Weathering Condition	Crystals per mm ²	% Calcite	% (001) Calcite
Freshly cleaved	31±20	81±7	4±2
0.5 h at 35-40 % humidity	60±30	97±2	7±4
1.0 h at 35-40 % humidity	4200± 300	100	93±2
1.5 h at 35-40 % humidity	1500± 700	97± 2	91 ±1
72 h at 35-40 % humidity	900±200	100	96±2
H ⁺ ion exchanged prior for 1 h at 35-40 % humidity	57±5	87±4	0
5 min water immersion after 1 h at 35-40% humidity	66±17	100	0
1.5 h weathering at 100 % humidity	350±160	86±9	0

Table 3.1: The effect of mica weathering conditions on the CaCO₃ nucleation density, polymorphism and percentage of epitaxial calcite crystals.

3.2.4 Early Growth Stages on Mica

CaCO_3 nucleation pathways on weathered mica substrates were determined through the morphological analysis of precipitates after a series of short growth times. CaCO_3 was precipitated from 5 mM aqueous solutions using the double decomposition precipitation method for growth periods of 0.5, 1, 2, 4, 6 and 10 minutes. Particle morphology was determined using HR-SEM, with samples analysed within 24 h of crystallisation. It was not possible to determine individual particle polymorphism using Raman spectroscopy due to the small particle size. Technical difficulties in isolating individual particles prevented electron diffraction measurements.

After a 30 second growth period the CaCO_3 precipitates were highly irregular, with an absence of defined edge features morphologically similar to calcite (Figure 3.12). The particles were evenly distributed across the mica surface, with dimensions in the range of 50-500 nm. Interestingly, many of the particles had uneven surface topographies, indicative of vaterite (Figure 3.12b) although smaller, approximately spherical particles consistent with amorphous calcium carbonate were also present (Figure 3.12c).

After a growth period of 2 minutes, similar irregular CaCO_3 particles were present. The particle number density was approximately double that for a 30 s growth period, yet the dimensions of these particles were in the same 50-500 nm range (Figure 3.13a). However, epitaxial calcite crystals were also present, signified by a characteristic tetrahedral shape and long range lateral alignment of the interfacial angles (Figure 3.13b). The ratio of the number of irregular CaCO_3 particles in relation to the number of calcite crystals was approximately 10:1. However, on the estimation that the average dimensions are 1 and 0.3 μm for calcite and irregular CaCO_3 particles respectively, more than 70% of the total CaCO_3 material was in the form of epitaxial calcite. HR-SEM images of individual precipitates are shown in figure 3.14. The calcite crystals had typical dimensions in the range of 1-2 μm , although a smaller number of sub-micron crystals were observed. The smallest observed tetrahedra calcite particle is shown in figure 3.14c, morphologically identified by the characteristic 3-fold *c*-axis. The edges of this particle are highly irregular, in contrast to other the well defined calcite particles observed on

the same sample (Figures 3.14a, c). The projected edges of the tetrahedral were approximately 200 nm, and it is speculated that this crystal marks the transition between the crystalline calcite and the metastable CaCO_3 phases.

After a 4 minute growth period there was an increase in the average dimensions of the calcite particles to 2-5 μm , with no sub-micron calcite particles observed (Figures 3.15a, b). No significant increase was witnessed in the number density of the calcite particles, with the same ratio between the number of irregular CaCO_3 particles and the number of calcite particles as observed for short growth periods. These particles had the same irregular surface features as for 0.5 and 2 minute growth periods, with morphological analysis consistent with vaterite (Figure 3.15c). No regular spherical particles consistent with ACC were observed for this growth period, in contrast to a 30 second growth period.

After a 6 minute growth period there was a further increase in the dimensions of the calcite particles to 3-6 μm (Figure 3.16a-b). Irregular CaCO_3 particles were still present at this growth period, with a slight reduction in the ratio between the number of these particles to the number of calcite particles of 8:1. Although the average dimensions of these irregular was consistent with shorter growth periods (Figure 3.16c), the relative increase in the dimensions of the epitaxial calcite crystals meant that these irregular particles accounted for less than 0.1% of the total CaCO_3 precipitates by volume. This trend continued for an 8 minute growth period, after which the dimensions of the irregular CaCO_3 particles were more than one order of magnitude smaller than the calcite particles (Figure 3.17c). Figure 3.17b shows epitaxial calcite crystals on weathered mica after a 1 h growth period, for the same solution concentration. Here, no irregular sub-micron particles were observed, with all the CaCO_3 material precipitating as epitaxial calcite.

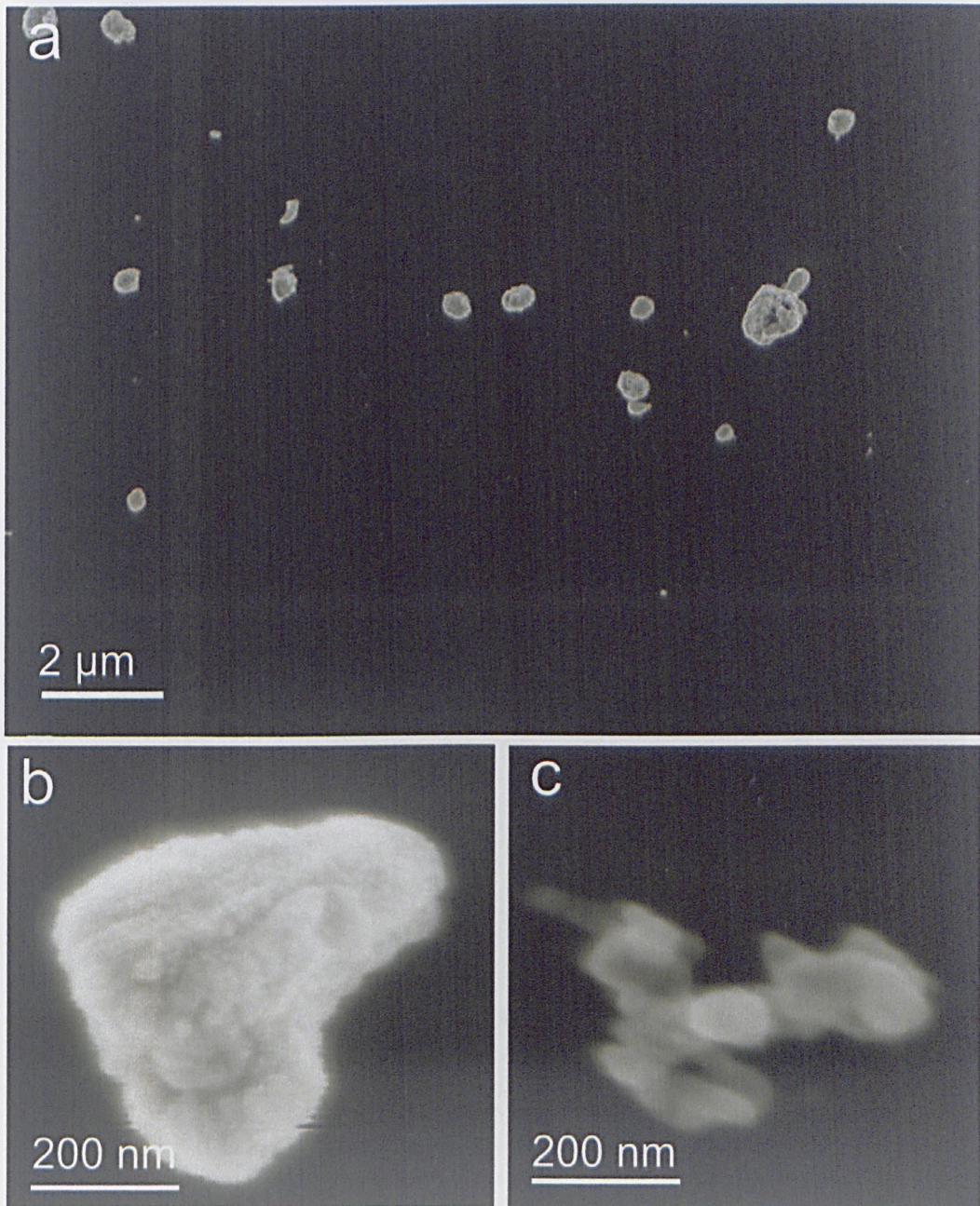


Figure 3.12: SEM images for the precipitation of CaCO_3 on weathered mica after a 30 s growth period, 5 mM solution concentration. **a** Overview, with only irregular CaCO_3 particles present, of average dimensions 200-500 nm. **b** These irregular CaCO_3 particles had uneven surface topographies, and irregular shapes, consistent with vaterite. **c** Smaller, approximately spherical particles with smooth surface features were observed with 50-100 nm feature sizes, consistent with ACC.

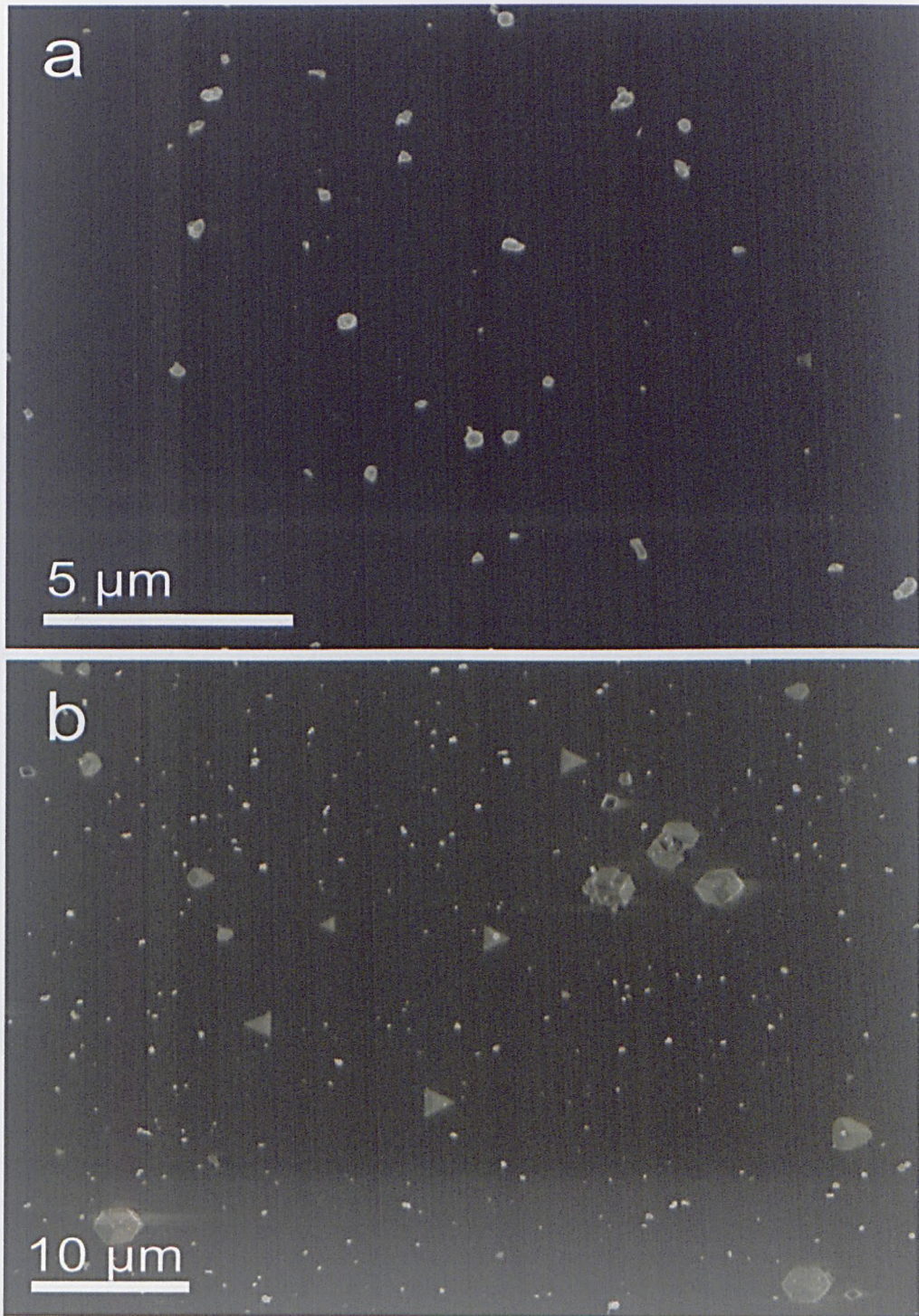


Figure 3.13: SEM overviews for the precipitation of CaCO_3 on weathered mica after a 2 minute growth period, 5 mM solution concentration. **a** A region mostly populated with irregular particles CaCO_3 particles, with only a single epitaxial calcite particle present. **b** A region populated with epitaxial calcite crystals and irregular CaCO_3 particles.

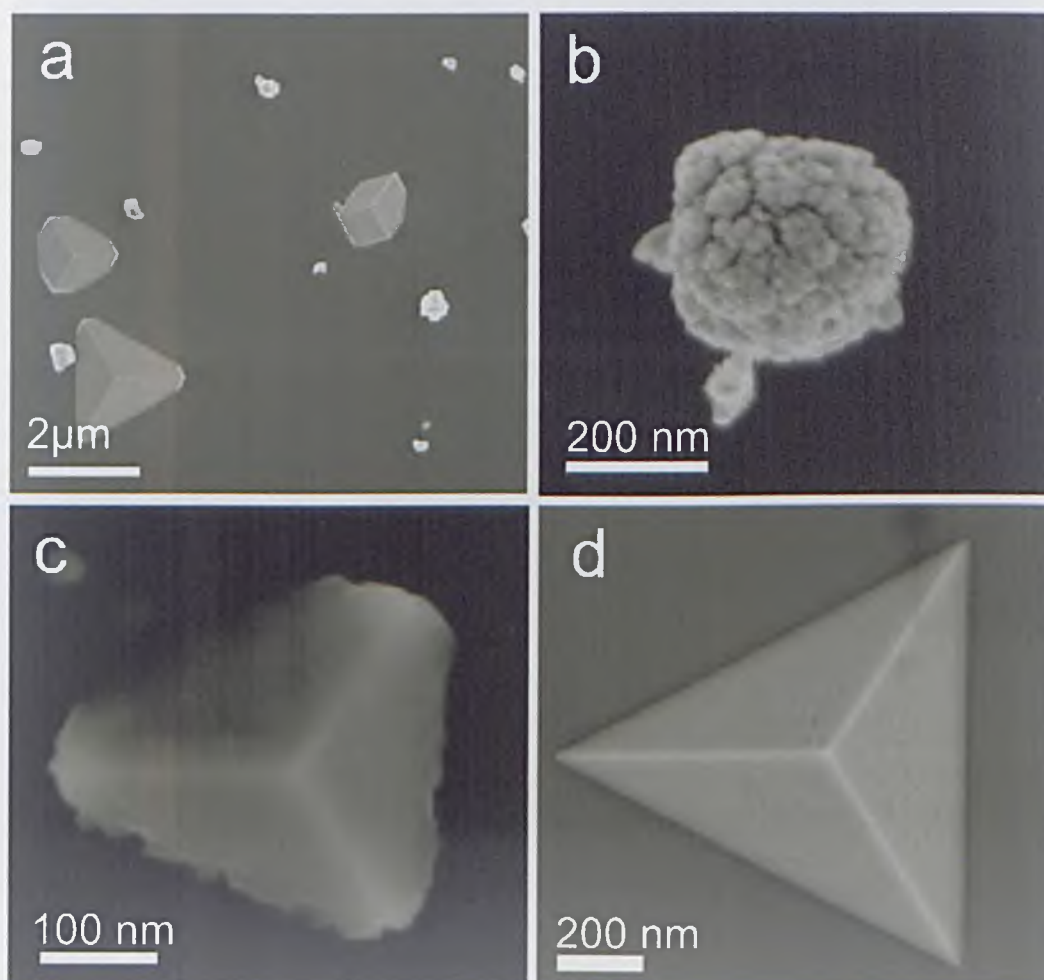


Figure 3.14: High magnification SEM images for the precipitation of CaCO_3 on weathered mica after a 2 min growth period, 5 mM solution concentration. **a** Both epitaxial calcite crystals and irregular CaCO_3 particles were present in an approximate 1:10 ratio. **b** An irregular CaCO_3 particle, morphologically consistent with calcite. **c** the smallest observed calcite particle, defined by the regular 3-fold c -axis, although irregular edge features can be seen suggesting a transition from the amorphous state to the crystalline state. **d** A typical calcite tetrahedral with $1\mu\text{m}$ approximate dimensions and well-defined edges.

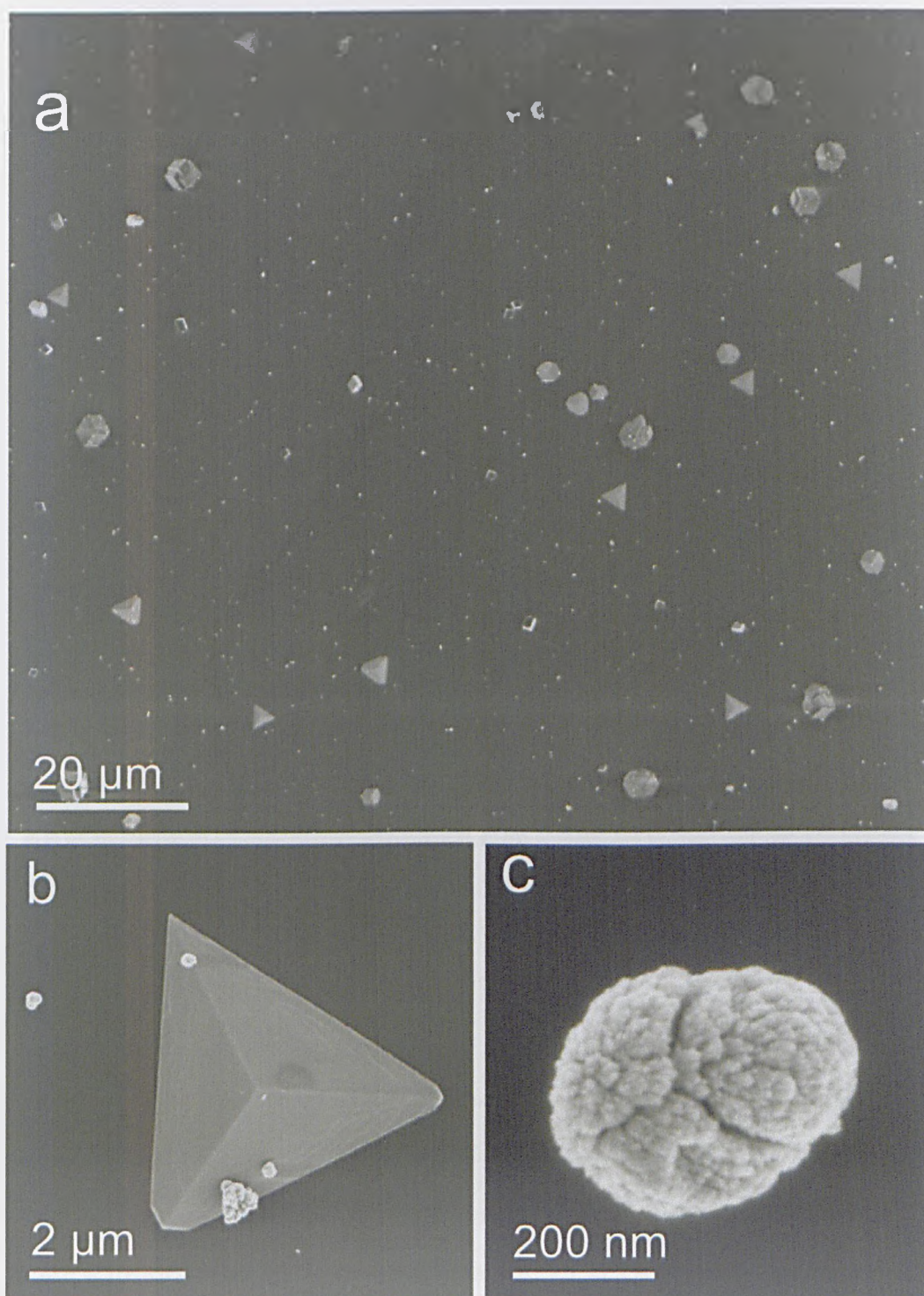


Figure 3.15: SEM images for the precipitation of CaCO_3 on weathered mica after a 4 minute growth period, 5 mM solution concentration. **a** Overview, with both epitaxial calcite crystals and irregular CaCO_3 particles observed in an approximate 1:10 ratio. **b** A calcite tetrahedral, average edge length $\sim 3 \mu\text{m}$. **c** An irregular CaCO_3 particle with a non-uniform surface topography, consistent with vaterite.

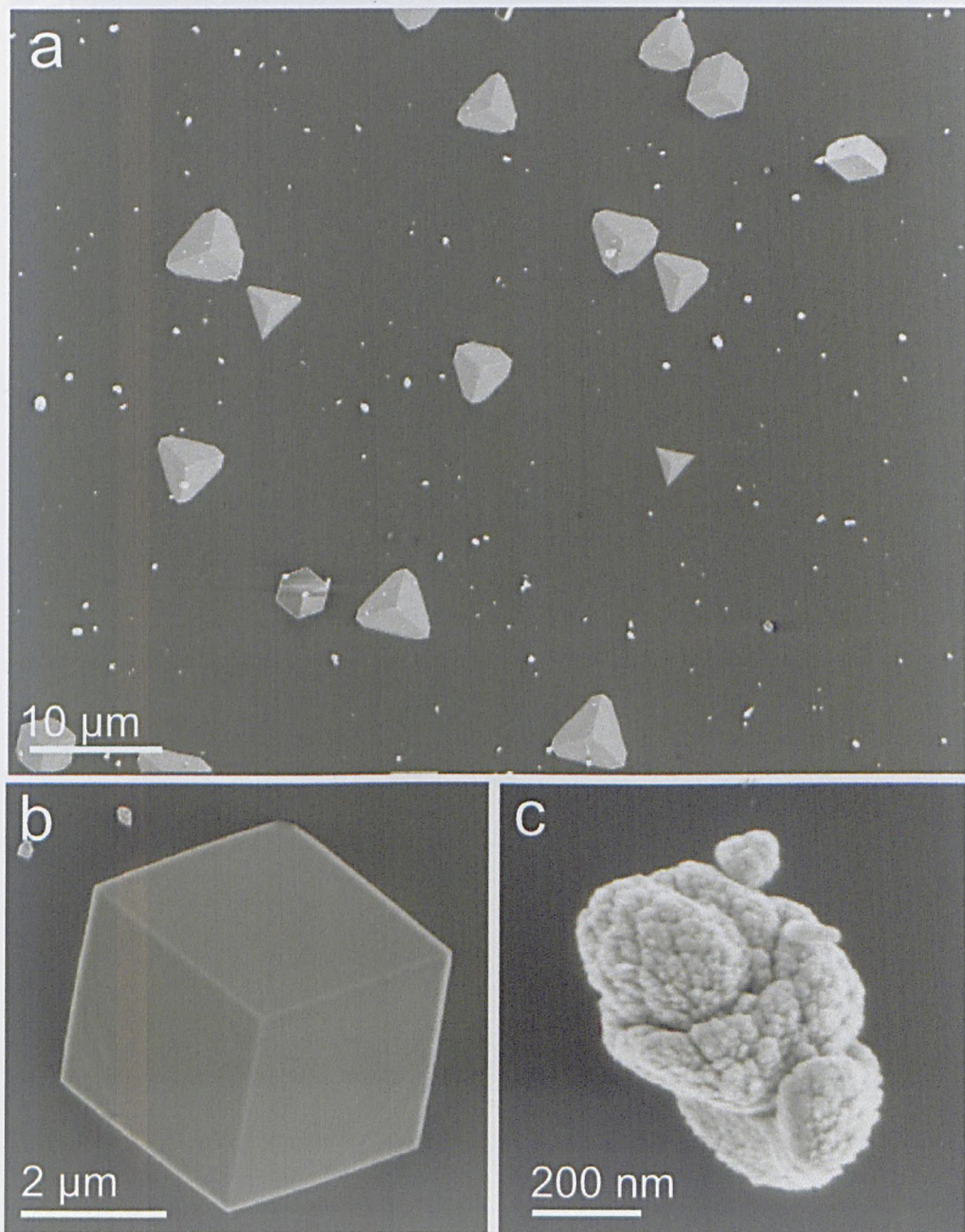


Figure 3.16: SEM images for the precipitation of CaCO_3 on weathered mica after a 6 minute growth period, 5 mM solution concentration. **a** Overview, with both epitaxial calcite crystals and irregular CaCO_3 particles observed in an approximate 1:8 ratio. **b** A calcite rhombohedral, average edge length $\sim 2.5 \mu\text{m}$. **c** An irregular CaCO_3 particle with a non-uniform surface topography, consistent with vaterite.

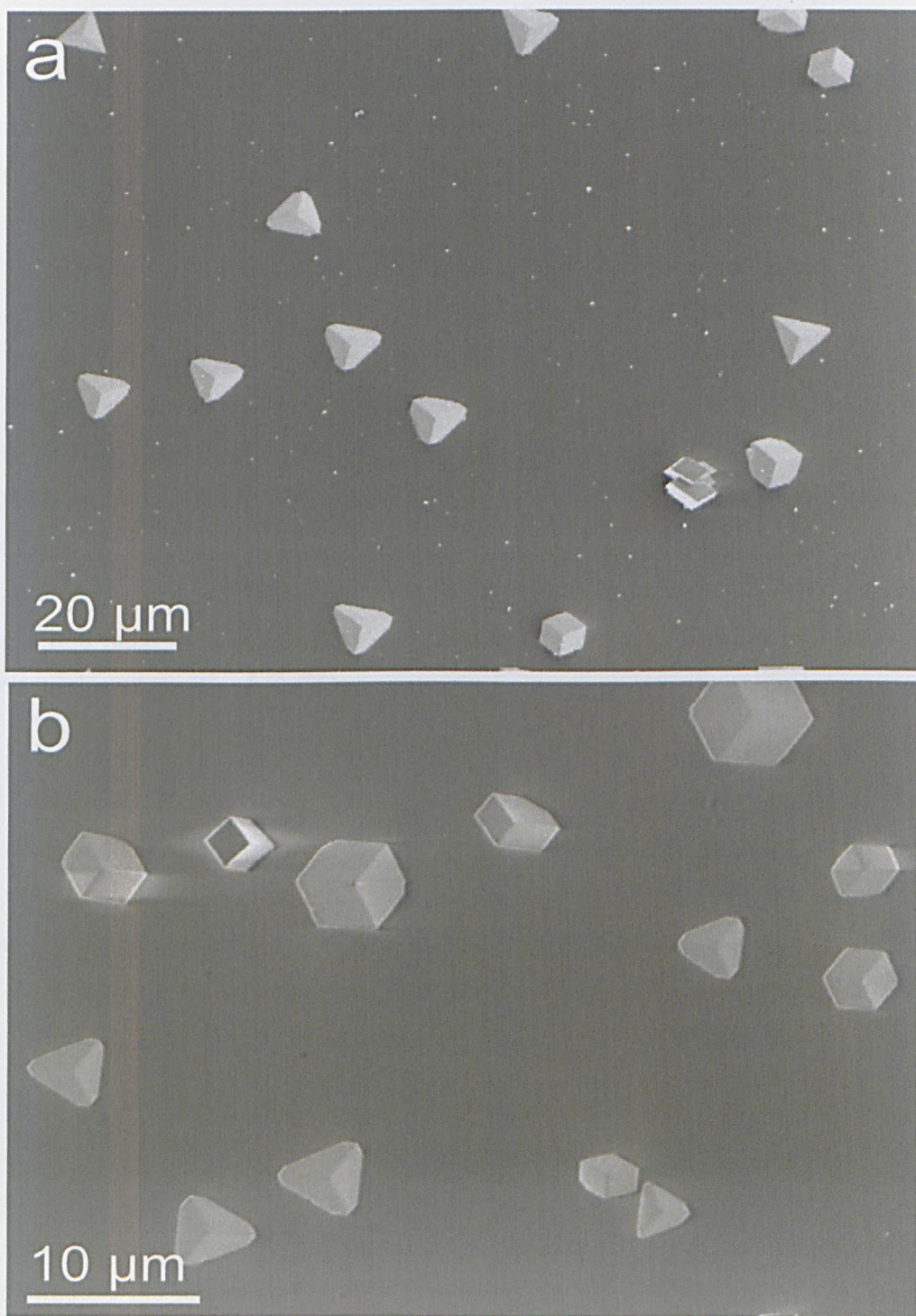


Figure 3.17: SEM overviews for the precipitation of CaCO_3 on weathered mica from a 5 mM solution for a growth period of **a** 8 minutes, showing irregular CaCO_3 particles present in addition to the epitaxial calcite crystals and **b** 1 h showing epitaxial calcite particles and an absence of irregular CaCO_3 particles.

3.3 Discussion

The epitaxial growth of alkali halides on freshly cleaved mica surfaces has been attributed to a lattice match between the (111) plane of the halide and the (001) basal mica cleavage plane although relatively large mismatches have still been reported to promote epitaxial overgrowth up to 23% in the case of NaCl [133]. For the epitaxial growth of CaCO_3 on mica, the spacing between adjacent K^+ sites on mica is 0.518 nm [128] and the Ca-Ca spacing of calcite in the (001) plane is 0.499 nm [128], which corresponds to a lattice mismatch below 4%. It is therefore a surprising result that the epitaxy of calcite only occurs on weathered mica, and that freshly cleaved mica does not support epitaxy. In addition, neither the mica weathered at 100% or <5% humidity, nor ion-exchanged prior to or after weathering at atmospheric humidity, supported the epitaxial growth of calcite. There is a difference in the configuration of surface potassium ions between freshly cleaved mica and mica weathered under different conditions, which clearly influences the epitaxial overgrowth of CaCO_3 .

It was shown by Ostendorf *et al.* [149] that the adjacent site spacing of the K^+ ions was 0.57 ± 0.05 nm for the bound potassium carbonate crystallites. This corresponds to a lattice mismatch of approximately 14% between calcite in a (001) orientation, which is considerably larger than the mismatch between calcite and the (001) mica basal cleavage plane. This suggests that although the presence of K_2CO_3 crystallites is a requirement for the formation of epitaxial calcite crystals, it is unlikely that the calcite crystals form epitaxially on the crystallites.

One obvious difference between the epitaxial crystallisation of calcite on mica and that of the widely reported alkali halides is the relatively weak adsorption of Ca^{2+} to mica. There is a strong adsorption of the alkali metal ions Na^+ , K^+ and Cs^+ to mica, whereas Ca^{2+} will only adsorb to mica at concentrations above approximately 0.1 M due to the high free-energy penalty of dehydrating the heavily hydrated calcium ions in solution [152]. This free-energy cost is likely to be exacerbated by the presence of competing sodium ions in solution. A second difference between the formation of calcite and alkali halides on mica lies in the relative saturation concentrations. CaCO_3 is only sparingly soluble in water ($\sim 1\text{mM}$),

approximately 4 orders of magnitude less than NaCl, and it is likely that the surface ionic concentration will influence epitaxial formation of calcite. Indeed it was shown by Upreti and Walton [153] that the critical heterogeneous supersaturation increases with lattice mismatch.

It is proposed that the K_2CO_3 crystallites form pseudo-nucleation sites where calcium ions may readily approach the mica surface. The crystallites are only transiently present, as demonstrated by the ion-exchange experiments, so they must only govern the nucleation of calcite at the mica interface and not the subsequent growth. This strengthens the supposition that the epitaxial calcite forms on the mica and not the crystallites. In addition, the K_2CO_3 crystallites act as a highly localised source of carbonate ions, yielding surface sites with an increased concentration of both calcium and carbonate ions. This hypothesis is supported by the data in table 3.1 with the epitaxial calcite number density decreasing with weathering period, possibly due to the formation of fewer but larger crystallites after prolonged drying periods.

That epitaxial growth is dependent on more than a simple lattice match is not limited to the case of calcite on mica. It was shown by Conrad *et al.* [154] that the BaF_2 surface is a poor ice nucleator, despite a near perfect lattice match because the ice only partially wets the BaF_2 surface. The epitaxial growth from solution is complicated by the presence of ionic concentration gradients close to the surface, affected by hydrated and electrostatic effects. Indeed, in the case of calcite, dehydration of the calcium ions is necessary before adsorption at the growth face [155].

The first part of the chapter demonstrated that the nature of the mica substrate influences a wide range of crystallisation parameters, including the nucleation density, orientation and, to some degree, polymorphism. The results presented in section 3.2.4 consider the actual $CaCO_3$ nucleation pathway on weathered mica. Irregular $CaCO_3$ particles were observed for short growth periods with the frequency gradually decreasing over time and vanishing altogether after a 1 h growth period. In contrast, calcite particles appear at a later time period than the irregular $CaCO_3$ particles, yet increased in size over time. After a 30 s growth period, the irregular particles account for 100% of the total precipitated material, falling

to approximately 30% after a 2 minute growth period and less than 0.1% after 6 minutes. Only epitaxial calcite was observed after a 1 h growth period. After a 30 s growth period, there were two types of irregular CaCO_3 particles: approximately spherical with smooth edge features consistent with ACC, and highly uneven surface topographies, consistent with vaterite. After growth periods of 2 minutes and more, only the vaterite and calcite type particles were observed.

These results were broadly similar a recent study by Yamanaka *et al.* [156] using AFM to study the heterogeneous nucleation of CaCO_3 on different substrates, including mica. Figure 3.18 is from that work and shows the transition from ACC into calcite. There is a close correlation in particle dimensions and morphology between figure 3.18b taken from that study and figure 3.14c. This suggests that the nucleation of calcite on mica proceeds via an amorphous precursor phase, since no calcite tetrahedra are observed with dimensions below 100 nm. Figure 3.18b is for a growth period of 15 minutes which does not correlate to the growth periods used here. However, irregular CaCO_3 particles were present after 8 minutes, so it is feasible that they could remain after 15 minutes. It should be noted that no consideration was made for the condition of the mica surface in this study. Furthermore, a systematic study of different growth periods was not undertaken.

Yamanaka *et al.* described a 3-stage growth process during which spherical deposits with an approximate radius of 100 nm first nucleated at the mica surface. The spherical deposits had a low overall contact angle, attributed to a high affinity between ACC and mica. The second stage involved the lateral growth of the deposit perpendicular to the mica surface. In the final stage, there was a transformation into crystalline calcite. In this model, it is suggested that the calcite crystal initially starts in a tetrahedral form, becoming rhombohedron during the growth process. This contradicts the findings here, where the calcite configurations were not observed to change with time. This model also does not take into account the vaterite particles observed here, so an alternative model must be introduced (Figure 3.19).

It is proposed that CaCO_3 crystallisation begins with the nucleation of ACC at the mica interface. Clearly the condition of the mica substrate is important, and the

results here suggest that the presence of surface K_2CO_3 crystallites may be necessary for the heterogeneous nucleation of ACC at the surface. There is a rapid conversion from ACC into more thermodynamically stable $CaCO_3$ polymorphs. Vaterite particles account for >90% of the precipitates after 30 s, with the remaining material morphologically similar to ACC. The remaining amorphous particles must convert to calcite between 30 s and 2 minutes, since there is no significant increase in the number of calcite particles for further growth periods, yet there is an absence of spherical particles. The calcite particles must grow at the expense of the vaterite particles, with the vaterite particles vanishing after 1 hour due to the Ostwald's step process. Indeed, the Ostwald's step growth of calcite at the expense of vaterite has been reported by Kawano *et al.* [157].

The model described by Yamanaka *et al.* does not adequately describe the appearance of tetrahedral, rhombohedra and intermediate calcite configurations, since the relative number of particles does not change as a function of time. It is proposed here that the calcite configuration is governed by the contact angle formed between the ACC particle and must therefore be determined before transformation into the crystalline (calcite) phase. Otherwise a substantial pinning at the three phase boundary would be required.

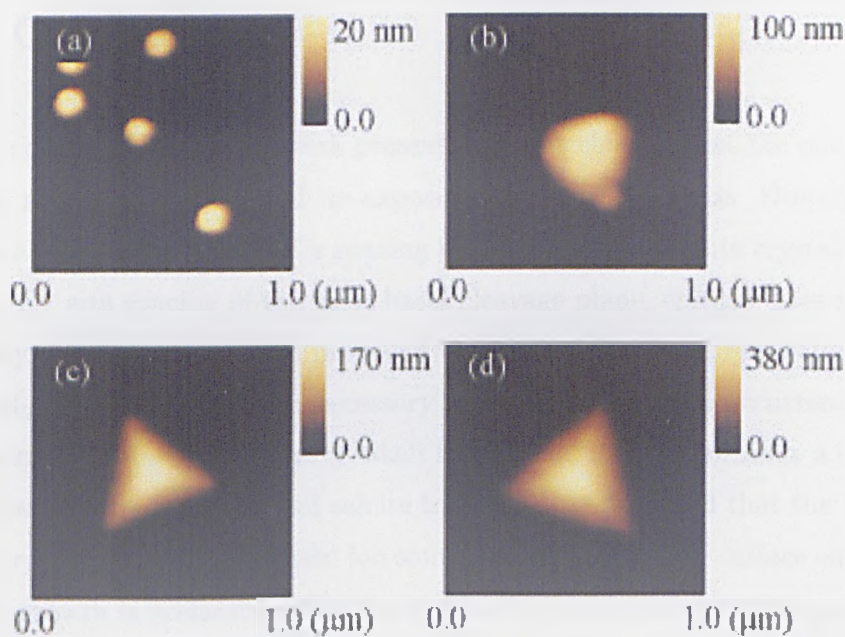


Figure 3.18: AFM images of early stage CaCO_3 growth on a mica surface taken from reference [156]. **a** Spherical particles, indicative of ACC, **b** intermediate particles and **c** calcite tetrahedra.

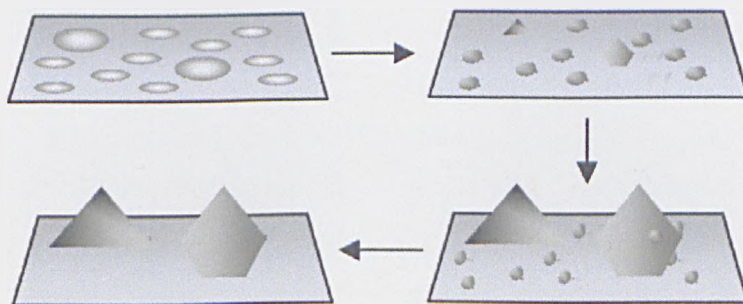


Figure 3.19: Schematic model representing the proposed early stage CaCO_3 growth on a mica surface. Firstly, ACC nucleates at favourable nucleation sites at the mica surface. Secondly, the majority of ACC transforms into vaterite, yet a small proportion transforms directly into calcite. Thirdly, the calcite particles will grow at the expense of vaterite particles, due to an Ostwald's step process. Finally, all the vaterite particles will dissolve as the supersaturation of the system falls.

3.4 Conclusions

It can be concluded from the work presented in this chapter that the mica surface is highly sensitive to details of its exposure to the atmosphere. Despite a close lattice match between the Ca-Ca spacing in (001) oriented calcite crystals and the adjacent K^+ site spacing of the mica basal cleavage plane, epitaxy does not occur on freshly cleaved mica. It is proposed that the presence of naturally forming surface K_2CO_3 crystallites is a necessary intermediary for the occurrence of epitaxial calcite. Unlike in the case of alkali metal ions, there is normally a large free energy cost for the adsorption of calcite to mica. It is proposed that the transient K_2CO_3 crystallites act as localised ion sources, yielding specific surface sites where epitaxial growth is preferable. The short growth time experiments suggest that it is ACC which first nucleates at the mica surface, before transforming into calcite, since no calcite particles with dimensions below 100 nm were observed.

Chapter 4

Crystallisation on Self-Assembled Monolayers

This chapter considers the nucleation and growth of CaCO_3 on self-assembled monolayers (SAMs) of alkylthiols on gold. Using homogeneous carboxyl-terminated SAMs, a high degree of control over CaCO_3 polymorphism, orientation and nucleation density is afforded, due to favourable interactions between the inorganic mineral and the organic monolayer. An overview of SAMs is presented in section 4.2, including details of the deep-UV photo-patterning method. The results section begins with SAM characterisation data, using water contact angle measurements and X-ray photoelectron spectroscopy (XPS) (section 4.3.1). CaCO_3 crystallisation on homogeneous SAMs resulted in the exclusive growth of calcite, mainly in orientations parallel to the (012) and (015) growth planes. The effects of solute concentration, alkanethiol solvent and precipitation method on the crystallisation on these surfaces are described in section 4.3.2. Using patterned functionalised SAMs, crystallisation is restricted to defined regions, with nucleation suppressed elsewhere due to a localised undersaturation (4.3.3). The early growth stages of CaCO_3 on homogeneous SAMs is considered in section 4.3.4, with the results broadly analogous to those of CaCO_3 on weathered mica described in section 3.2.4. Irregular amorphous particles are initially present, decreasing in number as a function of time, and vanishing altogether after growth periods greater than 1 h.

4.1 Introduction

It was shown in section 3.1 that ordered epitaxial calcite growth occurs on crystalline mica surfaces weathered under certain conditions. The ordered overgrowth of calcite was limited to a (001) orientation, since the epitaxial growth was due in part to the lattice match between calcite and mica. The face selective growth of calcite in several orientations has been achieved using organic surfaces of alkylthiol-on-metal self assembled monolayers (SAMs) [134–136, 158–161]. Using CO₂H terminated alkylthiols on gold, Aizenberg *et al.* demonstrated the face-selective growth of calcite in 6 different orientations, dependent upon the metal substrate, alkyl chain length and the functionalised group [34, 134, 162]. The uniform orientation of the crystals formed on each SAM is governed by the specific interfacial structure of the oriented, homogeneous SAM, which is in turn controlled by the chain length, tilt angle and metal substrate.

Growth on heterogeneous SAMs demonstrates the control over orientation and polymorphism of an inorganic material, CaCO₃, using a functionalised organic surface. Continuing on from these studies, Aizenberg *et al.* restricted crystallisation to specific nucleation sites using patterned functionalised SAMs [135]. Using the micro-contact printing method developed by Whitesides and co workers [163, 164], the nucleation of CaCO₃ at favourable nucleation sites on patterned SAMs results in mass transport away from less favourable nucleation areas, resulting in regions of localised undersaturation across the surface.

This chapter begins with an overview of SAMs, and includes characterisation data of both homogeneous and patterned SAMs.

4.2 Structure and Formation of SAMs

SAMs are the result of the spontaneous formation of molecular assemblies on defined substrates. There are many different SAM systems including silanes on silicon oxides [165] and glass [166], *n*-alkanoic acids on aluminium oxides [167] and silver [168], and organosulphates on metal surfaces [169]. However, the most studied and characterised SAMs are those of alkanethiols on gold [170]. First described

by Nuzzo and Allara in 1983 [171], alkanethiols on gold SAMs were initially used as an alternative to the often unstable Langmuir-Blodgett monolayers. A relative ease of preparation and the absence of a stable gold oxide layer under atmospheric conditions are reported advantages of these monolayers [172] (the formation of a stable Au_2O_3 layer has been reported in the presence ozone under UV irradiation [173]).

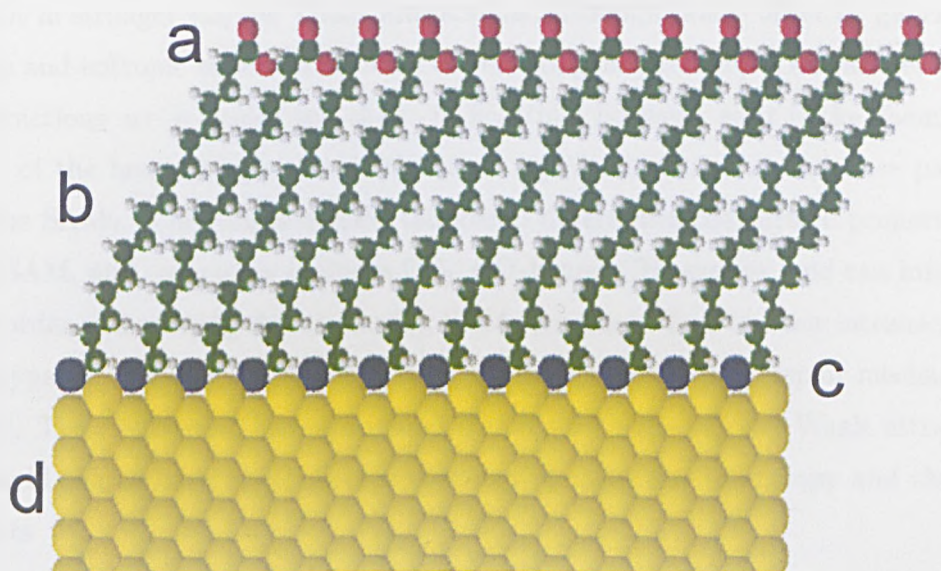
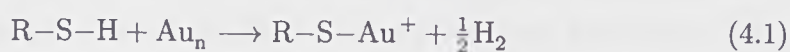


Figure 4.1: Schematic diagram of the components of a mercaptohexadecanoic acid SAM. **a** Functionalised tail group, **b** alkylthiol chain, **c** mercapto head group and **d** gold substrate. Showing hydrogen (grey), carbon (green), oxygen (red), sulphur (blue) and gold (yellow) atoms to scale

Alkylthiol SAMs have the same basic structure, comprising of a surface active head group, an alkyl chain and a functionalised tail group. The general structure is $\text{R}(\text{CH}_2)_n\text{SH}$ where R denotes the functionalised tail group (Figure 4.1). The head group consists of a *mercapto* SH group, which forms a true valence bond with the gold substrate [174]. This exothermic interaction can be considered as the oxidative addition of the S-H bond, followed by the reductive elimination of a hydrogen atom [170].



The high free-energies associated with this reaction, of the order of -120 kcal/mol, results in a high occupancy of available binding sites, pushing together previously adsorbed molecules in the process [62]. The hydrocarbon alkyl chain typically consists of between 10 and 18 carbon atoms, with a constant second nearest carbon atom distance of 2.52 Å [175]. As the alkylthiol chains coalesce, short range, dispersive, van der Waals forces result in further close packing. Longer chains result in stronger van der Waals interactions, although this is offset by gauche defects and entropic effects in the case of very long chains [115]. The van der Waals interactions are typically less than -10 kcal/mol however, so it is the chemisorption of the head groups that is the most significant factor in the close packing of the SAMs. The functionalised tail group determines the surface properties of the SAM, and commonly includes CF_3 , CO_2H and CH_3 groups, and can influence the order and packing density during SAM formation. Due to their intrinsic thermodynamic stability, SAMs tend to be defect-free and exhibit repair mechanisms [134]. The exothermic mercapto bond coupled with the van der Waals attraction of alkyl chains more than offset free-energy changes due to entropy and thermal effects.

For adsorption to Au (111) surfaces, a close packed surface phase exists in which the sulphur atoms form a thiolate complex with the gold atoms in a $\sqrt{3} \times \sqrt{3}$ overlayer [176]. Vibrational spectroscopy studies have revealed that the chains are packed in an orthorhombic manner, with two chains per unit cell in an all trans conformational state [177]. When the head-head spacing is greater than the touching van der Waals distance of the alkyl chains, the chains are reported to tilt in such a way to maximise the van der Waals interactions, and thus minimise the free energy of the system [178, 179]. Fourier transform infrared spectroscopy (FTIR) studies have confirmed this, revealing a characteristic tilt α of $\sim 26\text{-}28^\circ$ from the planar normal and a $\sim 52\text{-}55^\circ$ angle β about the molecular axis for alkanethiols on gold (Figure 4.2) [178].

80-90% of the monolayers reportedly form within the first few minutes, due to chemisorption of the head group and the straightening out of the alkyl chains, with the first of these processes typically 3-4 times faster than the second [180]. There is a final ordering process relating to the reorientation of the terminal groups, although this occurs over a longer timescale of up to 24 hours. The formation of

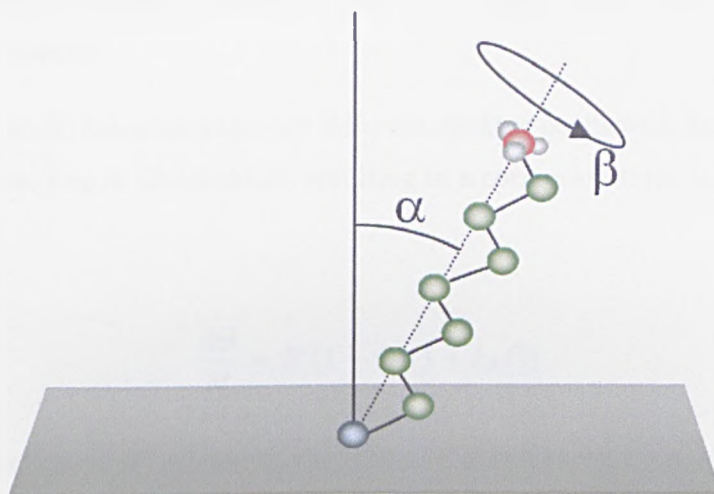


Figure 4.2: Schematic diagram showing the geometry of a SAM, dependent on the chain tilt angle α and the chain twist angle β .

the SAMs has been modelled using the Langmuir adsorption isotherm. As each head group binds to the surface, the number of available sites decreases

$$\frac{d\Theta}{dt} = R(1 - \Theta) \quad (4.2)$$

where Θ is the relative surface coverage and R is a growth constant, giving rise to a simple growth law

$$\Theta = 1 - e^{-Rt} \quad (4.3)$$

Here, the growth rate is proportional to the number of binding sites on the surface. This model represents an ideal system, since in reality there are intermolecular interactions between the adsorbed molecules, with different energies associated with adsorption at island domain boundaries as opposed to isolated sites. The model also assumes there is no limitation caused by diffusion of adsorbents from the bulk liquid phase.

A diffusion limited model takes the form

$$\Theta = 1 - e^{-R't^{1/2}} \quad (4.4)$$

when taking into account that $\Theta = R't^{1/2}$ in cases where growth is governed entirely by diffusion.

The Kisliuk model takes into account different sticking coefficients between covered areas and those free of alkanethiols, resulting in a correction term to the Langmuir model [181].

$$\frac{d\Theta}{dt} = R'(1 - \Theta)(1 + k_E\Theta) \quad (4.5)$$

where the coefficient R' relates to the effect of diffusion on monolayer formation and is proportional to the square root of the diffusion coefficient. The Kisliuk factor, k_E takes values between 0 and 1 and defines the degree of mobility of the precursor, or initially bound, alkylthiols [182]. The resultant surface coverage is

$$\Theta = \frac{1 - e^{-R'(1+k_E)t}}{1 + k_E e^{-R'(1+k_E)t}} \quad (4.6)$$

The Kisliuk adsorption isotherm gives an effective approximation of substrate coverage, however as in the case of the Langmuir adsorption isotherm, the second and third stages of SAM growth are not accounted for [183].

Experimentally, the SAM formation rate is dependent on several control parameters. It has been reported that increasing alkyl chain length results in a slower initial adsorption [184]. This was found to be the case for both polar (ethanol) and non-polar (dichloromethane) solvents, and is a consequence of the reduced molecular mobility of the longer chains. At low concentrations, the SAM formation is related to the alkanethiol concentration; at higher concentrations, the formation rate is independent, presumably limited by kinetic factors. The chemical nature of the solvent itself affects a number of properties of an alkanethiol molecule, including solubility, mobility, steric constraints and polarity [185].

4.2.1 Patterning of SAMs Using Deep-UV Photolithography

The deep-UV patterning is a three-stage process, with exact experimental details listed in section 2.2.2. A single component x -terminated SAM (usually hydrophobic) is formed before exposing to short wavelength, $\lambda=254$ nm UV light through a quartz photomask. This photocleavage process yields a loosely bound sulphate group, which XPS studies have shown can be readily removed by rinsing with a polar solvent [186]. The high energy UV light reacts with atmospheric oxygen atoms, breaking the O-O bond and creating highly reactive ozone, by a process known as ozonolysis [187]. The ozone undertakes non-selective reactions with all parts of the thiol group, breaking the mercapto bond and cleaving the thiol. This surface is then backfilled in a solution of a y terminated thiol, thus backfilling the photocleaved regions. The cleavage rate is dependent on chain length, closepacking and UV wavelength [187].

Patterned SAMs were formed using deep-UV photolithography for several reasons:

- Only commercially available thiols are required, in contrast with short wavelength soft-UV photolithography, which requires the bespoke synthesis of photo-sensitive thiols. An in depth discussion of soft-UV photolithography is included in references [117] and [188]
- The functionalised tail groups can be substituted for any available thiols, making this a highly versatile method
- The use of an expensive e-beam for the production of PDMS stamps is not required, in contrast to micro-contact printing (described in reference [163])
- There is a near 100 % photo cleavage yield, in contrast to soft UV photolithography (typically around 50 % [188])

Surface	DCM		Ethanol	
	Advancing θ	Receding θ	Advancing θ	Receding θ
MHA	55 ± 1	16 ± 1	55 ± 2	15 ± 1
ODT	109 ± 1	99 ± 1	109 ± 2	95 ± 2
Au	84 ± 2	61 ± 1	-	-

Table 4.1: Advancing and receding water contact angles for MHA and ODT SAMs prepared in DCM and EtOH with acetic acid solvents respectively. The advancing and receding contact angle of pure gold surfaces are included

4.3 Results

4.3.1 Characterisation of SAMs

Homogeneous SAMs were characterised using contact angle measurements as described in section 2.4.1. Solid-liquid-vapour contact angles were measured for water droplets on MHA and ODT surfaces, in addition to Au control surfaces. SAMs were prepared in accordance to the procedures described in section 2.2.2, using both ethanol with acetic acid and DCM solvents (Table 4.1). There was agreement with literature for the hydrophobic ODT SAM, with an advancing angle of $(109 \pm 2)^\circ$ when formed in ethanol [189, 190]. A large degree of hysteresis was observed for the hydrophilic MHA SAM, with an advancing and receding angles of $(55 \pm 2)^\circ$ and $(15 \pm 1)^\circ$ respectively, when formed in ethanol. Although the advancing angle approached those of Wang *et al.* [191], it is worth stating that there is considerable ambiguity in the literature, with the nature (advancing, receding or sessile) of the drop often not stated. Whilst the receding contact angle of gold under UHV has been reported as 0° [192], the measured gold contact angle was significantly higher, presumably due to adsorbed impurities at the high energy metal surface. However, the measured contact angles were lower for MHA surfaces in comparison to bare gold substrates, suggesting that these impurities are displaced during the chemisorption of the head group.

Laibinis *et al.* suggested that a thiolate exchange occurs during the immersion of a functionalised SAM in a secondary thiolate solution [193]. This has implications during backfilling since the contrast between hydrophilic and hydrophobic regions could potentially be reduced. ODT SAMs formed in 0.1 mM ethanol solutions

were immersed in a 0.1 mM MHA ethanol solution for a time period of 0 - 24 h, with advancing and receding water contact angles shown in figure 4.3. A steady decrease in contact angle was observed, with the advancing angle falling from $(109 \pm 2)^\circ$ initially to $(104 \pm 2)^\circ$ after 2 hours. After a 24 h immersion period in a 0.1 mM MHA ethanol solution the advancing and receding water contact angles were $(90 \pm 2)^\circ$ and $(76 \pm 2)^\circ$, similar to those values reported by Laibinis *et al.* [193].

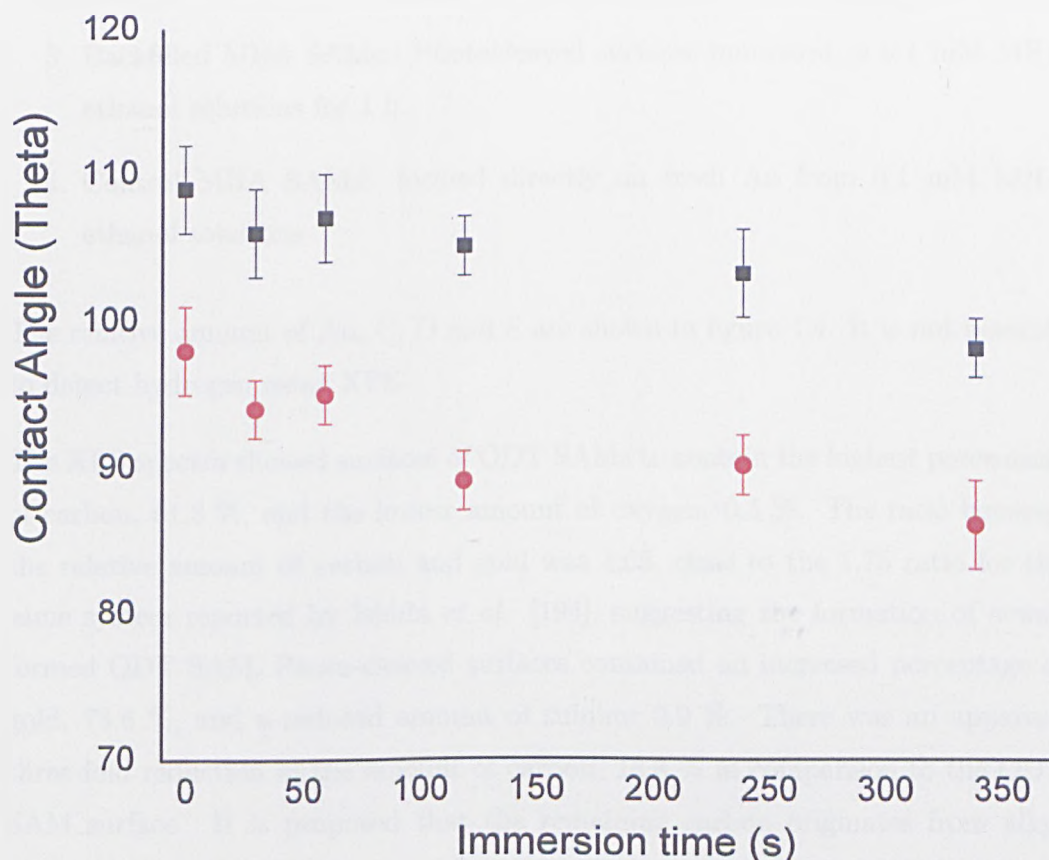


Figure 4.3: Advancing (black squares) and receding (red circles) contact angles as a function of immersion time for ODT SAMs in 0.1 mM MHA & ethanol solution.

The water contact angle data suggest that a significant thiol exchange occurs after a 24 hour backfill period, with this effect is likely to be enhanced at the boundaries on patterned SAMs, due to reduced Van der Waals interactions. In addition, a greater hysteresis between advancing and receding angles was witnessed with increased immersion time, indicative of a more disordered surface. From these data a 1 hour backfill period was chosen, since although the complete close packing of a SAM takes up to 24 hours, the surface degradation associated with thiol exchange is more significant.

The deep-UV photocleavage process was characterised at each stage by XPS, with the following surfaces considered:

1. ODT SAMs:- formed from 0.1 mM ethanol solution.
2. Photocleaved surfaces:- ODT SAMs exposed to 254 nm wavelength UV light for 60 min before sonication in ethanol for 10 min.
3. Backfilled MHA SAMs:- Photocleaved surfaces immersed in 0.1 mM MHA ethanol solutions for 1 h.
4. Control MHA SAMs:- formed directly on fresh Au from 0.1 mM MHA ethanol solutions

The relative amount of Au, C, O and S are shown in figure 4.4. It is not possible to detect hydrogen using XPS.

The XPS spectra showed surfaces of ODT SAMs to contain the highest percentage of carbon, 61.3 %, and the lowest amount of oxygen, 0.5 %. The ratio between the relative amount of carbon and gold was 1.69, close to the 1.75 ratio for the same system reported by Ishida *et al.* [194], suggesting the formation of a well formed ODT SAM. Photo-cleaved surfaces contained an increased percentage of gold, 73.6 %, and a reduced amount of sulphur 0.9 %. There was an apparent three-fold reduction in the amount of carbon, 18.8 % in comparison to the ODT SAM surface. It is proposed that the remaining carbon originates from alkyl chains fragmented during photo-cleavage. There was a significant reduction in the amount of sulphur, 0.9 %, suggesting that the fragmented alkyl chains are only loosely bonded to the surface, and they are assumed to be displaced during backfilling. Comparisons between backfilled and control MHA SAMs shows close agreement in relative percentages of oxygen (O_{1s}), 8.1 % and 8.4 % and sulphur 2.1 % and 2.8 % respectively. There was a slight increase in the amount of gold, 37.3 % to 35.3 % and reduction in the amount of carbon, 49.7 % to 52.5 % in comparison between the backfilled and control SAMs.

A possible anomaly in the XPS data arises from the relative amount of oxygen on the photo-cleaved surface, 6.7 %, which is significantly increased from a pure ODT surface, 0.5 %. It is tentatively proposed that oxidation of the gold surface

occurs during the deep UV process, since it has been shown by others that gold will form a stable oxide when irradiated with UV light in the presence of ozone [173].

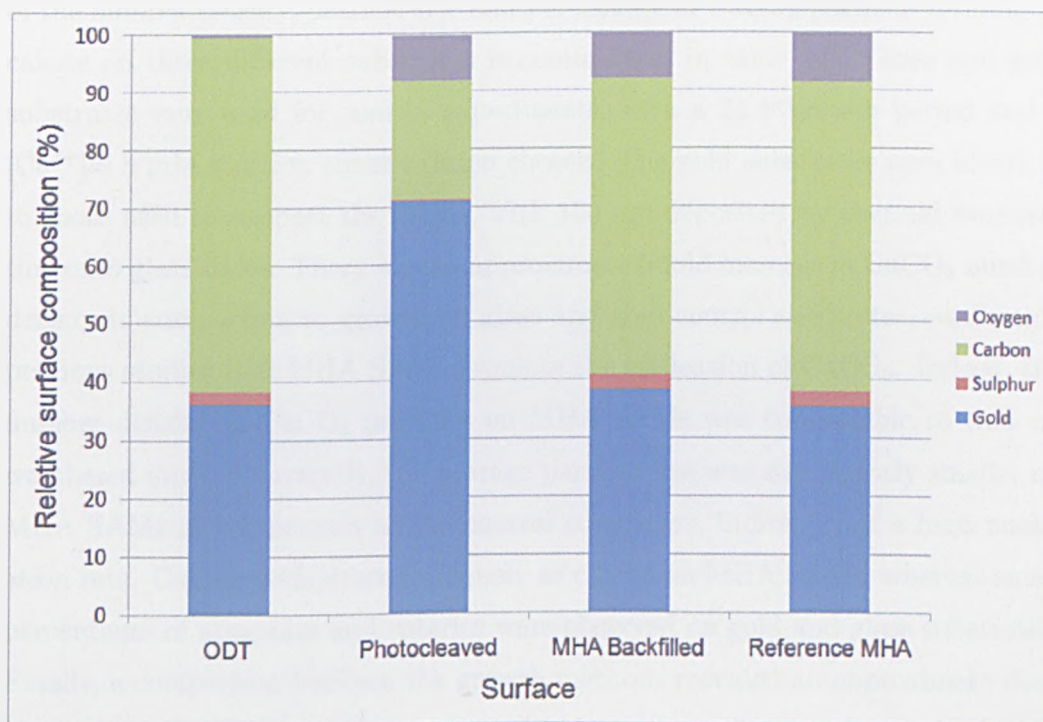


Figure 4.4: Relative elemental surface compositions of SAMs at each stage of the deep-UV photo-patterning process.

4.3.2 Crystallisation on Homogeneous SAMs

Oriented, face selective growth of calcite was observed on carboxyl-terminated SAMs, formed in solutions of mercaptohexadecanoic acid (MHA). The observed orientations were mainly parallel to the (012) and (015) growth planes, in agreement with literature [134, 136]. Calcite crystals in these orientations are shown in figure 4.5 along with simulated calcite crystals in these orientations. The calcite orientations on MHA SAMs were different to those observed on weathered mica, which facilitated true epitaxial growth in a (001) orientation (Figure 3.4) and those on freshly cleaved mica and glass slides, on which no preferential growth was observed.

Several variables were considered in order to find optimal conditions for face selective growth. Calcite was precipitated using both the double decomposition and gas diffusion methods outlined in section 2.3 (Figures 4.6, 4.7). A systematic study of the number density, particle size and percentage of CaCO_3 particles forming as calcite on three different substrates is summarised in table 4.3. Glass and gold substrates were used for control experiments, with a 24 h growth period and a $[\text{Ca}^{2+}] = 8 \text{ mM}$ solution concentration chosen. The gold substrates were identical to those used to support the SAMs, with 100 nm deposited by thermal evaporation onto glass slides. There was an approximate 5-fold increase in CaCO_3 number density in comparison to growth on glass and gold control substrates, confirming previous studies that MHA SAMs promote the nucleation of CaCO_3 . Indeed, the number density of CaCO_3 particles on MHA SAMs was comparable to that on weathered mica. Conversely, the average particle size was significantly smaller on MHA SAMs in comparison to the control substrates, indicative of a high nucleation rate. CaCO_3 precipitated uniquely as calcite on MHA SAMs, whereas small percentages of aragonite and vaterite were observed on gold and glass substrates. Finally, a comparison between the growth methods revealed an approximate doubling in the CaCO_3 number density and halving in precipitate size on both gold substrates and MHA SAMs using the double decomposition growth method in comparison to the gas diffusion growth method.

Conditions	Orientation		
	(012)	(015)	Other
EtOH - DD	10	37	53
EtOH - GD	42	44	14
DCM - DD	12	12	76
DCM - GD	18	57	25

Table 4.2: Percentage orientation of calcite crystals on MHA SAMs formed in 0.1 mM EtOH & acetic acid and DCM solvent. Crystals formed by double decomposition (DD) and gas diffusion (GD) methods at 5 mM, 12 h growth period

The percentage of face selective calcite growth on MHA SAMs was determined as a function of precipitation method and the solvent within which the MHA SAM was formed (Table 4.2). The double decomposition growth method yielded a higher percentage of face selective growth in (012) and (015) orientations. (012) or (015) face selective calcite growth was observed in 47% and 86% of cases for

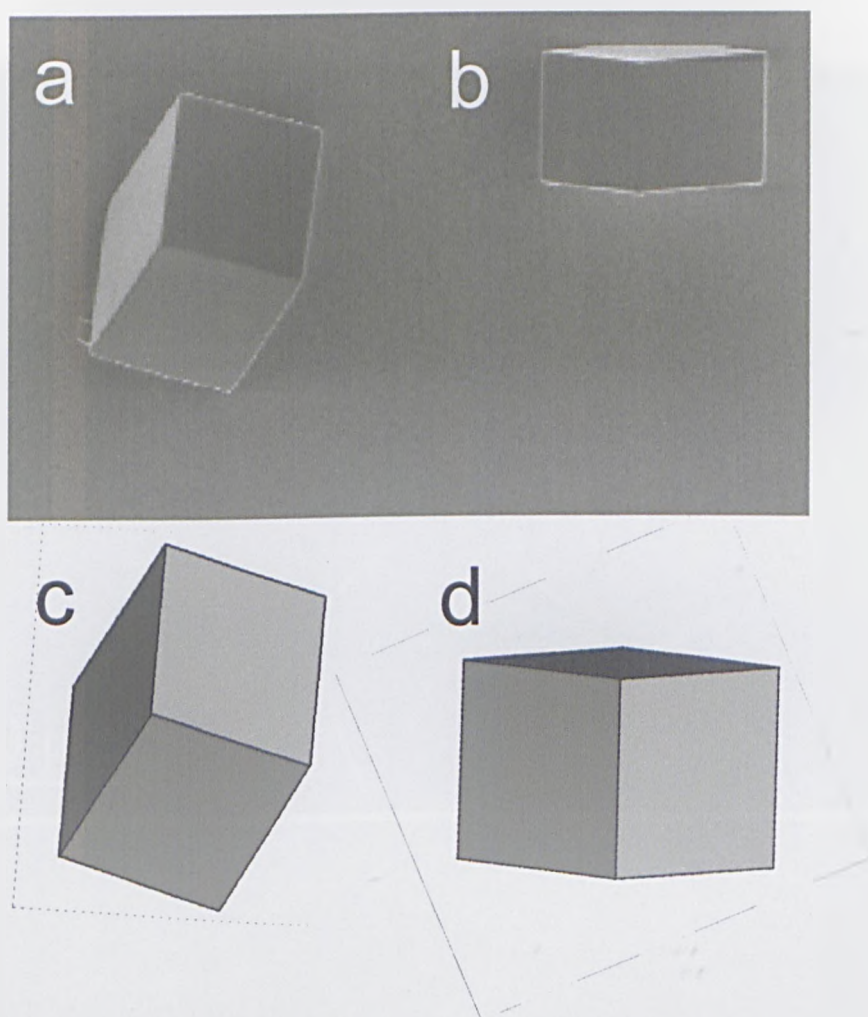


Figure 4.5: **a, b** SEM images of calcite growth on carboxyl-terminated SAMs in **a** (012) and **b** (015) orientations. **c, d** Corresponding SHAPE simulations

double decomposition and gas diffusion growth methods respectively (12 h growth period, 5 mM concentration, EtOH & acetic acid solvent). A small increase in the percentage of (012) and (015) face-selective calcite crystals was observed for SAMs formed in EtOH & acetic acid solvent in comparison to those formed in DCM solvent (Figures 4.6, 4.7). For identical growth conditions (12 h growth period, 5 mM gas diffusion method), 86 % and 75 % of calcite crystals were face selective for SAMs formed in EtOH with acetic acid and DCM solutions, respectively.

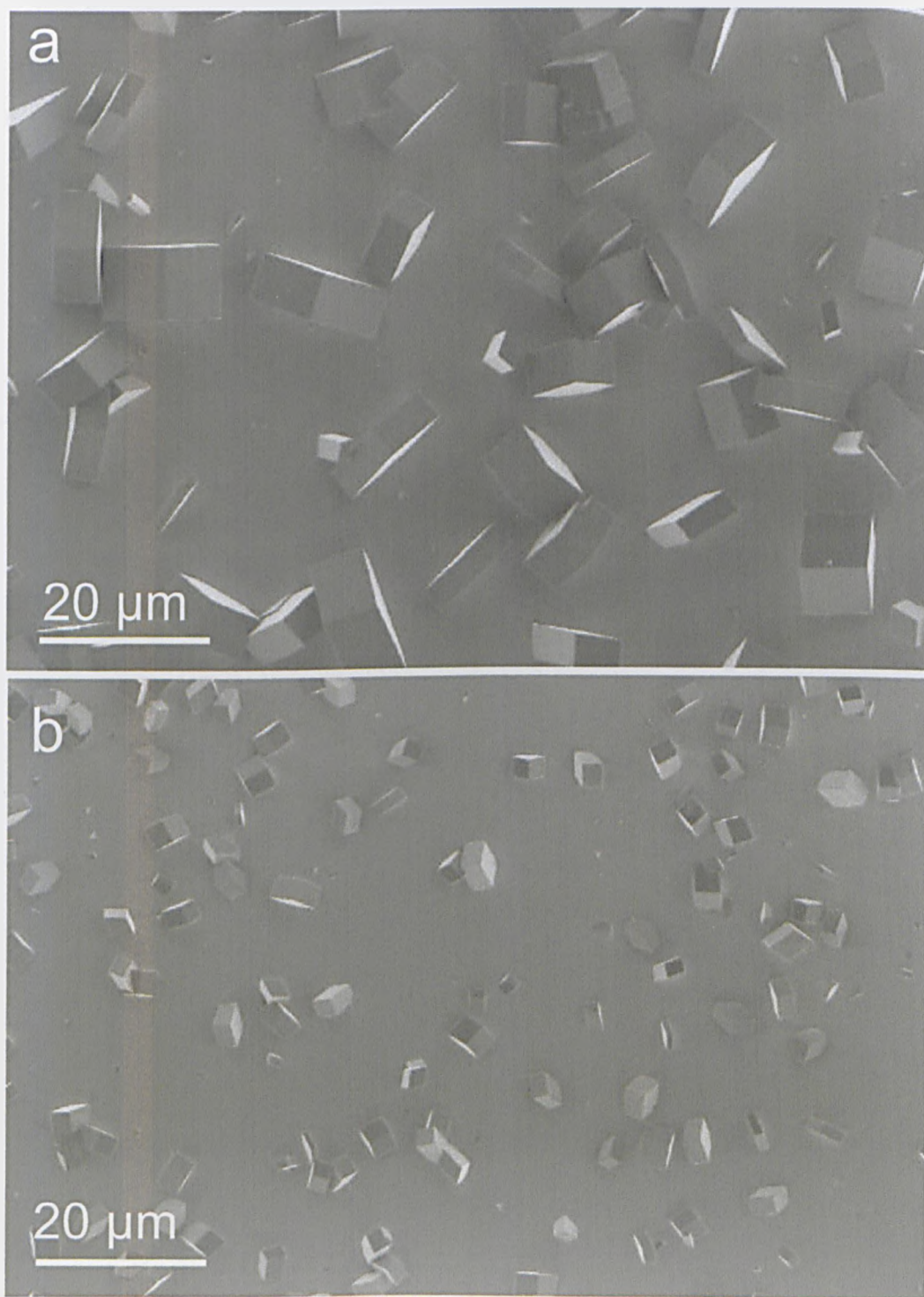


Figure 4.6: SEM images of face selective growth calcite growth on carboxyl-terminated SAMs formed in 0.1 mM DCM MHA solutions. CaCO_3 was precipitated from $[\text{Ca}^{2+}] = 5\text{mM}$ solutions using **a** gas diffusion method and **b** double decomposition growth method.

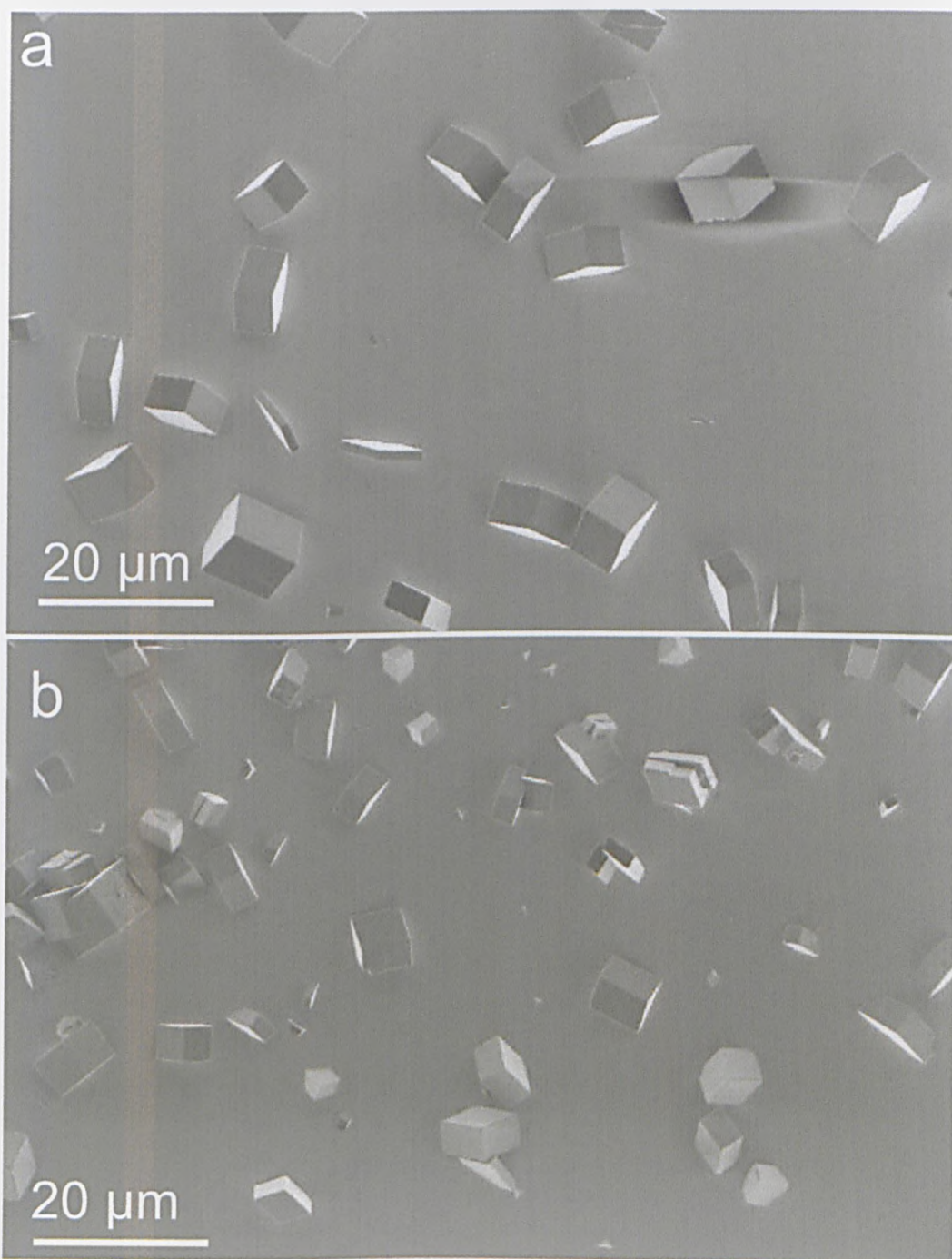


Figure 4.7: SEM images of face selective growth calcite growth on carboxyl-terminated SAMs formed in 0.1 mM ethanol with acetic acid MHA solutions. CaCO_3 was precipitated from $[\text{Ca}^{2+}] = 5\text{mM}$ solutions using a gas diffusion method and **b** double decomposition growth method.

Growth Method Substrate	Gas diffusion			Double decomposition		
	Glass	Gold	MHA	Glass	Gold	MHA
Number per mm^2	530±200	350±60	3100±600	800±300	1400±200	6800±1000
Particle size (μm^2)	109±30	58±6	25±5	98±20	28±10	9±2
Calcite percentage	91	90	100	99	93	100

Table 4.3: Nucleation density, particle size and polymorphism for $CaCO_3$ particles on glass, gold and MHA SAM substrates for both precipitation methods. 8 mM solution concentration, 24 growth period.

4.3.3 Growth on Patterned SAMs

The growth of CaCO_3 was considered on deep-UV patterned SAMs, formed in accordance to the procedure outlined in section 2.2.2. The formation of arrays of oriented calcite crystals on patterned SAMs has been reported by Aizenberg and others [135, 195, 196]. In these cases the SAMs were patterned by microcontact printing [135], or by e-beam lithography [195], whereas the work presented here shows the oriented growth of calcite on deep-UV patterned SAMs for first time. Section 7.1 considers the growth of CaCO_3 in picolitre droplets supported on patterned SAMs, necessitating the bulk growth of CaCO_3 on the same surfaces as a control.

CaCO_3 growth on patterned SAMs was attempted using only the gas diffusion precipitation method, since this precipitation method was shown to result in a slight increase in face-selective calcite growth on homogeneous MHA SAMs (section 4.3.2) with precipitation preceded by a slow rise in solution supersaturation. SAMs were patterned with circular hydrophilic regions within a hydrophobic background, with the size and spacing of the circular regions limited by the photo-mask design. Patterned calcite growth was obtained on two circular patterns; 20 μm diameter circles at a 20 μm edge-edge spacing (Figure 4.8), and 10 μm diameter circles at a 14 μm edge-edge spacing (Figure 4.9). The patterned substrates were formed in accordance to the procedure described in section 2.2.2.

Multiple calcite crystals (7 ± 2) per site were generally observed on the large circular regions after a 12 h growth period, $[\text{Ca}^{2+}] = 5\text{mM}$ (Figure 4.8). The CaCO_3 crystals formed uniquely as calcite, with the absence of aragonite and vaterite consistent with the growth on homogeneous SAMs (section 4.3.2). The growth was also face selective, with over 70% of crystals in orientations parallel to the (012) and (015) growth planes. There was a reduction in the number of crystals per site for the 10 μm diameter patterned SAM under the same growth conditions. Again, the crystals exclusively formed as calcite, on this occasion with 3 ± 2 crystals per site. There was a similarly high percentage of face selective growth, accounting for 65% of calcite crystals. The number of calcite crystals per active site was dependent on location of the sample in the vessel, with a higher number of crystals per active site closer to the air-solution interface. Since the air-solution interface was small

in comparison to the solution volume, the number of calcite crystals varied as a function of distance to the interface (Figure 4.10). Closer to the interface there was an increase in the number of calcite crystals, with up to 11 per site. Conversely, at a larger distance from the interface, no more than three calcite crystals were observed per site. At the larger distance the crystals had typical dimensions of 8 μm in comparison to the typical crystal dimensions of 4 μm found closer to the interface. This is thought to be a consequence of the precipitation method, since supersaturation arises due to the the dissolution of CO_2 at the solution-air interface. There is therefore a higher supersaturation closer to this interface, accounting for the increased nucleation rate and smaller crystal size.

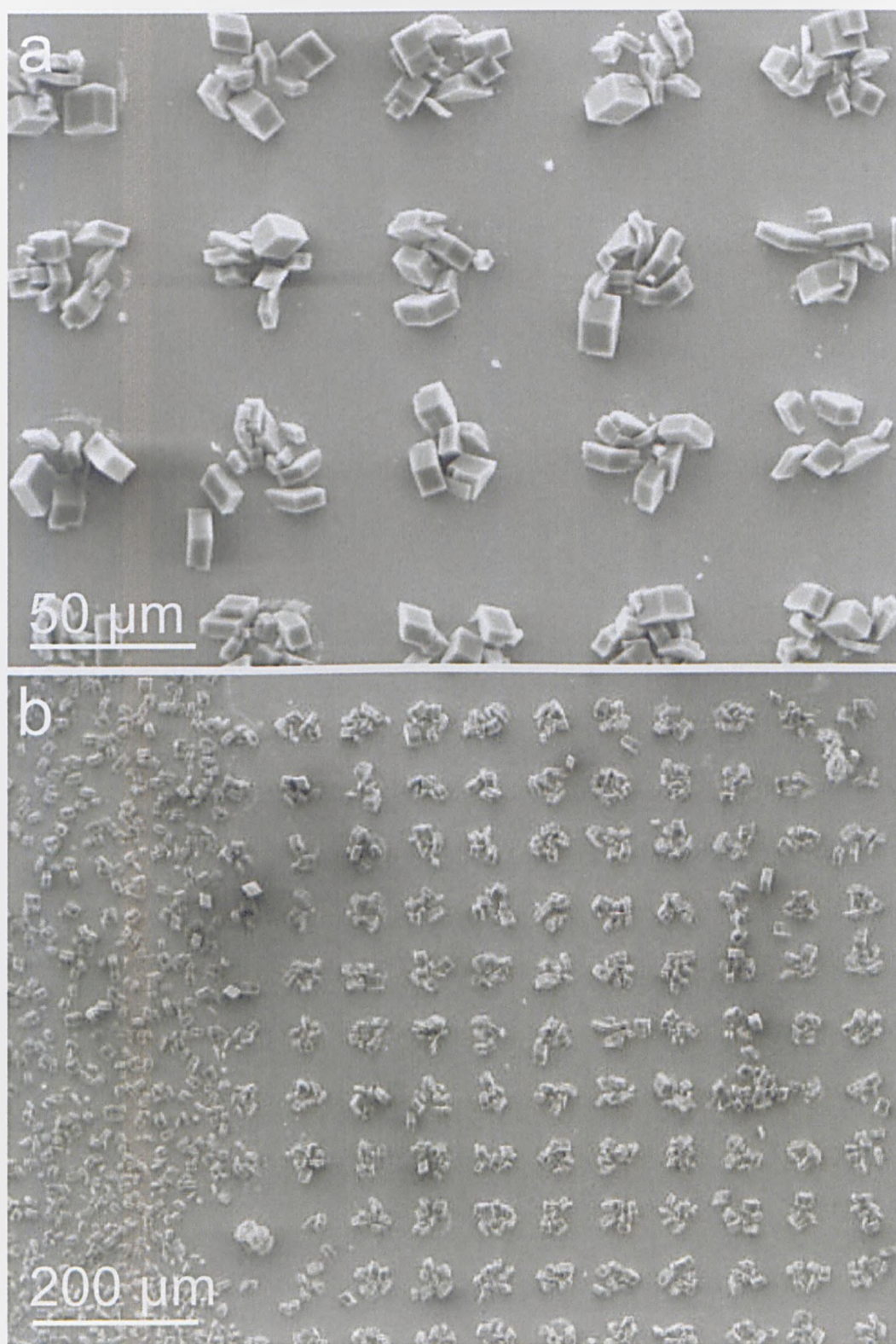


Figure 4.8: SEM images of CaCO_3 growth on 20 μm spaced 20 μm diameter circular patterned SAMs at a high and b low magnification. $[\text{Ca}^{2+}] = 5\text{mM}$ double decomposition precipitation method, 12 h growth period.

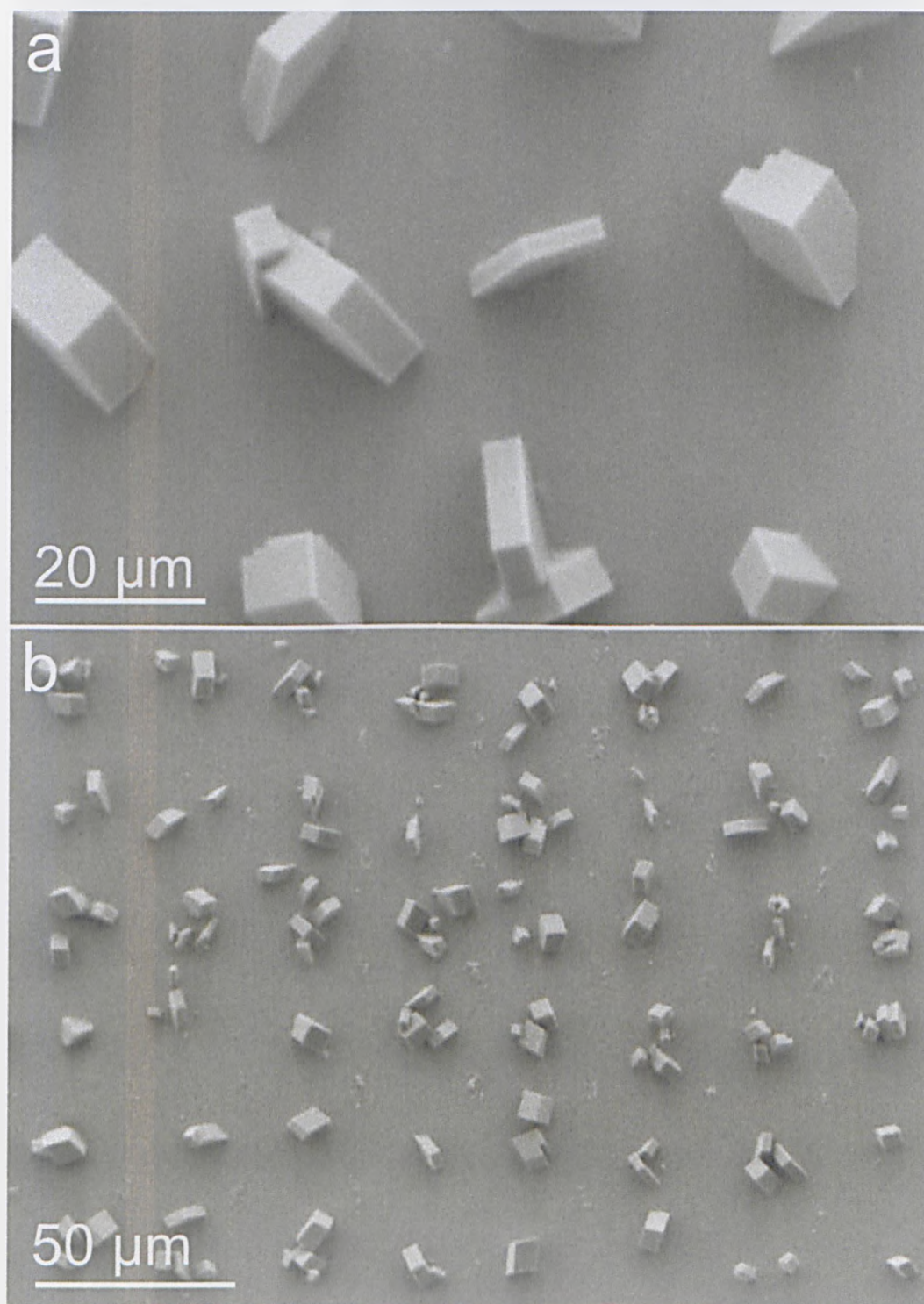


Figure 4.9: SEM images of CaCO_3 growth on $14\ \mu\text{m}$ spaced $10\ \mu\text{m}$ diameter circular patterned SAMs at **a** high and **b** low magnification $[\text{Ca}^{2+}] = 5\text{mM}$ double decomposition precipitation method, 12 h growth period.

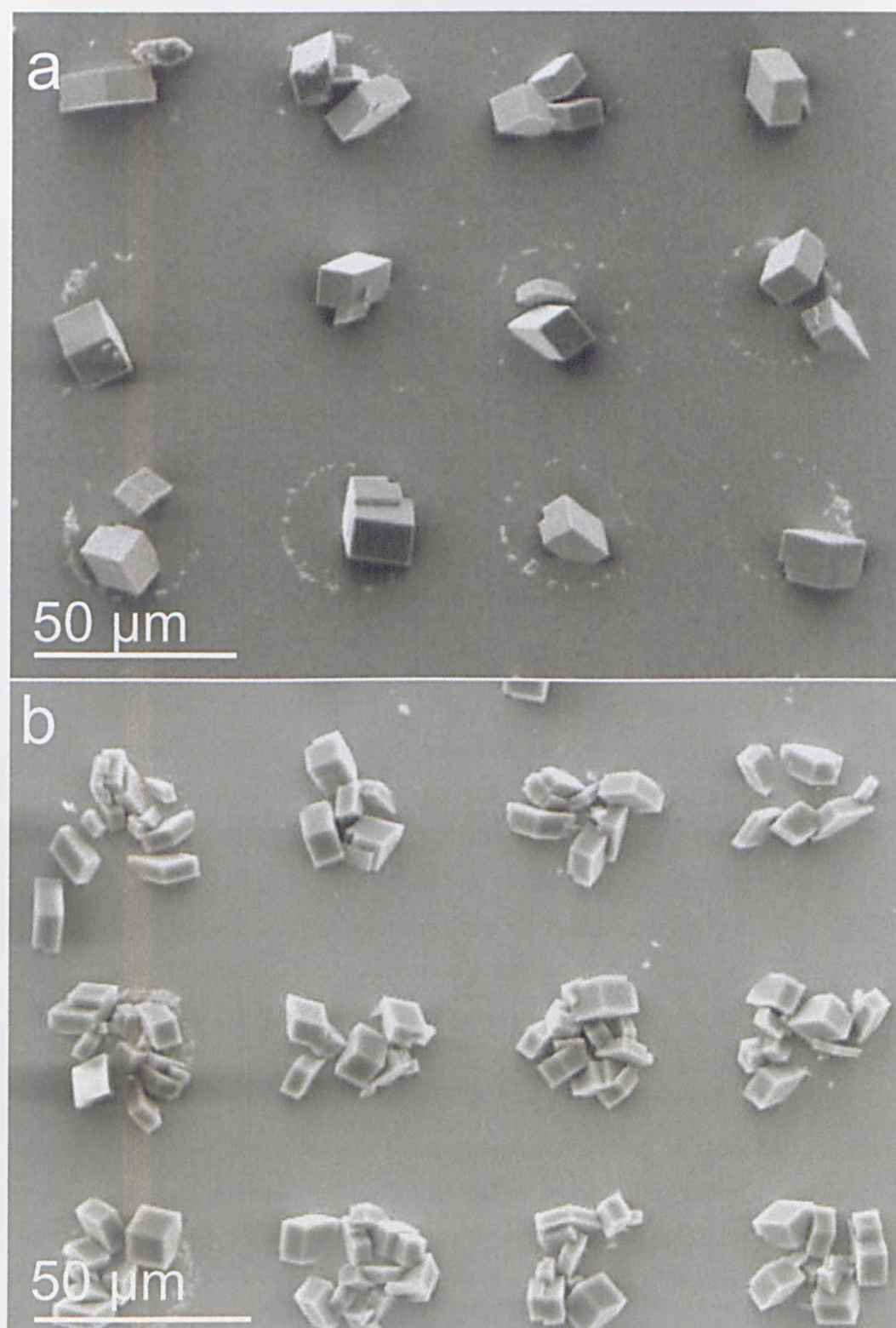


Figure 4.10: SEM images of CaCO₃ growth on 25 μm spaced 20 μm diameter circular patterned SAMs positioned **a** the vessel top, closer to the air-solution interface and **b** the vessel bottom, further from the air solution interface. [Ca²⁺] = 5mM double decomposition precipitation method, 12 h growth period.

4.3.4 Early Growth Stages on SAMs

Analogous to the results presented in section 3.2.4, CaCO_3 nucleation pathways on MHA SAMs were determined through the morphological analysis of precipitates after a series of short growth times. After a 1 hour growth period, well defined single-crystal calcite with dimensions greater than $1 \mu\text{m}$ were present on MHA SAMs, with an absence of aragonite, vaterite and ACC particles. After growth periods less than 1 minute the CaCO_3 particles were highly irregular, morphologically similar to vaterite and ACC, comparable to the early growth stages on mica (section 3.2.4). Here, growth periods of 0.5, 1, 2, 5 and 10 minutes were investigated for two initial solution concentrations, 2.5 and 5 mM. Table 4.4 quantifies the relative amounts of irregular CaCO_3 precipitate, vaterite and calcite as a function of growth time in addition to the observed size range of the irregular, sub-micron CaCO_3 precipitates and the average calcite dimensions (defined as the largest projected point-to-point distance).

After a 30 second growth period the CaCO_3 particles were highly irregular, consisting of aggregates of 30-120 nm diameter particles (Figure 4.11). These particles were mostly spherical, with apparently smooth surfaces and an absence of the well defined interfacial axes associated with calcite. The amorphous nature of these particles is shown in figures 4.11b-e. Individual particles are shown in figures 4.11b,e, however particle aggregation occurred in over 90% of cases (Figure 4.11c). The particles were morphologically similar to ACC particles precipitated from bulk solution (chapter 6) and were markedly different to the irregular CaCO_3 particles observed on weathered mica surfaces after the same growth period, which had uneven surface topographies similar to vaterite. In addition to the irregular, sub-micron CaCO_3 particles, larger vaterite particles were also present, identified by a roughened platelet-like surface. However, no regular calcite particles were observed. Similarly, for a 2.5 mM concentration no calcite particles were observed after 30 seconds, although in this case there was a higher number density of vaterite particles ($700 \pm 200/\text{mm}^2$), and a ~ 30 fold decrease in the number density of sub-micron irregular CaCO_3 particles ($45000 \pm 2000/(\text{mm}^2)$) (Figure 4.12).

After a 1 minute growth period, irregular ACC type precipitates were observed for initial solution concentrations of 2.5 and 5 mM (Figure 4.13). These particles

Parameter	Growth time (min)					
	0.5	1	2	5	10	60
ACC number density (mm ²) ⁻¹	1600000 ± 600000	22000 ± 6000	34000 ± 4000	32000 ± 4000	29000 ± 9000	0
ACC diameter size range (nm)	30-120	60-240	40-180	30-160	60-120	-
Vaterite number den- sity (mm ²) ⁻¹	361	526	40	50	0	0
Calcite number density (mm ²) ⁻¹	0	370	584	822	1957	6140
Average calcite di- mensions (μm)	0	2.5	1.8	1.4	2.9	4.8

Table 4.4: CaCO₃ polymorphism and size as a function of growth time for precipitation from 5 mM solutions on MHA SAMs.

were similar in appearance to those observed after growth periods of 30 seconds, although with a significant reduction in particle number density. In addition, face selective growth of single crystal calcite was observed at both concentrations, parallel to the (012) and (015) growth planes (Figure 4.14). These particles had dimensions in the range of 0.8-3 μm , an order of magnitude increase in the dimensions of the ACC- and vaterite- type particles. In addition, transitional particles were observed with dimensions in the range of 100 nm and with an apparent tetrahedral shape (Figure 4.13c). However, these particles were extremely rare, accounting for less than 1% of the analysed particles, and were speculated to be close to the transitional point between amorphous and crystalline phases.

Figure 4.15c is an SEM overview of precipitation from 5 mM CaCO_3 solutions after a 2 minute growth period, showing a continuation of the trend observed after a 1 minute growth period. Irregular CaCO_3 particles were present at both $[\text{Ca}^{2+}] = 2.5$ mM and $[\text{Ca}^{2+}] = 5$ mM solution concentrations, with the same characteristic spherical shape for a 1 min growth period (Figure 4.15c). Again, face selective calcite was observed at both concentrations, with dimensions in the range of 0.8-3 μm (Figure 4.15b). On the assumption that there is an order of 10:1 ratio between the number of amorphous to single crystal calcite particles and that the average dimensions of the amorphous and calcite particles are 100 nm and 1 μm respectively, $\sim 99\%$ of the total CaCO_3 material is in the form of calcite. A similar trend was observed after 5 minutes, with both face selective calcite and irregular CaCO_3 particles present at both solution concentrations (Figure 4.16).

After a 10 minute growth period the precipitates were almost entirely in the form of single crystal calcite, again with growth fixed to (012) and (015) orientations (Figure 4.17). For a 5 mM solution concentration, there were 29000 ± 9000 irregular, sub-micron particles per mm^2 , with a 60-120 nm diameter size range. Figure 4.17c is of a ~ 100 nm dimension pre-crystal with a tetrahedral morphology, which is speculated to be a very early stage calcite particle. In contrast, only regular face selective growth of calcite was observed after a 1 h growth period, with no irregular sub-micron CaCO_3 or vaterite present at either concentration.

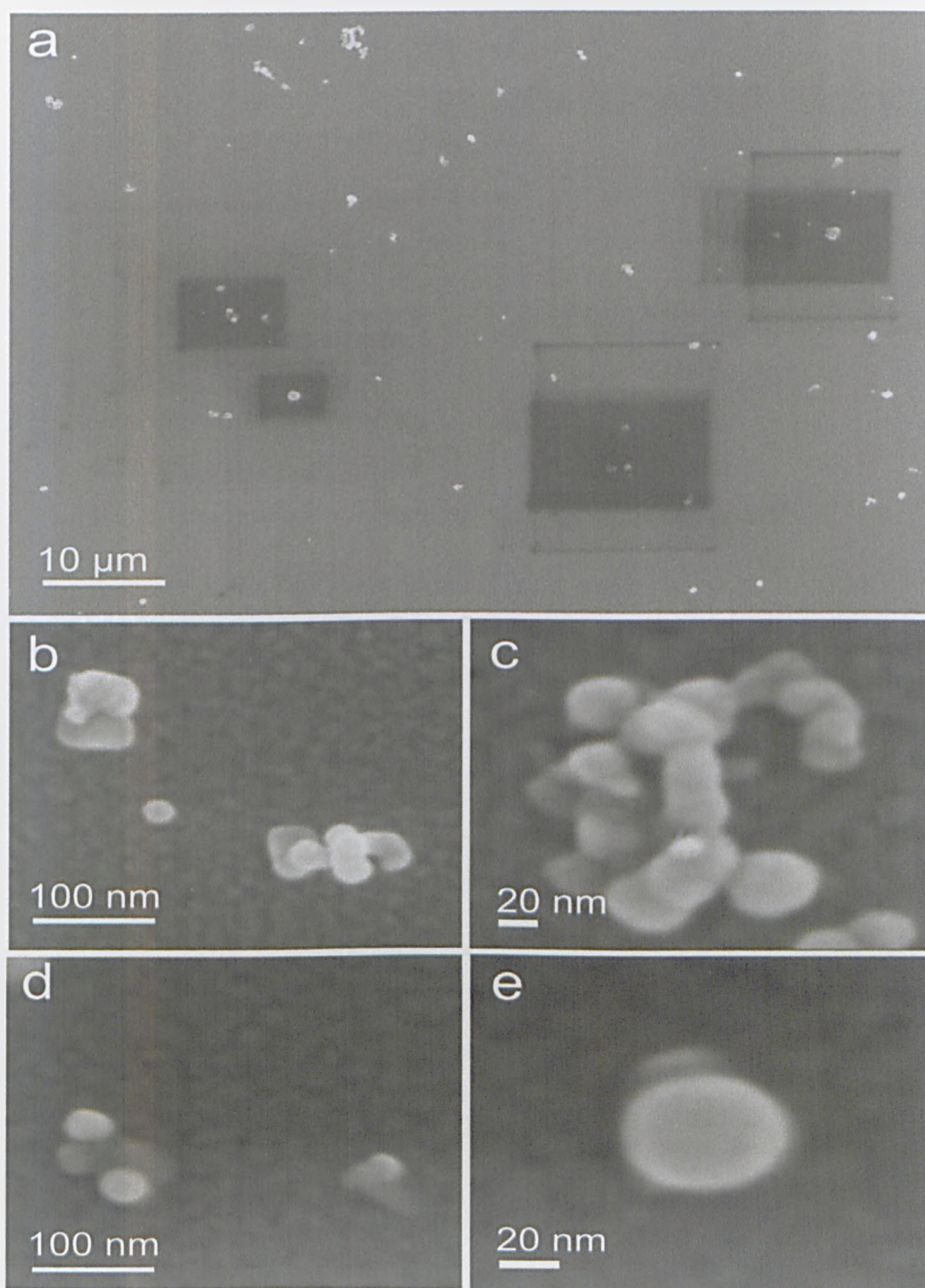


Figure 4.11: SEM images of CaCO_3 precipitates on MHA SAMs after a 30 s growth period, $[\text{Ca}^{2+}] = 5\text{mM}$. **a** SEM overview, showing aggregates of irregular particles **b-e** High magnification images of individual particles showing **b** individual and aggregates of 20-55 nm diameter ACC particles, **c** a single aggregation of 20-40 nm diameter ACC particles, **d** two individual 40 nm diameter ACC particles and 2 non spherical, irregular CaCO_3 particles and **e** a single 50 nm diameter ACC particle.

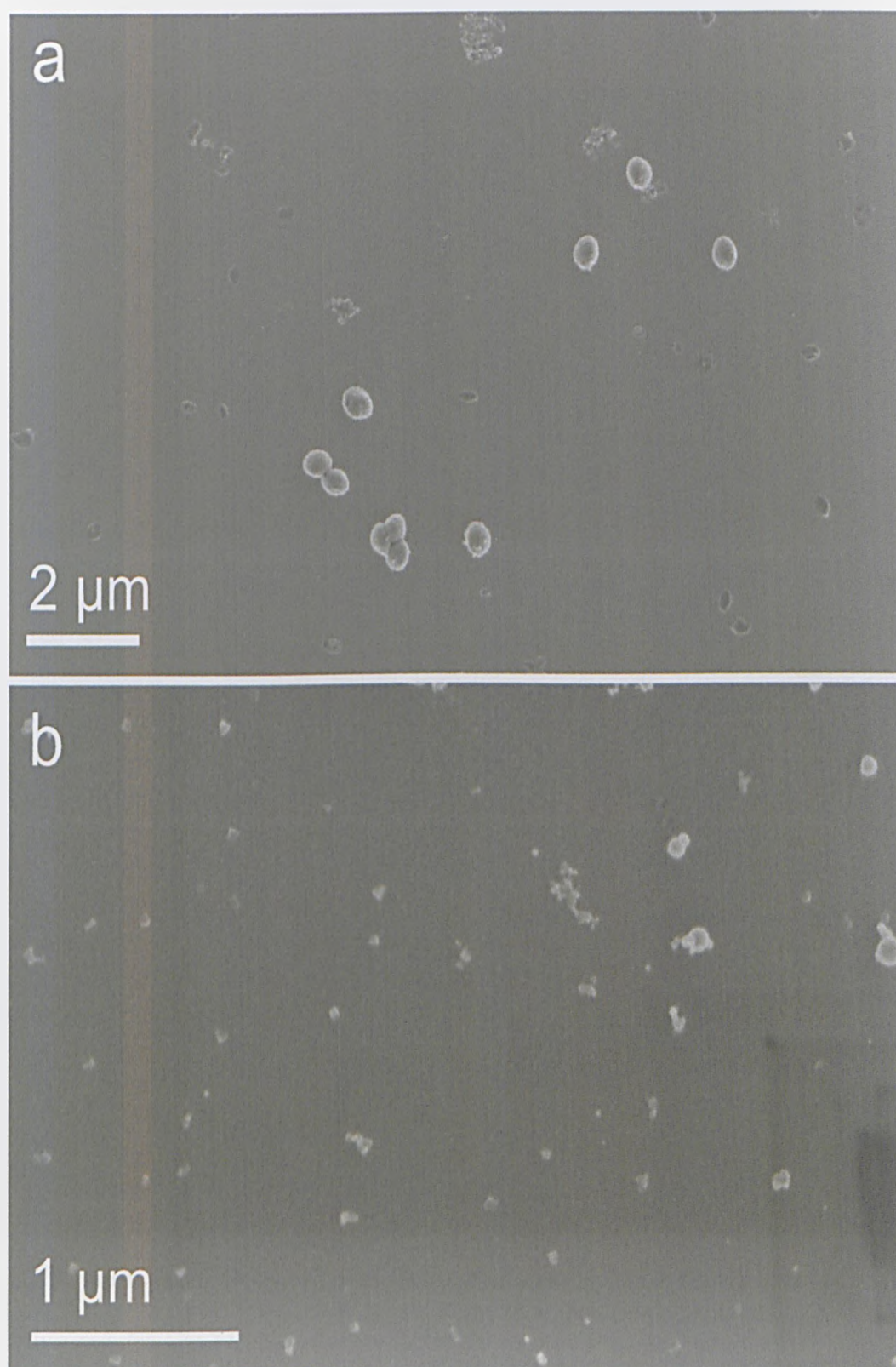


Figure 4.12: SEM overview CaCO₃ precipitates on MHA SAMs after a 30 s growth period as a function of solution concentration. a [Ca²⁺] = 2.5 mM b [Ca²⁺] = 5 mM .

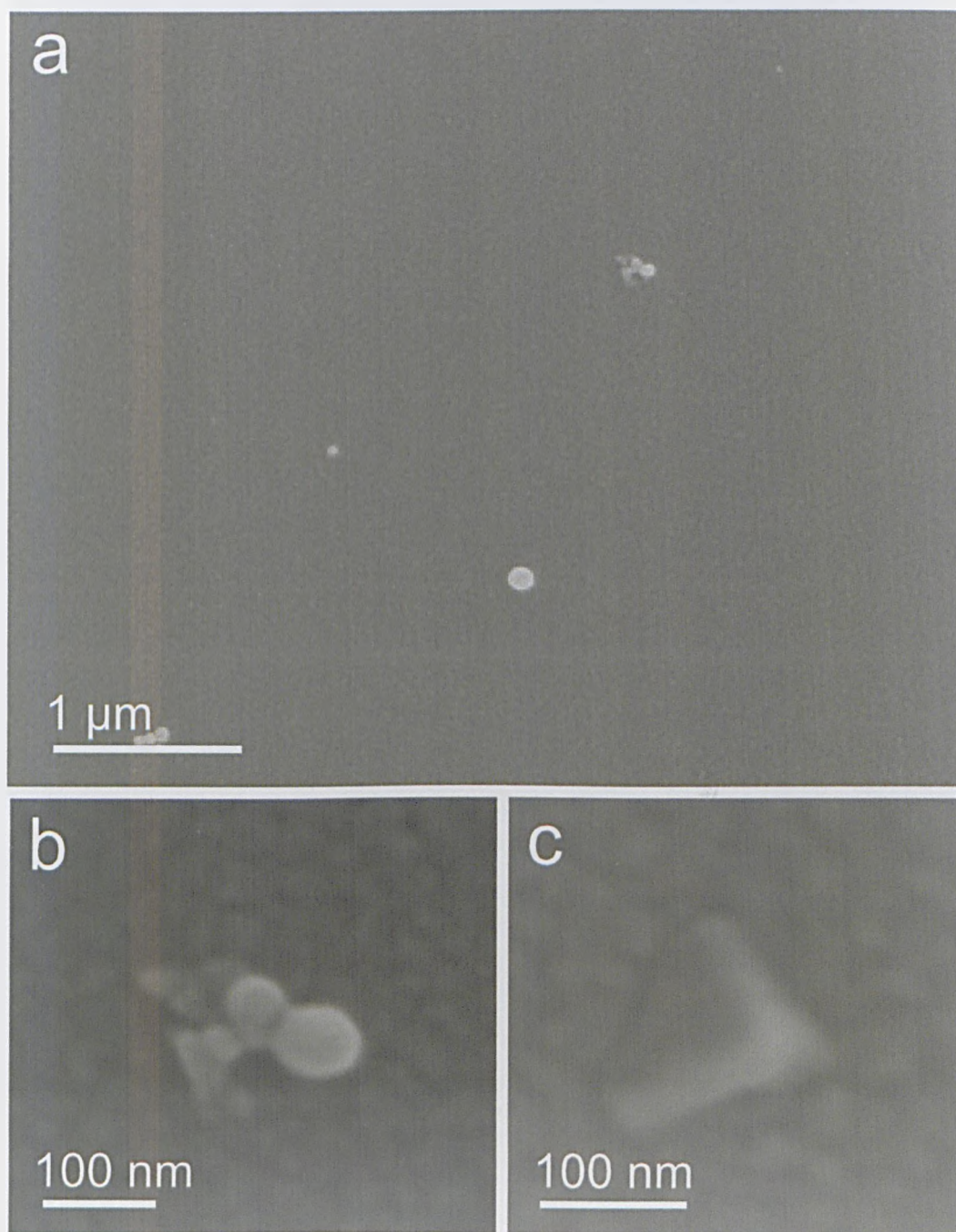


Figure 4.13: SEM images of CaCO_3 precipitates on MHA SAMs after a 1 min growth period, $[\text{Ca}^{2+}] = 5 \text{ mM}$ solution. **a** SEM overview of a region containing only irregular CaCO_3 precipitates, **b** an aggregation of 20-60 nm diameter ACC-type particle and **c** an individual tetrahedral CaCO_3 calcite particle, indicative of calcite.

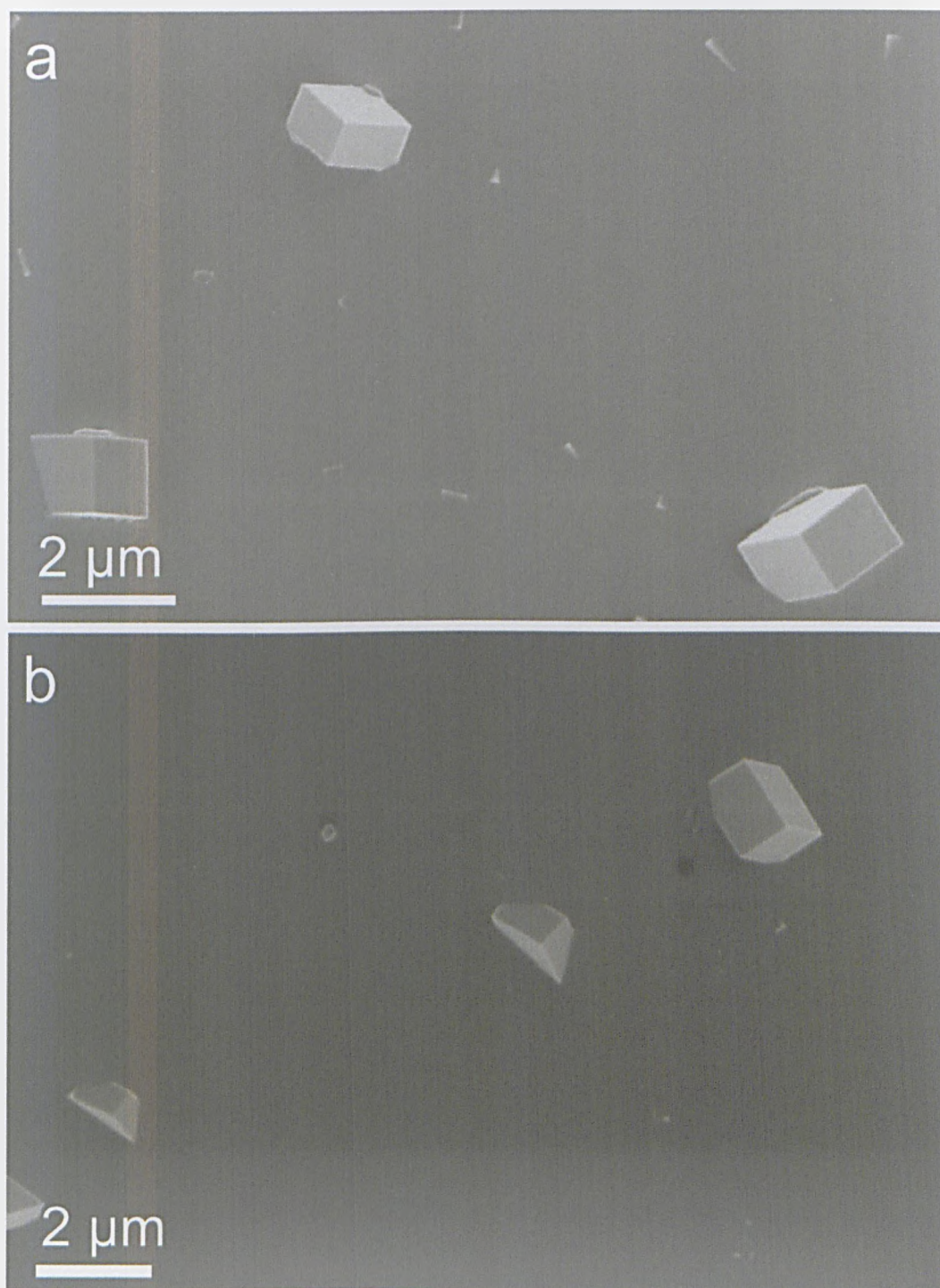


Figure 4.14: SEM overview of CaCO_3 precipitates on MHA SAMs after a 1 min growth period, as a function of solution concentration. a $[\text{Ca}^{2+}] = 2.5 \text{ mM}$, b $[\text{Ca}^{2+}] = 5 \text{ mM}$. Face selective calcite crystals, parallel to the (012) and (015) growth planes were observed at both concentrations, with smaller, irregular CaCO_3 precipitates also observed.

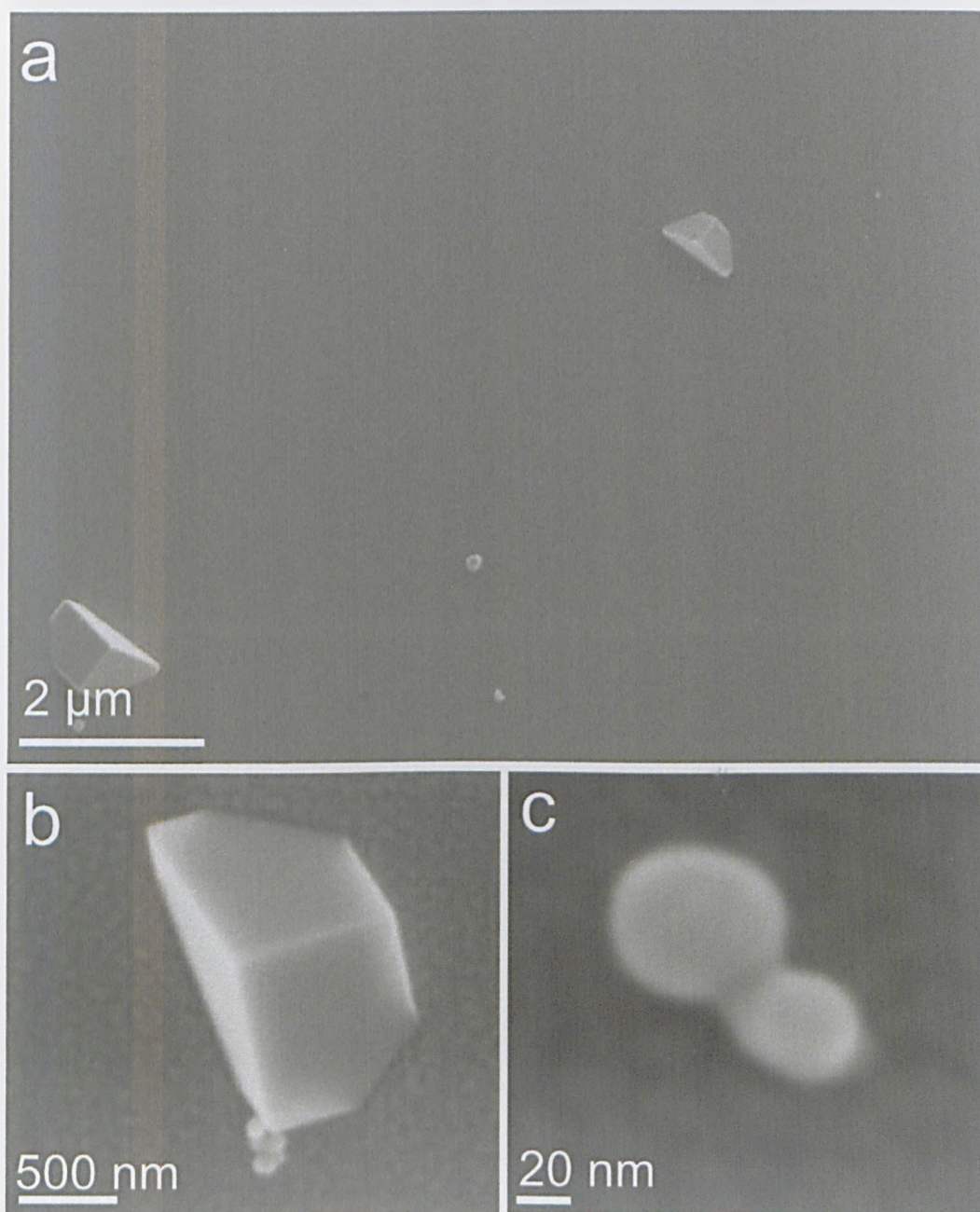


Figure 4.15: SEM images of CaCO_3 precipitates on MHA SAMs after a 2 minute growth period, $[\text{Ca}^{2+}] = 5 \text{ mM}$. **a** SEM overview showing a region of both face selective micrometer-sized calcite crystals and irregular ACC-type particles. **b** High magnification image of an individual (012) oriented calcite crystal. **c** High magnification image of 30-60 nm diameter ACC-type particles.

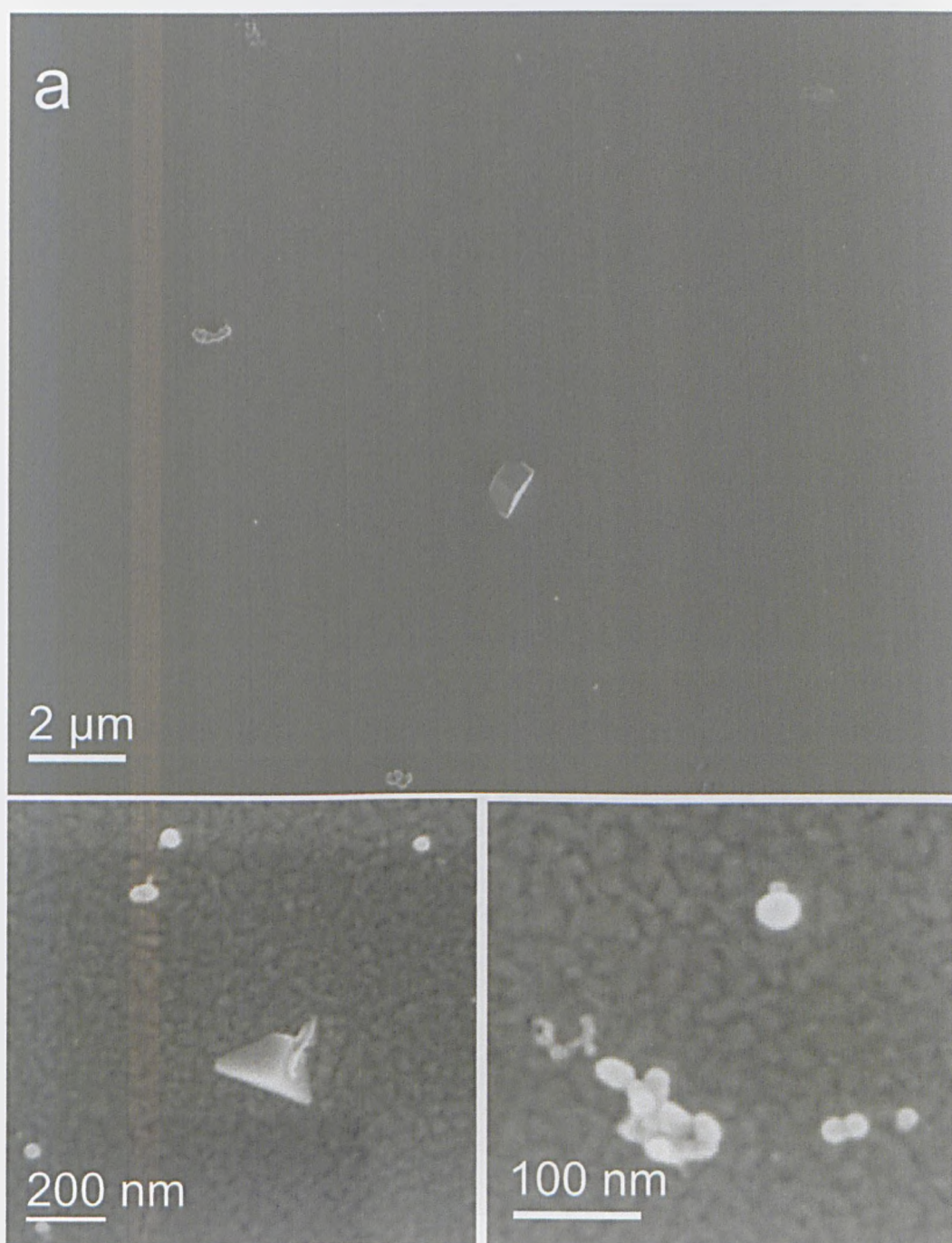


Figure 4.16: SEM images of CaCO_3 precipitates on MHA SAMs after a 5 min growth period, $[\text{Ca}^{2+}] = 5 \text{ mM}$. a SEM overview showing both face selective calcite and irregular CaCO_3 particles, b an individual $\sim 200 \text{ nm}$ calcite tetrahedron, and c aggregates of 20-40 nm ACC-type particles.

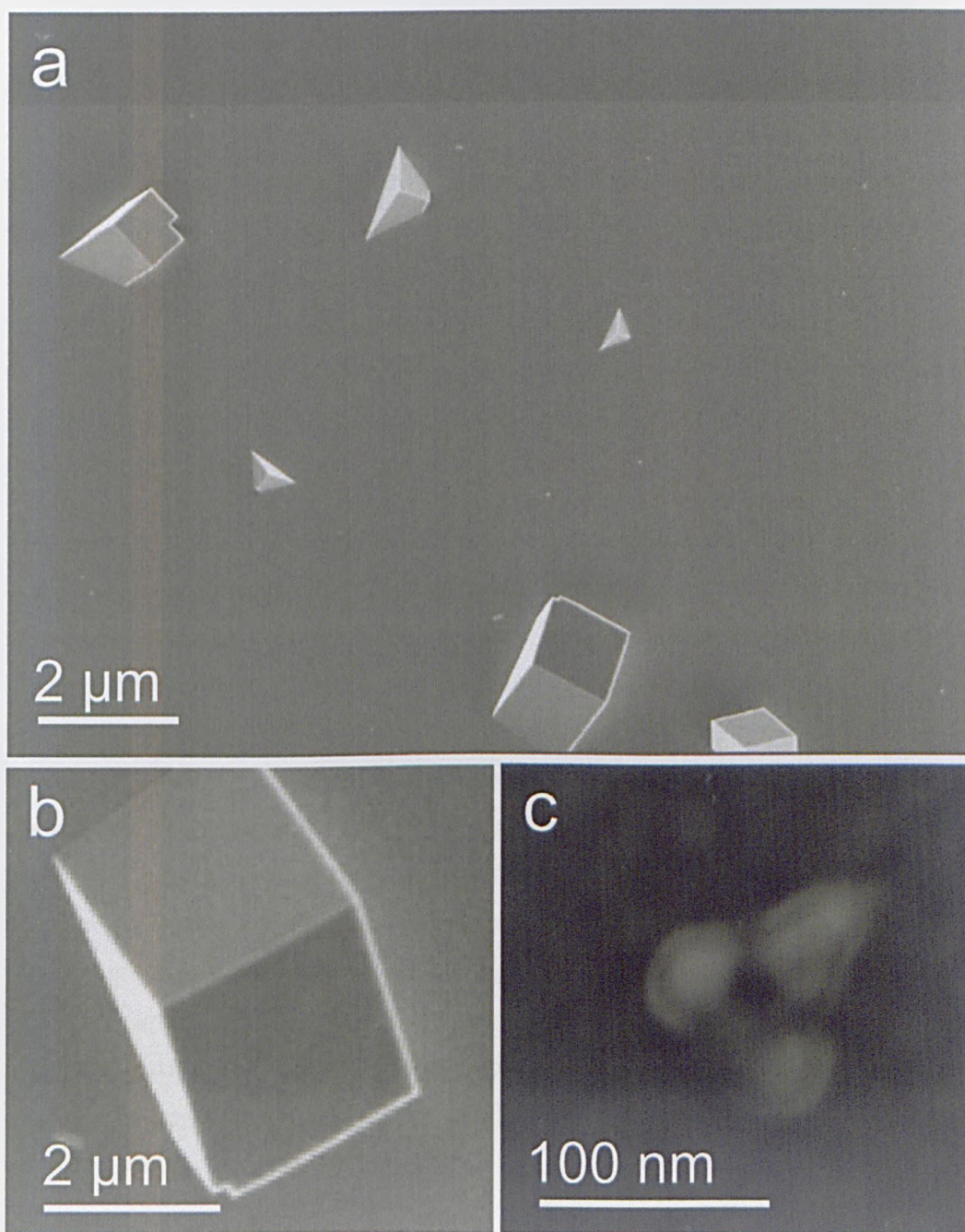


Figure 4.17: SEM images of CaCO_3 precipitates on MHA SAMs after a 10 min growth period, $[\text{Ca}^{2+}] = 5 \text{ mM}$. **a** SEM overview, showing face selective calcite, particle dimensions $0.8\text{--}2 \mu\text{m}$. **b** A high magnification image of a (015) oriented calcite crystal, **c** A high magnification image of an irregular CaCO_3 with an apparent tetrahedral shape.

4.4 Discussion

The results demonstrate that the heterogeneous nucleation and growth of CaCO_3 can be moderated using functionalised SAMs, with an increased nucleation rate, control over polymorphism and orientation on homogeneous SAMs. A comprehensive consideration of the thermodynamics of calcite growth on carboxylic SAMs was presented by Travaile and co workers [197], who showed a significant reduction in the CaCO_3 nucleation barrier as a result of favourable interactions between the (012) calcite growth plane and the functionalised SAM surface. The occurrence of the (015) oriented calcite crystals was attributed to a higher initial pH for the growth method used here, in agreement with the results reported in reference [134].

The growth of CaCO_3 on patterned SAMs resulted in a control over the nucleation site, in addition to control over polymorphism and orientation. This was in agreement with the work by Aizenberg *et al* [135], who found a linear relationship between the number of crystals in each active site and the site area. It can be seen in figure 4.8b that the amount of deposited crystalline material is higher on patterned regions in comparison to homogeneous MHA SAMs (the boundary is on the left part of this image). This phenomena was reported by Aizenberg *et al.*, who attributed it to the influence of the patterned SAM on mass transport. The nucleation rate is higher on the carboxylic-terminated hydrophilic areas in comparison to the methyl-terminated hydrophobic regions, with the onset of crystallisation at the polar regions resulting in mass transport to the growth regions and a localised under-saturation at the hydrophobic region. This behaviour is described by the diffusion aggregation model (DDA) which predicts the characteristic length scale for which nucleation is inhibited [198].

$$l_d \approx \left(\frac{D}{F} \right)^{1/4} \quad (4.7)$$

where l_d defines the size of the depleted region, D is a diffusion coefficient (cm^2s^{-1}) and F ($\text{cm}^{-2}\text{s}^{-1}$) is the flux of material to the nucleation site. The diffusion coefficient can be found by solving the diffusion equation

$$\frac{\partial c}{\partial t} = D \frac{\partial^2 c}{\partial x^2} \quad (4.8)$$

where c is the localised concentration and x is the position. Taking the experimental parameters used here, ($d = 20 \mu\text{m}$, $t = 43200 \text{ s}$, $c = 10 \text{ mM}$), using the value of F quoted by Aizenberg *et al.* [135] and assuming a saturated solution concentration of 2.5 mM yields a characteristic length scale of $200 \mu\text{m}$. This correlates with the results here, where the spacing between adjacent nucleation sites is less than the calculated l_d , even allowing for an order of magnitude error in the calculated value. Within this region, the solution is undersaturated, accounting for a far lower nucleation rate at the hydrophobic regions in comparison to homogeneous reference surfaces.

The results here suggest that the precipitation of CaCO_3 on SAMs proceeds via an amorphous precursor phase with only amorphous particles present after a 30 s growth period. Analogous to the CaCO_3 growth on weathered mica, calcite particles were observed after 2 minutes, with the amorphous precipitates vanishing over time. However, in this case, ACC particles were observed on the surface after a 5 minute growth period, and a lower overall proportion of sub-micron vaterite particles. Crystallisation must therefore begin with the heterogeneous nucleation at the SAM-solution interface, with the transformation into calcite favoured over the transformation into vaterite.

This supposition was confirmed by recent simulations Duffy and co workers [199, 200], where crystallisation begins with contact between the ACC particle and the monolayer. A degree of ordering of the ACC particles influences the structure of the monolayer, which in turn results in a further ordering of the ACC particle in a positive feedback mechanism. This phenomena has been observed experimentally on Langmuir films by DiMasi *et al.* [201]. The ability of the monolayer to stabilise the ACC particle was reportedly dependent on several variables, including surface ionization, pH and localised concentration variables. The face selective growth on homogeneous SAMs is therefore dependent on more than a lattice match between the head group spacing and the Ca-Ca separation.

4.5 Conclusions

The results in this chapter demonstrate that the crystallisation of CaCO_3 , an inorganic material, on organic carboxyl-terminated SAMs results in control over polymorphism, orientation and particle dimensions. This has been reported by others, but was included here as control experiments, since these substrates are used in chapter 5 of this thesis to promote ordered crystal growth. The short growth time experiments on these surfaces suggest that crystallisation is initiated through an amorphous precursor phase, before transformation into calcite.

Using patterned SAMs, it was shown that crystallisation can be restricted to specified sites, due to depletion zones caused by localised concentration gradients. It is believed that this is the first time this principle has been demonstrated using the deep-UV photolithography method. Finally, deep-UV patterned SAMs were characterised using XPS and contact angle measurements, since these substrates are extensively used to support droplet arrays of aqueous solution in chapter 7.

Chapter 5

Crystallisation in Confinement

The work presented in this chapter considers the crystallisation of calcium carbonate on thiol-on-gold self-assembled monolayers (SAMs) between crossed cylinders, with the surface separation increasing radially from a region of contact. This annular configuration enables crystallisation to be systematically studied at a continuous range of surface separations, with the resultant morphology dependent on the degree of confinement. At large separations, the crystal habits are equivalent to those grown on flat, homogeneous substrates in bulk solution, affording control over the orientation, polymorphism and nucleation density. As the surface separation tends towards the dimensions of the unconstrained crystals ($\sim 10 \mu\text{m}$), interesting particle morphologies are observed, lacking any of the features associated with the three non-hydrated CaCO_3 polymorphs; calcite, aragonite and vaterite. Scanning electron microscopy and Raman spectroscopy suggest the presence of significant amounts of amorphous calcium carbonate (ACC), a known precursor phase of fundamental importance in the biomineralisation process. These ACC particles demonstrate remarkable stability when maintained within the wedge but rapidly crystallize on separation of the cylinders. It is shown that ACC is thermodynamically stable only at sub-nanometer surface separations, with the stability attributed to kinetic factors.

5.1 Introduction

An important characteristic of the biomineralisation process is its occurrence within confined, localised microenvironments, where spatial constraints and chemical conditions can be precisely controlled [23, 26, 27]. In these regions, organisms actively select the orientation, morphology and location of the biomineral, with known control mechanisms including ion-specific pumps and channels, pH control, and specific reactions with organic framework matrices [202]. However, biomimetic experiments aiming to study the processes are generally performed in bulk solution. There are many crystallisation phenomena however which cannot be satisfactorily described in terms of crystallisation from bulk solution. For the crystallisation of polyethylene within triblock co-polymers, Balsamo *et al.* found the melting point to decrease with an increased degree of confinement [203]. Another well known example is the precipitation of hydroxyapatite nanocrystals within the gaps in collagen fibers during bone formation, which is dependent on confinement [204]. In a molecular dynamic simulation, Camara and Bresme predicted solid argon to exist in a 1 nm pore at temperatures up to 45 % higher than the argon triple point [205].

That confinement influences crystallisation is perhaps unsurprising, considering the associated increase in surface area to volume ratio within confined systems. The relative importance of interfacial and surface energies therefore becomes augmented [206]. In addition, the kinetics are affected by crystallisation in confinement, particularly in the case of long chained macromolecules. Furthermore, the diffusion of material to the growth face is likely to be affected by confinement. Several models have been established to study crystallisation in confinement, including growth in zeolites within a mesoporous matrix [207], growth of calcium phosphate within micelles [208] and within nanometer-sized polymer membranes [209, 210]. In one experiment, Loste *et al.* [211] precipitated CaCO_3 within a track etch membrane, demonstrating that crystal morphology can be determined by spatial constraints alone.

Of particular relevance to the work presented here is the precipitation and subsequent stabilisation of ACC within confined volumes. It is accepted that the formation of the stable CaCO_3 polymorphs within living organisms proceeds via

the crystallisation of ACC into single crystal or polycrystalline phases. In one classic study, Aizenberg *et al.* precipitated ACC between two surfaces bridged by an array of micron sized pillars, with nucleation fixed to specified nucleation sites [212]. The formation of single crystal or polycrystalline calcite was dependent on the pillar separation, and it was proposed that the micropores act as sites for stress and water release, since in all cases the resultant pores were larger than the pillar diameters.

Previous models were often limited by the fixed geometry of the biological template, whereas the model here presents a simple system for the study of crystallisation of a fluid under varying degrees of confinement. An annular crossed-cylinder configuration is used, whereby the surface separation increases radially from a region of contact (Figure 5.1). A droplet of solution is held in place around the region of contact due to capillary action. The cylinder separation, h , as a function of distance from the region of contact, d , is given by

$$h = R - \sqrt{R^2 - d^2} \approx \frac{d^2}{2R} \quad (5.1)$$

where R is the radius of the glass cylinder (12.7 mm). The change in surface separation, Δh , across a $5 \mu\text{m}$ precipitate at a distance of $100 \mu\text{m}$ from the region of contact is considered below.

$$h + \Delta h = \frac{(d + \Delta d)^2}{2R} \approx \frac{d^2}{2R} + \frac{d\Delta d}{R} \quad (5.2)$$

where the higher order Δd term is assumed to be negligible.

$$\Delta h \approx \frac{d\Delta d}{R} \quad (5.3)$$

Substituting in for values of d , Δx and R

$$\Delta h \approx \frac{10^{-4} \times 0.5 \times 10^{-5}}{12.7 \times 10^{-2}} = 39.4 \text{ nm} \quad (5.4)$$

Due to the small changes in h as a function of d , crystallisation was therefore modeled between two parallel plates. h increases from a separation of zero at the contact region up to separations greater than 5 mm at the droplet edge. The surface separations calculated using equation 5.1 are shown in figure 5.2. The central aspect of this system is a large surface to volume ratio in close proximity to the region of contact.

Biom mineralisation invariably involves heterogeneous nucleation, whereby crystal growth occurs at the solid-liquid interface. It was shown in section 4.1 that monolayers of MHA on gold promote the ordered over growth on calcite, in agreement with the findings of others [134]. These monolayers were introduced to the crossed cylinder setup to promote nucleation and fix crystal orientation and polymorphism enabling changes in crystal habit to be established solely as a function of physical confinement.

A brief description of procedures is outlined in section 5.2. The results section is broadly divided into two parts: characterisation by SEM (section 5.3.1) and Raman spectroscopy respectively (section 5.3.2). The thermodynamic stability of ACC over calcite is considered in the discussion of results (section 5.4). Finally, TEM analysis of focused ion beam (FIB) sections taken from individual precipitates at various surface separations are included in section 5.5.

5.2 Experimental Methods

Half-cylindrical glass substrates were cut from tubing with an outer diameter of 25.4 mm and cleaned in accordance to the protocol listed in section 2.1. 50-150 nm gold films were deposited using the sputter-evaporation technique described in section 2.2.2, with a bespoke sample holder created to hold the half cylinders (Figure 5.1b). Substrates were left in 0.1 mM solutions of mercaptohexadecanoic acid (MHA) in DCM for 24 hours, maintained at 4° C (section 2.2.2).

Calcium carbonate was precipitated from aqueous solutions using double decomposition and gas diffusion methods (section 2.3). The crossed cylinders were held in place using a specially designed sprung sample holder, and were brought into

contact by slowly increasing the force applied to the top surface through the addition of ~ 100 g weights. Once in contact, a ~ 250 μ l drop of aqueous solution was introduced through a pipette. The growth period was varied between 1 and 24 hours. To terminate crystallisation, the samples were rinsed with milli-Q water whilst in contact; before separating and drying under nitrogen. Amorphous calcium carbonate was synthesised as a reference for Raman spectroscopy experiments using the procedure described by Koga *et al.* [213] Briefly, 0.1 M aqueous solutions of CaCl_2 , Na_2CO_3 and NaOH were combined in equal volumes at 4°C , before passing through 200 nm pore size filter paper and rinsing with ethanol. Raman spectra were obtained within 5 minutes of precipitation.

Surface separations were calculated using equation 5.1, with the region of contact identified from SEM images due to a slight deformation of the gold surface (Figure 5.4). Figure 5.3 shows an overview of the region of contact, including contours of equal surface separations up to 200 μm from the region of contact. Samples were usually characterised by Raman microscopy prior to SEM, due to the need for a 15 nm Pt conductive layer for SEM (section 2.4.4) which would reduce the sensitivity of Raman spectroscopy measurements.

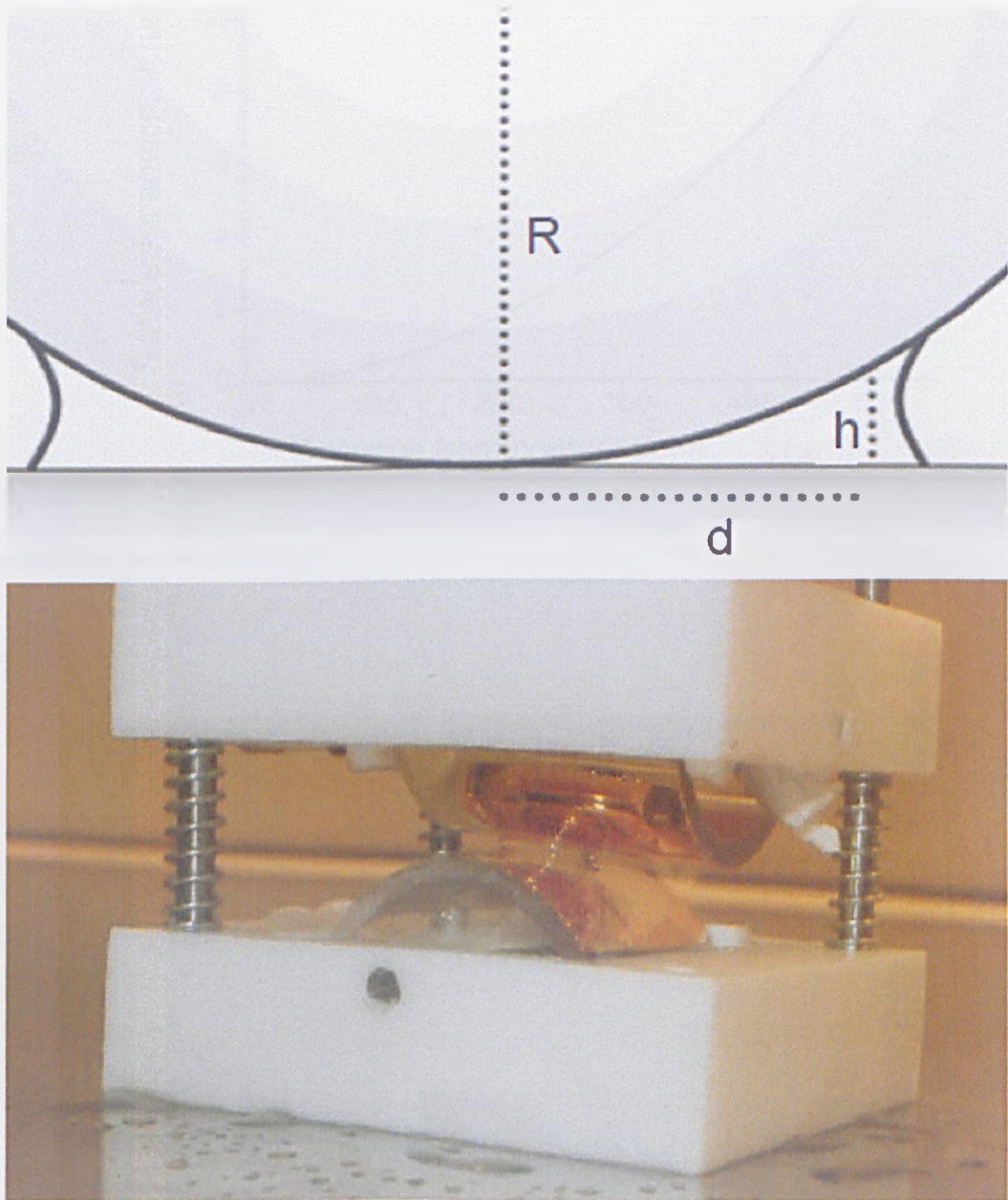


Figure 5.1: a Schematic diagram for the crossed-cylinder configuration, with radius of curvature R . The surface separation h , related to the distance from contact, x , by equation 5.1. b Photograph showing the crossed cylinder apparatus, cylinders in contact

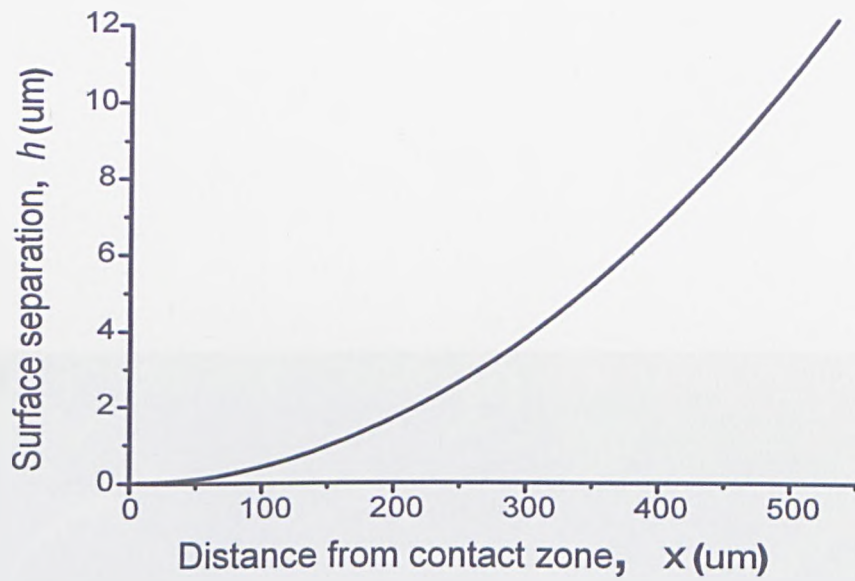


Figure 5.2: Surface separation as a function of distance from the contact region, according to equation 5.1.

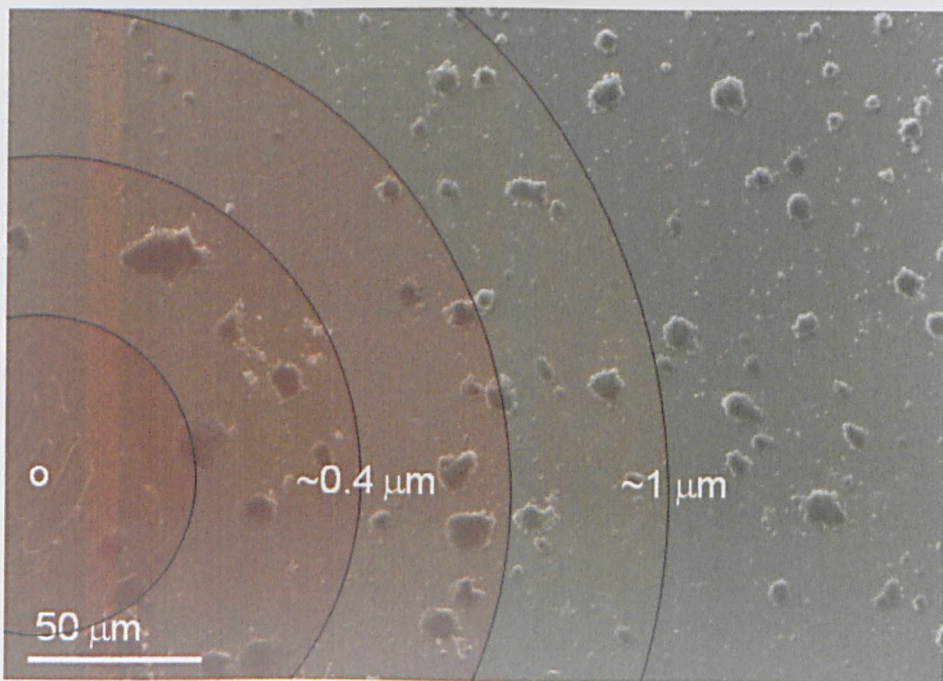


Figure 5.3: SEM overview of the region of contact, O. Contours are equidistant from the region on contact, in increments of 50 μm .

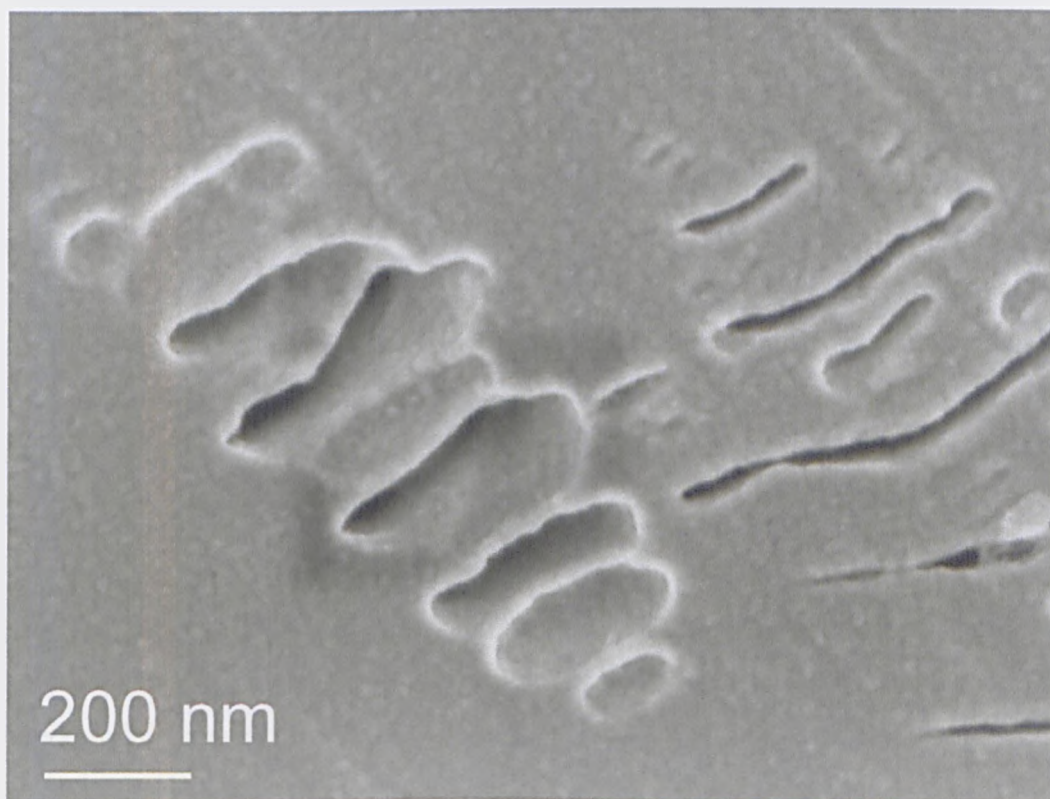


Figure 5.4: HR-SEM image of a typical region of contact, signified by a slight scratching of the gold surface.

5.3 Results

5.3.1 SEM Analysis

The nucleation density, orientation and morphology of CaCO_3 crystals grown at surface separations above $10\ \mu\text{m}$ were similar to those for crystals grown on the isolated control surfaces (Figure 5.5). Non-oriented calcite growth was observed on glass substrates, with a nominal percentage aragonite and vaterite present (Figure 5.6a), whereas the exclusive face-selective growth of calcite was observed on MHA SAMs (Figure 5.6b). The effect of the MHA SAM can clearly be seen in figure 5.6, accounting for an approximate 50 fold increase in crystal number density using both precipitation methods, in agreement with the studies on isolated control surfaces (Figure 5.5) (section 4.1). Crystals grown using the gas diffusion method had maximum dimensions in the range of $5 - 15\ \mu\text{m}$ whereas crystals precipitated using the double-decomposition growth method yielded slightly smaller crystals of $2 - 10\ \mu\text{m}$. The precipitate size was dependent upon the crystallisation method, growth period and solute concentration, yet independent of whether the crystals were grown at large surface separations or on isolated control surfaces.

Significant changes in crystal habit were observed at surface separations below $\sim 10\ \mu\text{m}$ (Figure 5.7). The crystals formed without the characteristic 3-fold symmetry axis or the rhombohedra faces associated with calcite, with multi-faceted irregular edges and flattened top surfaces (Figures 5.7, 5.8). The edge irregularity increased with decreasing surface separation, with figure 5.7 b corresponding to a surface separation of approximately $5\ \mu\text{m}$. The appearance of these irregular CaCO_3 precipitates was largely independent of the growth conditions. Figure 5.8 shows precipitates formed at a $\sim 3\ \mu\text{m}$ separation (24 h, gas diffusion method) at a 8 mM and b 4 mM concentrations. At both concentrations the precipitates were bounded by many small faces morphologically indicative of calcite, but with flattened upper surfaces.

The precipitate edges became progressively more irregular with increased confinement, shown in figure 5.9 for the same sample at surface separations of 2 and $\sim 0.5\ \mu\text{m}$ respectively. At separations of $2\ \mu\text{m}$ and below the regular edge features

associated with crystalline material were no longer apparent. Instead, an irregular, rounded edge was observed, characteristic of an amorphous precipitate. An overview of the the $\sim 0.4\text{-}2\ \mu\text{m}$ separation region is shown in figure 5.10a, with a higher magnification in figure 5.10b.

The fact that there were no morphological features characteristic of a crystalline material suggests that an amorphous precipitate forms at sub-micron separations. Further evidence of an amorphous phase was obtained by high resolution SEM immediately adjacent to the region of contact, revealing an aggregation of 10-50 nm spherical particles, characteristic of amorphous calcium carbonate (ACC) (Figure 5.11). To further investigate morphological changes arising from confinement, the surfaces were taken out of contact ($\sim 5\ \text{mm}$) and left in depleted solution for 1 hour immediately after growth (Figure 5.12). This resulted in a change in the features of the confined precipitates, with well-defined edges and faces. A representative sample shown in figure 5.12b presenting evidence for the transformation from ACC into calcite.

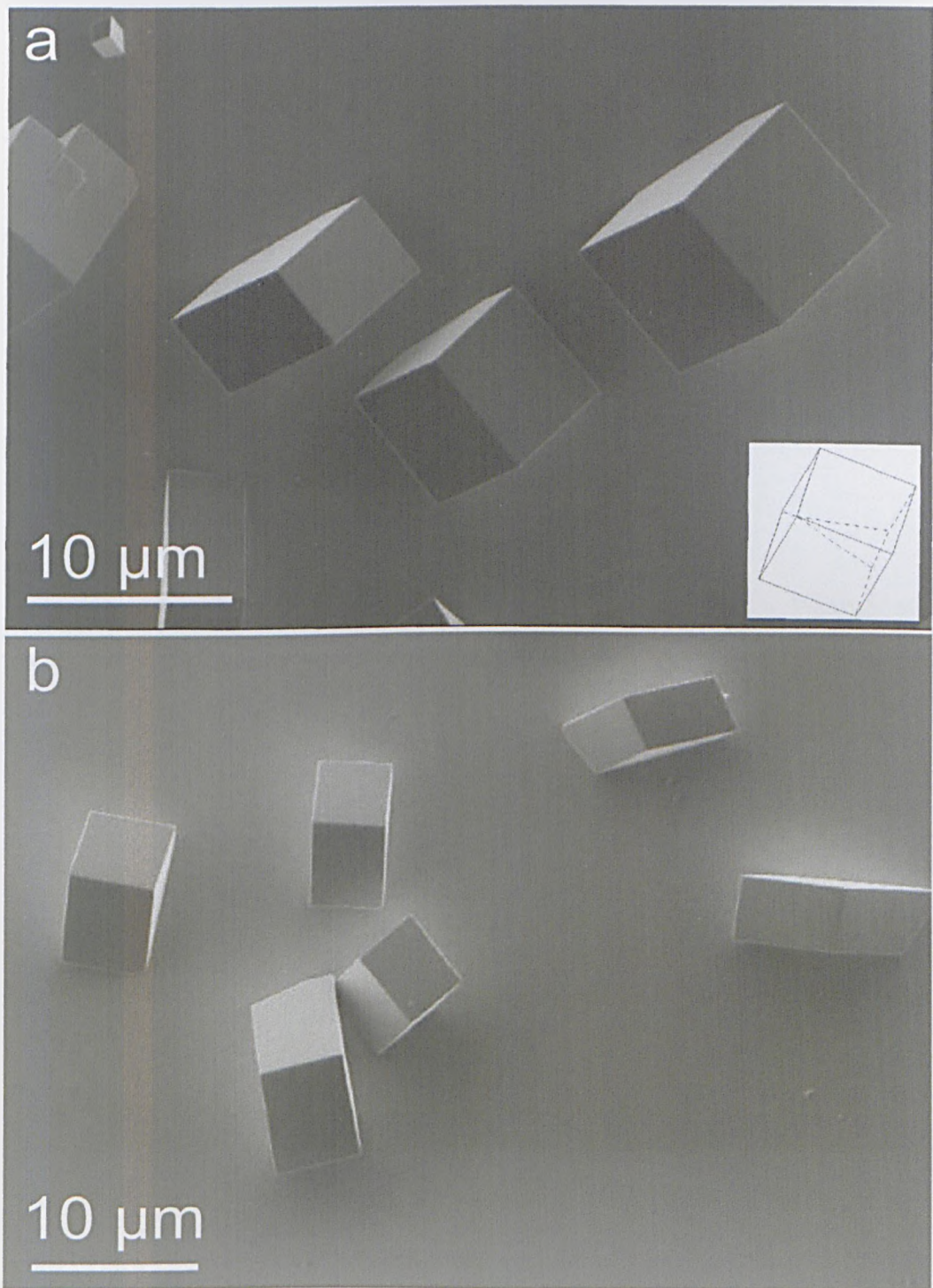


Figure 5.5: SEM images of CaCO₃ growth on MHA SAMs using the gas diffusion method ($[Ca^{2+}] = 4$ mM, for 24 h). **a** On isolated control surfaces and **b** millimeter separations. Inset: a SHAPE simulated rhombohedral calcite crystal in a (015) orientation.

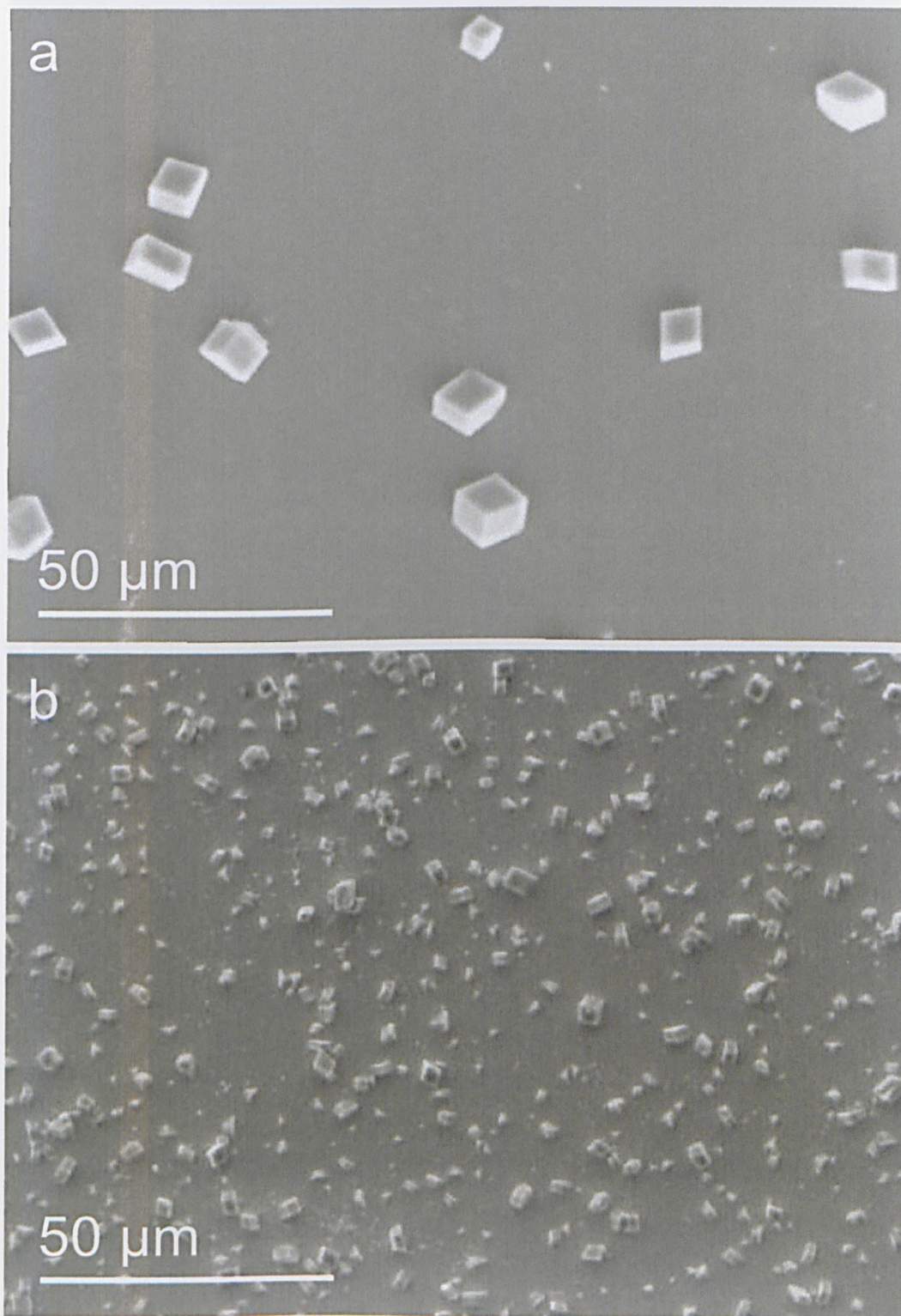


Figure 5.6: SEM images for CaCO_3 growth on MHA SAMs using the gas diffusion method ($[\text{Ca}^{2+}] = 8 \text{ mM}$, for 24 h) at millimeter separations. **a** directly on glass substrates **b** On an MHA SAM

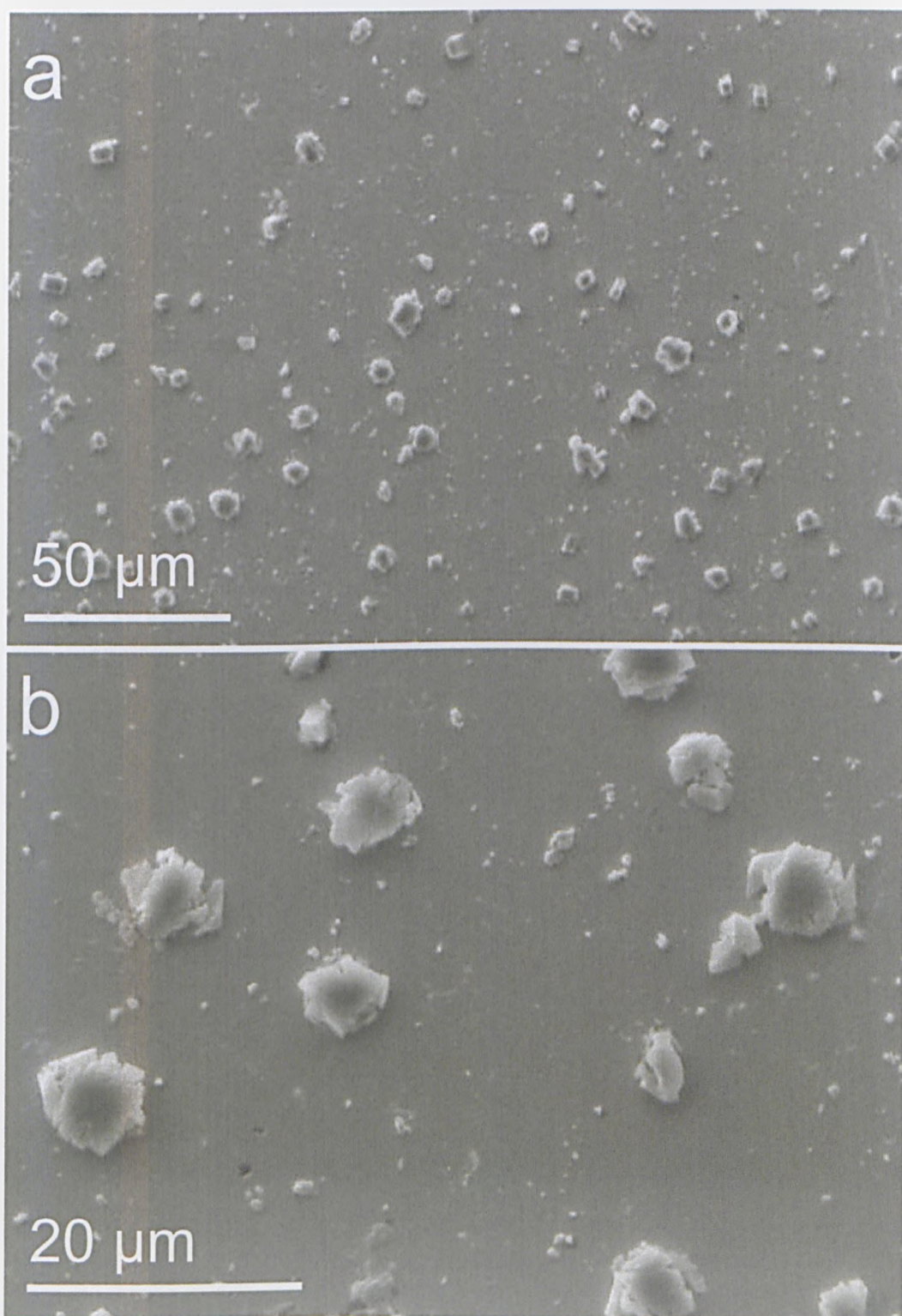


Figure 5.7: SEM images for CaCO₃ growth on MHA SAMs using the gas diffusion method ($[Ca^{2+}] = 8$ mM, for 24 h) at an intermediate surface separation of ~ 5 μm . **a** Overview image, with fully faceted calcite crystals towards the top right of the image. **b** medium magnification, showing multifaceted, irregular calcite crystals orientation.

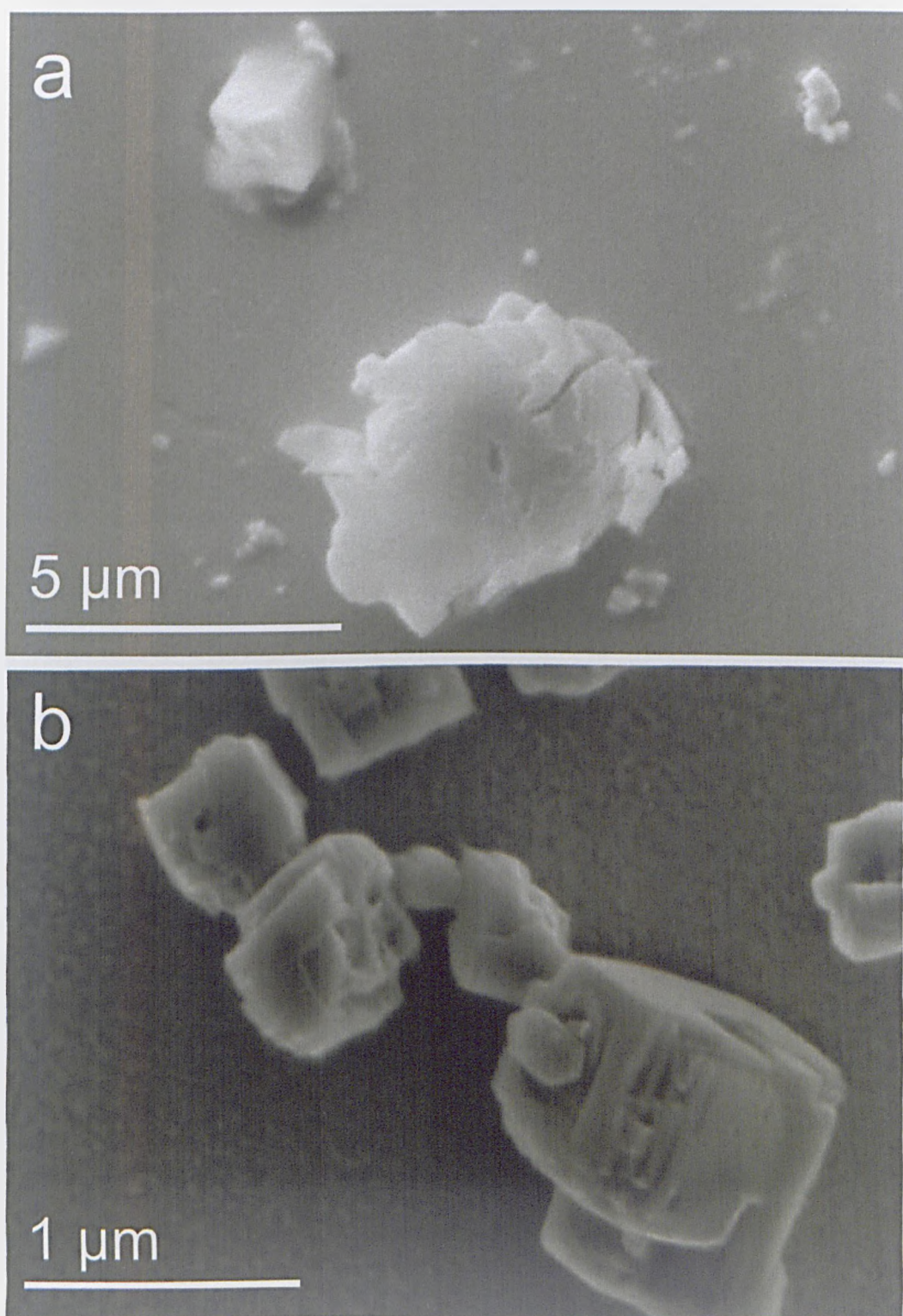


Figure 5.8: SEM images for CaCO_3 growth on MHA SAMs using the gas diffusion method (24 h growth period) at intermediate surface separations of $\sim 3 \mu\text{m}$. **a** $[\text{Ca}^{2+}] = 8 \text{ mM}$, **b** $[\text{Ca}^{2+}] = 4 \text{ mM}$.

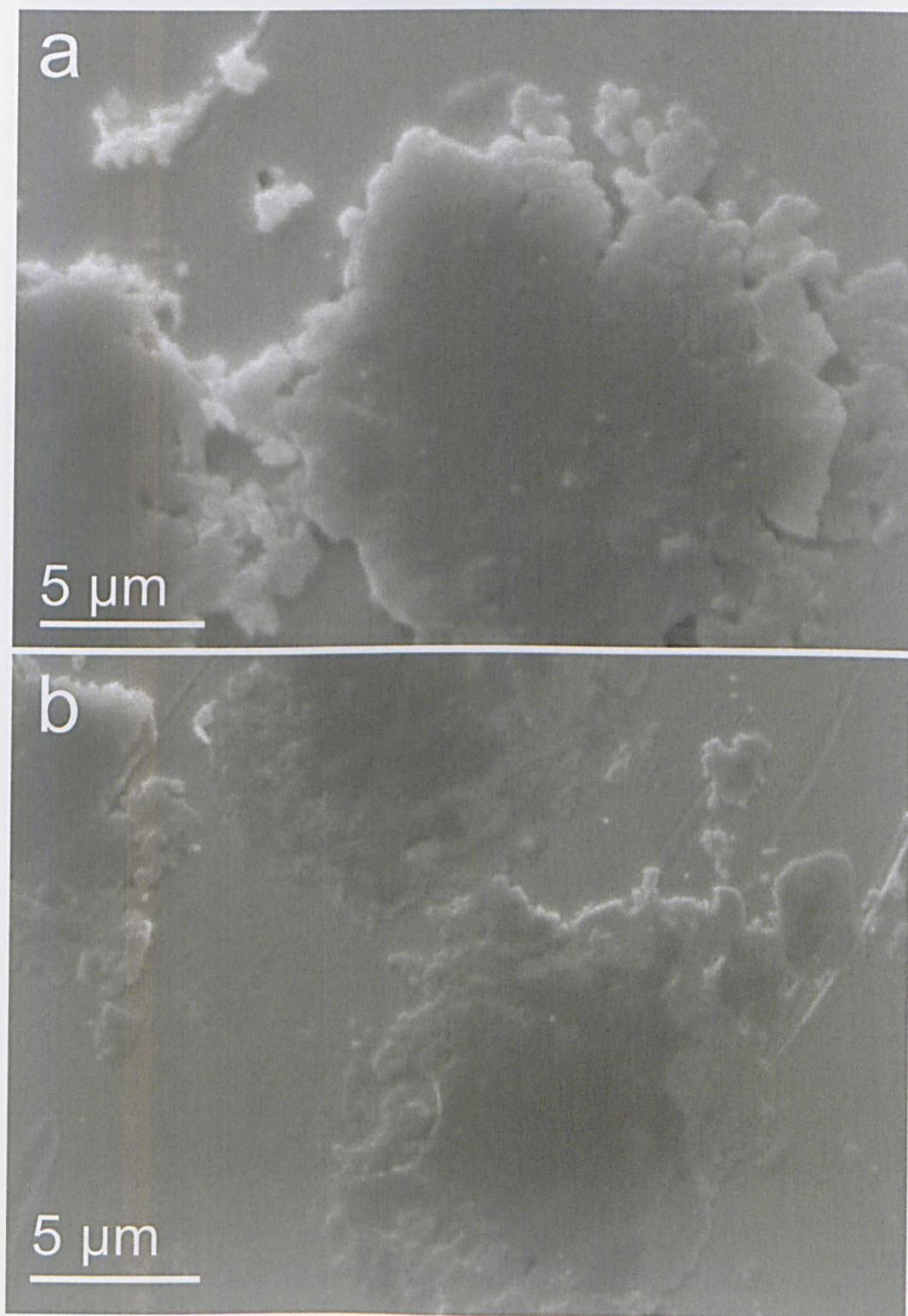


Figure 5.9: SEM images for CaCO_3 growth on MHA SAMs using the gas diffusion method ($[\text{Ca}^{2+}] = 8 \text{ mM}$, 24 h) at surface separations of a $2 \mu\text{m}$ and b $\sim 0.5 \mu\text{m}$.

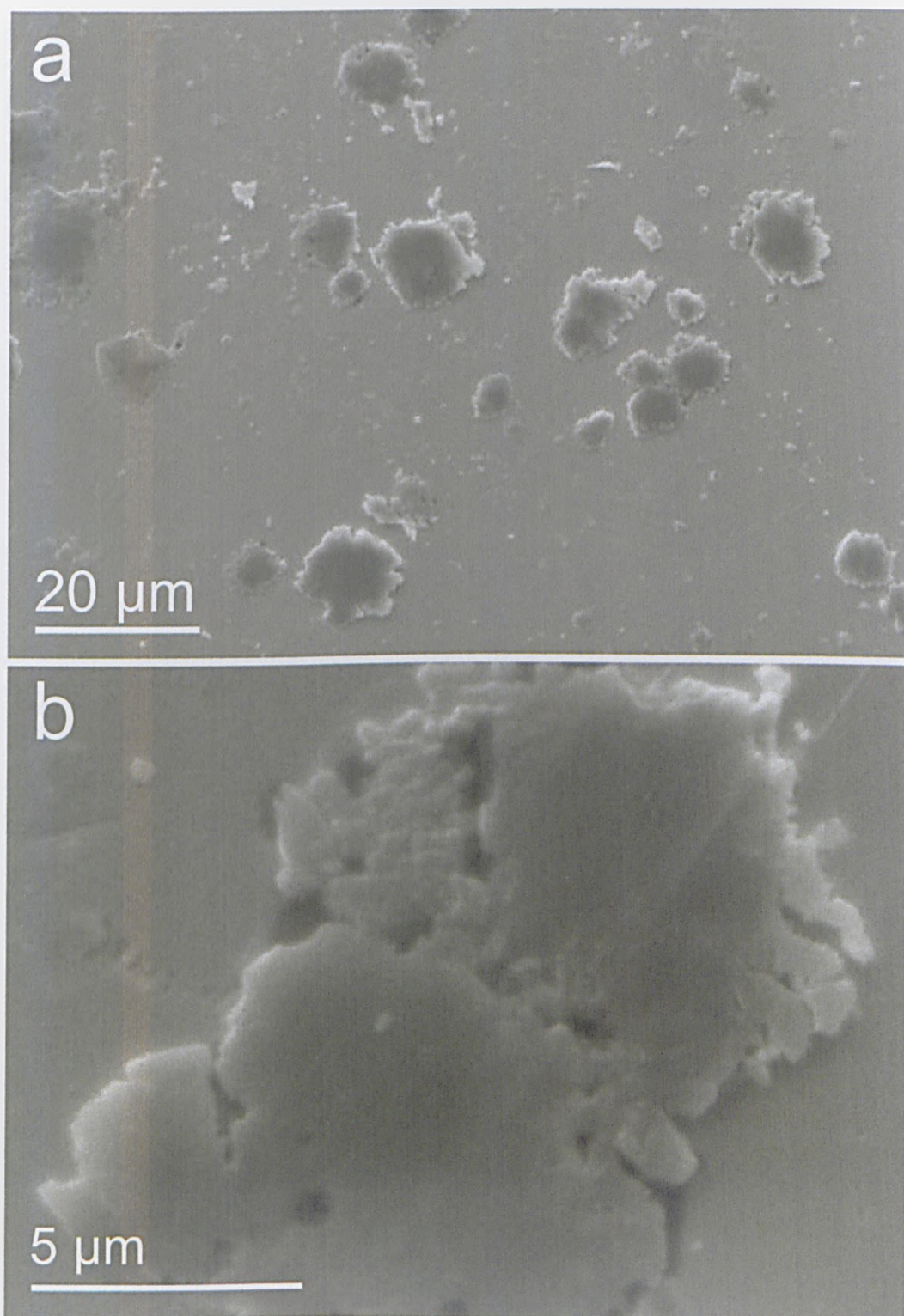


Figure 5.10: SEM images for CaCO₃ growth on MHA SAMs at intermediate surface separations of $\sim 3 \mu\text{m}$. Precipitates were formed using the gas diffusion method for a 24 h growth period at a concentration of **a** $[\text{Ca}^{2+}] = 8 \text{ mM}$, **b** $[\text{Ca}^{2+}] = 4 \text{ mM}$.

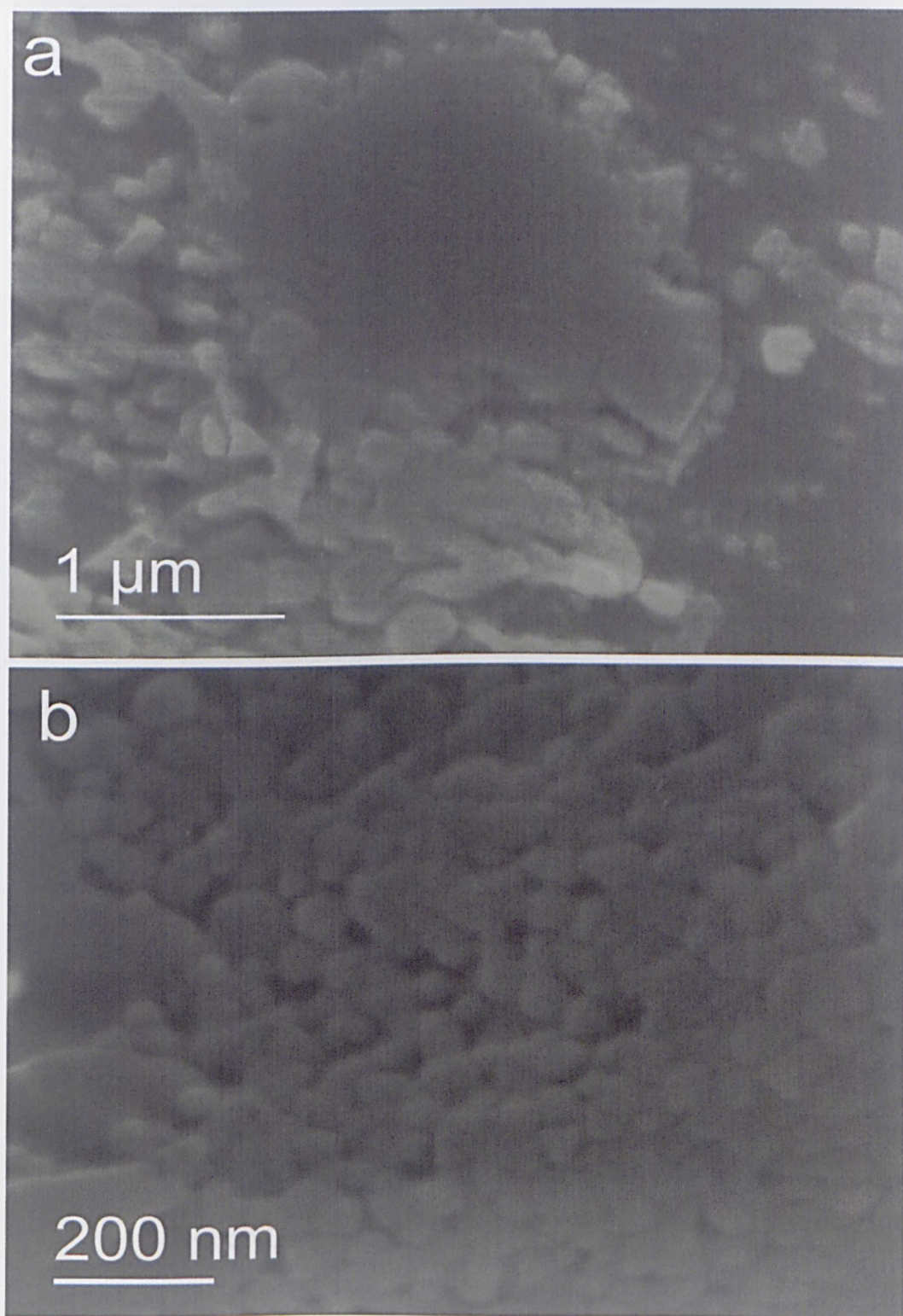


Figure 5.11: HR-SEM images of CaCO_3 precipitates supported on MHA SAMs at a sub-micron surface separation ($[\text{Ca}^{2+}] = 4 \text{ mM}$, double decomposition growth method, 24h). **a** 25,000 x magnification **b** 50,000 x magnification.

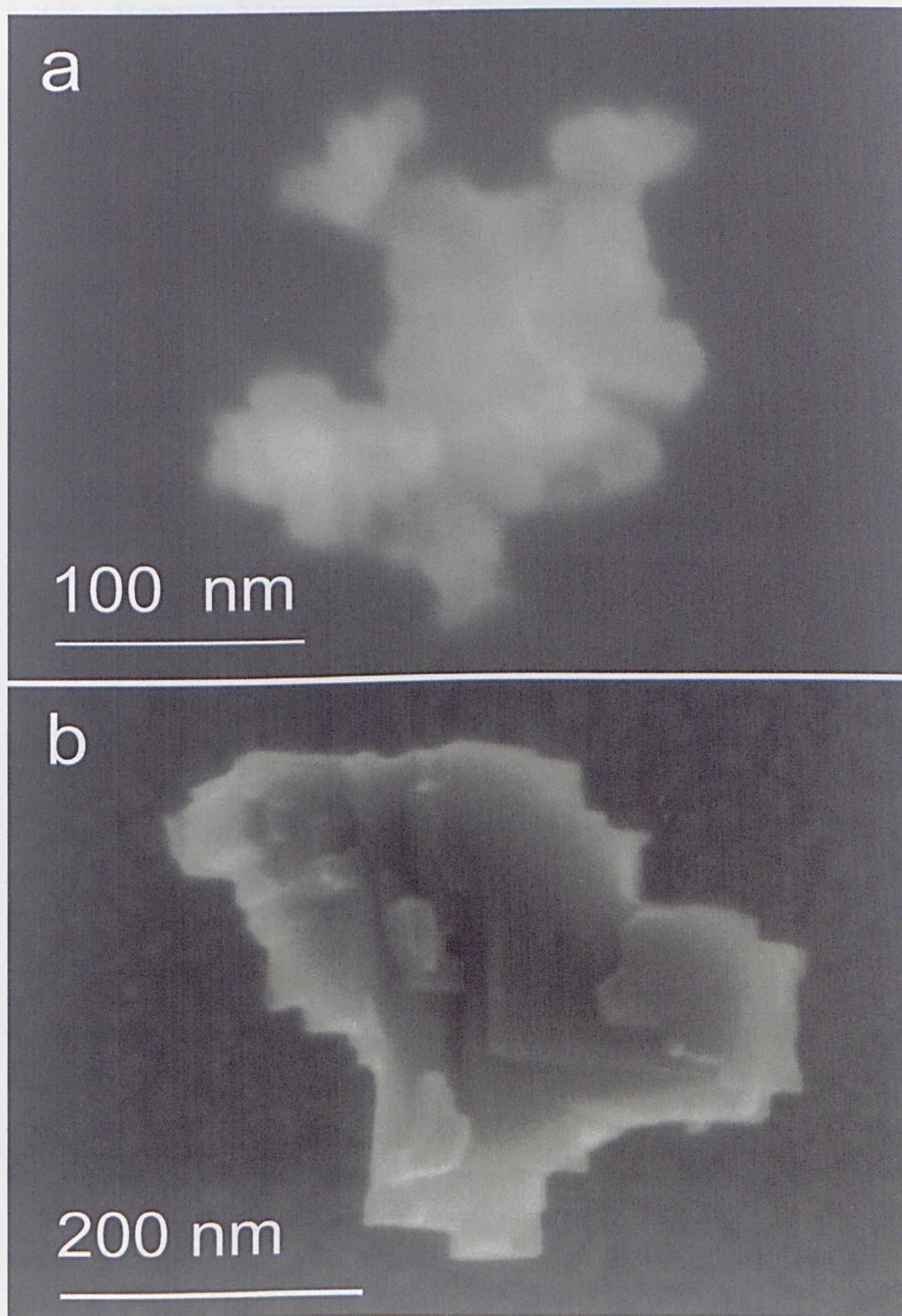


Figure 5.12: SEM images for CaCO_3 growth on MHA SAMs using the gas diffusion method ($[\text{Ca}^{2+}] = 4 \text{ mM}$, for 24 h) at an sub-micron surface separation. **a** Immediately after separation, **b** suspended in depleted solution for 1 h immediately after separation.

5.3.2 Raman Microscopy Analysis

There are important considerations in identifying CaCO_3 polymorphs from individual Raman spectra. The normal calcite vibrational modes were derived by Rutt and Nicola [214] based upon the correlation method described by Fateley *et al.* [215] and are listed in Table 5.1. Also included are the vibrational Raman modes for aragonite and vaterite from references [216] and [217] respectively. The most intense lattice vibrational modes are at 155 and 281 cm^{-1} for calcite [214] and 145, 180 & 208 cm^{-1} for aragonite [218]. There are 9 Raman lattice modes for vaterite, the most intense at 301 cm^{-1} and the double degenerate peak centered about 106 and 116 cm^{-1} respectively [219].

A substantial overlap occurs between the internal ν_1 vibrational modes of calcite and aragonite, at 1085 and 1089 cm^{-1} respectively, whereas vaterite is readily distinguished by the distinctive degenerate ν_1 mode centered at 1079 and 1084 cm^{-1} . Calcite and aragonite were differentiated by the position of the ν_4 modes at either 711 or 721 cm^{-1} . ACC was distinguished from other CaCO_3 by a significant broadening of the internal ν_1 mode centered at 1083 cm^{-1} , a general broad peak from 140-220 cm^{-1} and an absence of the ν_4 vibrational mode between 700-800 cm^{-1} . Raman spectra of synthetic calcite, aragonite, vaterite and ACC are shown in figure 5.13.

Raman spectra were obtained for individual CaCO_3 precipitates over a continuous range of separations. Particles were identified using optical microscopy at a 500x magnification, and matched to subsequent SEM images. Raman spectra confirmed that precipitates at separations greater than 10 μm were indeed calcite, verifying SEM morphological analysis. Raman spectra for CaCO_3 known to have grown at intermediate surface separations of 2-10 μm were consistent with calcite, albeit with a slight broadening of the 1085 cm^{-1} ν_1 peak, as expected for a polycrystalline sample [220]. In contrast, Raman spectra of CaCO_3 precipitates at surface separations of 1 micron and less showed features in common with synthetic ACC, with an order of magnitude decrease in intensity of the 1085 cm^{-1} ν_4 mode, an absence of the ν_4 and broadening of the lattice modes over 140-220 cm^{-1} . Raman spectra of the same particle showed a substantial conversion from ACC into calcite upon heating at 180° for 1h, as identified by an eight-fold increase in intensity of

the ν_1 mode at 1085 cm^{-1} , and the presence of the previously absent ν_4 mode 711 cm^{-1} . The spectra in figures 5.14 and 5.15 were taken after a 24 h growth period, ACC was found around the region of contact after a 72 h growth period.

Polymorph	Vibrational Mode (cm^{-1})			
	ν_1	ν_2	ν_3	ν_4
Calcite	1085	n/a	1450	711
Aragonite	1085	w	w	700 704
Vaterite	1074 1090	w	w	740 750

Table 5.1: The internal Raman active vibrational modes for calcite, aragonite and vaterite taken from references [214], [216] and [217] respectively. n/a denotes no Raman active mode where as w denotes a mode which is too weak to readily detect.

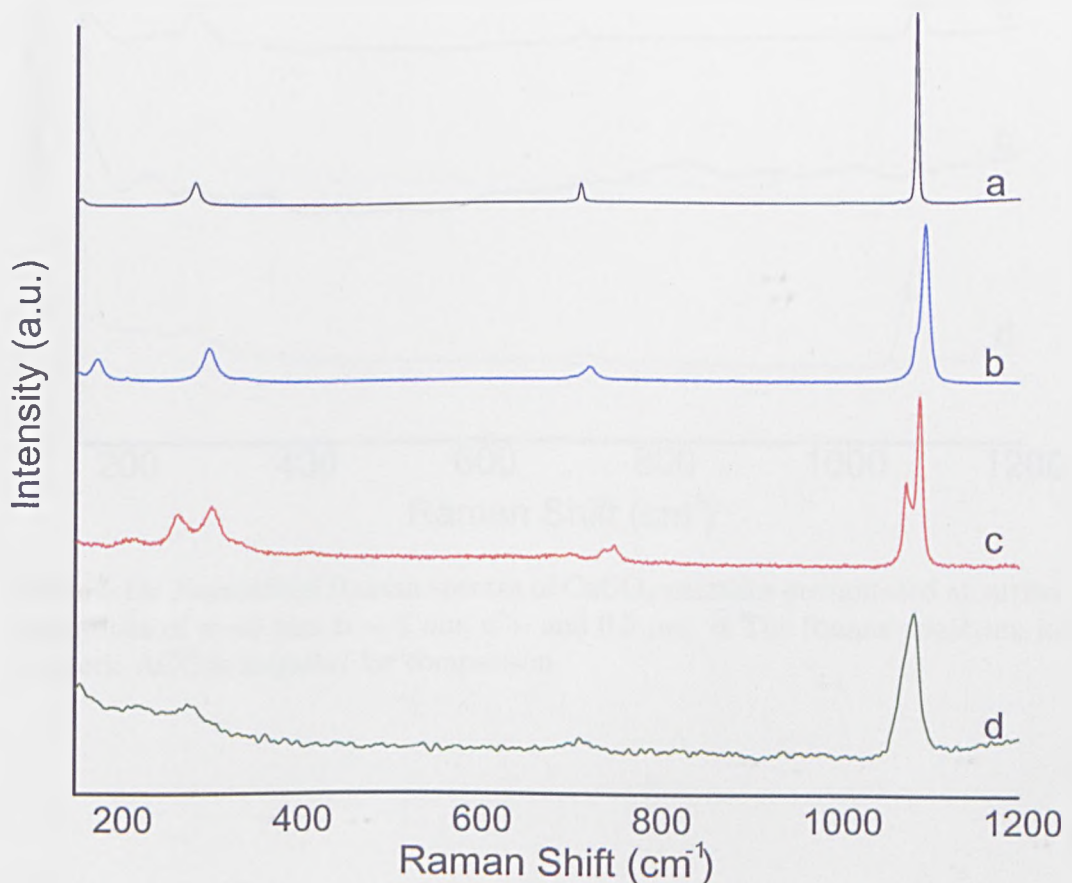


Figure 5.13: Normalised Raman spectra for synthetic samples of **a** calcite, **b** aragonite, **c** vaterite and **d** synthetic ACC, taken over a range of $180\text{-}1200\text{ cm}^{-1}$.

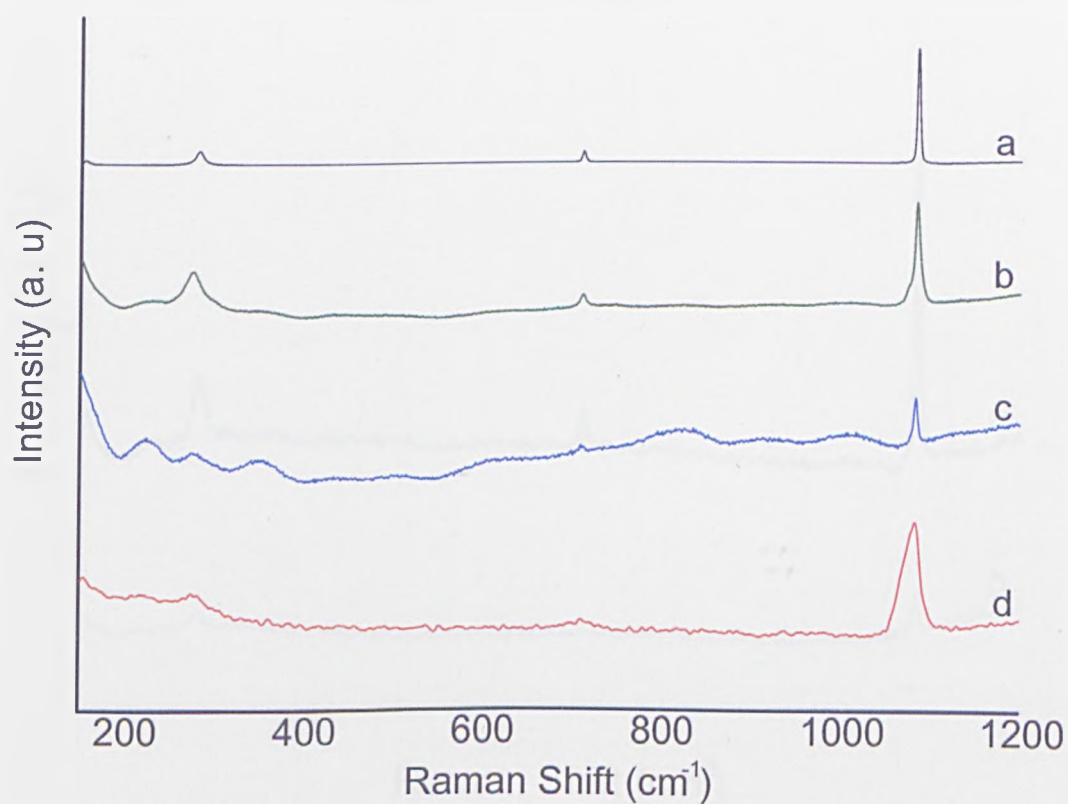


Figure 5.14: Normalised Raman spectra of CaCO_3 particles precipitated at surface separations of **a** ~ 5 mm **b** ~ 5 μm , **c** \sim and 0.5 μm . **d** The Raman spectrum for synthetic ACC is included for comparison.

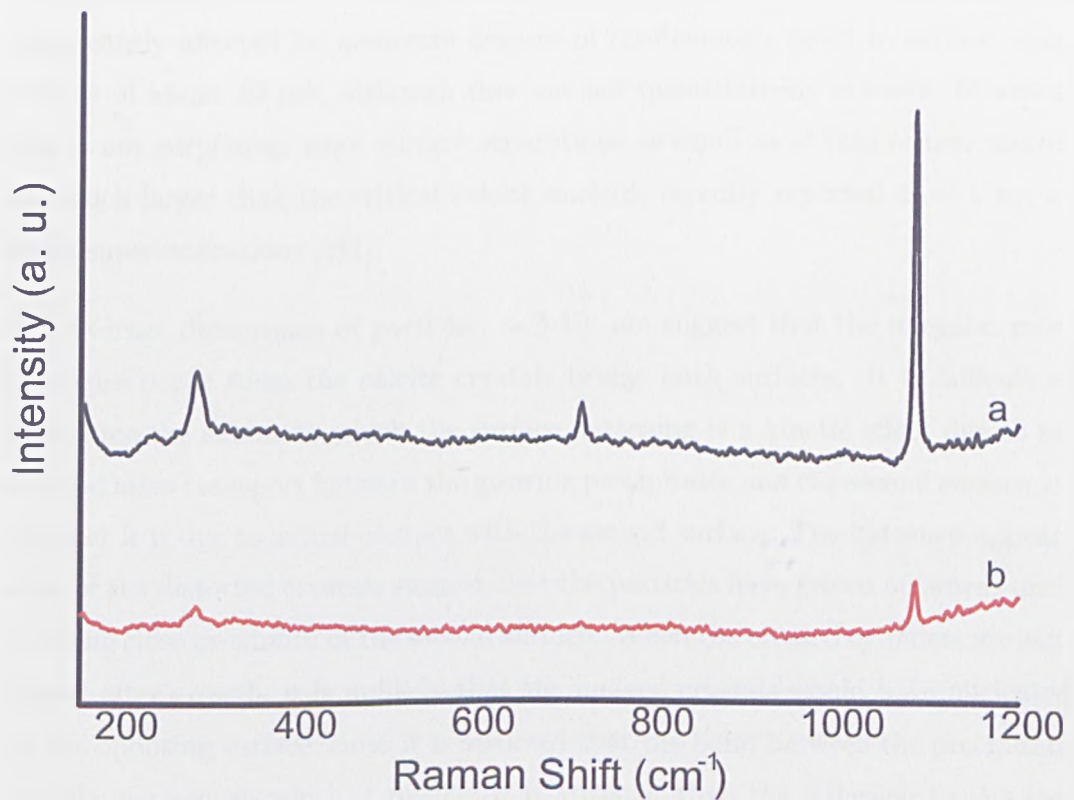


Figure 5.15: Normalised Raman spectra of the same CaCO_3 particle precipitated **a** after heating for 1 h at 180° **b** before heating. Double decomposition growth method, $[\text{Ca}^{2+}] = 5\text{mM}$, 24 h.

5.4 Discussion

The SEM and Raman spectroscopy data prove that significant changes in precipitate morphology occur as a result of confinement within an annular wedge. Changes in crystal habit were observed at surface separations as great as 10 μm , with multi-faceted, irregular calcite particles devoid of any characteristic 3-fold symmetry axes. SEM analysis suggests that the confinement does not greatly influence the nucleation of the precipitates. The average nucleation density was not significantly affected by moderate degrees of confinement, down to surface separations of about 10 μm , although this was not quantitatively studied. However, this is not surprising, since surface separations as small as of tens of nanometres are much larger than the critical calcite nucleus, recently reported as ~ 1 nm at these supersaturations [221].

The average dimensions of particles, ~ 5 -10, μm suggest that the irregular morphologies occur when the calcite crystals bridge both surfaces. It is difficult to determine the extent to which the surface flattening is a kinetic effect due to restricted mass transport between the growing precipitates and the second surface, or whether it is due to actual contact with the second surface. The flattened appearance of the distorted crystals suggest that the particles have grown outwards until reaching close proximity of the second surface. When the crossed cylinders are separated after growth, it is unlikely that the imaged crystals would have nucleated on the opposing surface, since it is assumed that the bond between the precipitate and the surface on which it nucleated is stronger than the adhesion to the second surface. The crystal habit became progressively more irregular with increased confinement, with SEM observations suggesting all regular edges associated with calcite are lost at sub-micron separations. This was confirmed with Raman microscopy, with the precipitate composition changing upon increased confinement. There was increased polycrystallinity at intermediate separations, with the confined particles appearing to consist principally of amorphous calcium carbonate at sub-micron separations. The amorphous nature of the sub-micron precipitates was further confirmed by their recrystallisation into calcite upon heating or incubation in solution.

Substances confined to porous media display phase transitions shifted from their bulk values [206]. Although the overall surface free-energy of the system remains constant, there is an increase in the ratio of surface free energy to bulk free energy in confinement. This arises from an increased surface area-to-volume ratio in confined systems, such that the phase with the smaller surface or interfacial free energy is favoured. This gives rise to wide range of phenomena such as capillary condensation and melting- and freezing point- depression of small particles and substances in porous media [222]. Temperature shifts in solid-solid phase transition [223] and the glass transition [224] in confinement have also been reported. Changes in the relative polymorph stability of calcium phosphate [225], globular protein (lysozyme) [226] and glycine [227] crystals precipitated from solution in various confined systems has been reported. Bulk transitions diminish and in some cases vanish altogether under extreme confinement, however this only applies to confinement in nanometer-sized pores, a three order of magnitude increase in the confinement considered in this study. The importance of the surface free energy is not restricted to sub-micron surface separations, however. Capillary rise and frost heave are examples of systems where the free energy of the substrate - liquid interface is lower than the substrate - vapour interface. In these cases the medium fills with liquid, although in contrast to sub-micron systems, the effect is not sufficiently large to shift the bulk melting point.

The capillary condensation of liquid below the bulk melting point of the substance is a phenomenon broadly analogous to the stabilisation of an amorphous phase (ACC) over a crystal phase (calcite) in confinement. The relative surface free energy terms results in the stabilisation of the liquid phase with respect to the vapour phase in a pore, and also a liquid phase over a crystalline solid below the bulk melting temperature. The transition between amorphous and crystalline phases presents a considerably more complex scenario than the transition between liquid and vapour phases. Defects, impurities, lattice strains as well as surface reconfigurations change the phase transition temperature. ACC, a non-crystalline isotropic phase, is approximated to resemble that of a liquid-vapour system. The surface free energy of ACC is assumed to be lower than that of the anhydrous CaCO_3 polymorphs, due in part to an absence of edges and corners, and contact between ACC and a solid substrate should be more favourable than contact

between calcite and the substrate.

A calculation is presented showing the maximum surface separation at which ACC is thermodynamically favoured over calcite, first described in the recent publication based on this work [202]. There are several assumptions made in this calculation, firstly that ACC is uniform in density, secondly that it can be approximated as a disc of radius r and thickness d (Figure 5.16) and thirdly that the surfaces are flat and form a continuous contact with the substrate.

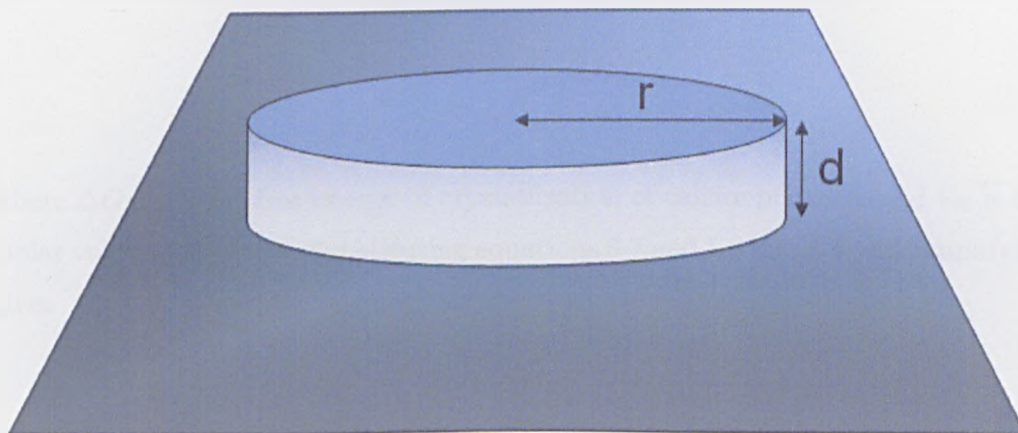


Figure 5.16: Schematic diagram showing the approximation of ACC as a disc of radius r and height d . The ACC particle is located near to the region of contact (top surface not shown).

The total free-energy for crystallisation is dependent on a bulk free-energy contribution, ΔG_{bulk} , and a surface-free energy contribution, $\Delta G_{surface}$. At equilibrium the surface and bulk free-energy terms are equal.

$$\Delta G = \Delta G_{surface} + \Delta G_{bulk} = 0 \quad (5.5)$$

The total surface free-energy contribution is the sum of precipitate-substrate and precipitate-solution terms, and relates to the difference in surface free-energy between calcite and ACC at each interface.

$$\Delta G_S = 2\pi r^2 (\gamma_{S/calcite} - \gamma_{S/ACC}) + 2\pi r d (\gamma_{W/calcite} - \gamma_{W/ACC}) \quad (5.6)$$

where γ represents the respective free energies of interfaces formed between various components denoted by the subscripts; calcite, ACC, substrate (S) and water (W). Equation 5.6 can be written in terms of the CaCO_3 -solution interface, $\Delta\gamma_L$ and CaCO_3 -substrate interfaces $\Delta\gamma_s$

$$\Delta G_{\text{surface}} = 2\pi r (r\Delta\gamma_s + d\Delta\gamma_L). \quad (5.7)$$

The bulk free energy term is related to the volume of the precipitate.

$$\Delta G_{\text{bulk}} = \pi r^2 d \frac{\Delta G_{\text{cryst}}}{V_M} \quad (5.8)$$

where ΔG_{cryst} is the free energy of crystallisation of calcite per mole and V_m is the molar volume of calcite. Substituting equations 5.7 and 5.8 into 5.5 and simplifying gives

$$2(r\Delta\gamma_s + d\Delta\gamma_L) = -rd \frac{\Delta G_{\text{cryst}}}{V_M}. \quad (5.9)$$

This can be written as

$$2 \left(\frac{\Delta\gamma_s}{d} + \frac{\Delta\gamma_L}{r} \right) = - \frac{\Delta G_{\text{cryst}}}{V_M}. \quad (5.10)$$

The molar volume of calcite is accepted as $V_m = 3.7 \times 10^{-5} \text{m}^3$ [228], and estimations can be made of $\Delta\gamma_s \approx 10 \text{mJm}^{-2}$ and $\Delta\gamma_L \approx 100 \text{mJm}^{-2}$ [202]. ΔG_{cryst} upon the transformation from ACC into calcite can be found from a CaCO_3 precipitation diagram. The change in chemical potential upon this transformation is obtained by subtracting the chemical potential change for the precipitation of ACC from solution from the chemical potential change for the precipitation of calcite from solution. Figure 1 of reference [228] gives a value $\Delta\mu = -7.3kT$ and therefore $\Delta G_{\text{cryst}} = -18 \text{kJmol}^{-1}$ at 20°C . Substituting numerical values into 5.10, and writing d and r in nm yields

$$\left(\frac{0.01}{d} + \frac{0.1}{r}\right) = 0.24 \quad (5.11)$$

The minimum radius, r , of the ACC precipitates at sub-micron separations represented in figure 5.11 is of the order of 10^3 nm. This yields a d value of the order of 0.1 nm according to equation 5.11. Permitting order of magnitude uncertainties in $\Delta\gamma_s$ and $\Delta\gamma_l$ gives the thermodynamic stability of ACC over calcite at a maximum surface separation of tens of nanometers. This is significantly smaller than the observed surface separations at which ACC was stabilised with respect to calcite.

There is a large gain in bulk free-energy upon the crystallization of ACC into calcite which negates surface free-energy losses at all but the smallest surface separations, of the order of 1 nm or less. It can therefore be concluded from these calculations that the stability of ACC at large separations must arise from kinetic factors. It can be expected that the transformation of ACC into calcite would be hindered within confined systems, due to limited contact between precipitate and solution. ACC is reportedly stable for long periods when isolated from solution and in non-aqueous solvents including ethanol [229]. This is in agreement with the results here, where calcite was stabilised with respect to calcite under confinement for periods of 72 hours.

The mechanisms of the ACC to calcite transition remains unclear. In particular, the expulsion of water during this process is not fully understood. The necessity for water expulsion in the transition from ACC into calcite was elucidated during the precipitation of CaCO_3 within cylindrical pores of track-edge membranes [209, 211]. Single crystals of calcite were obtained within 0.2-5 μm pores which were completely filled prior with ACC, whereas polycrystalline calcite was observed in large pores only partially filled prior with ACC. These studies support the results here, with the stability of ACC dependent on the availability of a dissolution-precipitation pathway.

5.5 Focused Ion-Beam Section Analysis

An attempt was made to examine the crystalline nature of CaCO_3 precipitates over a range of surface separations by taking FIB section of individual particles and examining them using TEM. The procedure loosely followed that described by Heaney *et al.* [230], with an SEM micrograph of each stage shown in figure 5.18. Firstly, a CaCO_3 particle was selected and a 50 nm thick $20 \times 5 \mu\text{m}$ Pt strip sputtered as a protective foil during the ion milling. Next, two trenches were excavated to a depth of $5 \mu\text{m}$ each side of the Pt strip, using a 30 kV Ga^+ beam operating at 200 nA (Figure 5.18b at a 45° tilt). One of the channels was cut with a shallow angle of approach, to allow for subsequent sample undercutting. The sample was further milled to a thickness of approximately 100 nm at reduced beam current ($\sim \text{pA}$) to remove any secondary material and enable electron transparency (Figure 5.18c). The sample was then undercut (Figure 5.18d) and welded on to a transportation tip (Figure 5.18e) before out lifting and welding onto a $100 \times 100 \mu\text{m}$ TEM grid (Figure 5.18f). TEM images were obtained using a Phillips CM 200 FEG-TEM.

Samples used in these measurements were prepared in a different way to the method described in section 5.2. 100 nm of gold was deposited onto freshly cleaved mica, $\sim 50 \mu\text{m}$ thick, before immersing in solutions of MHA in DCM for 24 h at 4°C . The mica sheets were then mounted onto the glass cylinders using carbon tape. The surfaces were brought into contact in the same way described in section 5.2, with CaCO_3 precipitated using the double decomposition method from 5 mM solutions for a 24 h growth period. Samples were prepared in this way due to difficulties in mounting the curved glass substrates onto the FIB sample holder, since this required a $2 \times 2 \text{ mm}$ sample size. The mica substrates were cut to size after crystal growth. Only two samples were prepared in this way: single crystal calcite precipitated at a large surface separation ($\sim 5 \text{ mm}$) and polycrystalline calcite precipitated at intermediate surface separations ($\sim 5 \mu\text{m}$) (Figure 5.19). FIB section analysis of CaCO_3 precipitated at sub-micron separations was not attempted due to financial limitations.

TEM micrographs of the single calcite sections suggest a uniform, single crystal structure. Figure 5.20a is for a FIB cross-section at a low magnification, showing

the mica substrate and a large CaCO_3 crystal separated by the a 100 nm gold layer, as shown by a dark band. There was continuous contact between the crystal and substrate, indicative of face selective growth. The protective Pt band can be seen encasing the CaCO_3 precipitate. The crystal appears uniform throughout, with only a small change in contrast suggesting the presence of few grain boundaries. Figure 5.21a is a high resolution TEM image of calcite structure viewed along the b -axis, with the Fourier sharpened image shown in figure 5.21b. These images show a close agreement with calcite cross sections presented by Yu *et al.* [231].

Figure 5.20b shows a low magnification FIB cross section of the polycrystalline calcite sample shown in figure 5.19b, contrasting sharply with the single crystal calcite. Here, multiple grain boundaries are present, defined by the multiple darkened bands. Furthermore, the crystal-substrate is highly irregular, only intermittent in contact with an absence of straight edge features. A higher magnification image of this interface is shown in figure 5.22a, on which the gold substrate appears as a dark band. An overview of a grain boundary is shown in figure 5.22b, with high magnification images showing the polycrystalline nature of the precipitate (Figure 5.23). Here, several lattice directors can be seen, contrasting to the single crystal calcite.

Crystallographic orientations were determined from the electron diffraction patterns. A schematic diagram of the setup is shown in figure 5.17. By making the small angle approximation to Bragg's law, the interplanar spacing can be determined.

$$d = \frac{\lambda L}{R} \quad (5.12)$$

where R is the measured spacing and λL is the camera constant dependent on the accelerating potential of the electron beam and the magnification of the diffraction pattern (λ is the wavelength of the incident electrons, L is the distance from the sample to the screen). The diffraction patterns CaCO_3 precipitated at large and intermediate surface separations are shown in figures 5.24a and 5.24b respectively. At a large separation the (104) calcite lattice spacing can be seen, whereas at an intermediate surface separation the spacings are indicative of calcite, although with a greater distortion. Significant growth planes are marked on the single crystal

calcite. Although these FIB section studies remain incomplete, it is immediately apparent that even moderate degrees of confinement influence the crystal growth.

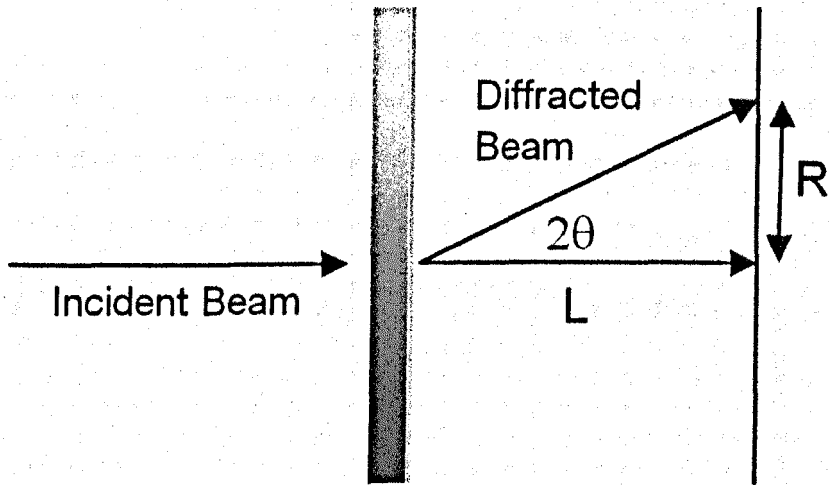


Figure 5.17: Geometric configuration of single crystal electron diffraction.

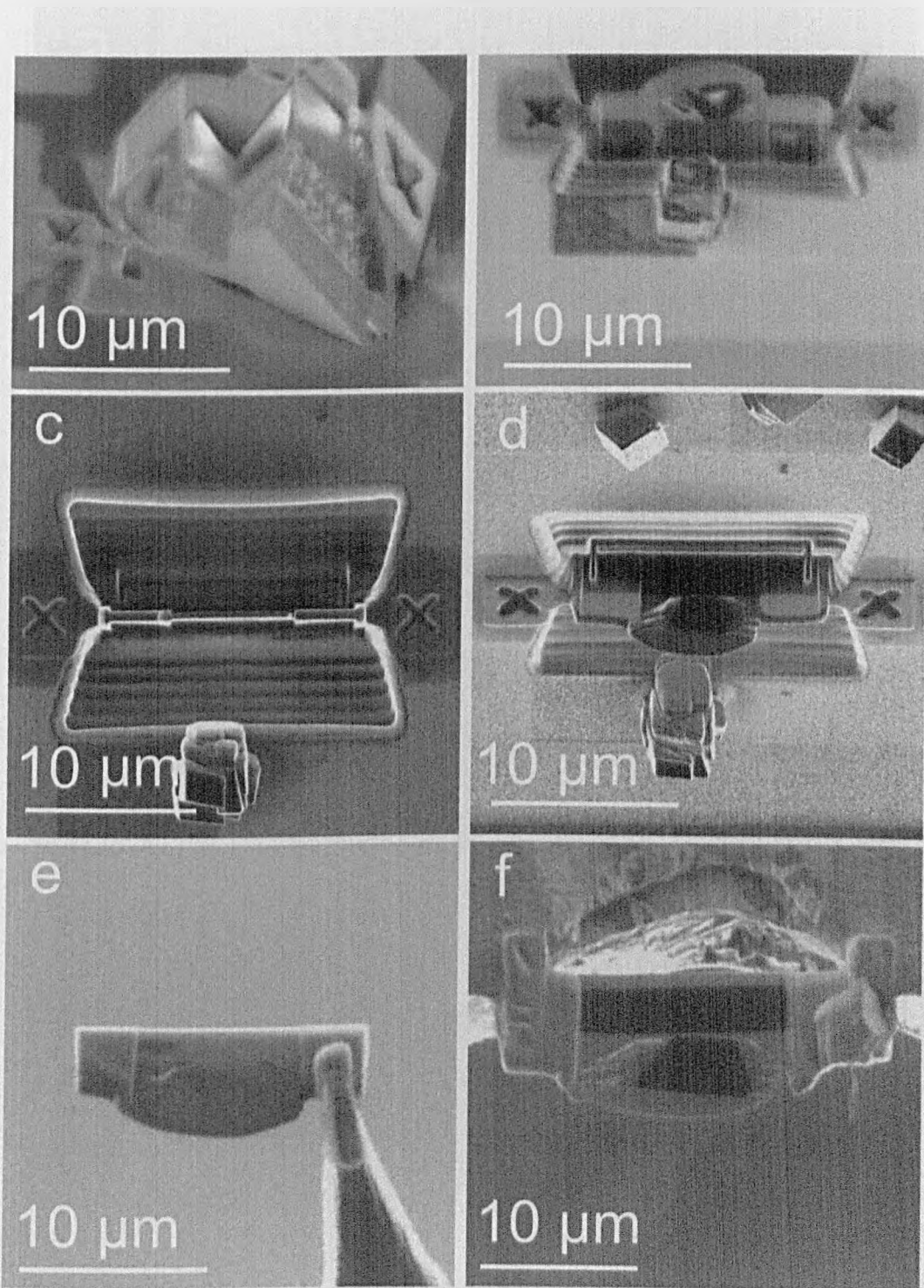


Figure 5.18: SEM micrographs showing the various stages of the FIB milling process. **a** Sample identification and sputter deposition of Pt layer (not shown), **b** coarse excavation of channels, **c** fine milling, **d** undercutting, **e** welding onto transportation tip and **f** welding onto TEM grid.

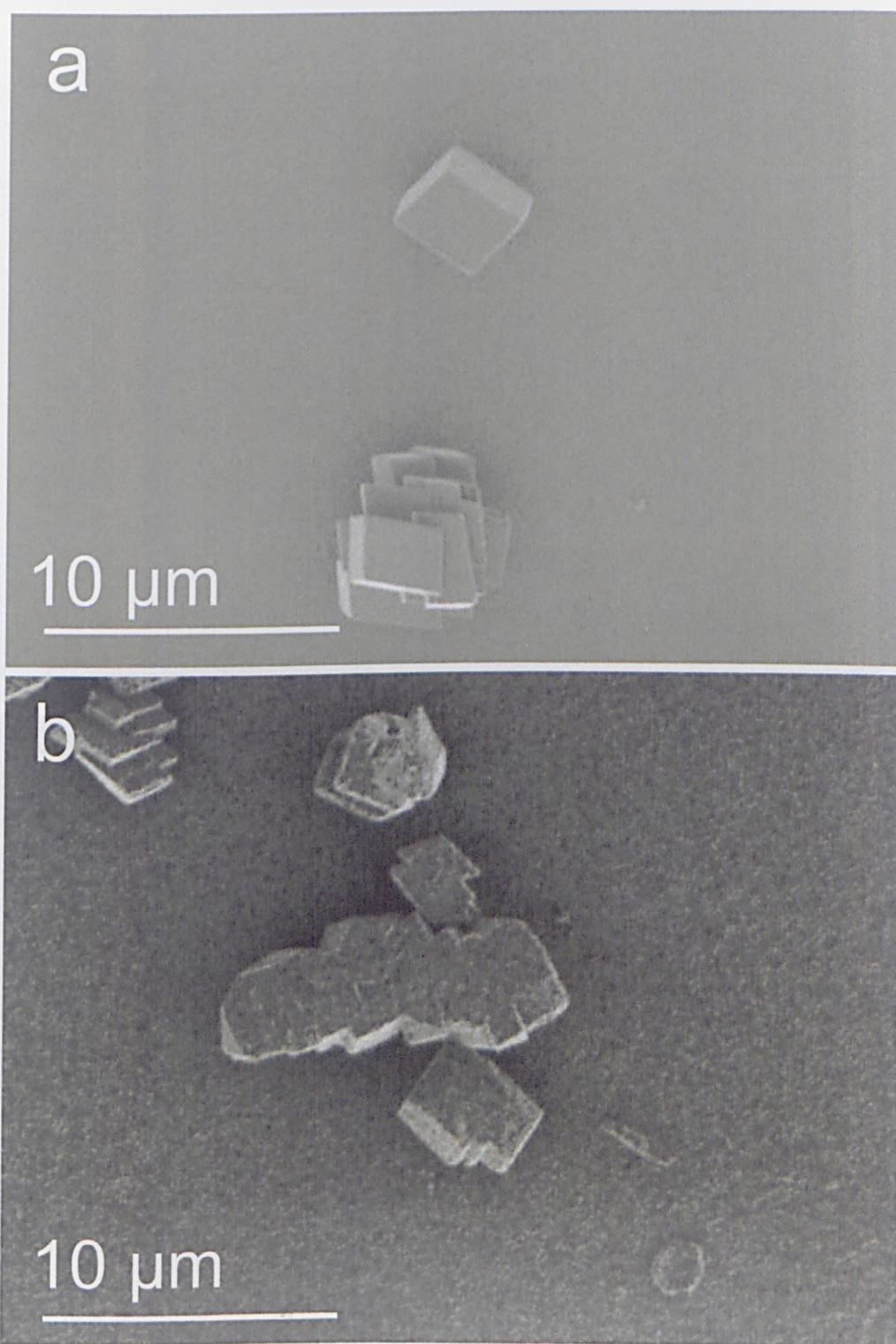


Figure 5.19: SEM micrographs of the CaCO₃ precipitates prior to FIB milling, supported on MHA gold on mica substrates. 5 mM double decomposition growth method, 24 h growth. **a** single calcite, precipitated at a large surface separations (~5 mm), **b** polycrystalline calcite precipitated at intermediate surface separations (~5 μm).

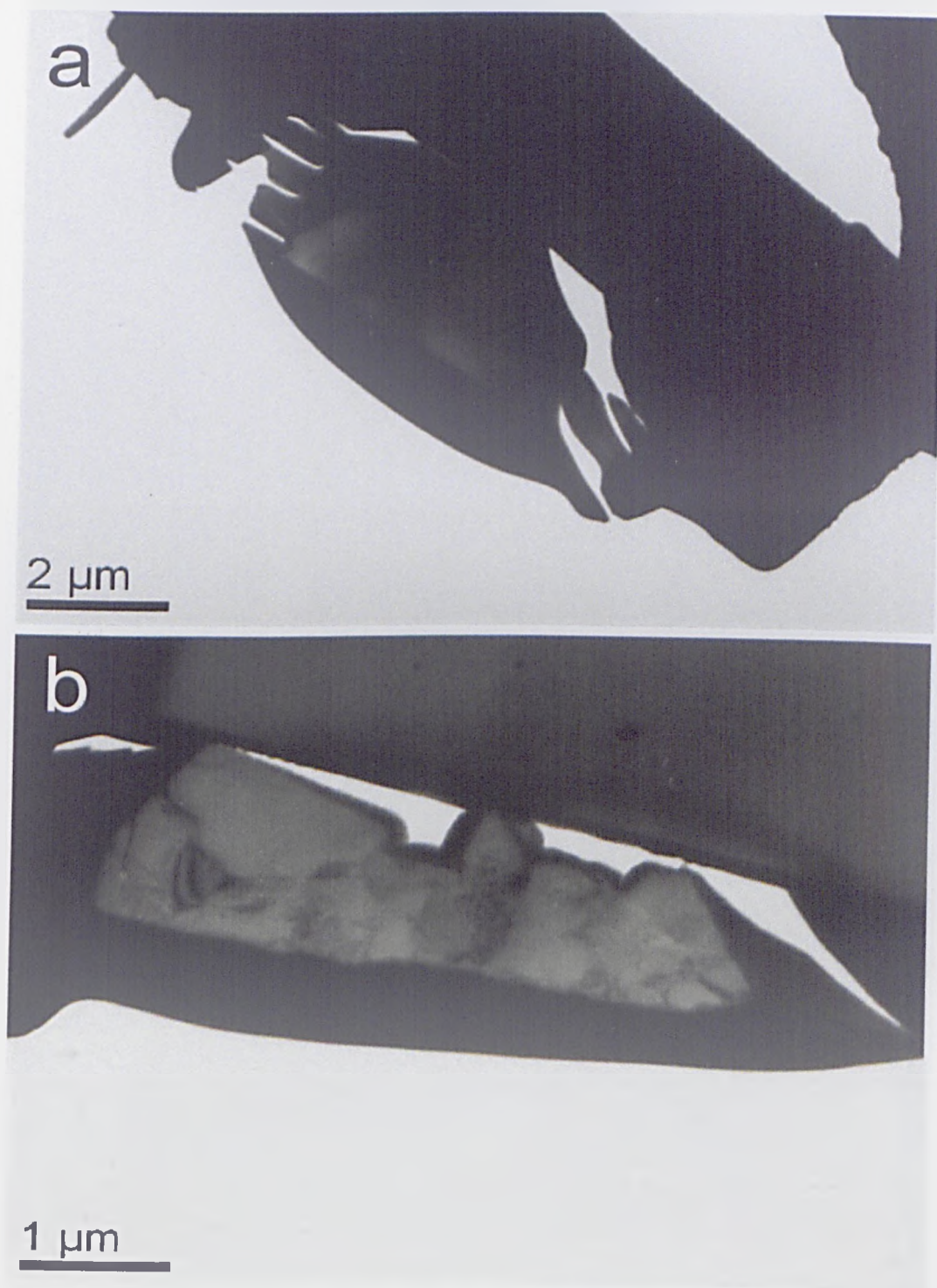


Figure 5.20: TEM micrographs of FIB sections for CaCO₃ precipitated at **a** large surface separations (5 mm) and **b** intermediate surface separations ($\sim 5 \mu\text{m}$).

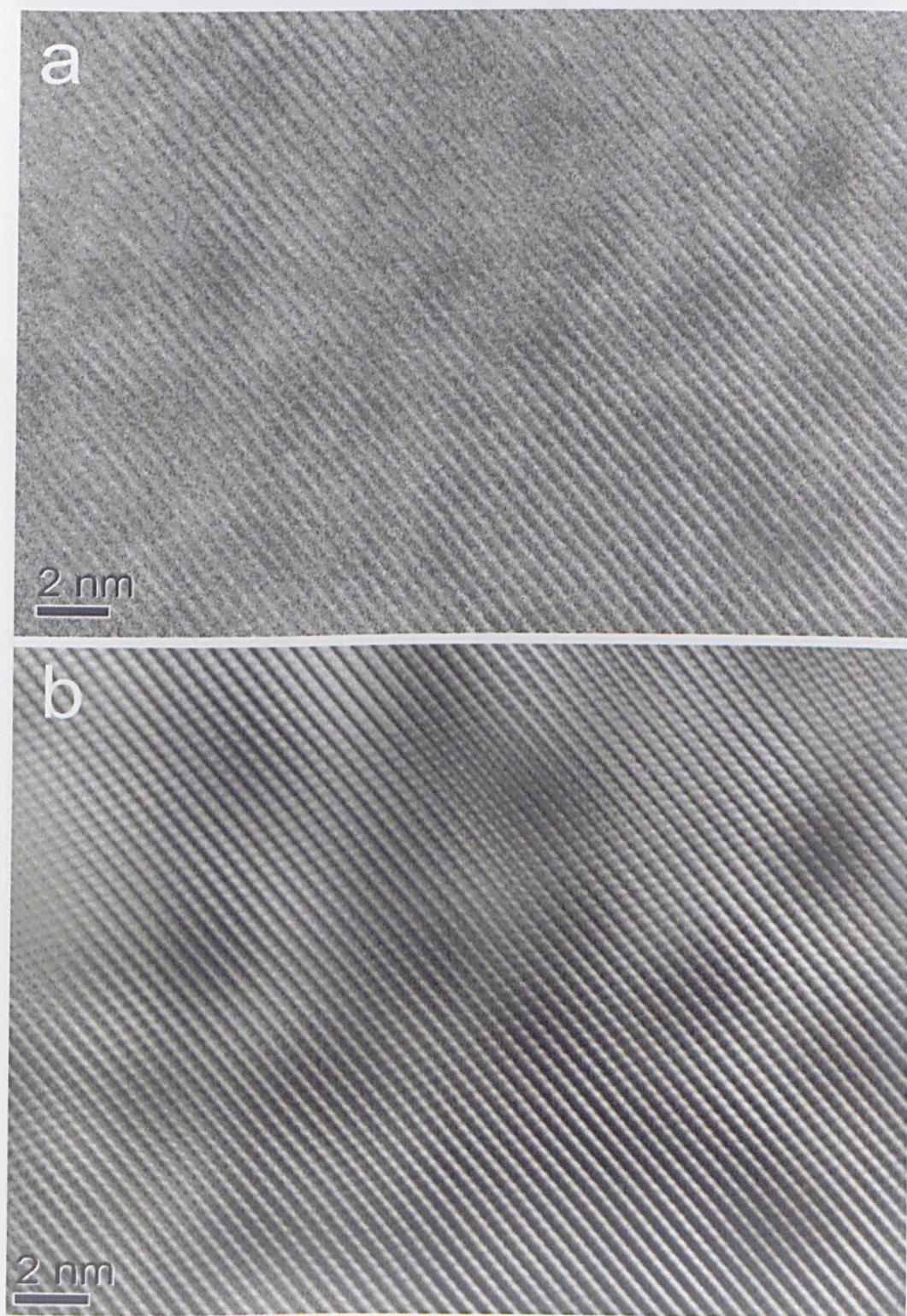


Figure 5.21: High resolution TEM image of a single crystal calcite FIB cross section. **a** Original image, **b** Fourier enhanced image.

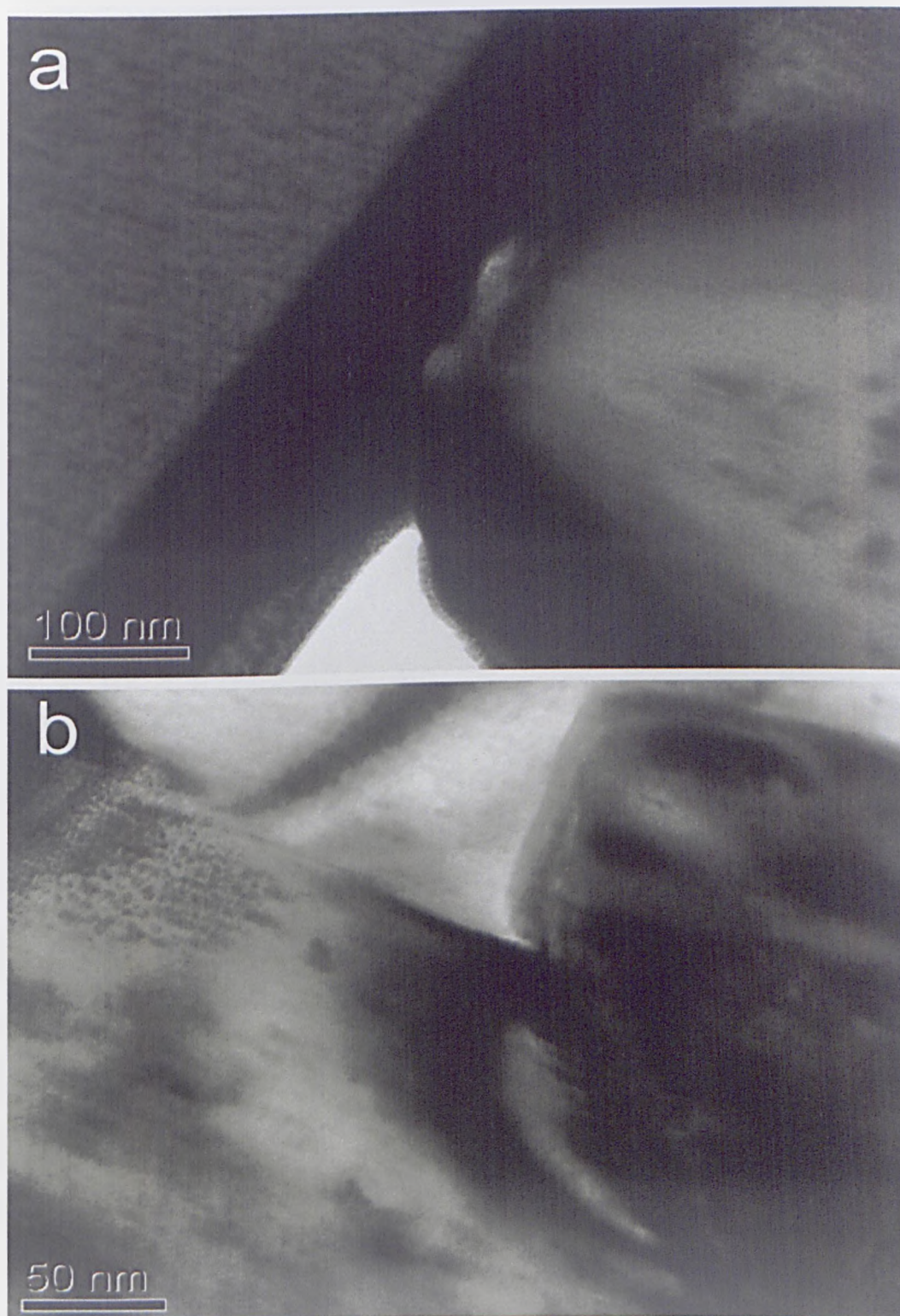


Figure 5.22: TEM overview of a CaCO_3 particle precipitated at an intermediate surface separation showing **a** the crystal-substrate interface for and **b** the presence of grain boundaries.

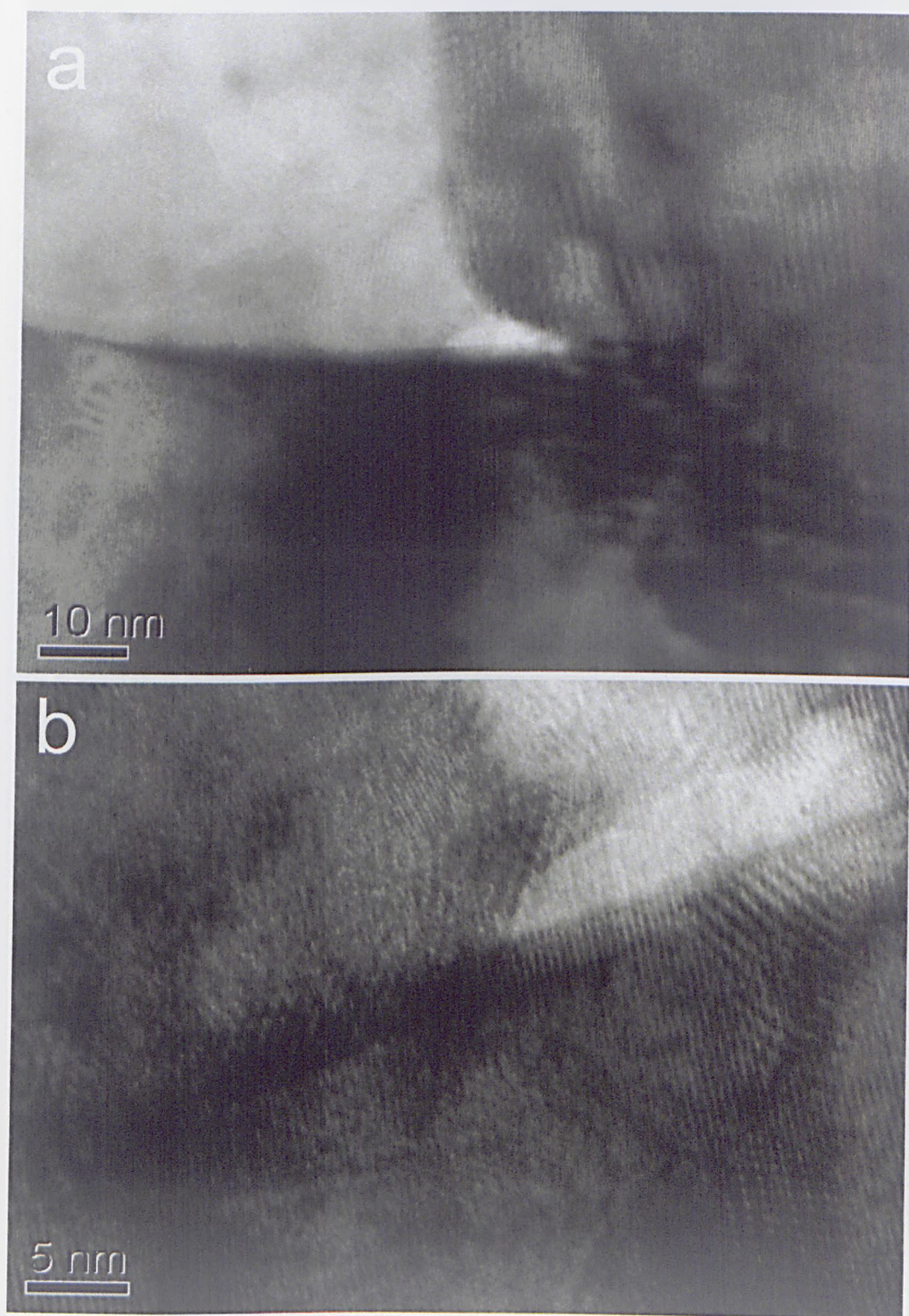


Figure 5.23: High magnification TEM images of CaCO_3 precipitated at intermediate surface separations.

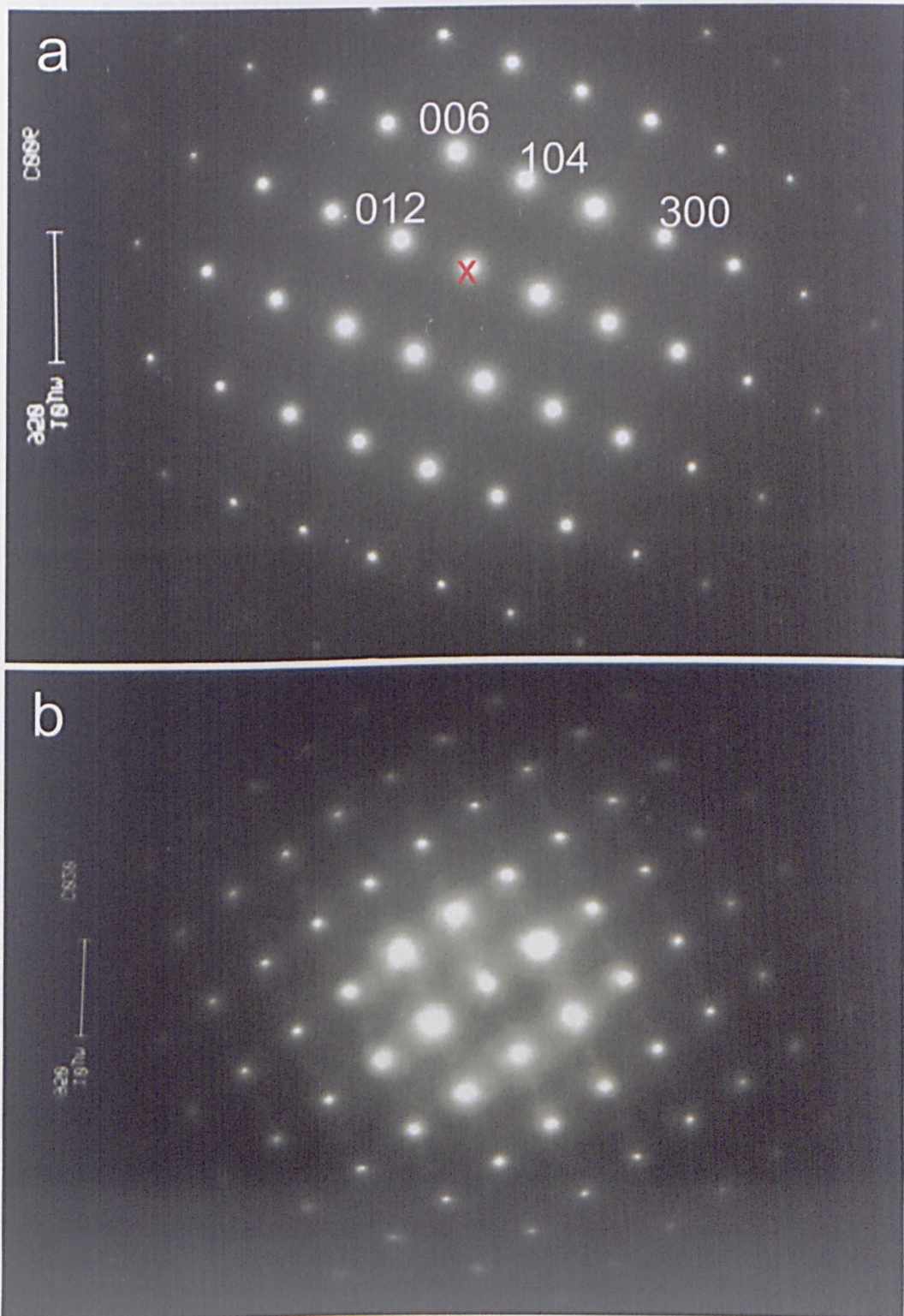


Figure 5.24: TEM electron diffraction patterns of CaCO_3 precipitated at **a** large surface separations ($\sim 5\text{mm}$), with the (012), (104), (006) and (300) planes identified from the central point, x, and **b** intermediate surface separations ($\sim 5\ \mu\text{m}$), showing a greater distortion of the individual spots.

5.6 Conclusions

It was shown in this chapter that the environment within which a mineral forms exhibits significant influence on the resultant crystal morphology. In highly confined systems, in this case around the region of contact of an annular wedge pore, ACC, an amorphous precursor phase, is stabilised with respect to calcite, a crystalline phase. There was a rapid transition from ACC to calcite upon the removal of the confining surface and subsequent incubation in depleted solution. Furthermore, heating of an amorphous particle after separation resulted in a transition to a crystalline state. The stabilisation of the amorphous phase was attributed to kinetic factors, since it was shown that ACC is thermodynamically preferable to calcite at sub-nanometer surface separations, at least three orders of magnitude less than observed here! Around the region of contact the solution-particle interface is extremely small, and it is proposed that the resultant hindrance of water expulsion from the amorphous phase prevents the transition to the crystalline phase.

The stabilisation of amorphous calcium carbonate over anhydrous CaCO_3 polymorphs under confinement has implications in the understanding of the biomineralisation processes. Biomineralisation invariably occurs within restricted volumes, and through a wide range of interactions with insoluble matrices and soluble macromolecular entities within these privileged micro-environments, a large degree of control over mineralisation process is afforded, including the nucleation site, crystal composition and morphology. The crystallisation of an inorganic biomineral through an amorphous precursor phase is not restricted to CaCO_3 however, with recent reported examples including calcium phosphates and iron oxide biomaterials. Since amorphous precursor phases are of obvious significance in biomineralisation, the work here shows that organisms may use confinement alone as a means for stabilisation, with the results indicating that stabilisation will occur at micrometer confinements depending on kinetic considerations. It is therefore concluded that although the crystallisation within a confined microenvironment provides a necessary environment for a variety of controlled interactions, it is suggested that confinement alone, and specifically the large surface area to

volume ratio, which may provide an additional control mechanism over biomineralisation.

Chapter 6

Precipitation of Calcium Carbonate in Bulk Solution

This chapter considers the nucleation pathways of CaCO_3 in bulk solution and how the occurrence of the amorphous precursor, ACC, is dependent on measurable quantities including solution concentration and volume. The early growth stages of CaCO_3 are investigated using spectrophotometry, with the transmitted intensity of light related to the size of crystal precipitate. Particles collected during the in situ spectrophotometry measurements were analysed using Raman spectroscopy to determine polymorphism, and TEM to determine the particle size distributions and relative degree of crystallinity. By relating the transmitted intensity to the known particle sizes of calcite and ACC, it was possible to determine the solution composition at a given time, and thus determine the nucleation pathway.

6.1 Introduction

During the course of the experiments presented in chapters 4 and 5 it was observed that the supersaturated CaCO_3 solutions, when mixed in accordance to the double decomposition growth method, would go cloudy at concentrations of $[\text{Ca}^{2+}] = 5$ mM and above (Figure 6.1a). Solutions mixed at concentrations $[\text{Ca}^{2+}] = 4$ mM and below remained clear, with the *turbidity* of the mixed solution the same as for initial CaCl_2 and Na_2CO_3 solutions. An intermediate increase in solution

turbidity was observed at concentrations of $[\text{Ca}^{2+}] = 4.5 \text{ mM}$. The concentration at which the solutions appeared cloudy was apparently independent of volume with the solutions appearing clear after periods ranging between 5 and 10 minutes, depending on concentration and solution volume. This is shown in figure 6.1, where the solution appears initially cloudy before clearing as the solution converts to calcite and settles at the vessel floor.

Since the solution turbidity is clearly dependent on both the size and number density of the particles, it is possible to use the attenuation of visible light as a means to determine the nucleation pathway for CaCO_3 . It will be shown later in this chapter that ACC particles are smaller than calcite particles, and it follows that the nucleation density will be higher. Therefore, a solution with a high number of ACC particles will contain significantly more scattering centres than a solution of calcite particles. This makes it possible to follow the transition from ACC to calcite in solution as a function of time. This section considers the nucleation of CaCO_3 in from bulk solution with and without Mg^{2+} additives, known to affect the lifetime of ACC.

Induction periods, the elapsed time between the creation of supersaturation and the formation of crystal nuclei, have been determined from the transmitted intensity of scattered light for various materials, including calcium oxalate [232], dimethylglyoxime [233], barium sulphate [234, 235], magnesium hydroxide [235, 236] and magnesium ammonium phosphate [235]. Faatz *et al.* [237] considered the precipitation of CaCO_3 using light scattering and reported that ACC is transiently stable without additives, although a different growth method was used to that described here. Similarly, Liu *et al* analysed the nucleation and growth of amorphous calcium carbonate using time resolved static light scattering and reported the formation of ACC spherulites [238]

Practically, induction periods, t_{ind} are easier to measure than nucleation rates. For spectrophotometry measurements, the nucleation of particles is succeeded by a fall in transmitted intensity of light through the solution due to Rayleigh scattering from small particles. The induction period is inversely proportional to the nucleation rate, J

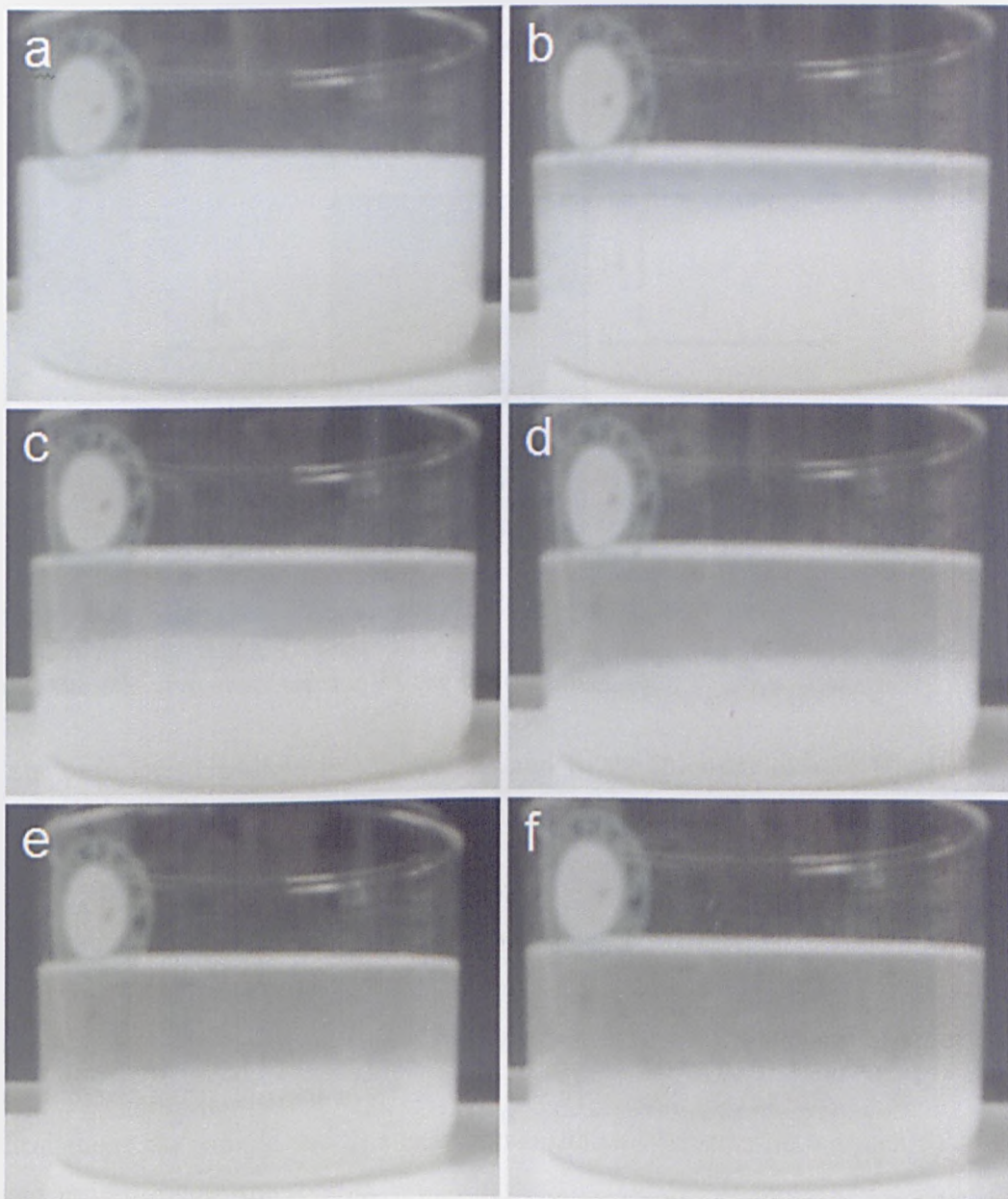


Figure 6.1: Chronological photographs showing a 5mM supersaturated CaCO_3 solution in a 100 ml vessel after a 30 s, b 2 min, c 4 min, d 6 min, e 8 min and f 10 minutes.

$$t_{ind} = \frac{1}{J} \quad (6.1)$$

According to Beer's Law, the transmitted intensity, I , of light through a solution is related to the projected areas of the particles in unit volume of suspension, A_p

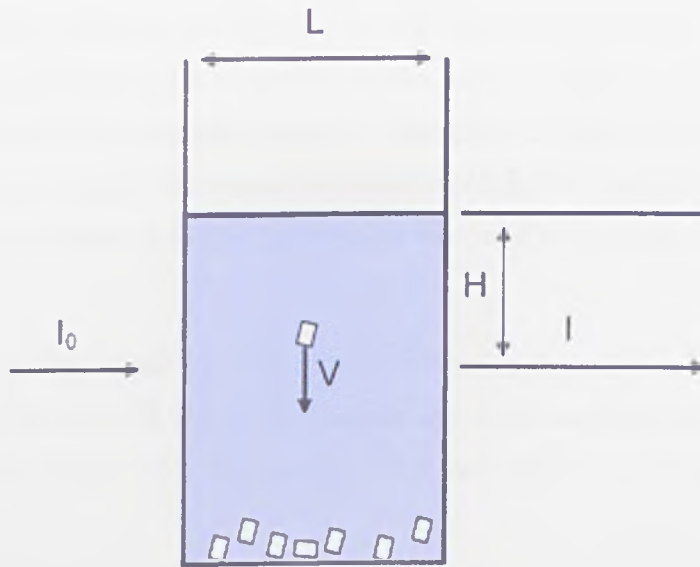


Figure 6.2: Schematic diagram showing the spectrophotometry cuvette, with the transmitted intensity, T , related to the initial intensity, T_0 by the path length, L , and the effective cross-section of the particles.

, the path length of light in solution, L , and to the intensity of light transmitted through pure water, I_0 [239].

$$\ln \frac{I_0}{I} = A_p L \quad (6.2)$$

The above is dependent on the following assumptions; 1) the absorbing particles act independently of each other, regardless of density, 2) absorption is uniform throughout the sample and 3) absorption is the only interaction between the incident radiation and the solutes.

In the case of CaCO_3 precipitating in solution, the situation is complicated by the sedimentation of calcite particles upon growth to a certain size. Gunn described the rate of sedimentation for a similar system, that of barium sulphate, using Stokes' law [235]. That derivation is briefly described here.

Upon reaching a certain size, the crystals will sediment at a terminal velocity, V , whereby the weight of the particle is equal to the drag force acting upon it, f .

$$f = 6\pi r V \mu \beta = \frac{4}{3} \pi r^3 (\rho_s - \rho) g \gamma \quad (6.3)$$

where β denotes the ratio of drag forces on a crystalline particle of dimension $2r$ to that of a sphere of radius r moving at the same velocity. γ is the ratio of the volumes between a crystalline particle of dimension $2r$ and an equivalent sphere of radius r . ρ and ρ_s are the respective densities of the crystalline precipitates and the spherical particles. g is the acceleration due to gravity and μ is the viscosity of the fluid.

There is no change in the amount of transmitted light until the largest particles have fallen a distance H from the free surface of the medium to a point below the light beam (Figure 6.2). Substituting H/t for V and rearranging equation 6.3 yields

$$r(t) = \sqrt{\frac{9\mu H\beta}{2t(\rho_s - \rho)g\gamma}} \quad (6.4)$$

giving the last particle to fall through the illuminated zone. The projected area in equation 6.2 at time t is related to $n(r)$ by

$$A_p = \pi \int_0^{r(t)} -\frac{dn(r)}{dr} r^2 dr = \frac{1}{L} \ln \left(\frac{I_0}{I} \right) \quad (6.5)$$

where $n(r)$ is the number of particles within a unit volume of size greater than r , where each $n(r)$ sized particles has a true surface area of $4\pi r^2$ and a projected area of πr^2 .

By differentiating both sides of the equation with respect to t it can be shown that

$$-\frac{dn(r)}{dr} = \frac{9\mu H\beta}{\pi L r^2 (\rho_s - \rho) g \gamma} \frac{d}{dt} \left(\ln \left(\frac{I_0}{I} \right) \right) \quad (6.6)$$

giving the measured concentration of particles as a function of change in transmitted intensity over time. In the case CaCO_3 precipitating from bulk solution, the situation is complicated by the fact that there are two particle types: ACC and calcite. Due to their small size ($r < \sim 100$ nm) and lower density, the ACC particles will not readily sediment, and it is assumed that sedimentation occurs only for calcite particles.

6.2 Experimental Methods

CaCO_3 was precipitated in accordance to the double decomposition method outlined in section 2.3. For these experiments, the solutions were stored under atmospheric CO_2 for a period greater than 3 days, unless otherwise stated. 1 ml of solution mixed directly in a 2 ml Plastibrand perspex cuvette. The solutions were always mixed in the same order, with 500 ml of Na_2CO_3 added to 500 ml of CaCl_2 , at a rate not exceeding 500ml/sec to prevent the formation of air bubbles in solution. Spectrophotometric measurements commenced within 2 seconds of mixing.

In situ spectrophotometry measurements were obtained using a Perkin Elmer Lambda 35 UV-Vis system, operating in a time-drive mode ($\lambda = 500$ nm, exposure time = 1s). The transmitted intensity, I , was recorded as a function of base intensity, I_0 , where I_0 was measured through an empty cuvette over a time period of 1200 s. Monochromatic light of 500 nm wavelength was chosen since the empty cuvettes did not absorb significantly at this wavelength, yet over 90% of the light was absorbed by a 5 mM CaCO_3 solution 30 s after mixing (Figure 6.3). In general, there was no significant difference in absorbance over a 250-650 nm range in wavelength, with considerable absorption (greater than 20%) occurring only in the UV range.

Raman spectra were obtained for precipitates extracted from CaCO_3 solutions during in situ spectrophotometric measurements, relating the polymorphism to the transmitted light intensity. Approximately 100 μl of supersaturated CaCO_3 solution was extracted from the cuvette during the spectrophotometric measurement before passing through 200 nm filter paper and rinsing with ethanol. The precipitates were then transferred onto a glass slide and analyzed using a Raman microscope within 5 minutes of extraction. Particles were extracted after growth times of 15 s, 1 minutes, 2 minutes and 5 minutes for $[\text{Ca}^{2+}]$ solution concentrations of 2.5, 5 and 10 mM. Each spectrum was plotted as a function of absolute and relative intensity. The absolute intensity shows the difference in peak height for the different spectra, with the same exposure time and laser power settings used for each experiment. The spectra are normalised between 0 and 1 on the

relative intensity scale, in order to clearly show the peak broadening inherent in amorphous spectra.

TEM images were taken for CaCO_3 particles extracted from solution after short growth periods of 15 s, 1 minute and 5 minutes, at concentrations of $[\text{Ca}^{2+}] = 2.5$ and 5 mM. Polymer coated $100 \times 100 \mu\text{m}$ Formvar TEM grids were immersed in 50 ml of supersaturated CaCO_3 solution for the set growth period before rinsing with ethanol and drying under N_2 . Low magnification images were obtained by first viewing the TEM grid using SEM, without first applying a Pt layer.

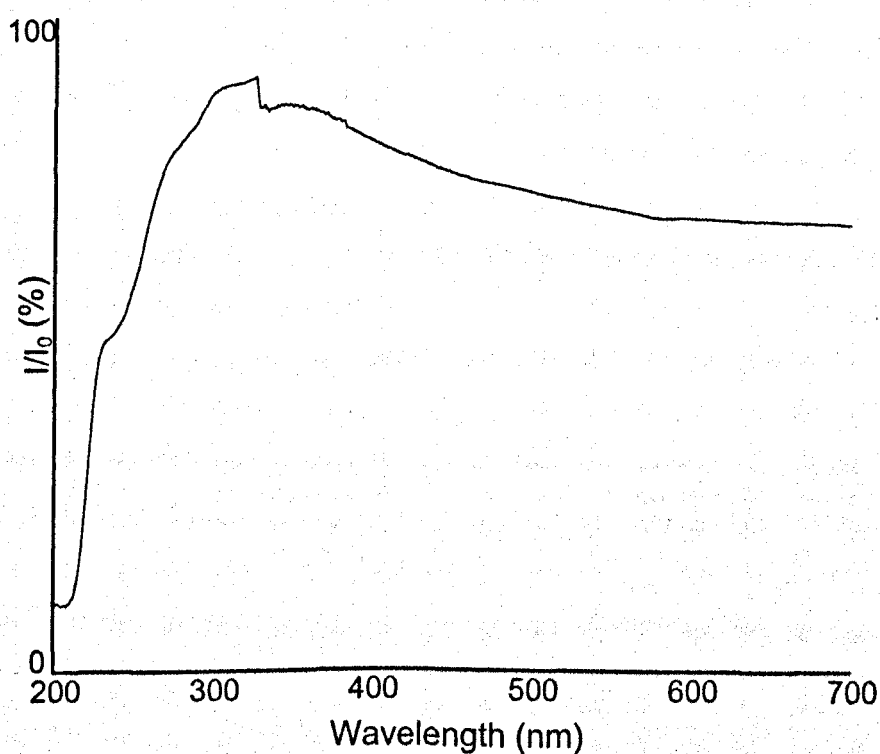


Figure 6.3: UV-Vis absorption over 200-700 nm, measured for a $[\text{Ca}^{2+}]$ 5 mM solution 30 s after mixing. A wavelength of $\lambda=500$ nm was used for the spectrophotometry measurements

6.3 Results

6.3.1 Spectrophotometry Analysis

6.3.1.1 Precipitation of Calcium Carbonate Without Additives

In situ spectrophotometry measurements were recorded during the initial precipitation of CaCO_3 from solution, with the induction time dependent upon the solution concentration. An immediate fall in intensity was observed for solution concentrations of $[\text{Ca}^{2+}] = 5$ mM and above, falling below 10% after 60 seconds at a concentration of $[\text{Ca}^{2+}] = 5$ mM. This trend was observed for all concentrations in the range of 5-10 mM, with the fall in intensity succeeded by a sharp increase in intensity after timescales varying between 60 and 250 s (Figure 6.4). Interestingly, a secondary reduction in intensity was observed during the recovery process for all cases within the concentration range, yielding a small peak with the width of the order of 30s and a fall in intensity between 4 and 10% (Figure 6.4a-g).

At initial concentrations of $[\text{Ca}^{2+}] = 4$ mM and below, the intensity profile was considerably different, with no reduction in intensity greater than 5% observed during the first 500s. A small reduction in I/I_0 was observed between 600s and 800s, of approximately 15% for $[\text{Ca}^{2+}] = 4$ mM and 5% for $[\text{Ca}^{2+}] = 2$ mM. A subsequent increase in intensity was witnessed in both these cases, without any secondary reductions in I/I_0 . A solution concentration of $[\text{Ca}^{2+}] = 4.5$ mM marked the transition between these two domains, with the intensity minima occurring approximately 200s later than for an initial concentration of $[\text{Ca}^{2+}] = 5$ mM. The I/I_0 minima values were 36% and 21% for $[\text{Ca}^{2+}] = 4.5$ and 5 mM respectively, although the rates of recovery of I/I_0 values were comparable. A small secondary reduction in intensity was again observed at a concentration of $[\text{Ca}^{2+}] = 4.5$ mM, albeit on this occasion after more than 600s.

Interestingly, the solution pH strongly influenced the solution turbidity (Figure 6.5). The transmitted intensity through solutions equilibrated with atmospheric CO_2 recovered quicker than in the case of solutions made from fresh Milli-Q water. Solutions made from fresh Milli-Q water remained turbid over 20 minutes at concentrations of $[\text{Ca}^{2+}] = 5$ mM and above. At a concentration of $[\text{Ca}^{2+}] = 2.5$ mM,

the solutions remained clear regardless of whether the solutions were equilibrated with atmospheric CO_2 . The pH was 5.7 for CO_2 -equilibrated CaCl_2 solutions and 6.2 for fresh CaCl_2 solutions. There was no significant change in pH of the Na_2CO_3 solutions, with values of 10.95 and 11.02 for fresh- and CO_2 -equilibrated solutions respectively. To further quantify the effect of pH on solution turbidity, a series of experiments were undertaken, in all cases taken for $[\text{Ca}^{2+}] = 10$ mM initial solution concentrations (figure 6.6). Firstly, the solutions were mixed at a high pH with the prior addition of a small volume of NaOH to the CaCl_2 solution yielding a pH of 9.8 (Figure 6.6a). This resulted in the solution remaining turbid over 1200 s, with the intensity never recovering above 20 %. Secondly, the CO_2 was bubbled through the fresh solutions for 20 min, yielding a CaCl_2 pH of 3.8 (Figure 6.6b). In this case, the solution remained clear throughout, with no fall in intensity observed during 1200 s. Next, CO_2 equilibrated CaCl_2 solutions were mixed with fresh Na_2CO_3 (Figure 6.6c) and vice versa (Figure 6.6d). In both cases, there was a fall and subsequent rise in intensity, similar to the result observed when both solutions were CO_2 equilibrated (Figure 6.6e). In contrast, the solutions remained turbid when both solutions were made fresh (Figure 6.6f).

6.3.1.2 Precipitation of Additive-Stabilised ACC

ACC is reportedly stabilised by various additives, including block co-polymers [240], NaOH [213], magnesium salts [241] and phosphonates [242]. The results presented here consider the effect of Mg^{2+} additives on the stability of ACC using spectrophotometry. Equal volumes of 10-40 mM MgCl_2 and 40 mM CaCl_2 aqueous solutions were combined, yielding solution concentrations of $[\text{Ca}^{2+}] = 20$ mM, $[\text{Mg}^{2+}] = 5$ -20 mM. This solution was then mixed with a 20 mM Na_2CO_3 aqueous solution in a 1:1 ratio in a cuvette to initiate precipitation. The final ionic concentrations were therefore $[\text{Ca}^{2+}] = 10$ mM, $[\text{Mg}^{2+}] = 2.5$ -10 mM and $[\text{CO}_3^{2-}] = 10$ mM.

The induction time and recovery period increased with the $[\text{Mg}^{2+}]$ additive concentration (Figure 6.7). A 2.5 mM Mg^{2+} salt concentration resulted in a 600 s increase in the time period for which I/I_0 remained below 25% in comparison to the control sample without additives. For Mg^{2+} ionic concentrations of 5 mM and

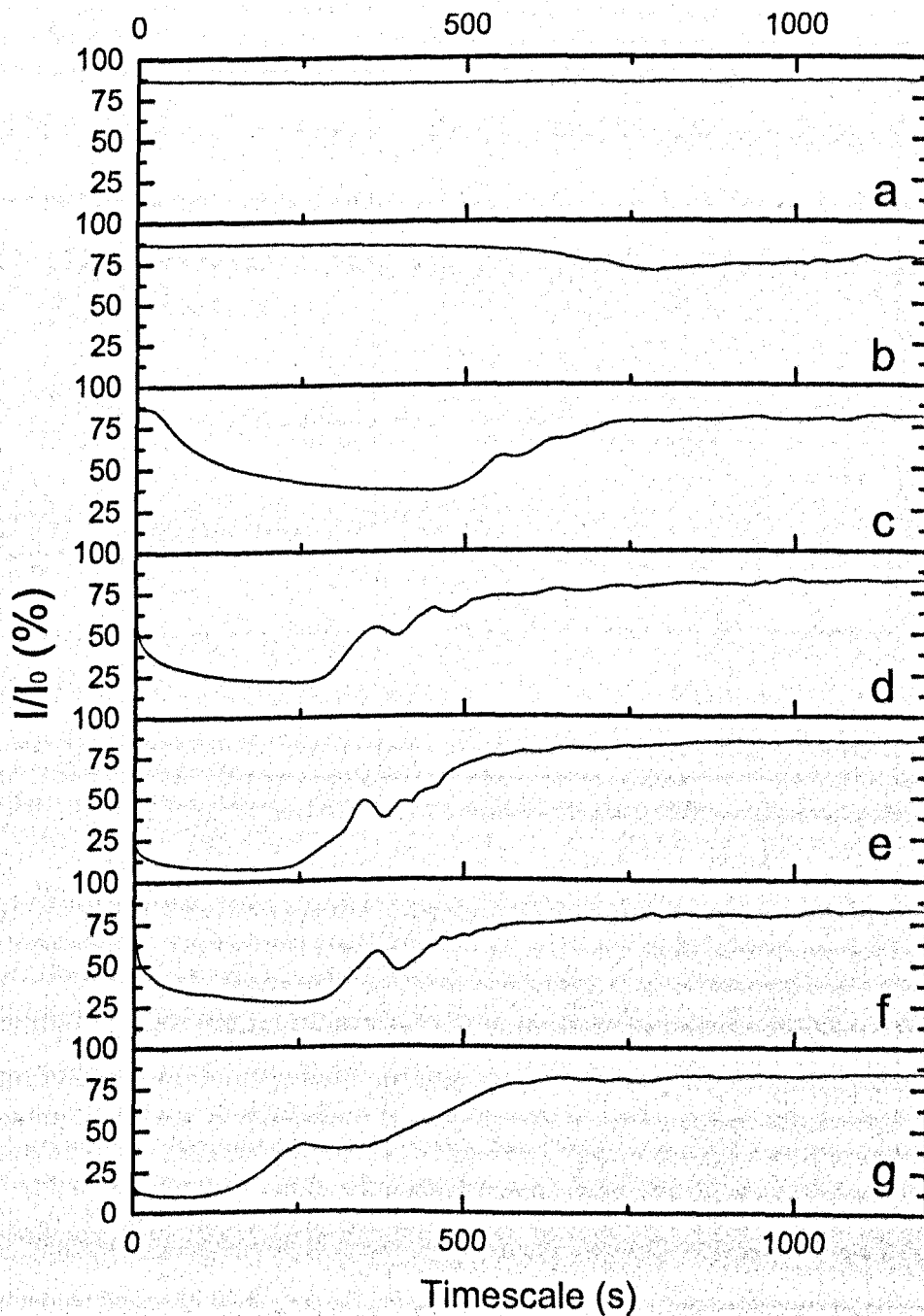


Figure 6.4: In situ spectrophotometry measurements of the transmitted intensity, I/I_0 , as a function of time. $[Ca^{2+}] =$ a-g 2, 4, 4.5, 5, 6, 8 and 10 mM respectively.

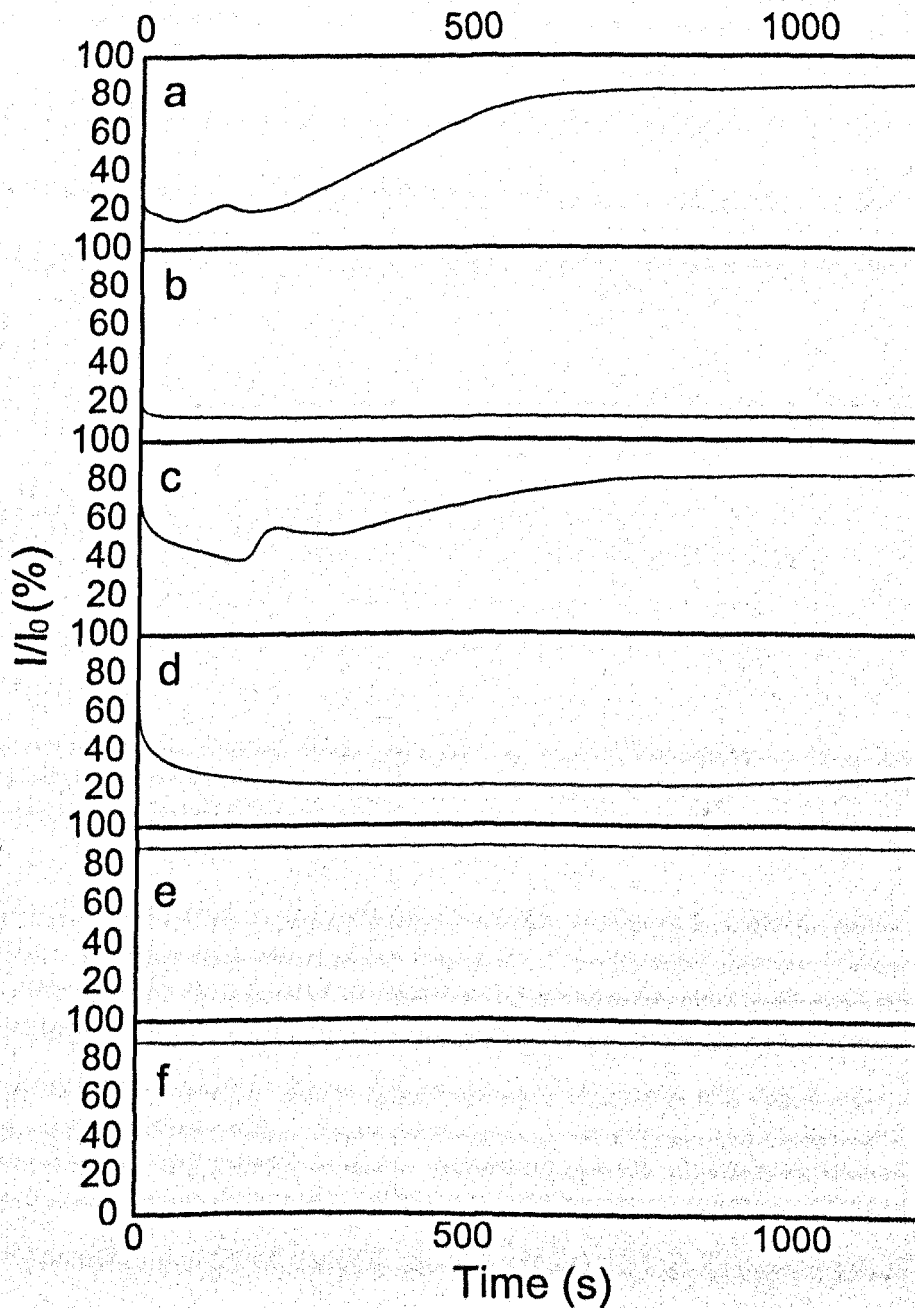


Figure 6.5: In situ spectrophotometry measurements of CO_2 equilibrated a, c, e and fresh b, d, f CaCO_3 solutions. $[\text{Ca}^{2+}]$ concentrations a, b, 10 mM, c, d 5 mM and e, f 2.5 mM.

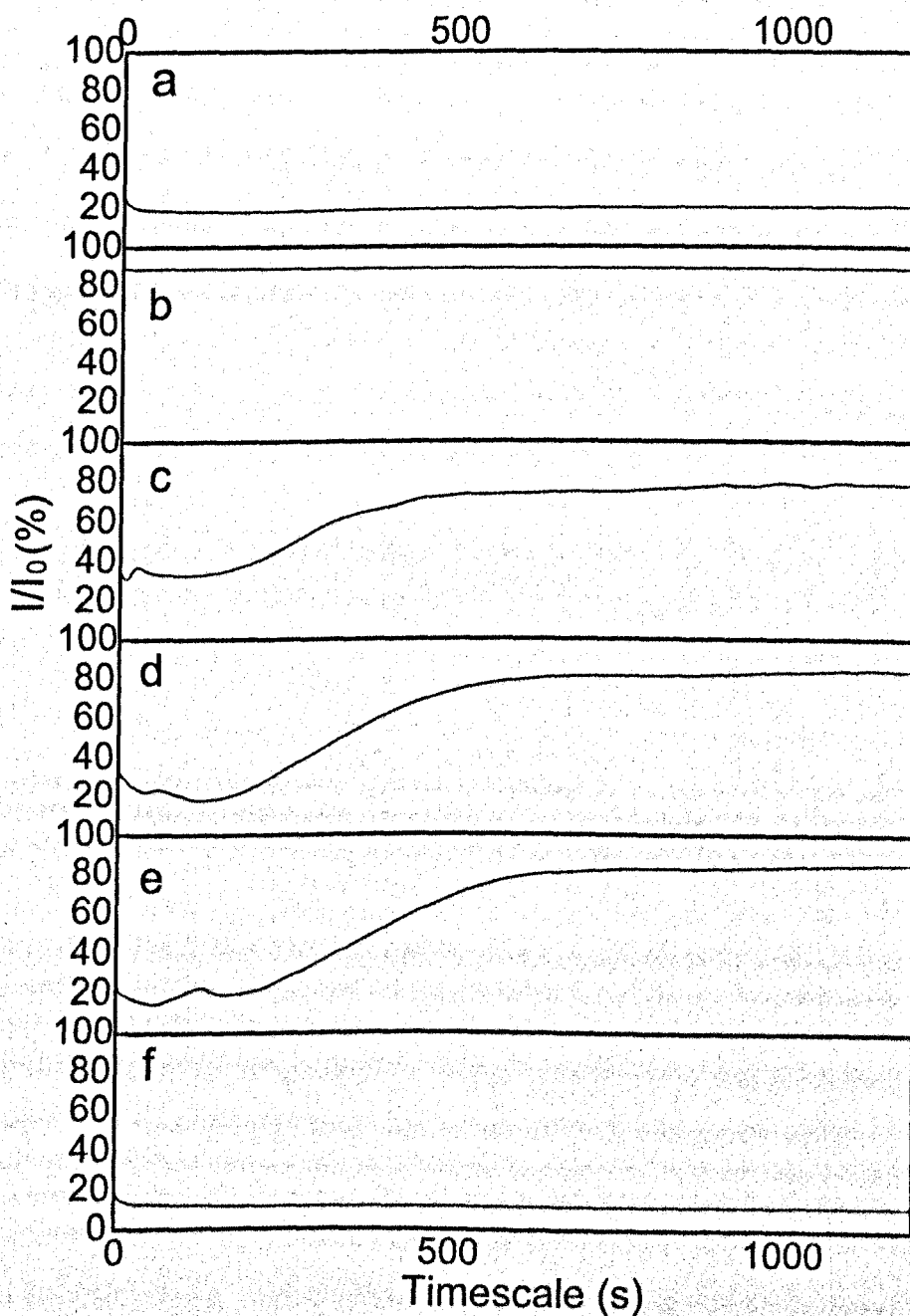


Figure 6.6: In situ spectrophotometry measurements for the precipitation of CaCO_3 from 10 mM aqueous solutions under different conditions. **a** High initial pH, **b** CO_2 bubbled through prior to mixing, **c** CO_2 equilibrated CaCl_2 solution only, **d** CO_2 equilibrated Na_2CO_3 solution only, both solutions CO_2 equilibrated and **f** both solutions fresh.

7.5 mM this period increased to 850 s and 1000 s respectively, whereas a Mg^{2+} ionic concentration of 10 mM yielded no recovery in I/I_0 over 1200 s. In addition, the intensity recovery rates and final intensity values were reduced with increased Mg^{2+} salt concentration (data not shown).

6.3.2 Electrode Measurements

In situ electrode measurements recorded the pH as a function of time for CaCO_3 solution concentrations of $[\text{Ca}^{2+}] = 2.5$ mM and $[\text{Ca}^{2+}] = 5$ mM (Figures 6.8). There was a sharp, instantaneous increase in pH upon the addition of Na_2CO_3 solution to the CaCl_2 solution (initial pH=6.9) rising to 10.4 and 10.8 for 2.5 mM and 5 mM concentrations respectively. In both cases the sharp rise proceeded a gradual relaxation towards pH values of approximately 10.2 after 1200 seconds, attributed to the fall in free Ca^{2+} and CO_3^{2-} ions during precipitation. Interestingly, the time scale of maximum pH appeared largely independent of concentration, appearing after approximately 145 and 135 s for 2.5 mM and 5 mM concentrations respectively. For a 5 mM CaCO_3 solution concentration there was an approximate correlation in time periods for the maximum pH and maximum turbidity. For a $[\text{Ca}^{2+}] = 2.5$ mM solution concentration, the maximum pH occurred more than 5 minutes before the maximum turbidity (although no significant fall in turbidity was recorded at this concentration).

6.3.3 Raman Spectroscopy Measurements

Raman spectra of precipitates collected from $[\text{Ca}^{2+}] = 2.5$ mM solutions were markedly different to those for $[\text{Ca}^{2+}] = 5$ and 10 mM solutions, with an order of magnitude decrease in the amount of material precipitated at the lower concentration. There was no evidence of ACC, with the Raman spectra of precipitates collected after all 4 growth times showing the four fundamental calcite peaks in the 100-1200 cm^{-1} range, at 160, 280, 711 and 1085 cm^{-1} respectively, in agreement with the literature values [214, 218](Figure 6.9b). There was a fourfold increase in the absolute maximum intensity of the 1085 cm^{-1} carbonate mode between 15

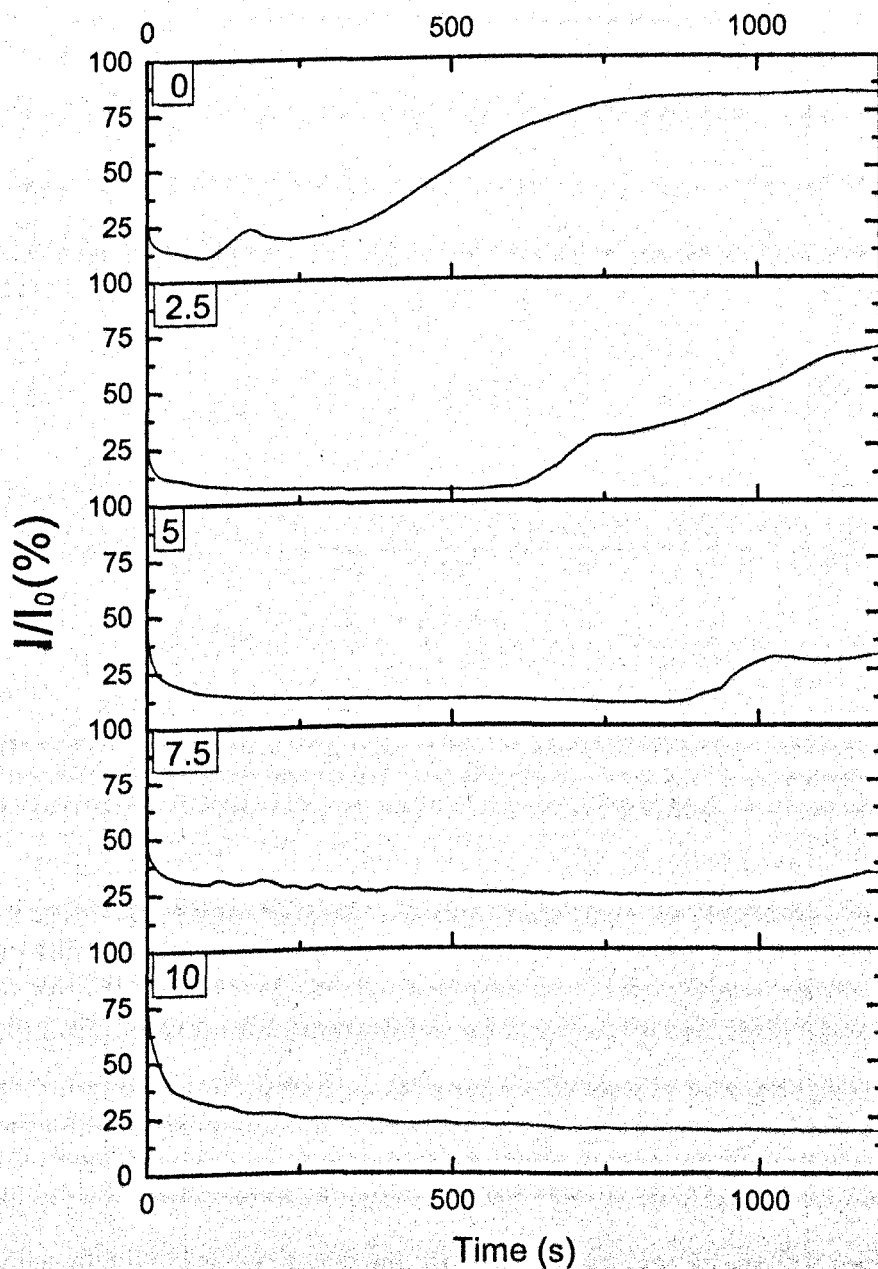


Figure 6.7: In situ spectrophotometry measurements for the precipitation of $CaCO_3$ from $[Ca^{2+}] = 10$ mM solutions, in presence of Mg^{2+} salts. The $[Mg^{2+}]$ concentrations are listed, in the range of $[Ca^{2+}] = 0-10$ mM

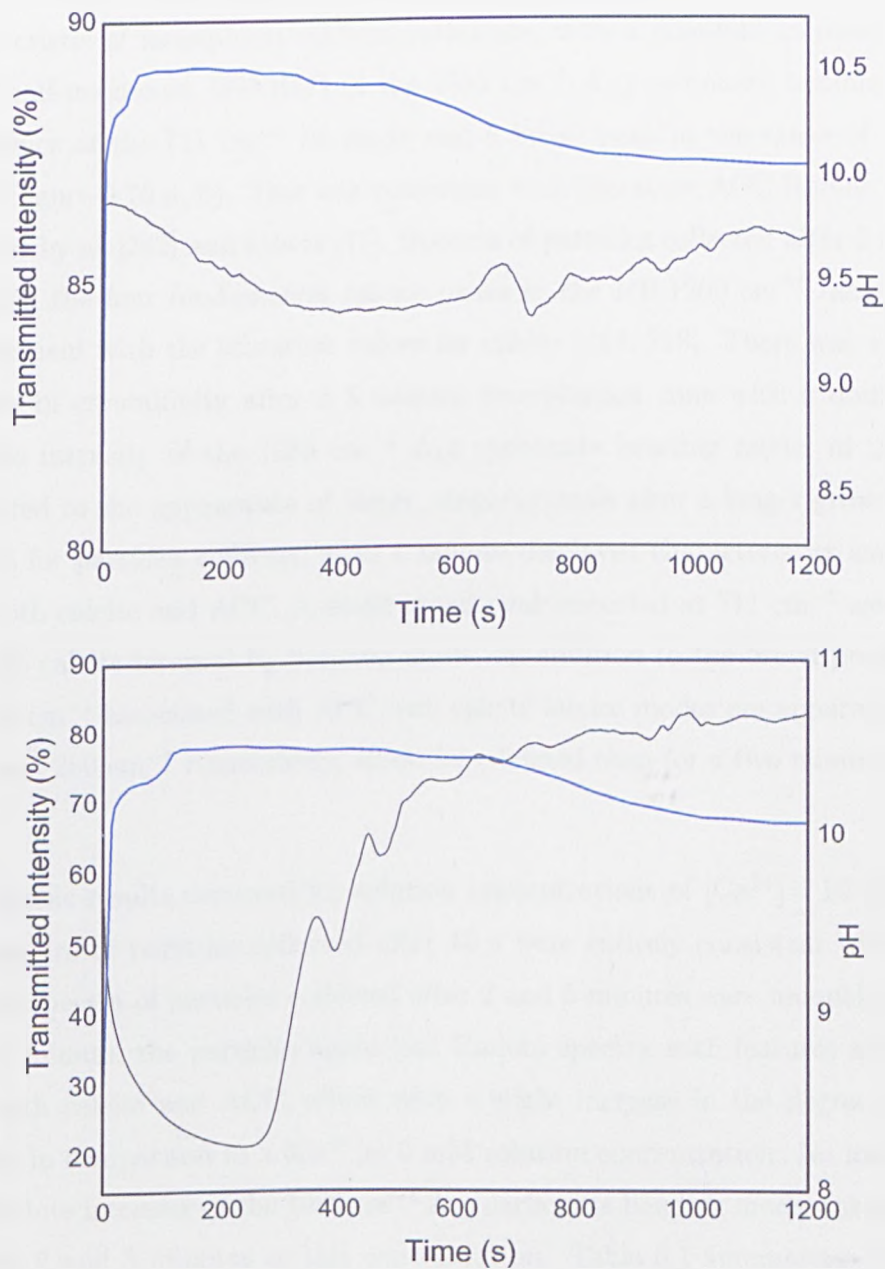


Figure 6.8: pH (right axis, blue line) and turbidity (left axis, black line) as a function of time, for CaCO_3 solution concentrations of 2.5 mM (top) and 5 mM (bottom).

s and 4 minutes, attributed to a stronger signal from a greater amount of precipitated material.

For a $[\text{Ca}^{2+}] = 5$ mM solution concentration, particles collected after 15 s were characteristic of amorphous calcium carbonate, with a nine-fold increase in full-width half-maximum (FWHM) of the 1085 cm^{-1} A_{1g} carbonate bending mode, an absence of the 711 cm^{-1} ν_4 mode and a broad peak in the range of $140\text{--}220\text{ cm}^{-1}$ (Figure 6.10 a, b). This was consistent with literature ACC Raman spectra reported by us [202] and others [27]. Spectra of particles collected after 2 minutes displayed the four fundamental calcite peaks in the $100\text{--}1200\text{ cm}^{-1}$ range, again in agreement with the literature values for calcite [214, 218]. There was a further increase in crystallinity after a 5 minute precipitation time with a doubling in absolute intensity of the 1085 cm^{-1} A_{1g} carbonate bending mode, in this case attributed to the appearance of larger, single crystals after a longer growth time. Spectra for particles collected after 1 minute displayed characteristics associated with both calcite and ACC. A small broad peak occurred at 711 cm^{-1} associated with the calcite internal E_g bending mode. In addition to the broad peak in the $140\text{--}220\text{ cm}^{-1}$ associated with ACC, two calcite lattice modes are apparent at 154 cm^{-1} and 280 cm^{-1} respectively, albeit less defined than for a two minute growth time.

Comparable results occurred for solution concentrations of $[\text{Ca}^{2+}] = 10$ mM. Raman spectra of particles collected after 15 s were entirely consistent with ACC, whereas spectra of particles collected after 2 and 5 minutes were uniquely calcite. After 1 minute, the particles again had Raman spectra with features associated with both calcite and ACC, albeit with a slight increase in the degree of crystallinity in comparison to a $[\text{Ca}^{2+}] = 5$ mM solution concentration. No increase in the absolute intensity of the 1085 cm^{-1} A_{1g} carbonate bending mode was observed between 2 and 5 minutes at this concentration. Table 6.1 summarises both the absolute intensities and relative broadness of the 1085 cm^{-1} carbonate modes for the three solution concentrations after 15 s, 1 and 2 minutes.

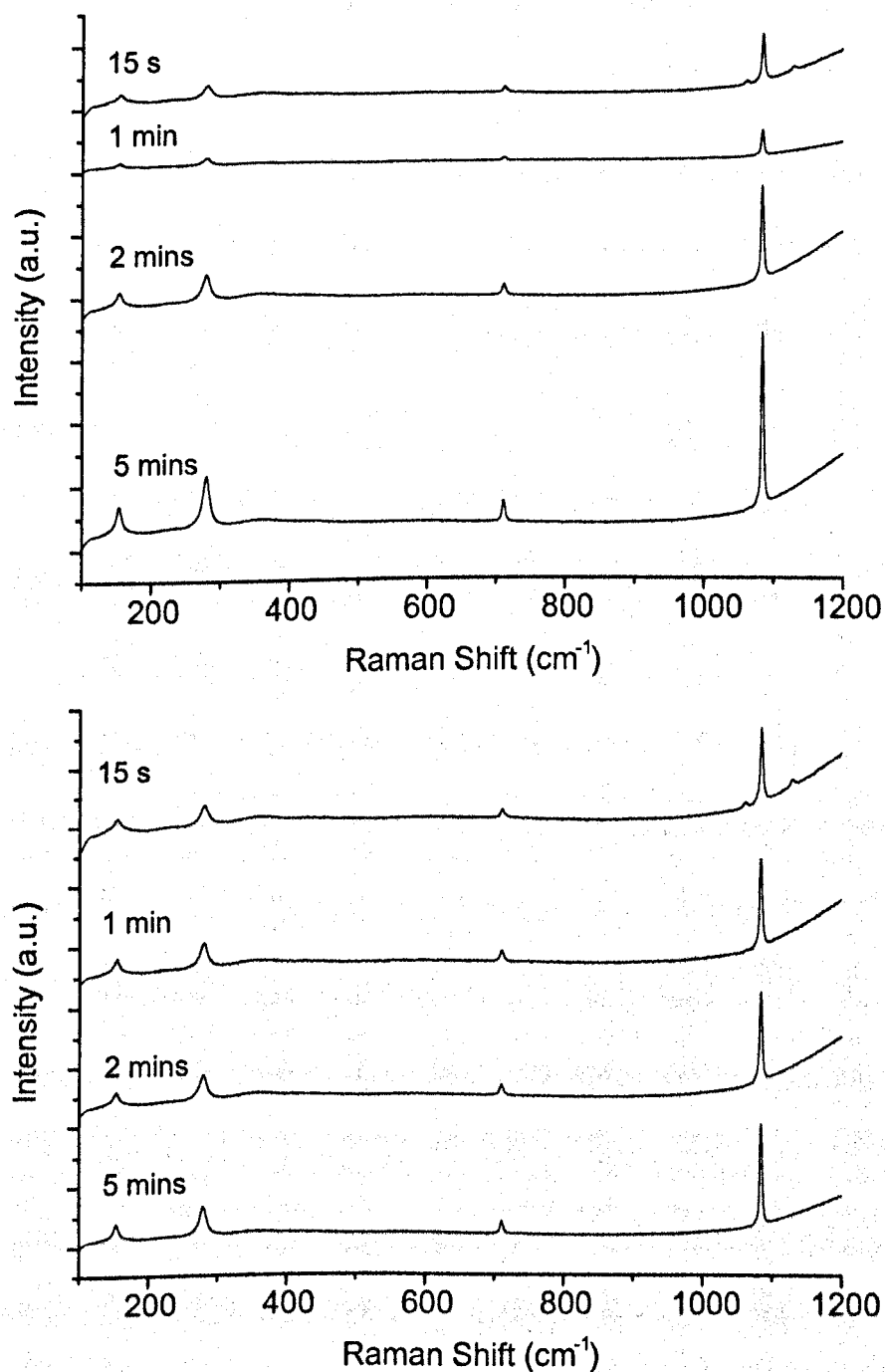


Figure 6.9: Raman spectra of CaCO_3 precipitates as a function of growth time, 2.5 mM CaCO_3 solution concentration. **Top** Absolute intensity scale, **Bottom** relative intensity scale. Baselines are displaced for different spectra.

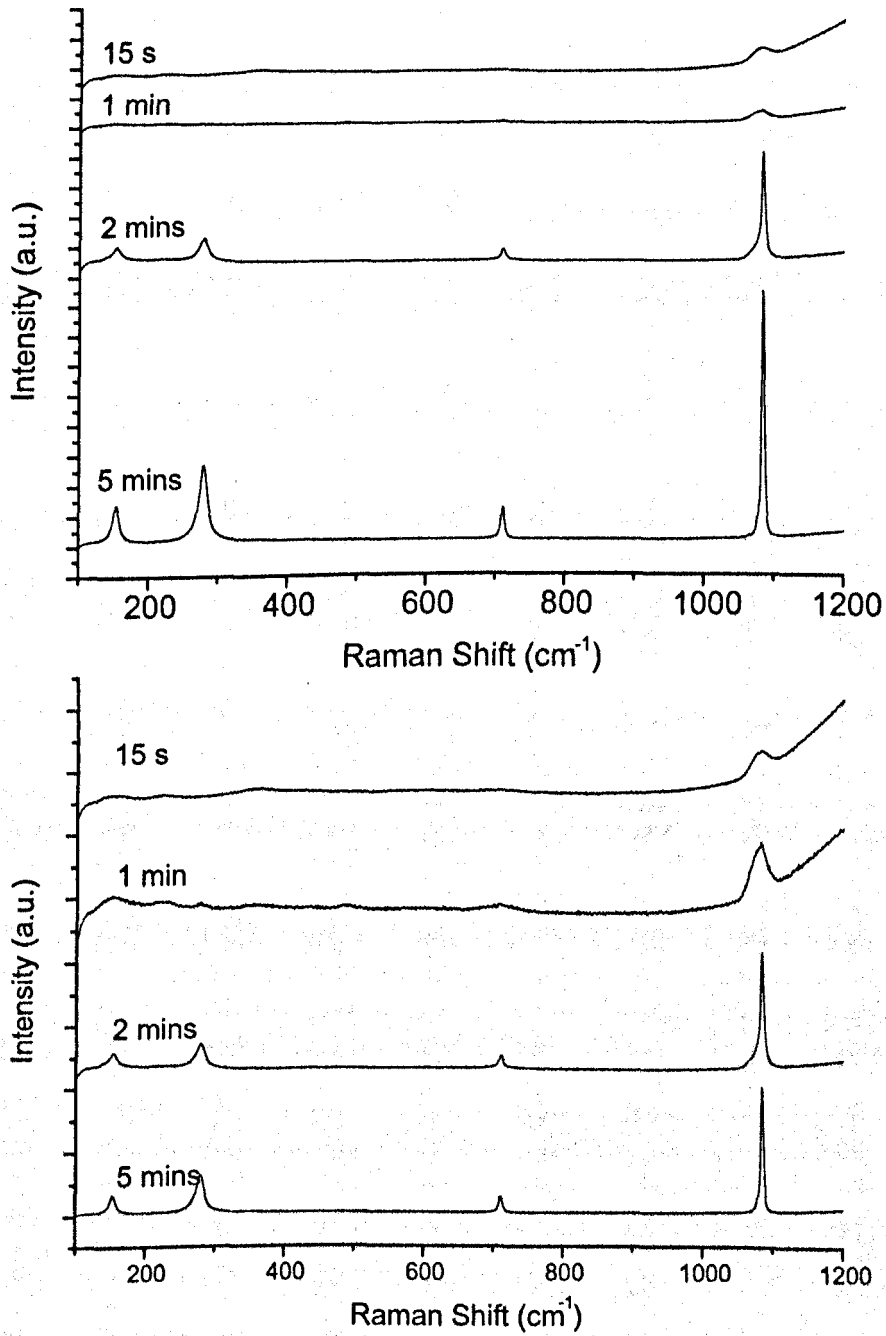


Figure 6.10: Raman spectra of CaCO_3 precipitates as a function of growth time, 5 mM CaCO_3 solution concentration. **Top** Absolute intensity scale, **Bottom** relative intensity scale. Baselines are displaced for different spectra.

Concentration (mM)	15 s	1 min	2 min	5 min
2.5	80/6	50/5	160/8	300/6
5	20/40	20/45	190/8	440/6
10	25/45	45/20	330/8	350/8

Table 6.1: The intensity (left of forward slash, arbitrary units) and full-width, half-max (FWHM) (right of forward slash, cm^{-1}) of the 1085 cm^{-1} carbonate mode as a function of growth time, for initial concentrations of $[\text{Ca}^{2+}] = 2.5, 5$ and 10 mM .

6.3.4 EM analysis

An SEM overview of CaCO_3 particle concentration and polymorphism as a function of growth time and solution concentration is shown in figure 6.12. For a $[\text{Ca}^{2+}] = 2.5 \text{ mM}$ CaCO_3 solution concentration there were no large aggregates or calcite crystals after 15 s, a small number of calcite crystals after 1 minute (~ 2 per grid area) and an intermediate number (7 ± 2 per grid area) of calcite crystals after 5 minutes. Higher magnification SEM images revealed an abundance of sub-micron particles over the range of growth periods at this concentration with an average diameter of $40 \pm 20 \text{ nm}$. There was an absence of sub-micron precipitates in the regions immediately adjacent to the calcite crystals (Figure 6.13), indicative of the localised depletion zones described by Aizenberg *et al.* [135]

For a $[\text{Ca}^{2+}] = 5 \text{ mM}$ CaCO_3 solution concentration there was a significant increase in the amount of material precipitated for all time periods, as is shown in figure 6.12. Here, large particle aggregations were observed after 15 s growth periods (Figure 6.14a). These particles were apparently spherical with a maximum diameter of approximately 100 nm, consistent with previous images of ACC [243]. Similar results were obtained for a 1 minute growth period at this concentration, again with aggregations of spherical particles. In this case however, no calcite rhombohedra were observed and both the number and size of sub-micron particles were significantly higher. After 5 minutes there was a large number (14 ± 5 per grid area) of calcite crystals, with approximate dimensions greater than $2 \mu\text{m}$. In addition, there were smaller sub-micron particles, albeit with an order of magnitude reduction in number density.

TEM was used for high magnification morphological analysis with particle crystallinity determined using electron diffraction. Figure 6.16 shows CaCO_3 precipitates from a $[\text{Ca}^{2+}] = 5 \text{ mM}$ solution after a 1 minute growth period. The diffraction pattern is characteristic of an amorphous material, with no apparent crystalline features. Figure 6.17 shows the respective diffraction patterns after a 1 minute growth period ($[\text{Ca}^{2+}] = 5 \text{ mM}$) to that of synthetic calcite nanoparticles, which show clear crystalline features.

For a $[\text{Ca}^{2+}] = 5 \text{ mM}$ solution concentration, the size of the particles was also dependent upon the growth period. After 15 s the particles were all amorphous with diameters ranging over 8-116 nm (Figure 6.15). Analysis of 44 particles found a mean particle diameter of $(64 \pm 7) \text{ nm}$, with particle aggregation in $\sim 25\%$ of cases. Approximately 15% of the particles had a diameter greater than 100 nm. Interestingly, the mean particle size was significantly lower after a 1 minute growth period, with analysis of 272 particles yielding a mean diameter of $(26 \pm 2) \text{ nm}$ (Figure 6.21). There was a small number of larger particles, with diameters of the order of $80 \mu\text{m}$ (clearly shown in figure 6.18). Less than 1% of the particles were greater than 100 nm in diameter, a considerable decrease in comparison to the 15 s growth period. It should be noted that no calcite crystals were observed after this growth period

After a 5 minute growth period at a $[\text{Ca}^{2+}] = 5 \text{ mM}$ initial solution concentration, measurements of 238 particles found a mean diameter of $(64 \pm 6) \text{ nm}$, comparable to a 15 s growth period (Figure 6.18). The distribution in particle sizes is shown in figure 6.22 in the range of 0-200 nm, with an average particle diameter of $(64 \pm 6) \text{ nm}$ comparable to a 15 s growth period. Here, however, there was a narrower distribution of particle diameters. In addition, there was a number of larger particles with diameters up to 500 nm, although these accounted for less than 5% of the total number of particles. There was a large degree of aggregation, with approximately 90% of the particles over 100 nm in diameter appearing as part of an aggregation. The most significant difference at a 5 minute growth period was the presence of calcite crystals with dimensions greater than $1 \mu\text{m}$. The large size of these crystals flooded the field of view of the TEM preventing morphological analysis and electron diffraction analysis. The crystals were apparently calcite, judging by the clear rhombohedron shape. Although the calcite particles were far fewer in number than the sub-micron spherical particles (14 ± 2 per $100 \times 100 \mu\text{m}$ grid area), they accounted for the majority of the CaCO_3 precipitate by volume. By estimating that the volume of the calcite crystals is of the order of $100 \mu\text{m}^3$, and that the volume of the amorphous particles is of the the order of $0.00025 \mu\text{m}^3$, each calcite crystal contains over 3×10^5 amorphous particles! Since the amorphous particle concentration is of the order of 100 per μm^2 on the TEM grid, approximately 20% of the total material remains as ACC.

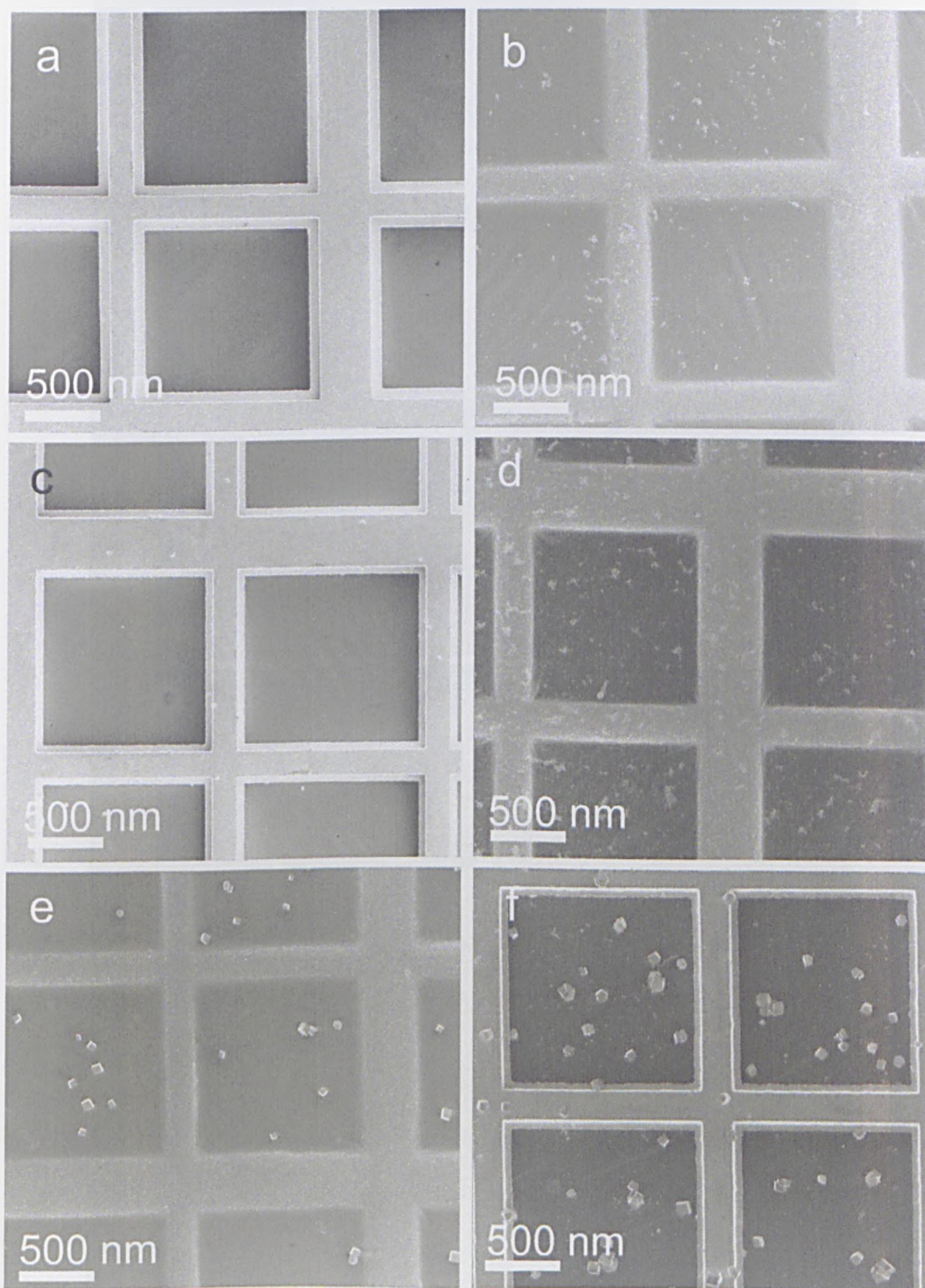


Figure 6.12: SEM overview of CaCO₃ precipitates on Formvar TEM grids as a function of growth time and solution concentration a 2.5 mM, 15 s b 5 mM, 15 s, c 2.5 mM, 1 min, d 5 mM, 1 min e 2.5 mM, 5 mins, f 5 mM, 5 mins.

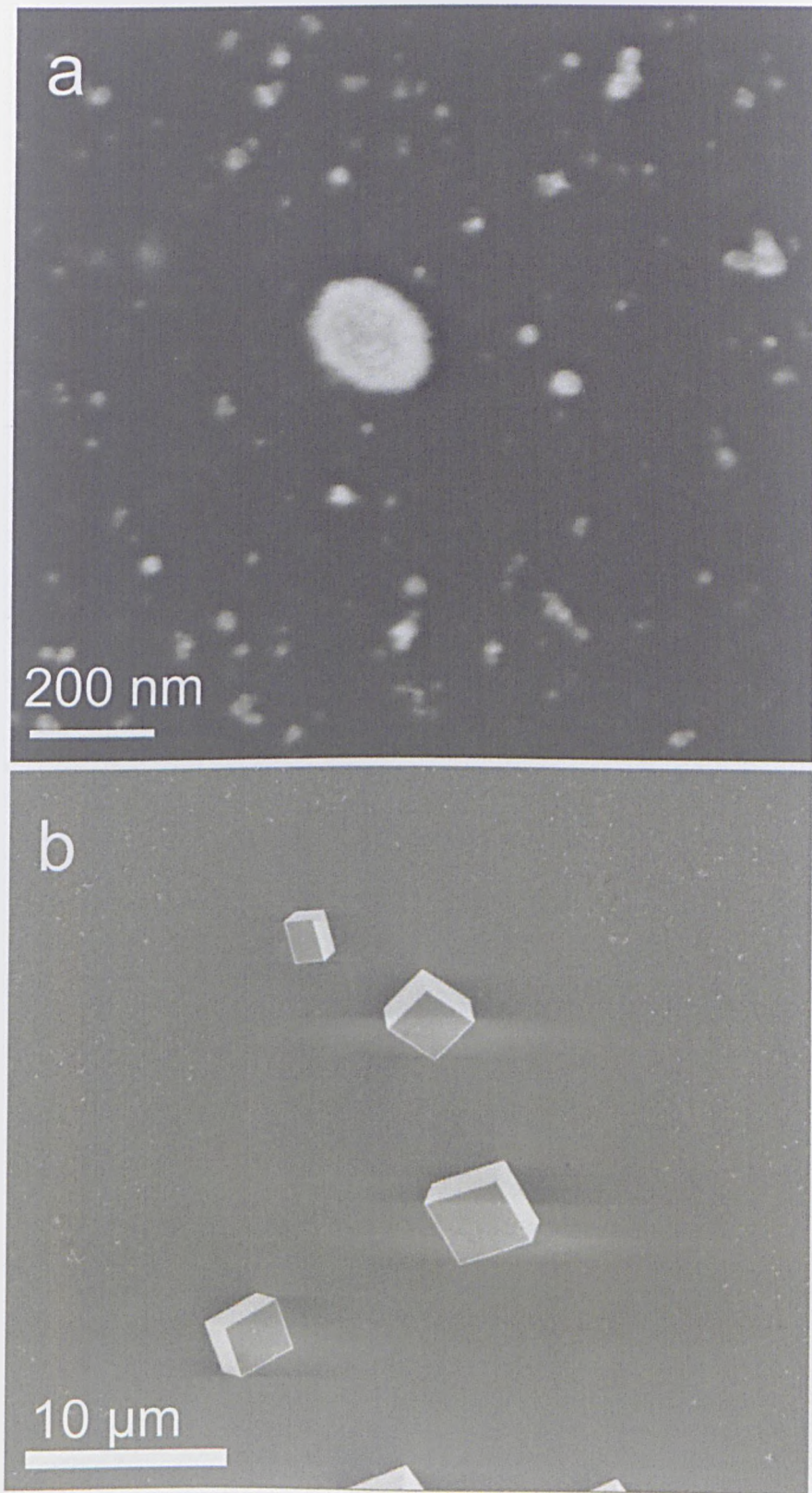


Figure 6.13: High resolution SEM images of CaCO_3 precipitates on Formvar TEM grids, 2.5 mM concentration. **a** 15 s growth period, **b** 5 minutes growth period. The depletion region surrounding the calcite crystals can clearly be seen.

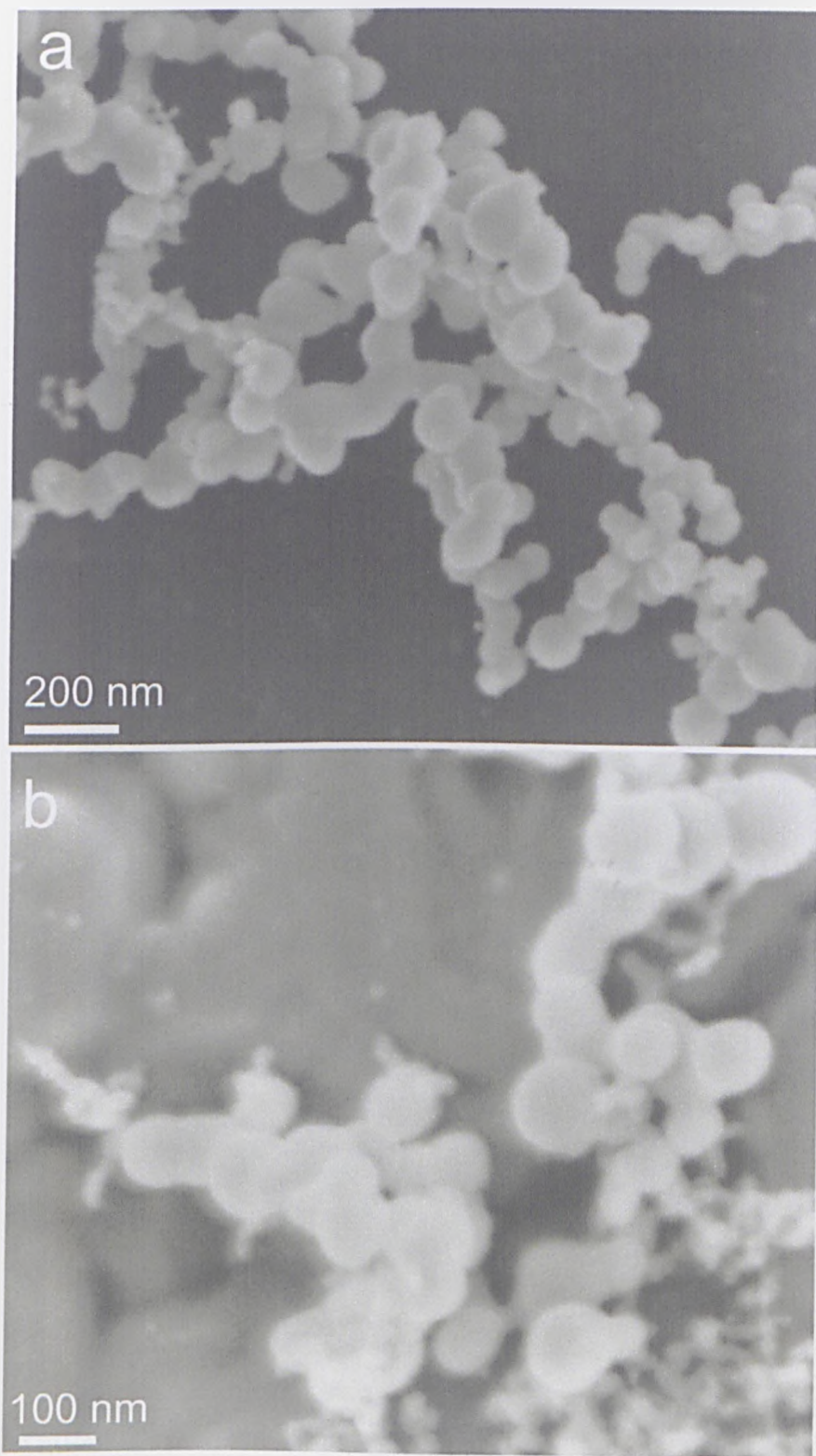


Figure 6.14: High resolution SEM images of CaCO_3 precipitates on Formvar TEM grids, 5 mM solution concentration. **a** 15 s and **b** 1 min growth periods, showing aggregation of sub-micron particles.

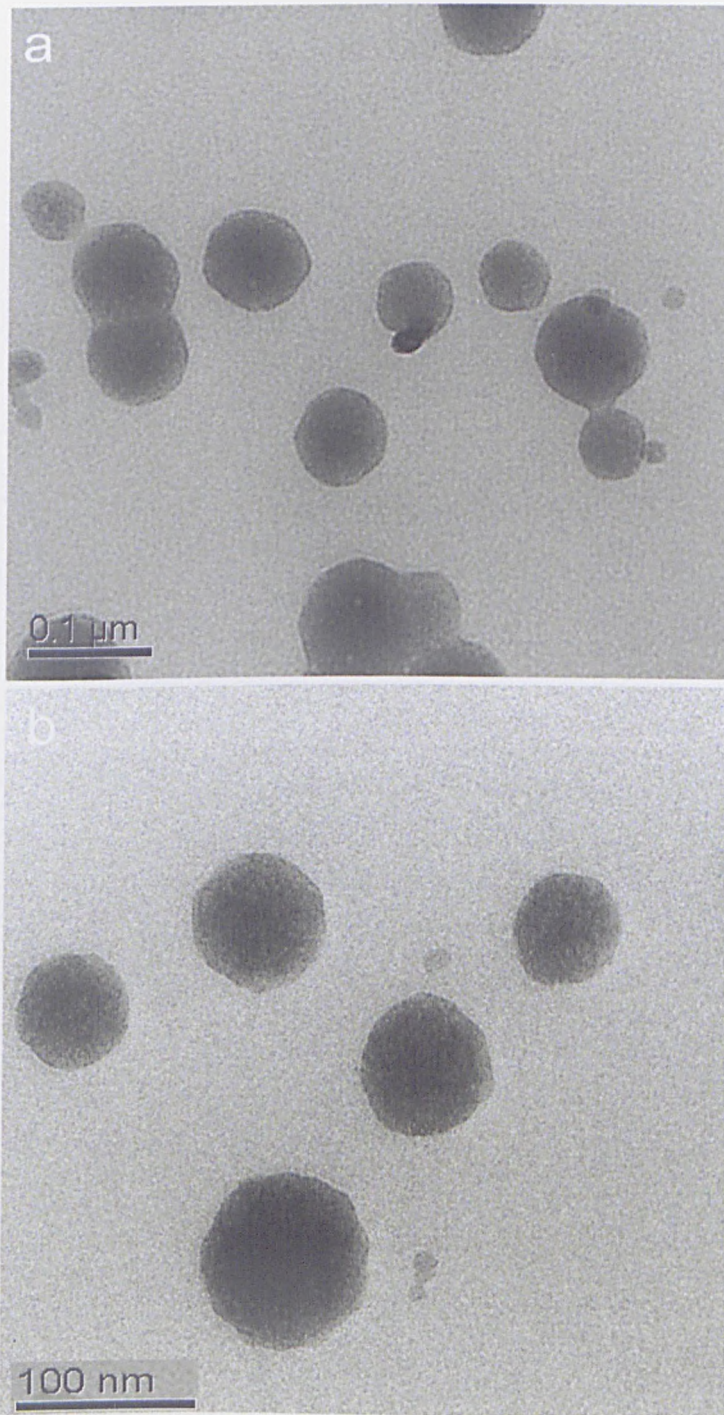


Figure 6.15: TEM micrographs of CaCO₃ precipitates on a Formvar TEM grid, for a 15 s growth period and a 5 mM solution concentration. **a** Aggregates of 2 or more particles tended to form, even after short growth periods. **b** A region of single CaCO₃ particles, showing a uniform distribution of 50-80 nm particles, consistent with ACC.

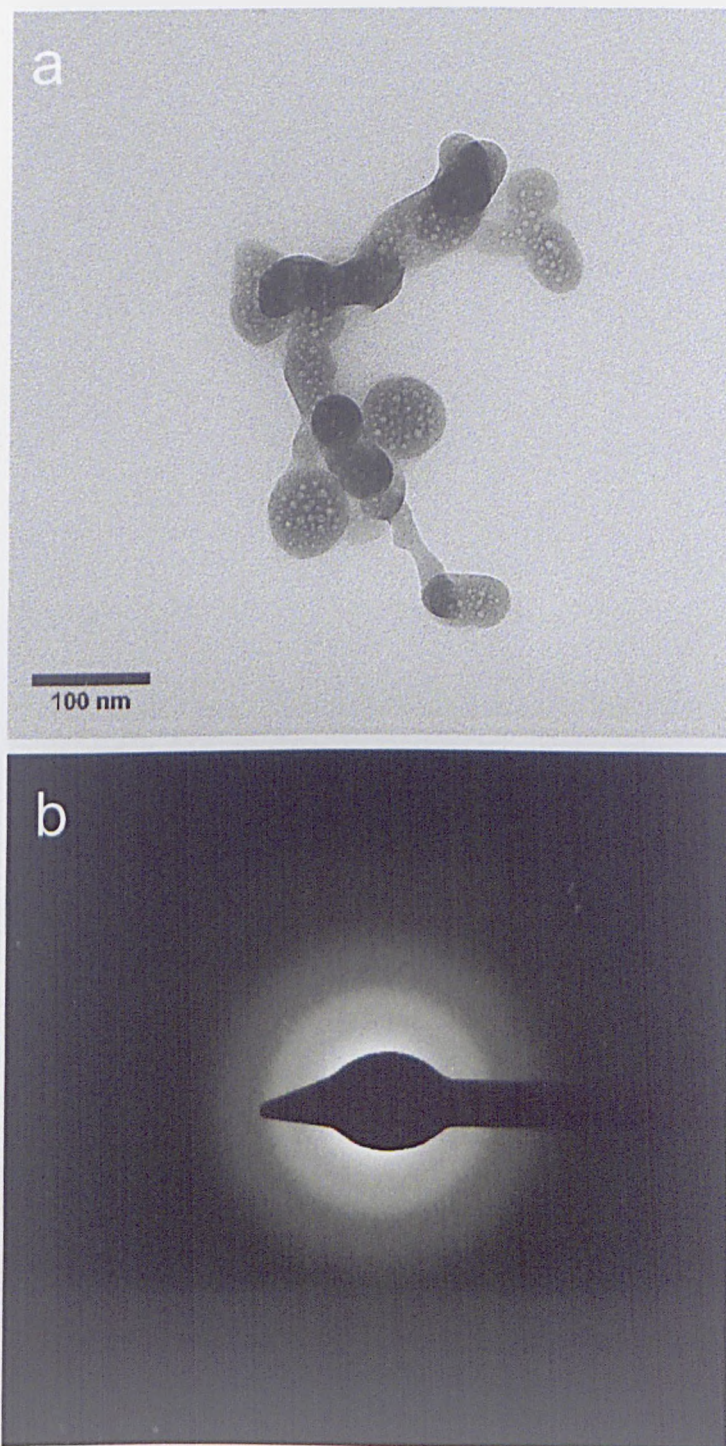


Figure 6.16: **a** TEM image for CaCO_3 precipitates on a Formvar TEM grid, for a 1 minute growth period at a $[\text{Ca}^{2+}] = 5 \text{ mM}$ concentration, showing an aggregation of 20-60 nm diameter particles. **b** Electron diffraction pattern of such particles, showing broad rings characteristic of amorphous calcium carbonate.

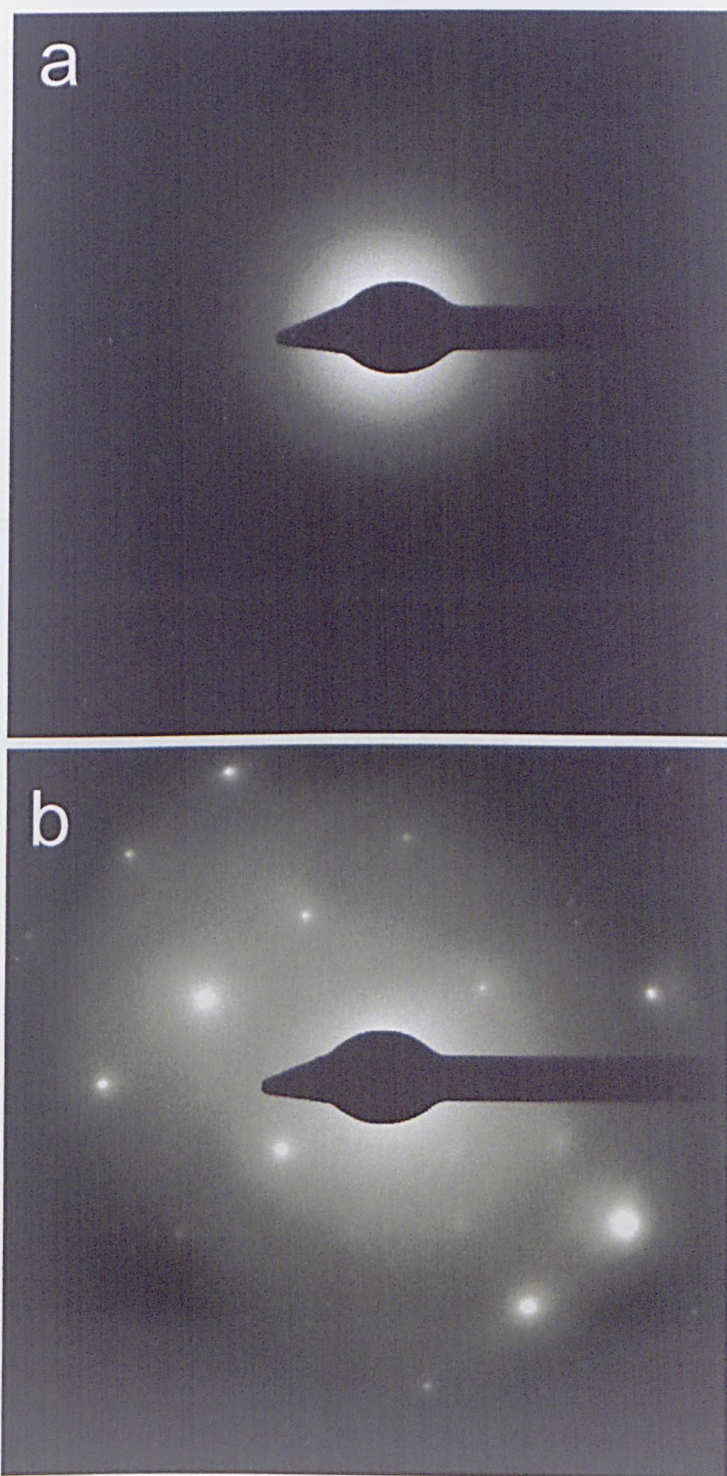


Figure 6.17: **a** TEM diffraction patterns for CaCO_3 precipitates on a Formvar TEM grid, for a 1 minute growth period at a $[\text{Ca}^{2+}] = 5 \text{ mM}$ concentration, showing broad rings characteristic of amorphous calcium carbonate. **b** Comparative diffraction pattern from a $100 \times 100 \text{ nm}$ calcite particle.

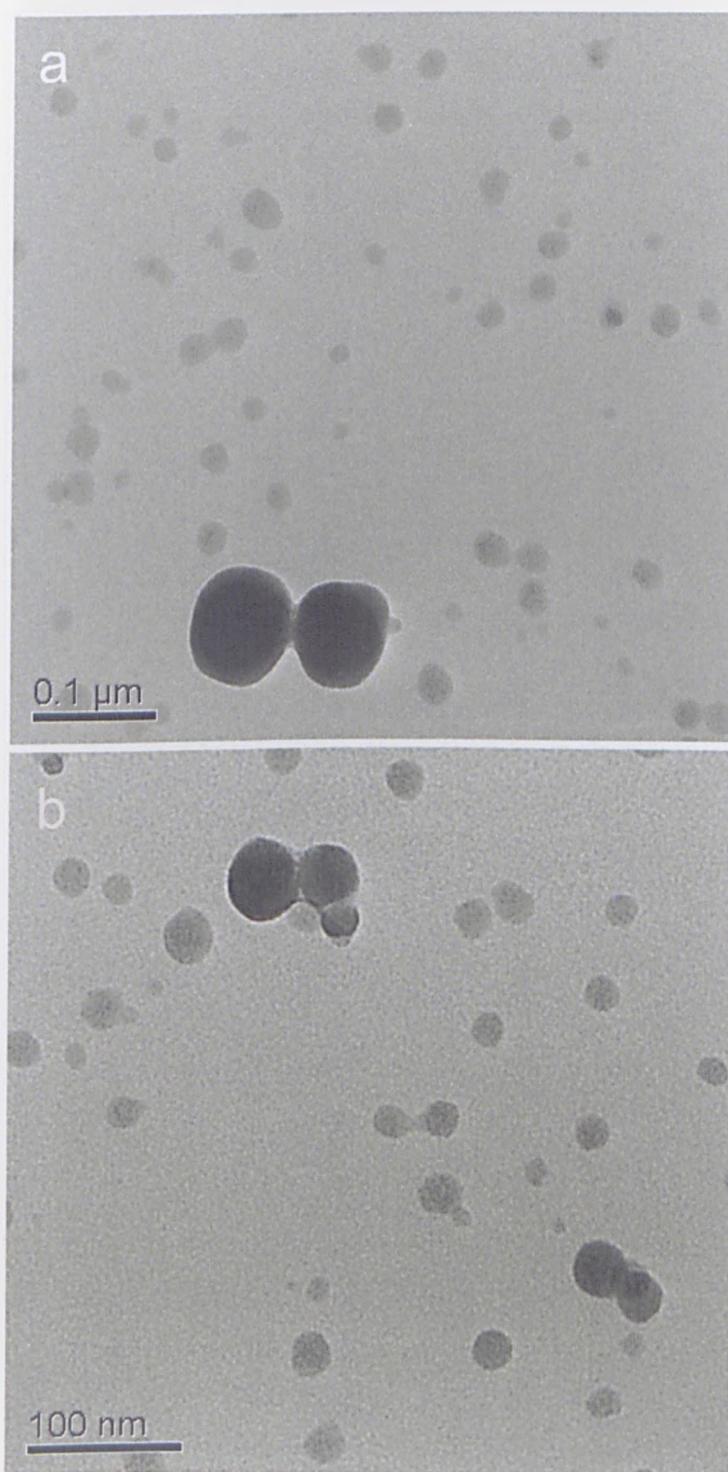


Figure 6.18: a, b: TEM micrographs of CaCO_3 precipitates on a Formvar TEM grid, for a 1 minute growth period at $[\text{Ca}^{2+}] = 5 \text{ mM}$ concentration.

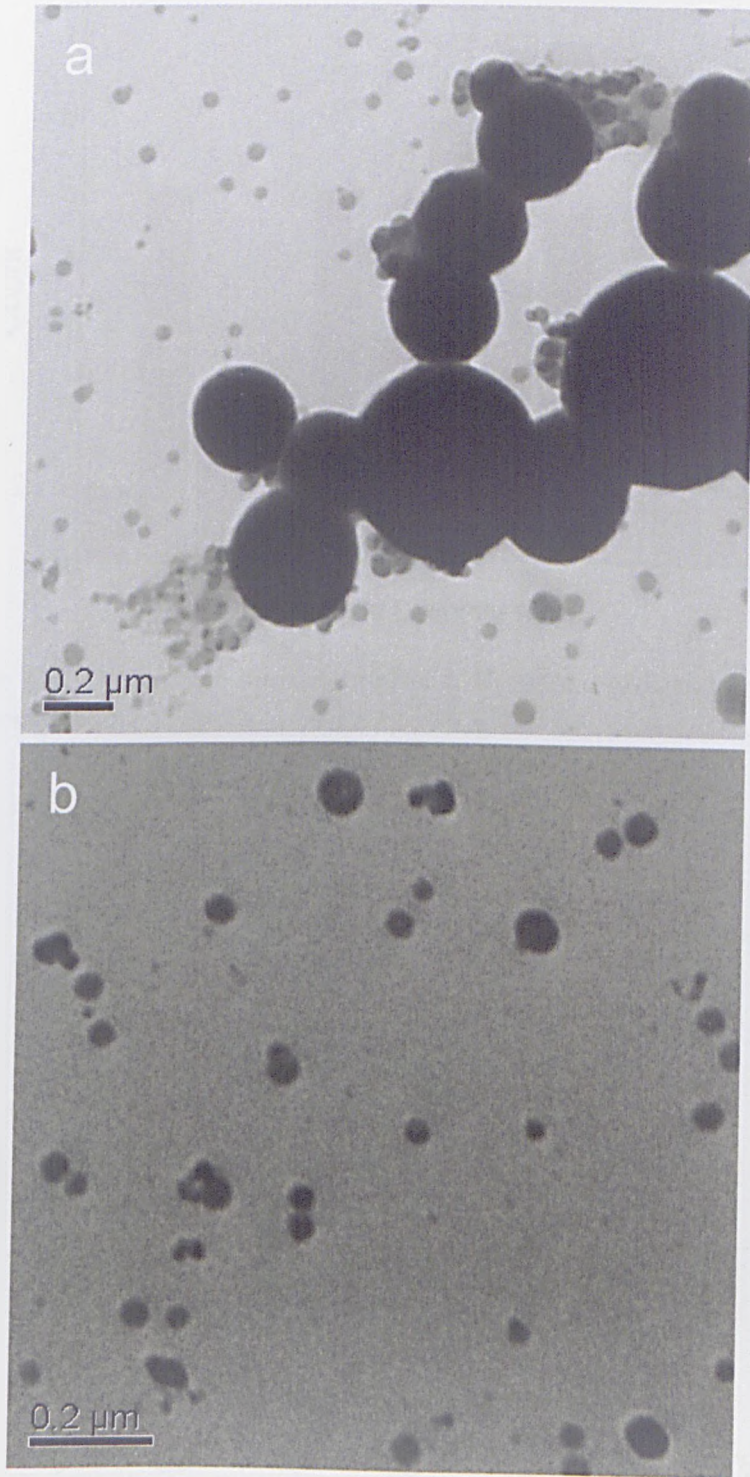


Figure 6.19: a, b: TEM micrographs of CaCO_3 precipitates on a Formvar TEM grid, for a 5 minute growth period at a $[\text{Ca}^{2+}] = 5 \text{ mM}$ solution concentration. Two domains of particle size can be seen.

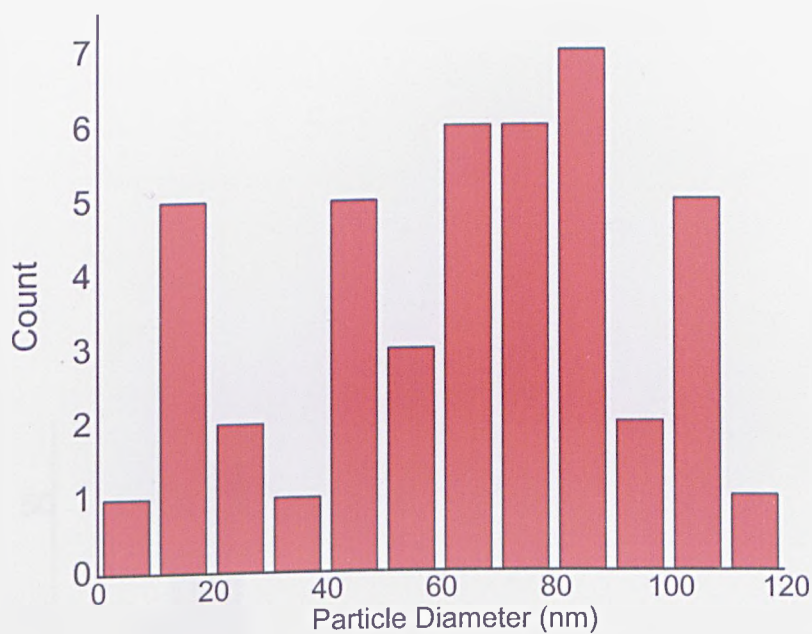


Figure 6.20: CaCO₃ particle diameters after a 15 second growth period, [Ca²⁺]= 5 mM concentration.

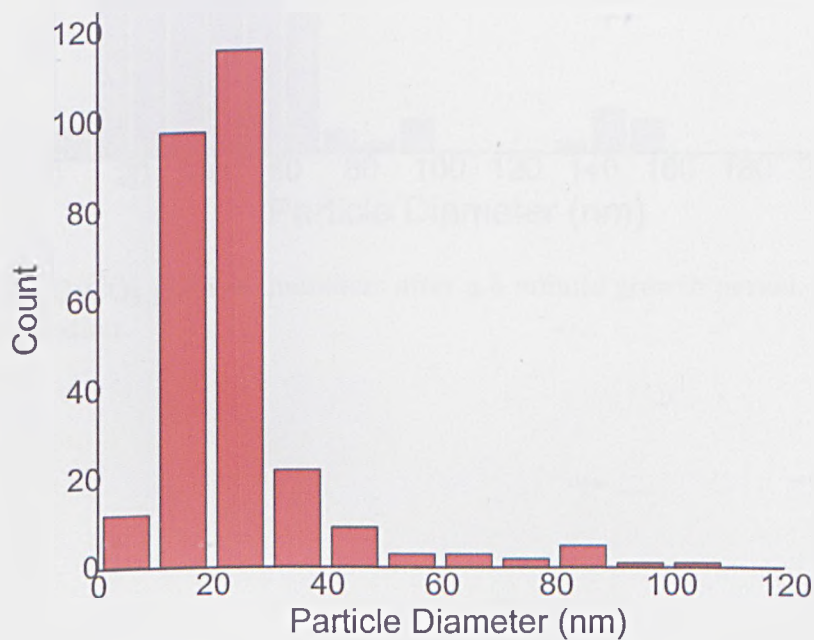


Figure 6.21: CaCO₃ particle diameters after a 1 minute growth period, [Ca²⁺]= 5 mM concentration.

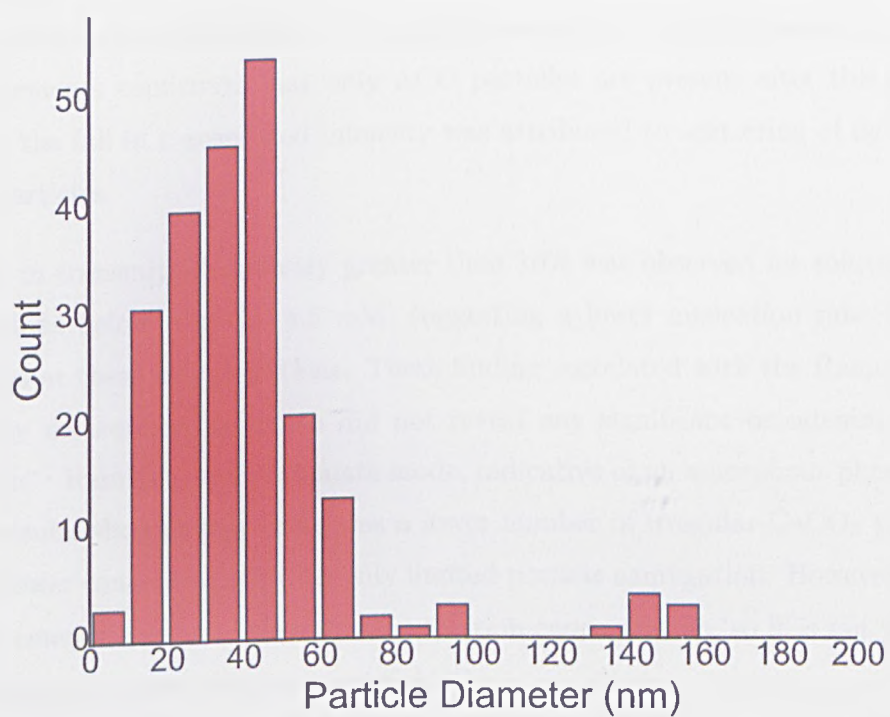


Figure 6.22: CaCO₃ particle diameters after a 5 minute growth period, [Ca²⁺]= 5 mM concentration.

6.4 Discussion

The results in this chapter present firm evidence for the formation of a transient amorphous precursor phase during the precipitation of CaCO_3 from bulk supersaturated solution. Since the particle dimensions and relative crystallinity could be determined *ex situ* for known growth periods, it was possible to relate the transmitted light intensity of the *in situ* spectrophotometry measurements to the particle composition. For solution concentrations of $[\text{Ca}^{2+}] = 5$ mM and above, there was an instantaneous fall in transmitted light intensity, with the ratio I/I_0 falling to less than 30% after a 15 s growth period. Since both Raman and TEM measurements confirmed that only ACC particles are present after this growth period, the fall in transmitted intensity was attributed to scattering of light from ACC particles.

No fall in transmitted intensity greater than 10% was observed for solution concentrations below $[\text{Ca}^{2+}] = 4.5$ mM, suggesting a lower nucleation rate of ACC particles at these concentrations. These findings correlated with the Raman spectroscopy measurements, which did not reveal any significant broadening of the 1085 cm^{-1} Raman active carbonate mode, indicative of an amorphous phase. The SEM results showed that there was a lower number of irregular CaCO_3 particles at the lower concentration, with only limited particle aggregation. However, TEM measurements were not taken for this solution concentration, so it is not possible to conclusively prove the presence of ACC.

These findings were in broad agreement with a recent small angle X-ray study of the nucleation and growth of CaCO_3 by Bolze *et al.*, who reported a large increase in ACC nucleation rate with increased degree of supersaturation [244]. This is also in agreement with theoretical models predicting a sharp increase in the nucleation rate with initial degree of supersaturation. In addition to a greater ACC nucleation rate at higher supersaturations, Bolze *et al.* also reported the aggregation of ACC particles to be dependent on the initial solution concentration. At a solution concentration of $[\text{Ca}^{2+}] = 4.5$ mM (described in terms of initial reactant concentration = 9 mM) there was minimal particle aggregation, whereas at 10 mM (= 20 mM initial reactant concentration), there was a high degree of particle aggregation, resulting in a short lifetime of the amorphous precursor phase.

The results presented here support those findings, since there was a large degree of particle aggregation and a more poly-dispersed size distribution at the higher concentration $[\text{Ca}^{2+}] = 5 \text{ mM}$ in comparison to the lower concentration, $[\text{Ca}^{2+}] = 2.5 \text{ mM}$, where very little aggregation was observed.

The transmitted intensity recovery period showed an apparent dependence with concentration (Figure 6.4). Since the ACC particle nucleation rate increases with solution concentration, it follows that there will be a greater frequency of collision of the particles. It has also been proposed that there is a decrease in the repulsive forces between particles in solution at lower reactant concentrations due to the screening of the particle surface charge by the surrounding electrolyte [245]. The free-energy gain upon transformation from ACC into calcite will increase with ACC particle size and aggregation. This would explain an increase in the increased recovery in transmitted intensity for a $[\text{Ca}^{2+}] = 10 \text{ mM}$ initial concentration in comparison to a $[\text{Ca}^{2+}] = 4.5$ solution.

The ex situ Raman measurements suggested an increased degree of crystallinity after a 1 minute growth period. However, no calcite particles were observed using TEM or SEM after this time period. In contrast, a large number of calcite particles were apparent at a solution concentration of $[\text{Ca}^{2+}] = 2.5 \text{ mM}$, indicative of the conversion from ACC into calcite. The SEM overview after a 1 minute growth period showed well-formed calcite particles with dimensions in excess of $1 \mu\text{m}$, whereas at 5 mM there was an aggregation of sub-micron amorphous type particles.

After a 5 minute growth period, an increase in transmitted intensity was observed for all initial solution concentrations greater than $[\text{Ca}^{2+}] = 4.5 \text{ mM}$. These findings correlate with the ex situ measurements, which suggested a significant conversion into calcite. The Raman spectra for all concentrations were indistinguishable from reference calcite after a 5 minute growth period, although the TEM measurements after 5 minutes suggested there was still a high number density of amorphous-type particles. It should be noted however that the Raman signal for calcite is at least one order of magnitude stronger than for the amorphous phase. The ACC particles in solution must therefore account for the fact that the transmitted intensity was lower after 5 minutes than after a 15 minute growth period for all concentrations higher than $[\text{Ca}^{2+}] = 4.0 \text{ mM}$.

Ballauff *et al.* reported a density of 1.49 g/cm^3 for ACC [245], where as Colfen and Volkel reported a density in the range of $1.1\text{-}1.7 \text{ g/cm}^3$ for ACC particles with diameters in the range of 2-8 nm, smaller than those observed here [246]. This is almost 50% lower than the calcite density of 2.7 g/cm^3 . The dimensions of the calcite particles were shown using SEM to be at least one order of magnitude larger than the ACC particles, measured after 5 minutes using TEM. Assuming the calcite particle to be spherical, and estimating the density of calcite to be twice that of ACC, and the radius to be 10 times greater, it follows from equation 6.4 that the calcite particle will settle at a rate 200 times faster than ACC particles. It therefore follows that the recovery in transmitted intensity is due to a conversion from ACC into calcite, with sedimentation of the larger calcite particles resulting in fewer scattering centres in solution.

The presence of transient ACC in bulk solution is an agreement with the findings of chapters 3 and 4, proving that ACC acts as a precursor phase during the face-selective or epitaxial growth of calcite on substrates. On both mica and SAM substrates, the solution concentration did not appear to exert any significant influence on the formation of ACC particles. However, in bulk solution there was a significant reduction in the formation of larger ACC particles below $[\text{Ca}^{2+}] = 4.5 \text{ mM}$. It follows from equation 1.24 that the substrate will act to lower the nucleation barriers, whereas there will be a higher activation barrier during the homogeneous nucleation of ACC in bulk solution. This effect is likely to be increased at both weathered mica and MHA SAM surfaces, since these both promote the growth of calcite, allowing the formation of ACC particles at concentrations not observed in bulk solution.

6.5 Conclusions

CaCO_3 particles were characterised ex-situ using three techniques: Raman microscopy, SEM and TEM for different growth periods and solution concentrations. The formation rate and stability of ACC was shown to be dependent on the initial solution concentration in the range of $[\text{Ca}^{2+}] = 2\text{-}10 \text{ mM}$, with an increased rate of ACC formation at initial solution concentrations of $[\text{Ca}^{2+}] = 5 \text{ mM}$ and higher.

These findings suggest that ACC acts as a precursor to thermodynamically stable CaCO_3 polymorphs in bulk solution, since the amount of ACC material decreased as a function of time.

Chapter 7

Crystallisation in Arrays of Picolitre Droplets

Surfaces patterned with regular arrays of circular, hydrophilic regions on a hydrophobic background were used to trap droplets of aqueous CaCO_3 solutions to investigate nucleation and growth within small volumes. Fluoroalkyl thiols were adsorbed on gold-coated mica surfaces and exposed to short-wavelength ($\lambda = 254$ nm) UV light through a quartz photo-mask with regularly spaced, circular holes (radius 2-10 μm). The photo-oxidised fluoroalkylthiols were subsequently replaced by backfilling with carboxylic-acid terminated alkylthiols, thus forming an array of approximately 20,000 circular hydrophilic regions on a hydrophobic background. By passing macroscopic volumes of solution across the surfaces, approximately hemispherical droplets were trapped on the circular hydrophilic regions, and these were stable for long periods when the ambient humidity was kept very close to 100%. Since each droplet could be considered independently, a statistical analysis of the precipitates within each droplet was used to relate the crystal form to the both the droplet volume and growth period. After a 24 hour growth period, face-selective calcite particles were observed, almost uniquely in a tetrahedral configuration. Amorphous calcium carbonate was observed for shorter growth periods, transforming into calcite after several minutes, analogous to growth in bulk solution.

7.1 Introduction

Various substances have been crystallised within restricted volume droplets. Chayen *et al.* [247] crystallised proteins (carboxypeptidase) from 1-2 μl droplets under oil, to eliminate the problem of evaporation. From an industrial perspective, several advantages for protein crystallisation using this method were reported; a reduced protein consumption, an increase in crystal stability and a greater ease of theoretical predictions, since the volume and composition of the droplet can be precisely determined. The crystallisation of the protein lysosome in levitated droplets of aqueous solutions has been reported by several groups, determining the induction time as a function of droplet volume [248, 249]. A recent paper by Tremel and co-workers demonstrated the crystallisation of CaCO_3 in acoustic levitated droplets, using wide angle X-ray scattering to prove the formation of CaCO_3 proceeds via ACC [250]. Myerson and co-workers [251] developed a technique for the crystallisation of organic compounds from droplets of aqueous solutions supported on engineered surfaces (feature sizes $\sim 25\text{-}750\ \mu\text{m}$). They reported that the polymorphism of glycine is dependent on the droplet volume, with a preference for unstable polymorphic forms within the smallest droplets.

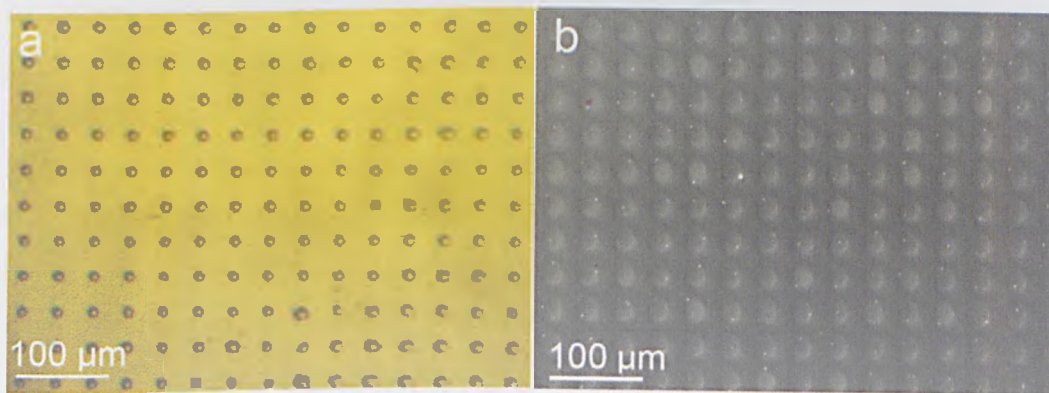


Figure 7.1: **a** Optical image of an array of supersaturated CaCO_3 droplets, **b** resultant SEM image, showing CaCO_3 particles located within the hydrophilic circular regions.

In this project, crystallisation was studied in supersaturated droplets of aqueous CaCO_3 solutions deposited onto patterned functionalised SAMs. The SAMs were patterned using the deep-UV photolithography method outlined in section

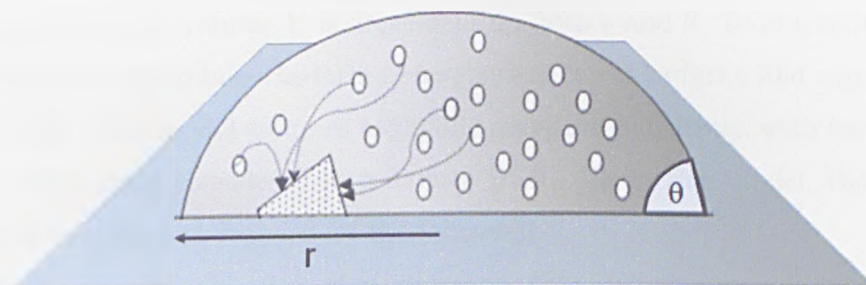


Figure 7.2: Schematic diagram showing crystallisation within a single droplet of droplet-substrate radius r and droplet-substrate contact angle θ .

2.2.2, with regular arrays of circular, hydrophilic regions upon a hydrophobic background. Each droplet was considered in isolation due to the almost instantaneous dewetting of the hydrophobic regions. Consequently, crystallisation within a droplet exerted no influence on the crystallisation within neighbouring droplets, with each patterned substrate therefore supporting arrays of up to 20,000 independent crystallisation volumes. Part of one such array is presented in figure 7.1, showing also the subsequent crystallisation from the droplets onto the patterned SAM.

Crystallisation in droplet arrays supported on patterned SAMs has been described by others, although the methods used were different to those described here. Whitesides and co-workers demonstrated the crystallisation of CuSO_4 and KNO_3 with 20-50 μm lateral dimensions [252] whereas Masuda *et al.* demonstrated colloidal crystallisation in droplets on patterned SAMs [253]. However, in both of these studies, crystallisation was the result of solvent evaporation, whereas it is believed that the work presented here demonstrates for the first time crystallisation from precipitation reactions in droplet arrays supported on patterned SAMs.

A schematic diagram of an individual droplet, of substrate-droplet interfacial radius r and droplet-substrate contact angle θ , is shown in figure 7.2. The droplet has two interfaces; droplet-substrate and droplet-air. It is assumed that heterogeneous nucleation is promoted only at the droplet-substrate interface, since it has been shown previously that these surfaces promote the nucleation of CaCO_3 . The droplet-substrate interfacial area, A_{ds} , is dependent only on r

$$A_{ds} = \pi r^2 \quad (7.1)$$

whereas the droplet volume V is dependent on both r and θ . To determine V the droplet is assumed to take the form of a spherical cap of radius a and cap height h (Figure 7.3). This model assumes negligible gravitational effects, with the validity of this assumption considered in reference [254]. Using this model, the droplet volume V is related to r and h by the following

$$V = \frac{\pi h}{6}(3r^2 + h^2) \quad (7.2)$$

where a and h are related by the following equation.

$$a = \frac{(r^2 + h^2)}{2h} \quad (7.3)$$

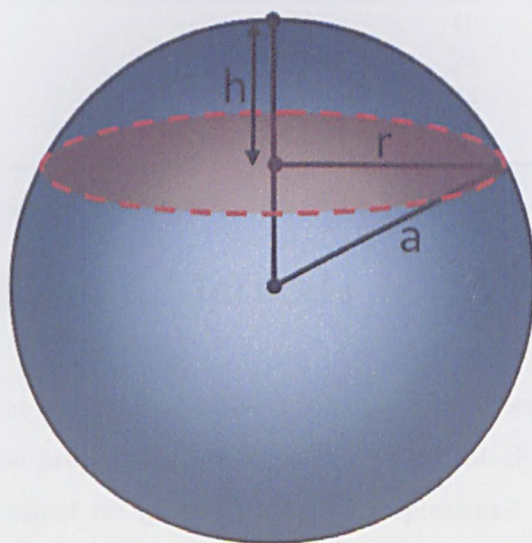


Figure 7.3: Schematic diagram of the spherical cap model, showing droplet volume as a function of droplet radius a , droplet-substrate interfacial radius r and cap height, h .

Figure 7.4 defines the edge-to-edge, x_{edge} , and centre-to-centre, x_{centre} , droplet spacings listed in table 7.1. The radii of the hydrophilic regions were 10, 5, 4 and 2 μm corresponding to the geometry of the photomask (Figure 7.5).

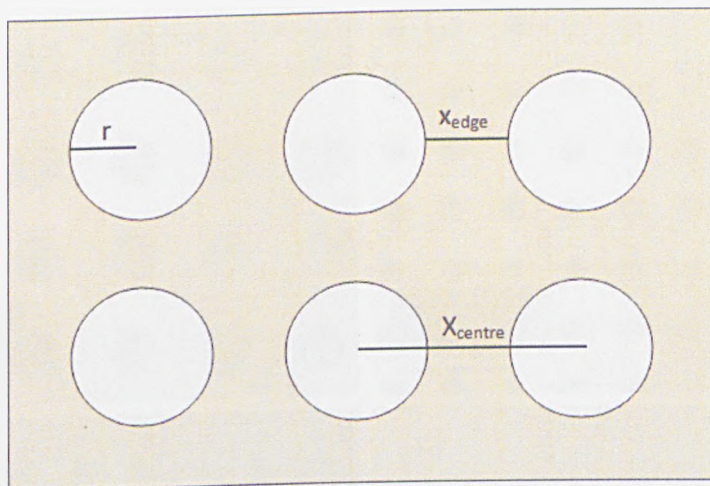


Figure 7.4: Schematic diagram defining the photomask spacings x_{centre} , x_{edge} and radius r .

Droplet Radius, r (μm)	x_{edge} (μm)	x_{centre} (μm)
10	20	40
5	14	24
4	16	24
2	15	19

Table 7.1: Photomask spacings x_{centre} and x_{edge} as a function of radius r .

7.2 Experimental Methods

The small radii of the droplets resulted in a rapid rate of evaporation at laboratory humidity. It was proposed by Birdi *et al.* [255] that the rate of evaporation of a sessile water droplet on glass is linearly proportional to the radius of the liquid-solid interface, yielding a rapid evaporation rate for the droplet radii used here. To overcome these problems, all growth experiments were performed in an equilibrated glove box maintained at 100% humidity by passing steam through the glovebox for 1 minute, 20 minutes prior to the crystal growth. CaCO_3 was precipitated using the double decomposition growth method, with ~ 2 ml of supersaturated CaCO_3 solution extracted and passed across the patterned substrates. Using a vacuum sealant, the samples were sealed within a Petri dish containing a small vial of water, ensuring a saturated environment. Growth periods were varied between 5 minutes and 24 h, at concentrations of 2.5 and 5 mM. Growth was

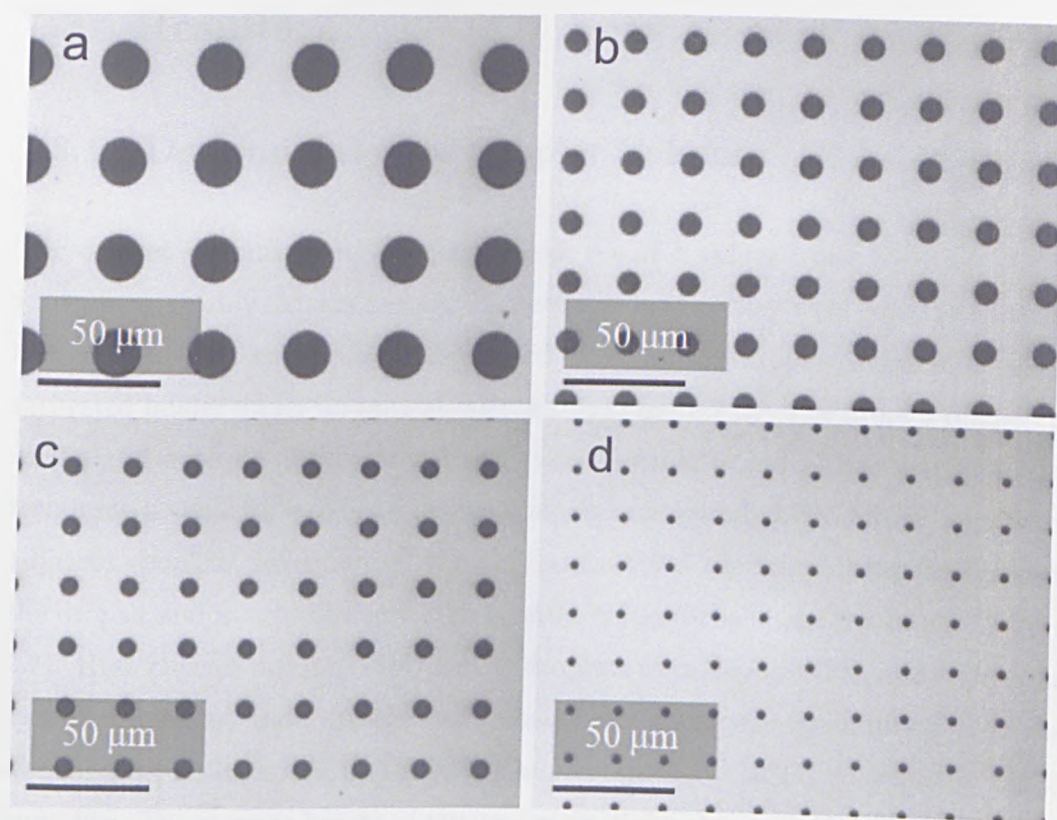


Figure 7.5: 400 \times optical image showing 4 photomask geometries. Radii; a 10 μm , b 5 μm , c 4 μm and d 2 μm .

terminated by rinsing surfaces under milli-Q water and drying under a nitrogen stream.

Crystal images were obtained using both low- and high-resolution SEM, although in this case no conductive Pt layer was deposited on the sample, since this made it impossible to observe the SAM patterning. Image distortion due to charge accumulation was not an inherent problem here due to the small size of the CaCO_3 precipitates and the presence of a conductive gold substrate.

7.3 Results

7.3.1 Determination of Droplet Volumes

The droplet volumes were calculated from r and h values using equation 7.2. r values were readily determined on the assumption that they were equal to the patterning size. This assumption was verified by examining droplet arrays in a sealed, saturated holder under an optical microscope (Figure 7.6). The droplet diameters were equal to those of the photo-mask. Considerable technical issues arose in determining a value for h , since a profile image was required. Light interference from adjacent droplets, reflection off the gold surface and the large distance between the droplet and microscope lens significantly reduced the image resolution (Figure 7.7). High concentration ($\sim 5\text{M}$) CaCl_2 droplets were deposited to allow for cross sectional imaging under atmospheric conditions, under the assumption that the wetting properties would be similar to supersaturated CaCO_3 solutions at 100% humidity. The average height of the $10\ \mu\text{m}$ radii droplets was $(3.6 \pm 0.6)\ \mu\text{m}$, with the relatively large uncertainty accounting for the limitations in image resolution. According to equation 7.2 this yields a cap volume of $(590 \pm 60)\ \text{fL} \approx 0.6 \pm 0.1\ \text{pL}$.

Measuring the solution-substrate contact angle was more complex than in the case of homogeneous MHA SAMs due to a pinning effect at the hydrophilic-hydrophobic border. For the $10\ \mu\text{m}$ radii droplets, an average of 6 sessile contact angles yielded a contact angle of $(43 \pm 6)^\circ$. The assumption is made that the contact angle of the highly concentrated CaCl_2 solution is the same as for the dilute CaCO_3 aqueous solution, which can only be true if γ_{sl} decreases to exactly compensate for the increase in γ_{lv} , since the surface tension of the concentrated CaCl_2 solution is more than $10\ \text{mNm}^{-1}$ higher than water (or dilute CaCO_3 aqueous solution) [256]. Table 7.2 lists the droplet-substrate interfacial area (A_{ds}), and the measured droplet volumes (V_{43}) for contact angles of 43° , on the assumption that the contact angle remains constant for each droplet size, hence the same r to h ratio. Also included are the droplet volumes at 90° contact angles for comparison (V_{90}).

r (μm)	A_{ds} (μm^2)	V_{43} (fL)	V_{90} (fL)
10	314	590 ± 60	2094
5	78.5	70 ± 20	262
4	50	40 ± 20	134
2	12.5	5 ± 3	16.7

Table 7.2: Droplet-substrate interfacial area (A_{ds}) and droplet volumes for contact angles of 43° (V_{43}) and 90° V_{90} , as a function of droplet-substrate interfacial radius r , calculated using equations 7.1 and 7.2 respectively.

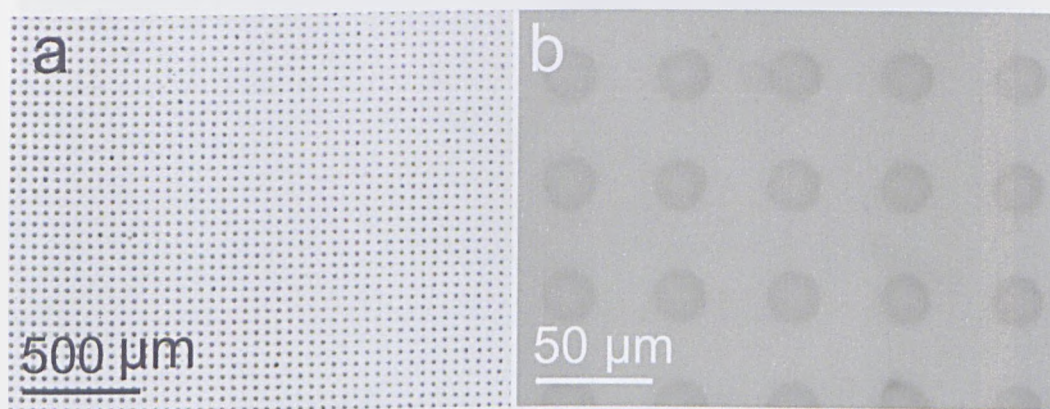


Figure 7.6: Optical images showing arrays of $10 \mu\text{m}$ radius droplets of supersaturated CaCO_3 solutions supported on patterned SAMs at two magnifications **a**, **b**.

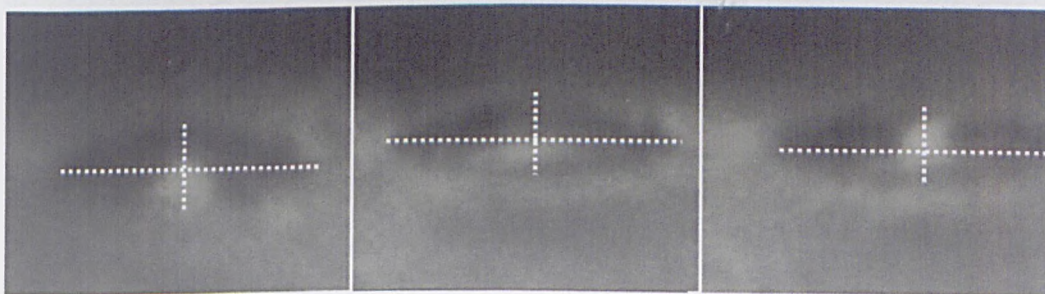


Figure 7.7: Side profile of 3 different $[\text{Ca}^{2+}] = 5 \text{ M}$ droplets, $10 \mu\text{m}$ radius.

7.3.2 Droplet Size Dependency

The number of CaCO_3 precipitates per droplet, polymorphism and crystal morphology were dependent on the droplet radius. Other factors known to influence these parameters in bulk solution, including the solution concentration and growth time, were kept constant here ($[\text{Ca}^{2+}] = 5 \text{ mM}$, 24 h growth period). The droplet occupancy was related to the droplet-substrate interfacial surface area. A low resolution SEM overview is shown in figure 7.8 from which the droplet occupancy

and projected particle sizes were readily determined. A statistical analysis of these parameters as a function of droplet radius is shown in table 7.3.

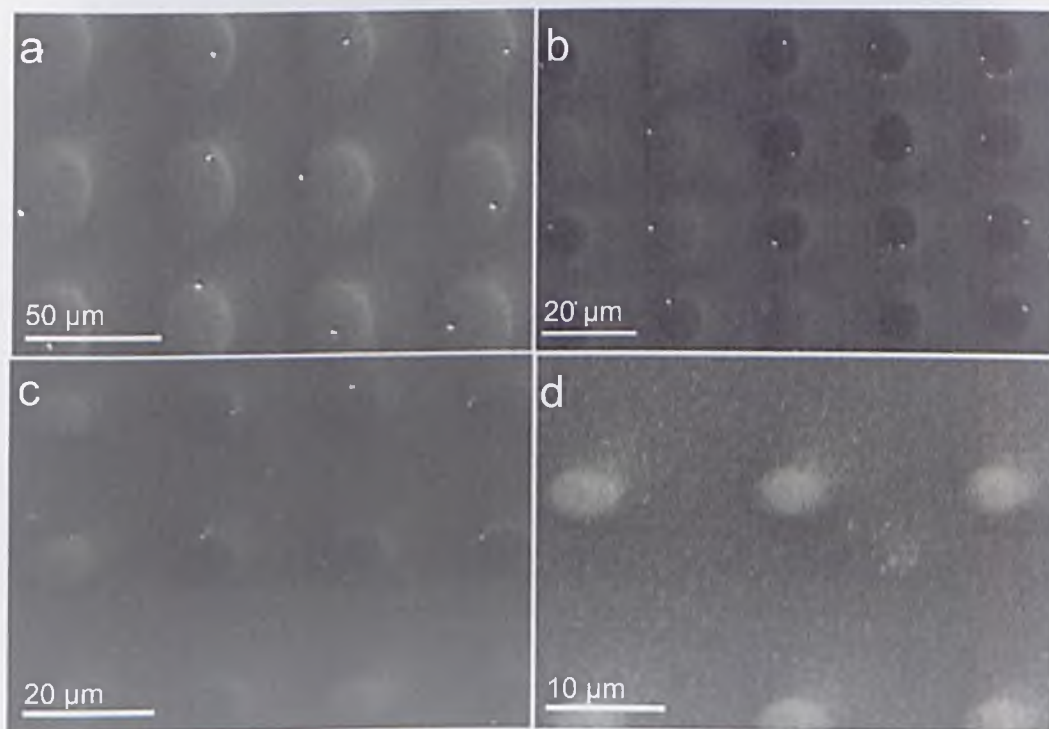


Figure 7.8: Low-Res SEM overview showing CaCO_3 particles as a function of droplet radius. **a** 10 μm , **b** 5 μm , **c** 4 μm and **d** 2 μm . $[\text{Ca}^{2+}] = 5 \text{ mM}$ CaCO_3 droplet concentration, 24 h growth period.

Parameter	Droplet radius (μm)		
	10 μm	5 μm	4 μm
Studied droplets	201	80	151
Droplet occupancy (%)	96.5	82	72
Multiple occupancy (%)	8.5	5	9
Average crystal size (μm^2)	1.21 ± 0.48	0.31 ± 0.12	0.25 ± 0.16

Table 7.3: Droplet occupancy, multiple occupancy and average CaCO_3 particle size as a function of droplet radius. $[\text{Ca}^{2+}] = 5 \text{ mM}$ CaCO_3 droplet concentration, 24 h growth period.

The droplet occupancy was related to the droplet radius, with the 10 μm radii droplets yielding an occupancy of 96.5%. The droplet occupancy decreased with radius, at 82% and 72% for radii of 5 and 4 μm respectively. Using low resolution SEM, no CaCO_3 particles were observed in 2 μm radii droplet, since features below $\sim 200 \text{ nm}$ could not be readily resolved. However, subsequent measurements using a FEG SEM revealed the occurrence of such particles (Figure 7.9)

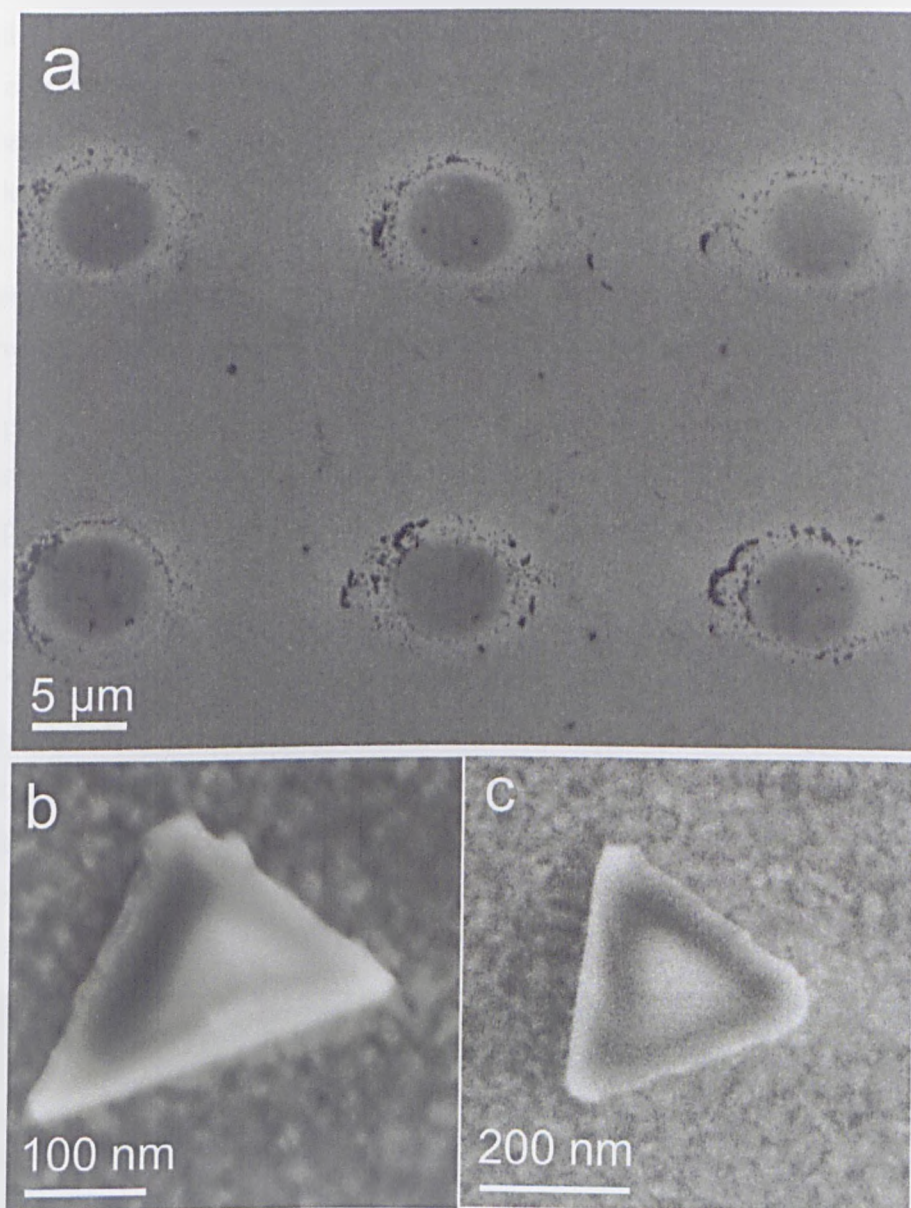


Figure 7.9: FEG SEM images of CaCO_3 particles precipitated from $2 \mu\text{m}$ radii droplets. 24 h growth period, $[\text{Ca}^{2+}] = 5\text{mM}$. **a** overview of 6 droplets, **b-c** high magnification images of individual calcite tetrahedra, impossible to distinguish using low-res SEM

There was no significant change in the percentage of droplets with multiple occupancy, that is containing more than 1 CaCO_3 particle, for droplet radii of 10 and $4 \mu\text{m}$, at 8.5 and 9% respectively. Only 5% of $5 \mu\text{m}$ radii droplets contained 2 or more particles, attributed to the stochastic nature of the crystallisation process.

Interestingly, the CaCO_3 particles tended to be located near to the droplet boundary (Figure 7.10). A study of 289 $10 \mu\text{m}$ radii droplets from three different samples

found $74\pm 4\%$ of CaCO_3 particles to be located within $2\ \mu\text{m}$ of the droplet boundary, corresponding to only 36% of the total droplet area. In the case of $4\ \mu\text{m}$ radius droplet arrays under the same growth conditions, a study of 140 individual droplets found that $78\pm 6\%$ of particles were located within $1\ \mu\text{m}$ of the droplet edge, corresponding to $\sim 44\%$ of the total droplet area. Although these results are statistically significant, it is not thought that this effect exerted any influence on the resultant morphology, and is not given any further consideration here.

The particle size distributions were determined from SEM images using ImageJ software, following the procedure described in section 2.5. In all cases, the CaCO_3 precipitates from droplets were an order of magnitude smaller than the crystals precipitated from bulk solution under equivalent conditions (section 4.3.2). The particle size distributions for 10, 5 and $4\ \mu\text{m}$ radius droplets are shown in figures 7.11, 7.12 and 7.13 respectively. Unsurprisingly, particles precipitated from the $10\ \mu\text{m}$ droplets had the largest projected area of $1.2\pm 0.5\ \mu\text{m}^2$, falling to 0.31 ± 0.12 and $0.25\pm 0.16\ \mu\text{m}^2$ for 5 and $4\ \mu\text{m}$ radius droplets respectively. For the smaller droplet sizes, no particles with projected areas larger than $1\ \mu\text{m}^2$ were observed, whereas for the $10\ \mu\text{m}$ radii droplets, particles with projected areas as large as $3\ \mu\text{m}^2$ were observed.

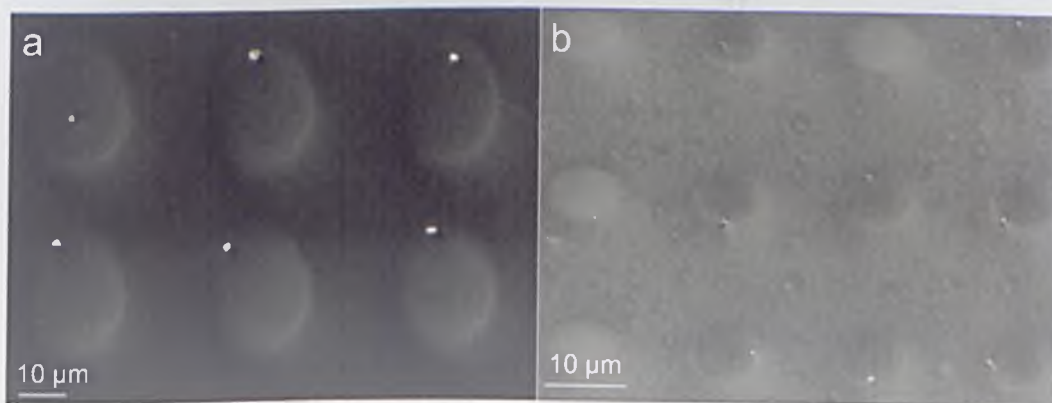


Figure 7.10: Low-resolution SEM images showing the CaCO_3 particle location, $[\text{Ca}^{2+}] = 5\ \text{mM}$, 24 h growth period. **a** $10\ \mu\text{m}$ radii droplets where $74\pm 4\%$ of the particles were within $2\ \mu\text{m}$ of the droplet boundary. **b** $4\ \mu\text{m}$ radii droplets, where $78\pm 6\%$ of particles were located within $1\ \mu\text{m}$ of the droplet boundary.

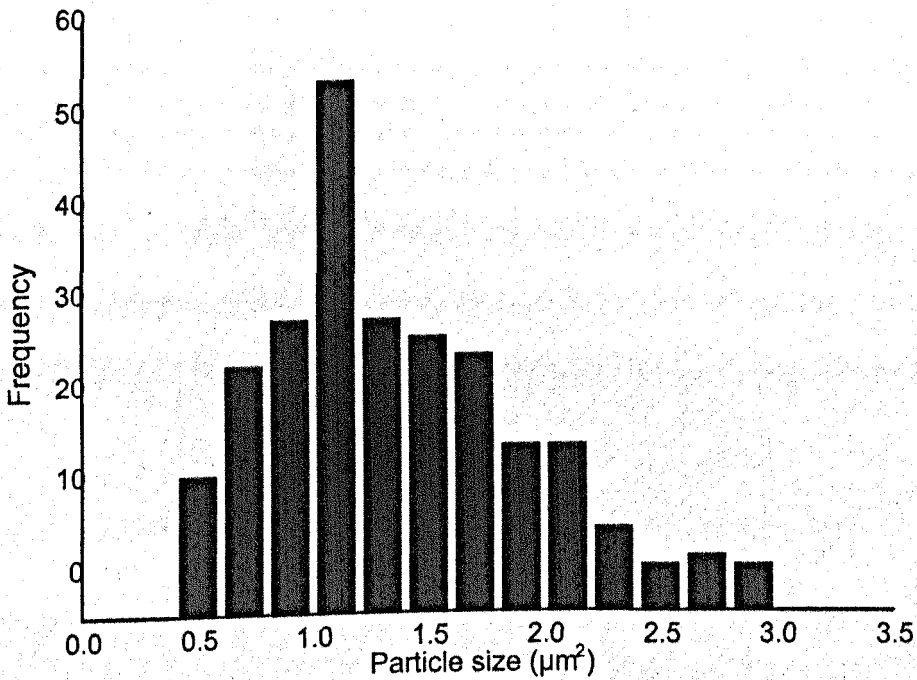


Figure 7.11: Size distribution of CaCO₃ particles precipitated from 10 μm radius droplets, 24 h growth period, [Ca²⁺] = 5 mM. 200 μm bin size.

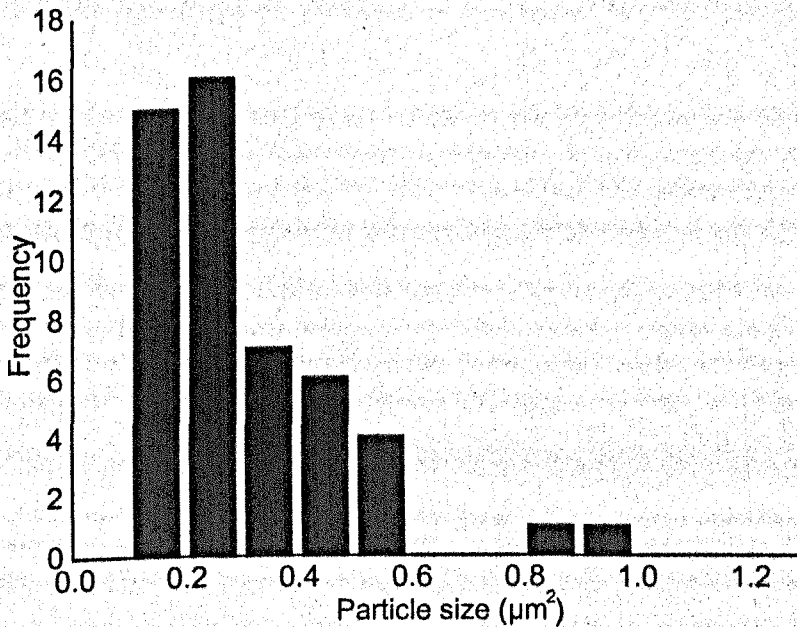


Figure 7.12: Size distribution of CaCO₃ particles precipitated from 5 μm radius droplets, 24 h growth period, [Ca²⁺] = 5 mM. 100 μm bin size.

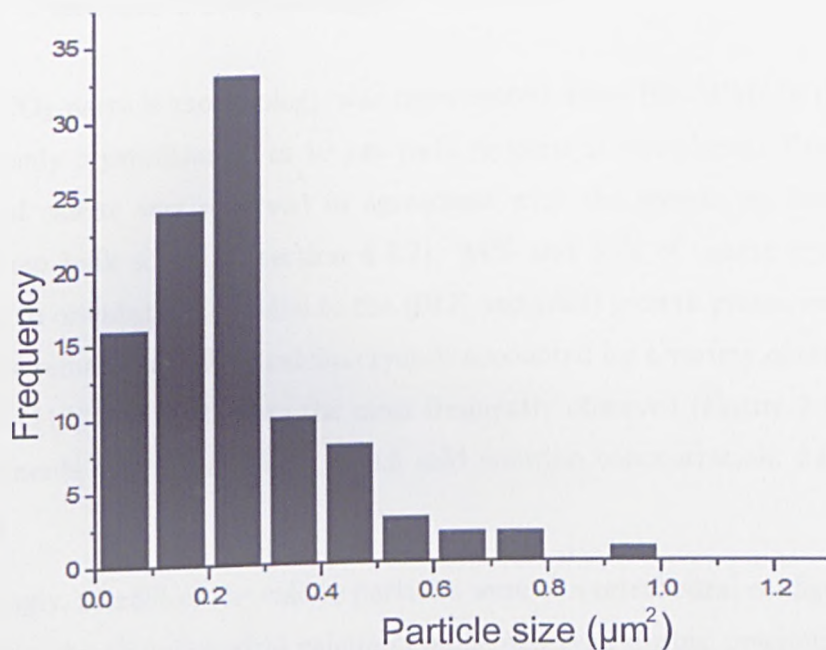


Figure 7.13: Size distribution of CaCO₃ particles precipitated from 4 μm radius droplets, 24 h growth period, [Ca²⁺] = 5 mM. 100 μm bin size.

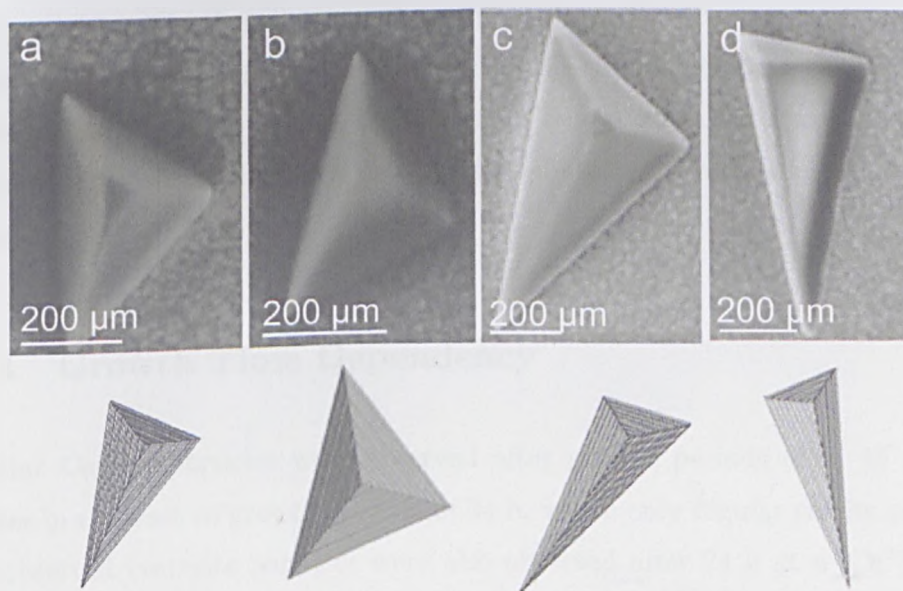


Figure 7.14: **top** HR-SEM images of individual face selective calcite tetrahedra, observed within 10 μm radius, 2.5 mM droplets after a 24 h growth period. **a** 44% of calcite particles were in a (012) orientation, **b** 33% of calcite particles were in a (015) orientation. The remaining 23% of calcite particles were in a variety of orientations, of which **c** (113) and **d** (122) were the most frequent. **bottom** SHAPE simulated calcite tetrahedra in corresponding orientations.

7.3.3 Particle Morphology

The CaCO_3 particle morphology was investigated using HR-SEM. In this results section, only crystallisation in 10 μm radii droplets is considered. Face selective growth of calcite was observed in agreement with the growth on homogeneous SAMs from bulk solution (section 4.3.2). 44% and 33% of calcite crystals were observed in orientations parallel to the (012) and (015) growth planes respectively, whilst the remaining 23% of calcite crystals accounted for a variety of orientations, of which (113) and (122) were the most frequently observed (Figure 7.14). These measurements were at a $[\text{Ca}^{2+}] = 2.5 \text{ mM}$ solution concentration, 24 h growth period.

Interestingly, $90 \pm 5\%$ of the calcite particles were of a tetrahedral configuration, in contrast to the rhombohedral calcite crystals observed during precipitation from bulk solution on the same surfaces (section 4.3.2). Single calcite tetrahedra, oriented parallel to the (012) and (015) growth planes, were observed at 5 and 10 mM concentrations after the same growth period (Figure 7.16b-c), although a higher number of both non-oriented and multi-faceted calcite particles were also present (Figure 7.16d-e). 56% and 42% of CaCO_3 particles were of the form of oriented, single-faceted, calcite tetrahedra at 5 and 10 mM respective solution concentrations, although the relative calcite orientations were not systematically studied.

7.3.4 Growth Time Dependency

Irregular CaCO_3 particles were observed after growth periods of 5, 15 and 30 minutes in contrast to growth periods of 24 h, where only regular calcite particles were observed (vaterite particles were also observed after 24 h at a $[\text{Ca}^{2+}] = 10 \text{ mM}$ concentration, although these accounted for less than 1% of the total number of precipitates)(Figure 7.17). A comparative study of precipitates from 5 mM, 10 μm radii droplets found the relative proportion of these irregular particles to decrease with time. Face selective calcite was observed in 32 ± 5 , 85 ± 4 and $94 \pm 4\%$ of droplets for time periods of 5, 15 and 30 minutes respectively, with a minimum of 50 droplets investigated in each case. The percentage of face selective calcite

after 30 minute and 24 h growth periods was therefore comparable, however after 30 minutes, amorphous, spherical ~ 100 nm diameter particles were also present. This can be seen in figure 7.17c, showing 8 ACC particles and a single face selective calcite crystal within the same droplet.

High magnification SEM images were used for the morphological analysis of irregular, short growth time CaCO_3 particles (Figure 7.18). After 5 minutes the precipitates were consistent with the ACC particles, synthesised and characterised in chapter 6, consisting of aggregates of 60-150 nm particles (Figures 7.17 b and 7.18 a, b). Irregular CaCO_3 particles were observed in $10 \mu\text{m}$ radius droplets for 15-120 minute growth periods, at 2.5, 5 and 10 mM concentrations (Figures 7.17 d, f) and 7.18 c, d). However, these precipitates displayed a highly non-spherical morphology with irregular surface topographies and could not be therefore readily classified as ACC. Figure 7.18e is at an apparent intermediate stage, showing a broadly tetrahedral shape with irregular edges. Figure 7.18f shows an early stage, sub-micron calcite crystal, defined by the regular edges.

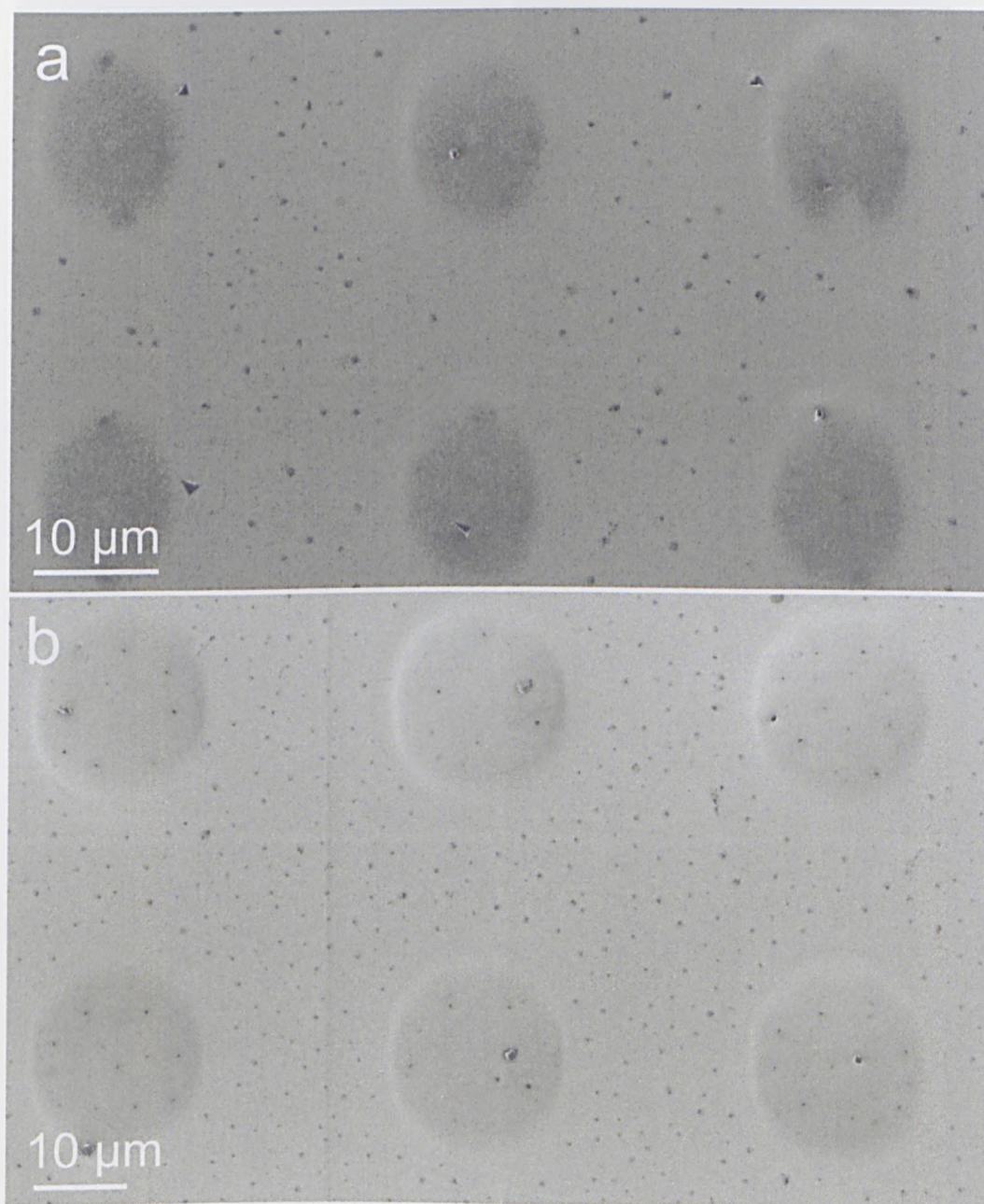


Figure 7.15: SEM overview of CaCO_3 precipitates from $[\text{Ca}^{2+}] = 5 \text{ mM}$ solutions, 24 hour growth periods for **a** $5 \mu\text{m}$ radius droplets and **b** $10 \mu\text{m}$ radius droplets. For all droplet radii, the CaCO_3 precipitates were observed in the form of face selective calcite tetrahedra in over 90% of cases after a 24 h growth period.

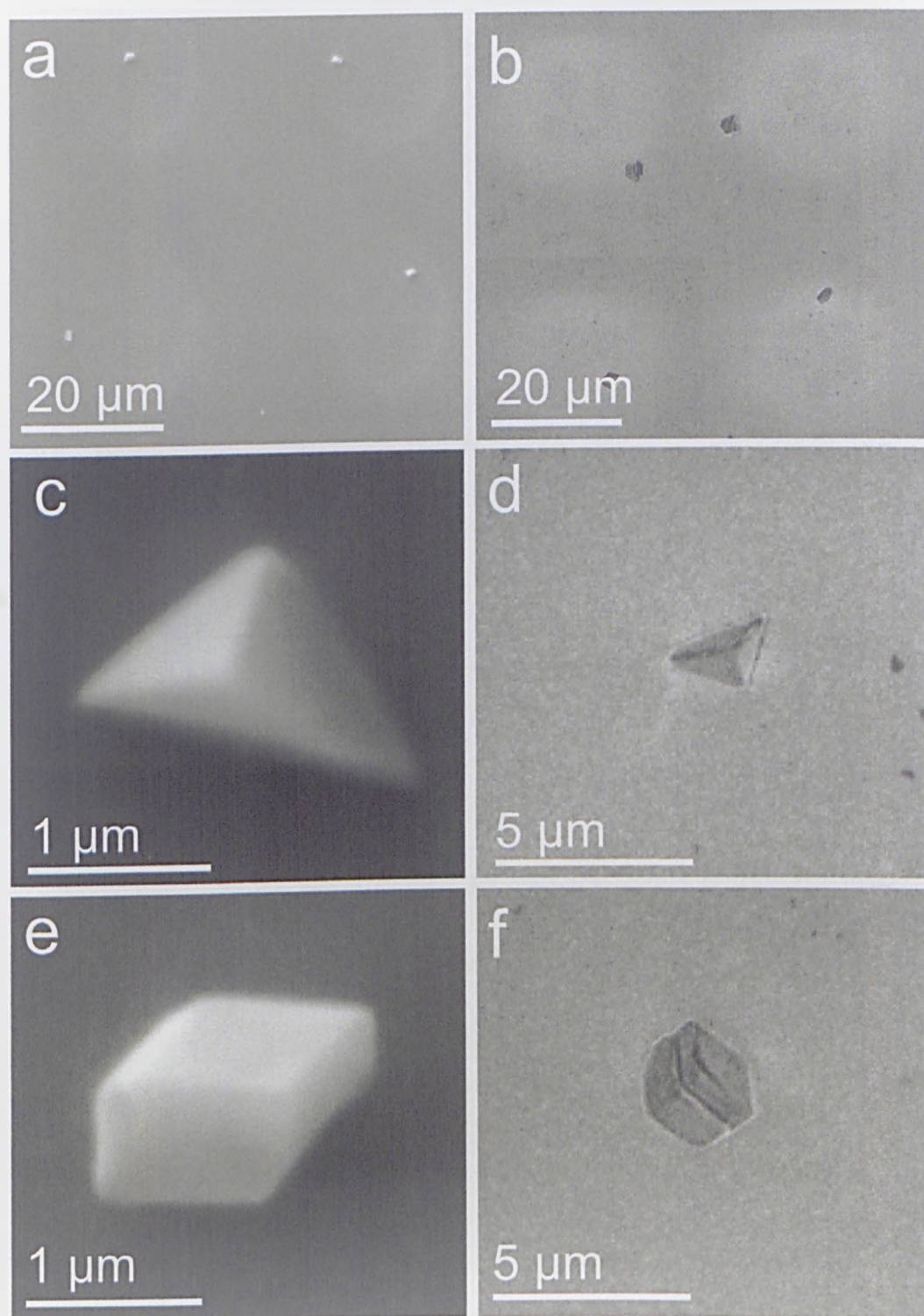


Figure 7.16: SEM images of the precipitation of CaCO_3 within $10 \mu\text{m}$ radii droplets after 24 hours, **a, c, e** $[\text{Ca}^{2+}] = 5 \text{ mM}$, **b, d, f** $[\text{Ca}^{2+}] = 10 \text{ mM}$. **a, b** Overview, showing the occupancy of 4 respective droplets, **c, d** individual (012) oriented calcite tetrahedra. **e** non-oriented calcite crystal, **f** multifaceted calcite particle.

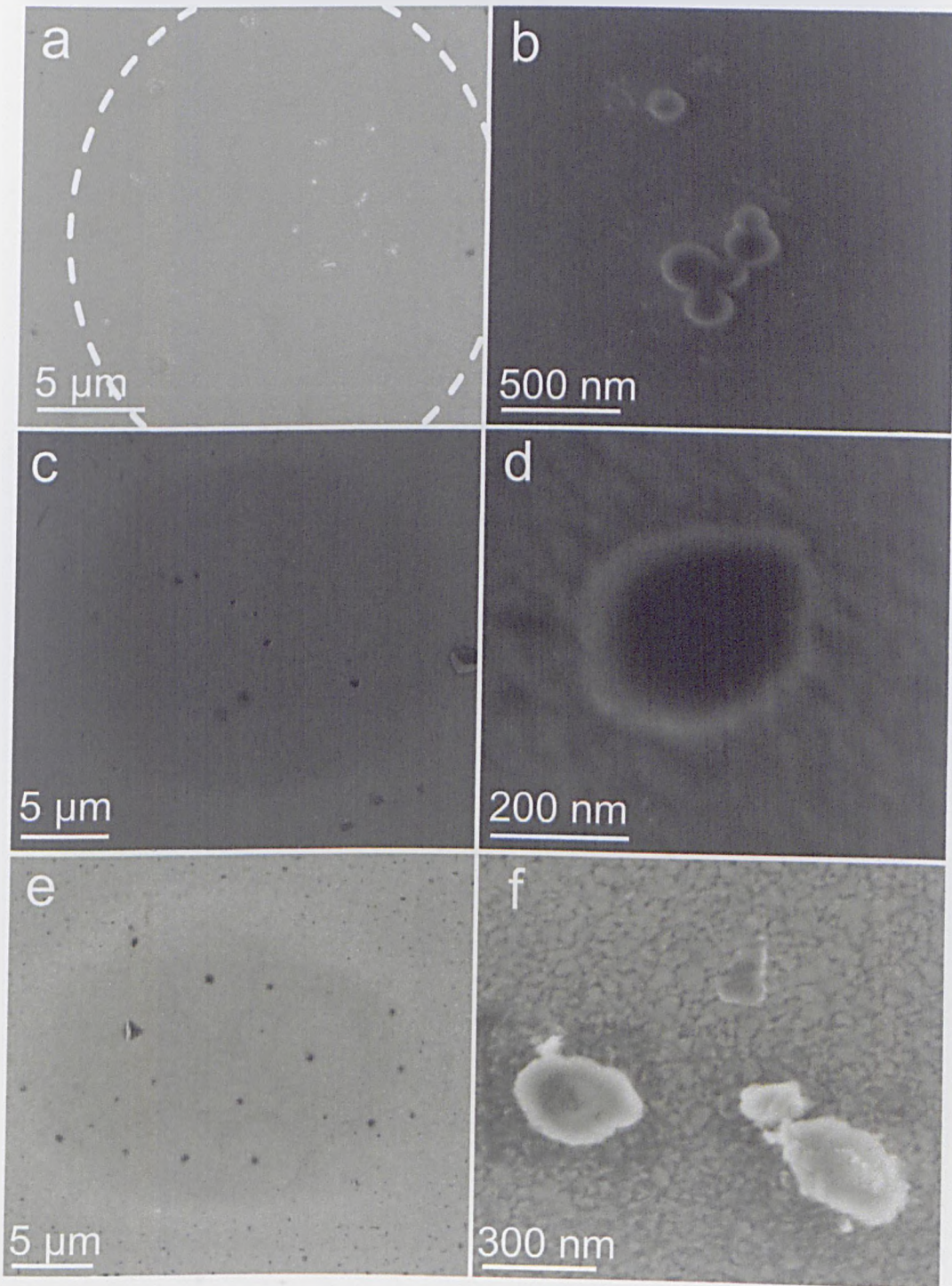


Figure 7.17: SEM images of CaCO₃ particles in 10 μm radius droplets after growth periods of **a-b** 5 minutes, **c-d** 15 minutes and **e-f** 30 minutes. **a, c, e** Overview of individual droplets for the respective growth periods as indicated by the darkened region (dashed outline in **a**). **a** only amorphous-type particles present, **c, e** both amorphous-type and calcite particles present. **b, d, f** High magnification images of individual irregular CaCO₃ particles after the respective growth periods.

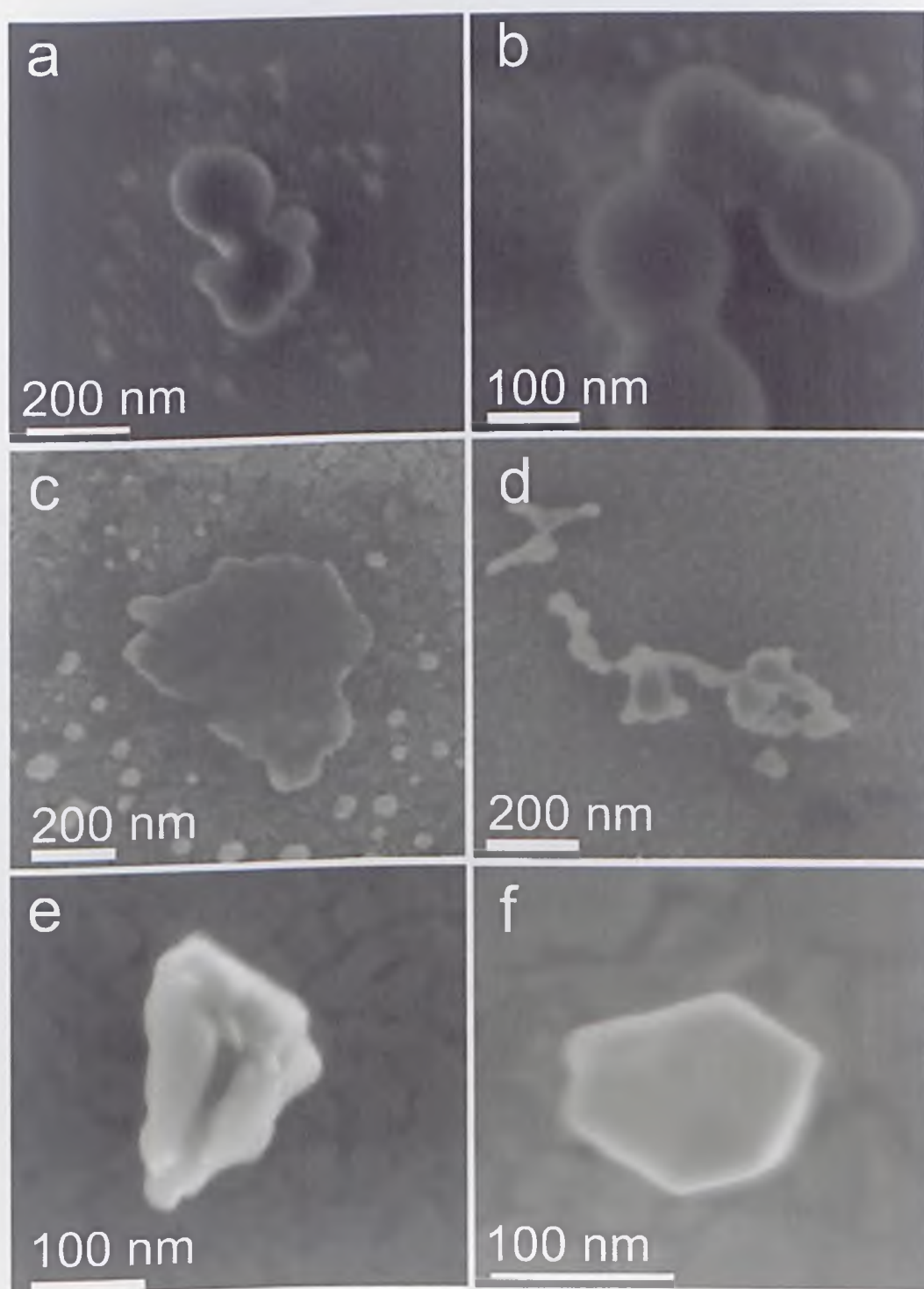


Figure 7.18: High magnification SEM images of individual irregular CaCO₃ particles, precipitated within 10 μ m radius droplets. **a, b** Spherical 60-150 nm diameter particles consistent with ACC, 5 minute growth period, 5 mM concentration, **c** irregular CaCO₃ precipitates after a 30 minute growth period, 5 mM concentration, **d** irregular CaCO₃ precipitates after a 2 h growth period, 10 mM concentration. **e** early stage calcite tetrahedral, 30 minute growth period, 2.5 mM concentration. **f** early stage calcite particle, 2 h growth period 5 mM concentration.

7.4 Discussion

The droplet occupancy was related to the droplet volume, and was greater than 70% for the three droplet sizes systematically studied after a 24 h growth period. Face-selective growth of calcite in orientations parallel to the (012) and (015) growth planes formed the majority of the particles, analogous to growth on the same surfaces from bulk solution presented in section 4.3.2. This validates the assumption made that nucleation occurs at the droplet-substrate interface as opposed to the droplet-air interface, since in that case random orientations would be expected.

There was a small distribution in projected particle size within each droplet, with the mean particle size decreasing with droplet volume. This is perhaps unsurprising considering the volume depends on the radius cubed, leading to an 8-fold increase in volume for a doubling in droplet radius. In all cases, the calcite dimensions were governed by the amount of material within the droplet, since the precipitation of CaCO_3 on the same surfaces from bulk solution under identical conditions yielded an order of magnitude increase in precipitate edge size.

It is possible to calculate the amount of material which will crystallise into calcite for the concentrations used here. The mass of material which will precipitate is the product of volume, concentration and molecular weight. Taking the case of a $10 \mu\text{m}$ radius droplet, the volume was estimated to be $\sim 0.5 \text{ pL} = 0.5 \times 10^{-15} \text{ m}^3$. For a solution concentration of $[\text{Ca}^{2+}] = 5 \text{ mM}$, and taking the solubility of calcite in water to be 1 mM gives an effective concentration of 4 mM . The molecular weight of calcite is approximately 100 g.mol^{-1} .

$$\begin{aligned} 0.5 \times 10^{-15} \text{ m}^3 \times 4 \times 10^{-3} \text{ M} \times 100 \text{ g.mol}^{-1} \times 1000 &= 2 \times 10^{-13} \text{ g} \\ &= 2 \times 10^{-16} \text{ kg} \end{aligned}$$

The volume is taken as mass/density, where the density of calcite is $2.7 \times 10^3 \text{ kg}$. The total volume of precipitate is therefore $7.4 \times 10^{-20} \text{ m}^3$. If the crystal is cubic, the length of each side is equal to the cube root, giving an edge length

of $0.42 \mu\text{m}$. This is of the order of the observed calcite edges, although the edges were greater than $1 \mu\text{m}$ in some cases. However, the calcite particles were mostly tetrahedral. In the case of a regular tetrahedron, the volume is approximately 12% of an equivalent cube of the same edge length. Also, there is a large uncertainty in the droplet volume, since a contact angle of 90° would yield a volume 4 times that used in this calculation. These factors are likely to account for the observed edge dimensions greater than $1 \mu\text{m}$. Nevertheless, this calculation suggests that the supersaturated solution will fully crystallise.

Single droplet occupancy was observed in more than 90% of cases for the three droplet sizes systematically studied after a 24 h growth period. This suggests the presence of localised concentration gradients within each droplet. The onset of crystallisation will result in mass transport to the growth face, which may result in an undersaturation of the droplet. If these results are analogous to the growth on patterned SAMs, then the depletion zone would be larger than the dimensions of the droplet radius. In any case, the effect of localised depletion zones is likely to be enhanced due to the limited amount of material within each droplet.

The short growth time experiments were broadly analogous to the results on homogeneous SAMs from bulk solution, although in this case growth periods less than 5 minutes were not considered. The results presented in section 4.3.2 were in agreement with other findings, suggesting that the formation of calcite begins with the homogeneous nucleation of ACC at the SAM interface. Here, regular ACC particles were observed after 5 minutes, and irregular CaCO_3 particles observed after growth periods up to two hours. The relative percentage of face selective calcite particles increased as a function of growth period between 5, 15 and 30 minutes. In some instances, ACC particles were observed within the same droplet as face selective calcite crystals, whereas no ACC particles were observed after 24 hours. That irregular CaCO_3 particles were present for longer time periods in droplets than in bulk solution suggests that the transition into calcite is in some way hindered by the limited volume.

The final observation was the almost exclusive occurrence of tetrahedral calcite particles in comparison to the rhombohedral calcite particles observed on equivalent surfaces in bulk solution. As proposed in section 3.3, the configuration of the

calcite particle is almost certainly determined early in the growth process, presumably by the contact angle formed between the ACC particle and the nucleating substrate. A tetrahedral configuration is indicative of a low contact angle between ACC particle and substrate, whereas a rhombohedral configuration suggests a high contact angle, or an aggregation of ACC particles before transformation. It is feasible that both lateral ACC growth and ACC particle aggregation will be hindered within the limited volume droplets, resulting in a higher percentage of tetrahedral configurations.

7.5 Conclusions

The results in this chapter show that crystallisation is affected by solution volume. Whilst the orientation and polymorphism of CaCO_3 particles formed within \sim picolitre volumes on patterned SAMs were not significantly different to those formed on equivalent surfaces from bulk solution, there was a marked change in both the configuration and dimensions of the calcite crystals. Calcite crystals were observed almost exclusively in a tetrahedral configuration, in contrast to the rhombohedral particles observed in bulk. The observed particle dimensions were of the order of the calculated values, suggesting that the solution droplet became fully depleted after 24 h. That sub-micron ACC particles were observed after short growth times (5 minutes-2 hours) but not after 24 hours further supports this supposition. It is believed that the effect of localised concentration gradients is enhanced in restricted volume systems, accounting for the fact that less than 10% of the droplets were multiply occupied. Finally, it is believed that this is the first time patterned functionalised SAMs have been used to support droplet arrays for the study of crystallisation by a precipitation reaction. This novel method is of potential application to many different systems, yielding a cheap and simple method to study nucleation and growth in many thousand independent small droplet volumes.

Chapter 8

Conclusions

The work of this thesis presents evidence for the formation of a transient amorphous precursor phase during the precipitation of CaCO_3 . The precipitation of CaCO_3 was considered in a variety of different systems, aiming to further understand the crystallisation pathways.

Whereas other studies of crystallisation in confinement were often limited by a fixed biological template, the model developed here enabled the systematic study of crystallisation under a continuous range of surface separations. Whilst regular calcite crystals were observed at large surface separations, analogous to growth in bulk solution, ACC was stabilised under moderate degrees of confinement. It was shown that ACC is thermodynamically preferable over calcite only at sub-nanometre surface separations, approximately three orders of magnitude less than observed here. The stabilisation of the amorphous phase was attributed to kinetic factors, with the small interface between the ACC particles and solution thought to hinder the expulsion of water from the amorphous phase.

A novel method for the study of crystallisation within independent solution volumes was developed. Patterned functionalised SAMs were used to support arrays of up to 20,000 droplets of supersaturated solution. These droplets were supported on MHA SAMs, enabling direct comparison with growth on the same surfaces from bulk solution. Calcite crystals were observed almost exclusively in a tetrahedral configuration within these droplets, with a low multiple occupancy suggesting a depletion of solution. Amorphous-type particles were present during the initial

growth stages, suggesting that transient ACC particles occur during precipitation in small volumes.

The CaCO_3 nucleation pathways in bulk solution were analysed in-situ using spectrophotometry and ex-situ using SEM, TEM and Raman spectroscopy. These results present clear evidence for the formation of ACC during the initial precipitation of CaCO_3 from supersaturated solutions in the concentration range of $[\text{Ca}^{2+}] = 5\text{-}10$ mM, with the stability of these particles apparently related to the concentration. Spectrophotometry measurements suggest that ACC can be stabilised using Mg^{2+} salts.

Growth on homogeneous SAMs resulted in the face selective growth of calcite in orientations parallel to the (012) and (015) growth planes, in agreement with the work presented by others. Amorphous-type particles were present during the early growth stages on these surfaces, before transforming into calcite after longer growth periods. No CaCO_3 particles could be morphologically identified as calcite with edge features below 100 nm, presenting evidence for the formation of calcite through an ACC precursor phase on these surfaces. Using patterned SAMs, crystallisation was restricted to specified sites, with undersaturation at polar-terminated regions a result of a localised depleted solution. It is believed that this is the first time that deep-UV photopatterned SAMs have been used to control the nucleation sites.

Finally, ACC particles were observed during the early growth stages on weathered mica analogous to the growth on MHA SAMs, again with no calcite particles with dimensions below 100 nm. Furthermore, it was shown that the mica surface is highly sensitive to details of its exposure to the atmosphere. Despite a close lattice match between the Ca-Ca spacing of the (001) calcite growth plane and the adjacent K^+ site spacing of the mica basal cleavage plane, epitaxy does not occur on freshly cleaved mica. It is proposed that the presence of naturally forming surface K_2CO_3 crystallites is a necessary intermediary for the occurrence of epitaxial calcite. Unlike in the case of alkali metal ions, there is normally a large free energy cost for the adsorption of calcite to mica. It is proposed that the transient K_2CO_3 crystallites act as localised ion sources, yielding specific surface sites where epitaxial growth is preferable.

Chapter 9

Future Work

The work in this thesis considered the formation and transformation mechanisms of one mineral, CaCO_3 . However, many of the methods developed here are well suited to study the crystallisation of a range of inorganic materials. Calcium phosphates (CaP), in particular hydroxyapatite ($\text{Ca}_{10}(\text{PO}_4)_6(\text{OH})_2$) are important biominerals, widely present in mammalian bone and tooth enamel. The crossed cylinder setup developed in chapter 5 presents an ideal configuration to investigate how confinement influences mineral formation over a continuous range. Stable amorphous calcium carbonate was observed within confined geometries around the region of contact, and it would be a point of interest to determine whether amorphous calcium phosphate (ACP) is also stabilised under confinement. Other inorganic materials without reported amorphous phases, including dolomite ($\text{CaMg}(\text{CO}_3)_2$), witherite (BaCO_3) and gypsum ($\text{CaSO}_4 \cdot 2\text{H}_2\text{O}$) should be considered in this system for comparative purposes.

The spectrophotometry experiments in chapter 6 present a simple method for determining nucleation pathways from the scattering of visible light. Provisional experiments using CaP, precipitated from two aqueous salt solutions similar to the double decomposition method here, suggest the presence of an amorphous precursor phase. Small volumes of solution extracted during these measurements and analysed using Raman spectroscopy showed an increase in crystallinity with time. The life time of ACP as a function of solute concentration should be determined using this system.

The technique developed to study crystallisation within arrays of picolitre droplets perhaps presents the largest scope for development. By placing the sample in a sealed cell between crossed-polarisers, in-situ nucleation statistics could be obtained at low magnification, since even sub-micron particles are visible using this setup. Furthermore, since amorphous calcium carbonate is isotropic, it can be readily distinguished from calcite under crossed-polarisers, enabling realtime monitoring of polymorphic transformations. This system should also be extended to study the crystallisation of CaCO_3 with various additives. Finally, the SAM functionality should be modified to consider the effect of terminal group on the nucleation process.

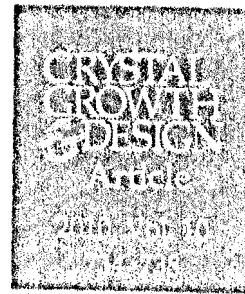
The epitaxial overgrowth of calcite on muscovite mica was demonstrated in chapter 3, and it remains to be determined whether a similar phenomena is observed on other types of mica, including phlogopite ($\text{KMg}_3\text{AlSi}_3\text{O}_{10}(\text{F},\text{OH})_2$), biotite ($\text{K}(\text{Mg},\text{Fe})_3\text{AlSi}_3\text{O}_{10}(\text{F},\text{OH})_2$) and lepidolite ($\text{K}(\text{Li}, \text{Al})_3(\text{Si}, \text{Al})_4\text{O}_{10}(\text{F}, \text{OH})_2$). Each of these micas has a pseudo-hexagonal surface unit cell, albeit with different site spacings to muscovite mica. The epitaxial overgrowth of calcite should therefore be investigated as a function of lattice miss-match. In addition, the effect of weathering conditions on the overgrowth of other carbonates on muscovite mica, including witherite, siderite and magnesite, should be studied.

Appendix A

Appendix A

Epitaxy of Calcite on Mica,

C. J. Stephens, F. C. Meldrum, Y. Mouhamad and H. K. Christenson, *Crystal Growth and Design*, 2010, 10(2), 734-738.



Epitaxy of Calcite on Mica

Christopher J. Stephens,[†] Youmna Mouhamad,[†] Fiona C. Meldrum,[‡] and Hugo K. Christenson^{*†}

[†]School of Physics and Astronomy and [‡]School of Chemistry University of Leeds, Leeds LS2 9JT, United Kingdom

Received September 15, 2009; Revised Manuscript Received October 27, 2009

ABSTRACT: We report for the first time the conditions under which oriented overgrowth of calcite occurs on muscovite mica. Calcite grows in a (001) orientation parallel to the basal cleavage plane on mica surfaces that have been weathered at ambient humidity (35–40%) for periods of at least 1 h, but no epitaxy is found on freshly cleaved mica. Nanometer-thin K_2CO_3 crystallites are known to form on mica surfaces weathered in this manner, and our experiments show that the presence of these crystallites during the initial stages of nucleation and growth is necessary for the epitaxial growth of calcite. Calcium ions do not adsorb to mica surfaces at the solution concentrations (≤ 20 mM) used in these experiments, and we suggest that the crystallites provide patches on the surface where the local concentration of both carbonate and calcium ions is high enough to promote epitaxy.

Introduction

Epitaxy, or the oriented growth of one crystal on another, is currently receiving considerable attention due to its importance for the manufacture of thin-film devices. Although most fabrication involves vapor-deposition methods, many liquid or solution-based processes are also used, for example, with ZnO films.¹ Epitaxial growth from solution has even been discussed in relation to varying growth rates of gallstones and kidney stones.² The first systematic studies of epitaxy were carried out as early as 80 years ago by Royer^{3,4} and involved the ordered growth of alkali halides (RbI, KBr, KCl, etc.) on mica from aqueous solutions. Using the same systems, Schulz⁵ subsequently obtained almost identical results with vapor deposition and solution precipitation, and he and Lisgarten⁶ attributed the epitaxy to a match between the lattice spacing in the (001) cleavage plane of mica and the nearest-neighbor spacing of the (111) halide surface. However, given that even a lattice mismatch of 23.2% (NaCl on mica⁶) permits epitaxial growth, it is clear that lattice match is not necessarily a dominant factor in facilitating epitaxy. In a study of six organic compounds growing from solution on 11 single-crystal substrates,⁷ little correlation between lattice match and preferred orientation was found, and it was concluded that effects due to intermolecular forces and growth anisotropy were more important. Similar conclusions have emerged from vapor-phase studies,⁸ and it is clear that epitaxy is a often highly system specific.^{7,9}

Muscovite mica is extensively used as a substrate for adsorption of species ranging from small biomolecules to bacteria and cells, and it is also the model surface of choice for many key surface techniques, including X-ray reflectivity, atomic force microscopy (AFM), shear force microscopy, and surface force measurements. This is due to the ease of cleavage to yield an atomically smooth surface, free of steps across areas of several square inches. Mica has a monoclinic layered hexagonal structure, with the ideal formula $KAl_2(AlSi_3)O_{10}(OH)_2$.

The layers consist of two SiO_4 tetrahedral sheets joined together by an AlO_6 octahedral sheet, and replacement of one in four Si atoms by Al gives rise to a negative charge that is balanced by potassium ions binding the layers together in the crystal. It is the relatively weak ionic bonds between the layers that leads to the perfect cleavage parallel to the (001) plane, with the potassium ions dispersed evenly but randomly between the new layers upon separation.¹⁰ Saturation of the oxygen bonds results in an inert and chemically stable surface.

Because of its high surface energy, rapid adsorption of water to mica from the atmosphere occurs immediately after cleavage.¹¹ Consequently, the work of cleavage in laboratory air is an order of magnitude smaller than in ultrahigh vacuum (UHV). The bound water does not desorb completely even at high temperatures under UHV. Of particular importance to the work presented here is the interaction between the surface potassium ions, carbon dioxide, and the adsorbed water on air-cleaved mica. This has been shown to lead to the epitaxial growth of thin crystallites on air-cleaved mica surfaces dried for a few days at humidities below about 40% (Figure 1).^{12,13} The supposition put forward by one of us over 15 years ago^{11,12} that these crystals are K_2CO_3 has only recently been verified by determining the unit cell parameters of the crystals with AFM.¹⁴ The surface density and diameter of these crystallites are dependent upon the mica weathering conditions, but they are usually only 1–5 nm thick.¹⁵ After air-cleaved surfaces are degassed in UHV at 200 °C for 2 h, the crystallites are 1–5 nm in diameter,¹⁵ but larger crystallites up to a micrometer in size form after prolonged drying at very low humidities,¹² presumably due to an Ostwald ripening process. At higher humidities (>50–60%), no crystallites are observed, in agreement with the high water solubility of K_2CO_3 (~8 m). Dissolution of the crystallites affects the properties of water condensed on mica from water vapor, and capillary condensates of pure water can only be obtained if the potassium ions are exchanged for hydrogen ions by dipping the mica surface in a weakly acidic solution (pH = 3).¹⁶ The only ions then present on the surface are hydrogen ions, which cannot give rise to any solid solute.

*To whom correspondence should be addressed. E-mail: h.k.christenson@leeds.ac.uk.

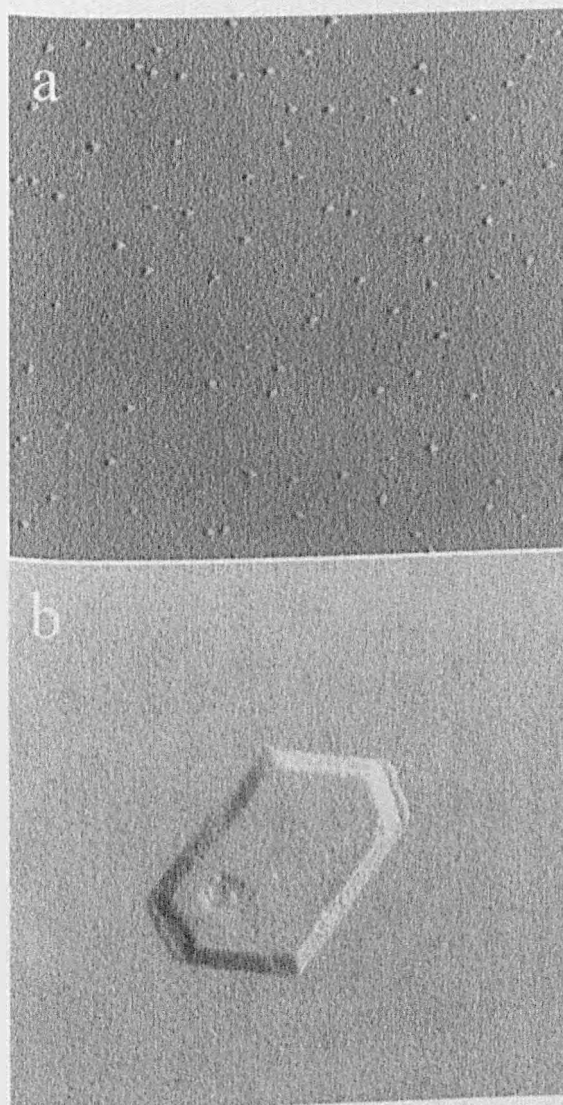


Figure 1. Transmission electron micrographs (image size $1 \times 1 \mu\text{m}$) of carbon replicas of mica surfaces:¹² (a) weathered at 100% humidity before drying over P_2O_5 for 2 days, revealing a large number of small K_2CO_3 crystallites; (b) weathered at 50% humidity for 1 h before drying over P_2O_5 for 2 weeks, showing a single, larger K_2CO_3 crystal. Reprinted from ref 12, copyright 1987, with permission from Elsevier.

In this paper, we show that muscovite mica can be successfully used to support the epitaxial growth of calcite, but only after weathering at low humidity. In particular, freshly cleaved mica does not promote epitaxy of calcite. Face-selective, templated growth of calcite has been reported on substrates such as self-assembled monolayers (SAMs) of ω -substituted alkanethiols on gold,^{17,18} Langmuir monolayers,^{19–21} functionalized polymer surfaces,²² and a number of minerals including lithium niobate,²³ dolomite²⁴ and zabuyelite (Li_2CO_3).²⁵

As the most abundant and stable of the CaCO_3 polymorphs, calcite is of biological, geological, and industrial importance.²⁶ It can be precipitated easily from aqueous solution and has a simple trigonal structure defined by a single 3-fold c -axis. Calcite is a widely used filler in a range of materials including paints, ceramics, powder coatings, and plastics. Elaborate calcite structures are common in nature,

and the control mechanisms involved in biomineralization in organisms such as sea urchins and molluscs are currently receiving significant attention due to the potential for the synthesis of advanced materials and not least because it is interesting in its own right.²⁶ Thanks to a large number of studies, there is a wealth of available knowledge of the nucleation and growth processes of calcite, both *in vivo* and *in vitro*.

Materials and Methods

Microscope-slide size pieces ($75 \times 25 \text{ mm}^2$) of muscovite mica (S&J Trading, New York, or Watanabe Co., Japan) were cleaved from both sides to a thickness of $\sim 50 \mu\text{m}$ at room temperature ($21\text{--}26^\circ\text{C}$). Samples weathered at ambient humidity (35–40%) were cleaved in a laminar flow cabinet, whereas samples weathered at 100% humidity were cleaved in a pre-equilibrated, humid glovebox and left to stand at 100% humidity for up to 3 days, before being immersed vertically in solution. Calcium carbonate was precipitated from aqueous solution using a double decomposition method adapted from the procedure described by Park et al.²⁷ whereby equal amounts of 4–20 mM equimolar aqueous solutions of CaCl_2 and Na_2CO_3 (Sigma–Aldrich) are mixed. After a growth period varying between 5 min and 24 h, the samples were rinsed with Milli-Q water before drying under a nitrogen stream. Scanning electron microscopy (SEM) images were obtained using a LEO 1530 FEG-SEM or a JEOL Neoscope benchtop SEM, for which samples were coated with a 5 nm Pt layer. Crystal sizes and orientations were determined using Image J software, with simulations of calcite orientations performed using SHAPE, v.7.3.1., which permits the measurement of the interfacial angles around the 3 fold c -axis and matches them to those of a simulated calcite crystal at a specified orientation.²⁸ X-ray diffraction (XRD) analysis was done with a Siemens Bruker D500 Theta/2theta X-ray powder diffractometer equipped with a 1.5405 Å Cu K α radiation source, measuring over a 10° to 60° 2θ range at a counting rate of $0.01^\circ 2\theta \text{ s}^{-1}$.

Results

Nonoriented calcite rhombohedra, bounded by $\{104\}$ faces, were observed on precipitation of calcite from a 10 mM solution onto freshly cleaved mica (Figure 2a), with ca. 20% of the CaCO_3 precipitating as vaterite (cf Table 1). Surfaces weathered at ambient humidity (35–40%) for 3 days prior to crystal growth supported the growth of a high density of oriented calcite crystals (Figure 2b,c). The crystals were oriented with the $[001]$ axis perpendicular to the substrate, as shown morphologically with the interfacial angles around the 3-fold c -axes all equal to 120° and by XRD (Figure 3). Lateral alignment of the interfacial angles was observed over a distance spanning the entire sample, in agreement with the absence of grain boundaries on the mica sheets. The orientations of the different calcite rhombohedra corresponded to 60° increments in rotation, as expected for the 3-fold c -axis on the hexagonal mica surface (Figure 2c). Measurements of the relative orientation of a sample of 30 adjacent calcite crystals showed a narrow distribution of angles with a spread of 6° and a standard deviation of 2° .

XRD spectra confirmed the epitaxial growth of calcite, despite the large background from the oriented mica substrate (Figure 3),²⁹ which was perpendicular to the plane of the incident and reflected X-ray beam. The intensity of the (006) calcite peak relative to the (104) peak is 200 times greater than in a powder spectrum,²⁹ showing convincingly that the (001) plane of calcite is aligned preponderantly parallel to the mica basal plane.

One hour of weathering at 35–40% was sufficient to ensure that almost all crystals precipitated on the mica were oriented (Table 1), and further increase in weathering tended merely to

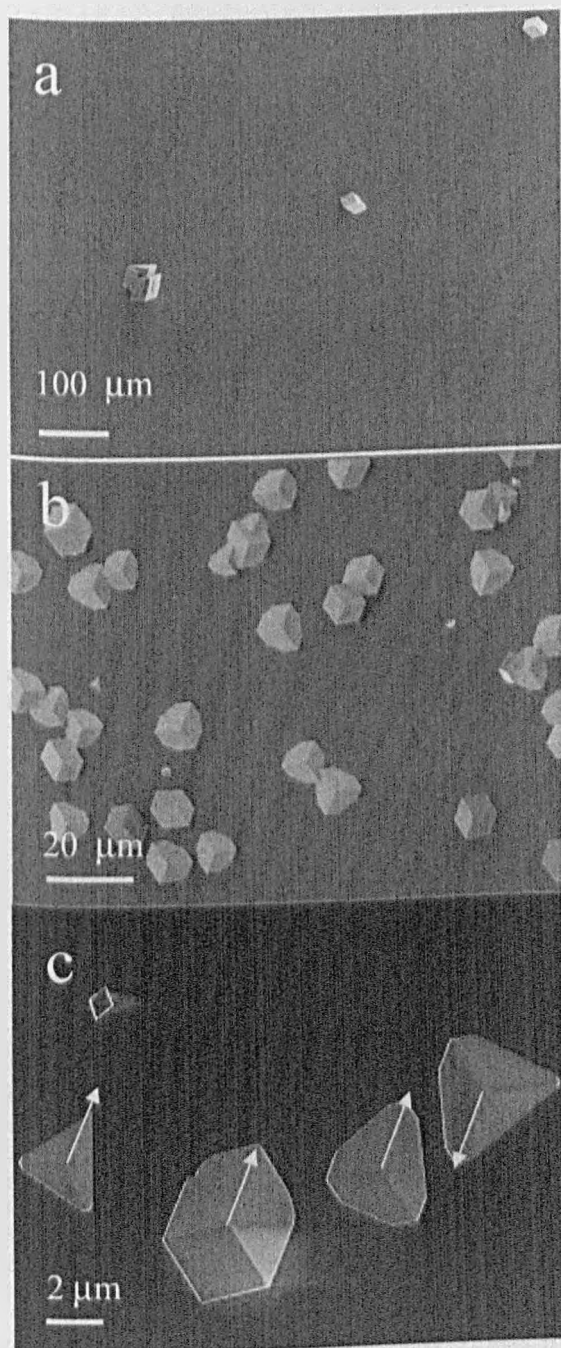


Figure 2. SEM images of calcite precipitated on (a) freshly cleaved mica and (b,c) mica weathered at 35–40% humidity for 3 days, grown for 2 h (a,b) or 1 h (c) from 10 mM solutions. Note the different scales of the three images. The relative number density of crystals and their size in panel a compared with those in panel b is typical. Panel c shows epitaxial calcite crystals with arrows to distinguish the two different orientations.

reduce slightly the number density without changing the proportion of epitaxial crystals. Na_2CO_3 and CaCl_2 solutions mixed at 10 mM and above were cloudy, in agreement with previous observations,³⁰ whereas solutions below this concentration remained clear. The cloudiness is due to the precipitation of amorphous calcium carbonate (ACC) in the form of 10–50 nm diameter spherules at higher supersaturations.^{31,32} Despite this, the epitaxy did not appear

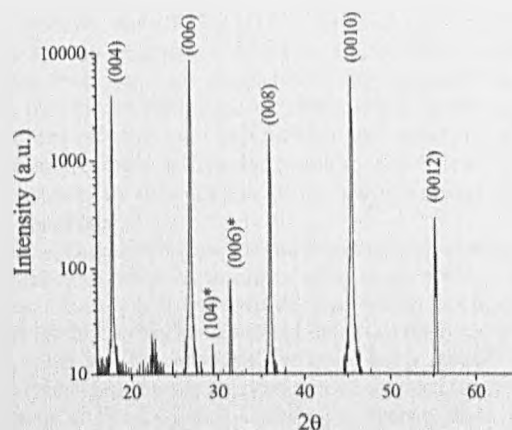


Figure 3. 2θ XRD spectrum of oriented calcite crystals grown for 2 h from a 10 mM solution on a sheet of weathered mica. The mica sheet is perpendicular to the plane of the incident and reflected X-ray beam and shows only reflections from layers parallel to the basal plane. These (no asterisks) are considerably more intense than the calcite peaks (asterisks) due to the much larger amount of material.

Table 1. Number Density and Percentage Oriented Calcite According to Weathering Conditions^a

weathering condition	crystal per mm ²	% calcite	% (001) calcite
freshly cleaved	31 ± 20	81 ± 7 ^b	4 ± 2
0.5 h at 35–40% humidity	60 ± 30	97 ± 2 ^b	7 ± 4
1.0 h at 35–40% humidity	4200 ± 300	100	93 ± 2
1.5 h at 35–40% humidity	1500 ± 700	97 ± 2	91 ± 1
72 h at 35–40% humidity	900 ± 200	100	96 ± 2
H ⁺ ion exchanged prior to 1 h at 35–40% humidity	57 ± 5	87 ± 4 ^b	0
5 min H ₂ O immersion after 1 h at 35–40% humidity	66 ± 17	100 ^b	0
1.5 h weathering at 100% humidity	350 ± 160	86 ± 9 ^b	0

^aAll crystal growth in 10 mM CaCl_2 and Na_2CO_3 solutions for 2 h.

^bMainly nonoriented {104} rhombohedra.

to depend on the concentration in the range of 4–20 mM. Epitaxial crystals were apparent already after 5 min growth time on weathered mica, but there was a range in crystal sizes even after 24 h of growth.

Mica weathered at 100% humidity in a glovebox for a time of 1.5 h did not support the epitaxial growth of calcite crystals (Table 1), and this did not change after weathering for 3 days. Likewise, no epitaxy was found with mica weathered for 3 days at ambient humidity and then immersed for 1 h in either CaCl_2 or Na_2CO_3 solution before the second solution was added to initiate precipitation. No epitaxy could be observed when the surface potassium ions of the mica were exchanged for hydrogen ions before crystals were grown (so that no K_2CO_3 crystallites can form), whether by ion exchange in HCl (pH = 3.0) for 5 min or in Milli-Q water for 1 h. Five minutes immersion in water after weathering for 1 h was sufficient to prevent any epitaxial growth of calcite (Table 1). In all cases, epitaxy was verified on control samples cut from the original weathered mica sheet before treatment by the above methods.

Discussion

The spacing between adjacent K⁺ sites on mica is 0.518 nm,²⁸ and the Cu–Ca spacing of calcite in the (001)

plane is 0.499 nm,²⁸ corresponding to a lattice mismatch of under 4%, which is a better fit than for most of the alkali halides. On the assumption that lattice match governs epitaxial growth, the surprising fact would not be why epitaxy occurs but rather why freshly cleaved mica does not support epitaxy. The obvious difference between freshly cleaved mica and mica weathered in a dry atmosphere is the presence of K_2CO_3 crystallites on the latter. The mica weathered at 100% humidity and the hydrogen mica also lack crystallites, and consequently neither supports epitaxy. The effect of the crystallites must be immediate upon mixing of the solutions because they dissolve very quickly due to the high solubility (8 m) of K_2CO_3 , as shown by the lack of epitaxy when the mica was immersed in either the Na_2CO_3 or the $CaCl_2$ solution before mixing. Five minutes of immersion in water after weathering but prior to crystal growth was also enough to preclude epitaxy.

Ostendorf et al.¹⁴ found a $K^+ - K^+$ spacing of 0.57 ± 0.05 nm for the K_2CO_3 crystallites, giving a lattice mismatch between calcite and the K_2CO_3 crystallites of $\sim 14\%$, which is considerably larger than that between calcite and mica. It hence seems unlikely that the K_2CO_3 crystallites themselves provide the substrate on which epitaxial growth occurs, although the results with NaCl on mica show that surprisingly large mismatches can give rise to epitaxy. Calcite and the alkali halides that show epitaxy on mica differ significantly in their respective water solubilities. The saturation concentrations of the alkali halides are of the order of 1–10 M, compared with a saturation concentration of $CaCO_3$ of about 1 mM or a difference of up to 4 orders of magnitude. The concentration of ions near a surface must have an important influence on the nucleation of epitaxial crystals, and it has been shown that the critical supersaturation for crystal nucleation in some cases increases with lattice mismatch.³³ Moreover, there is one additional factor that increases the difference between alkali halides and calcite. Unlike the alkali metal ions Na^+ , K^+ , and Cs^+ , which adsorb relatively strongly³⁴ to the negatively charged mica surface even from dilute (millimolar) solution, Ca^{2+} only adsorbs significantly to mica surfaces at concentrations above 0.1 M,^{35,36} which is much higher than that of the solutions used here. The large free-energy cost of removing water from the strongly hydrated calcium ions hinders adsorption at lower concentrations. The presence of sodium ions from the carbonate in our solutions would further reduce the adsorption³⁷ by competing for the negative sites on the mica surface.

On the weathered mica, however, the thin (only a few nanometers thick)¹⁴ K_2CO_3 crystallites that are transiently present after mixing the solutions form areas where calcium ions may more readily approach the surface, and furthermore the K_2CO_3 itself provides a source of carbonate ions near the surface. It seems natural to assume that the nucleation and subsequent growth of epitaxial calcite crystals are favored by an enhanced concentration of both calcium and carbonate ions. Furthermore, the observed decrease in the number density of epitaxial calcite crystals at prolonged weathering times (Table 1) is consistent with fewer but larger K_2CO_3 crystals that provide fewer viable nucleation sites, as found in the original investigation of the crystallites on mica.¹²

These results provide a very clear example of how epitaxial growth is not necessarily a simple function of lattice match. Epitaxy also requires wetting, as illustrated by the (111) surface of BaF_2 , which matches almost perfectly the basal face of hexagonal ice yet is a poor ice nucleator because ice

only partially wets $BaF_2(111)$.³⁸ Epitaxial growth of ionic crystals from aqueous solution is a much more complex process than vapor- or liquid-phase epitaxy, involving as it must the ion concentration profiles normal to the surface, which are affected by electrostatics and hydration effects. In addition, there is frequently (as in the case of calcite) the necessity of dehydration before incorporation into the growing crystal.³⁹

Our work demonstrates yet another surprising consequence of a relatively short exposure of mica to an ambient atmosphere. Clearly, it is essential for those who use mica as a model surface to be fully aware of details of the history of the mica substrate. For example, we note that a recent⁴⁰ AFM study of calcium carbonate precipitated on mica (from 3 mM solutions of Na_2CO_3 and $Ca(NO_3)_2$) presents SEM micrographs of calcite crystals on mica that appear similar in morphology to our epitaxial calcite crystals. However, the authors do not give sufficient details of the history of the mica surfaces for us to be able to make any useful comparison nor do they comment on possible epitaxy.

We suggest from our results that the crystallites on weathered mica K_2CO_3 are able to induce epitaxial growth on mica by providing patches on the surface where a considerably higher concentration of both calcium and carbonate ions is present briefly after mixing of the $CaCl_2$ and Na_2CO_3 solutions.

Acknowledgment. We acknowledge support from the EPSRC via a DTA for C.J.S. and allocation of some SEM time through the Leeds EPSRC Nanoscience and Nanotechnology Facility (LENNF). We thank Drs M. Ali and Y.-Y. Kim for assistance with XRD and SEM, respectively.

References

- (1) Ehrentraut, D.; Sato, H.; Kagamitani, Y.; Sato, H.; Yoshikawa, A.; Fukuda, T. *Prog. Cryst. Growth Charact. Mater.* 2006, 52, 280–335.
- (2) Lonsdale, K. *Nature* 1968, 217, 56–58.
- (3) Royer, M. *Bull. Soc. Fr. Miner.* 1928, 51, 7.
- (4) van der Merwe, J. H. *Faraday Discuss.* 1949, 5, 201–214.
- (5) Schulz, L. G. *Acta Crystallogr.* 1951, 4, 483–486.
- (6) Lisgarten, N. D. *Trans. Faraday Soc.* 1954, 50, 684–690.
- (7) Sarma, K. R.; Shlichta, P. J.; Wilcox, W. R.; Lefever, R. A. *J. Cryst. Growth* 1997, 174, 487–494.
- (8) Takayanagi, K.; Yagi, K.; Honjo, G. *Thin Solid Films* 1978, 48, 137–152.
- (9) Sato, H.; Shinozaki, S. *Surf. Sci.* 1970, 22, 229–252.
- (10) Muller, K.; Chang, C. C. *Surf. Sci.* 1969, 14, 39.
- (11) Christenson, H. K. *J. Phys. Chem.* 1993, 97, 12034–12041.
- (12) Christenson, H. K.; Israelachvili, J. N. *J. Colloid Interface Sci.* 1987, 117, 576–577.
- (13) Ohnishi, S.; Hato, M.; Tamada, K.; Christenson, H. K. *Langmuir* 1999, 15, 3312.
- (14) Ostendorf, F.; Schmitz, C.; Hirth, S.; Kühnle, A.; Kolodziej, J. J.; Reichling, M. *Langmuir* 2009, 25, 10764–10767.
- (15) Ostendorf, F.; Schmitz, C.; Hirth, S.; Kühnle, A.; Kolodziej, J. J.; Reichling, M. *Nanotechnology* 2008, 19, No. 305705.
- (16) Kohonen, M. M.; Christenson, H. K. *Langmuir* 2000, 16, 7285–7288.
- (17) Aizenberg, J.; Black, A. J.; Whitesides, G. M. *J. Am. Chem. Soc.* 1999, 121, 500–1509.
- (18) Travaile, A. M.; Donners, J. J. M.; Gerritsen, J. W.; Sommerdijk, N. A. J. M.; Nolte, R. J. M.; van Kempen, H. *Adv. Mater.* 2002, 14, 492–495.
- (19) Loste, E.; Diaz-Marti, E.; ZARBAKHSH, A.; Meldrum, F. C. *Langmuir* 2003, 19, 2830–2837.
- (20) Kewalramani, S.; Kim, K.; Stripe, B.; Evmenenko, G.; Dommett, G. H. B.; Dutta, P. *Langmuir* 2008, 24, 10579–10582.
- (21) Pouget, E. M.; Bomans, P. H. H.; Goos, J. A. C. M.; Frederik, P. M.; de With, G.; Sommerdijk, N. A. J. M. *Science* 2009, 323, 1455–1458.

- (22) Berman, A.; Ahn, D. J.; Lio, A.; Salmeron, M.; Reichert, A.; Charych, D. *Science* **1995**, *269*, 515–518.
- (23) Pokroy, B.; Zolotoyabko, E. *Chem. Commun.* **2005**, 2140–2142.
- (24) Garcia, E.; Alfonso, P.; Tauler, E.; Gali, S. *Cem. Concr. Res.* **2003**, *33*, 1449–1456.
- (25) Pastero, L.; Aquilano, D. *Cryst. Growth Des.* **2008**, *8*, 3451–3460.
- (26) Meldrum, F. C.; Cölfen, H. *Chem. Rev.* **2008**, *108*, 4332–4432.
- (27) Park, R. J.; Meldrum, F. C. *J. Mater. Chem.* **2004**, *14*, 2291–2296.
- (28) Archibald, D. D.; Quadri, S. B.; Gaber, B. P. *Langmuir* **1996**, *12*, 538–546.
- (29) Downs, R. T. (2006) The RRUFF Project: an integrated study of the chemistry, crystallography, Raman and infrared spectroscopy of minerals. Program and Abstracts of the 19th General Meeting of the International Mineralogical Association in Kobe, Japan. O03-13 URL: <http://ruff.info/> (September 2009).
- (30) Lose, E.; Park, R. J.; Warren, J.; Meldrum, F. C. *Adv. Funct. Mater.* **2004**, *14*, 1211–1220.
- (31) Ogino, T.; Suzuki, T.; Sawada, K. *Geochim. Cosmochim. Acta* **1987**, *51*, 2757–2767.
- (32) Clarkson, J. R.; Price, T. J.; Adams, C. J. *J. Chem. Soc., Faraday Trans.* **1992**, *88*, 243–249.
- (33) Upreti, M. C.; Walton, A. G. *J. Chem. Phys.* **1966**, *44*, 1936–1939.
- (34) Pashley, R. M. *J. Colloid Interface Sci.* **1981**, *83*, 531–546.
- (35) Pashley, R. M.; Israelachvili, J. N. *J. Colloid Interface Sci.* **1984**, *97*, 446–455.
- (36) Kjellander, R.; Marcelja, S.; Quirk, J. P. *J. Colloid Interface Sci.* **1988**, *126*, 194–211.
- (37) Alcantar, N.; Israelachvili, J.; Boles, J. *Geochim. Cosmochim. Acta* **2003**, *67*, 1289–1304.
- (38) Conrad, P.; Ewing, G. E.; Karlinsey, R. L.; Sadtchenko, V. *J. Chem. Phys.* **2005**, *122*, No. 064709.
- (39) Colfen, H.; Antonietti, M. *Mesocrystals and Nonclassical Crystallization*; Wiley: Chichester, U.K., 2008.
- (40) Yamanaka, S.; Ito, N.; Shimosaka, A.; Shirakawa, Y.; Hidaka, J. *Cryst. Growth Des.* **2009**, *9*, 3245–3250.

Amorphous Calcium Carbonate is Stabilized in Confinement,
C. J. Stephens, S. Ladden, F. C. Meldrum and H. K. Christenson, *Advanced
Functional Materials*, 2010, 13, 2108-2115 .

Amorphous Calcium Carbonate is Stabilized in Confinement

By Christopher J. Stephens, Sophie F. Ladden, Fiona C. Meldrum,* and Hugo K. Christenson*

Biomaterials typically form within localized volumes, affording organisms great control over the mineralization process. The influence of such confinement on crystallization is studied here by precipitating CaCO_3 within the confines of an annular wedge, formed around the contact point of two crossed half-cylinders. The cylinders are functionalized with self-assembled monolayers of mercaptohexadecanoic acid on gold. This configuration enables a systematic study of the effects of confinement since the surface separation increases continuously from zero at the contact point to macroscopic (mm) separations. While oriented rhombohedral calcite crystals form at large ($>10 \mu\text{m}$) separations, particles with irregular morphologies and partial crystallinity are observed as the surface separation approaches the dimensions of the unconfined crystals ($5\text{--}10 \mu\text{m}$). Further increase in the confinement has a significant effect on the crystallization process with flattened amorphous CaCO_3 (ACC) particles being formed at micrometer separations. These ACC particles show remarkable stability when maintained within the wedge but rapidly crystallize on separation of the cylinders. A comparison of bulk and surface free-energy terms shows that ACC cannot be thermodynamically stable at these large separations, and the stability is attributed to kinetic factors. This study therefore shows that the environment in which minerals form can have a significant effect on their stability and demonstrates that ACC can be stabilized with respect to the crystalline polymorphs of CaCO_3 by confinement alone. That ACC was stabilized at such large (micrometer) separations is striking, and demonstrates the versatility of this strategy, and its potential value in biological systems.

chemical reactions can be dramatically affected by confinement, stimulating a rapidly growing interest in this effect.^[1,2] For example, protein folding and macromolecular interactions can be affected by confinement, which mimics the crowded environment proteins inhabit *in vivo*.^[2,3] This Full Paper focuses on the influence of confinement on one important category of biological processes: biomineralization, the generation of mineral-based structures such as bones and teeth by organisms. It has long been recognized that biomaterials form within the confines of "privileged environments" delineated from the organism, where spatial constraints and chemical conditions can be precisely controlled.^[4,5] Within these localized microenvironments organisms actively select the mineral phase, and determine the morphology, orientation, and location of the biomaterial product through control of precursor ions and phases, and via interaction with soluble organic macromolecules and insoluble organic matrices.

Although biomineralization invariably occurs within restricted volumes, experiments aiming to mimic these processes are generally carried out in bulk solution. However, there are many crystallization phenomena, such as the precipitation of hydroxyapatite nanocrystals in the gaps in

collagen fibers during bone formation, that cannot be adequately described in terms of crystallization from bulk solution.^[6,7] Indeed, it is immediately clear that confinement must have a significant influence on mineral formation as the relative importance of surface and interfacial energies increases.^[8] In addition, the interaction of a growing crystal with soluble macromolecules and the aggregation behavior of precursor mineral particles will change in constrained volumes.

Naturally, some systems that offer restricted reaction volumes have been used to produce crystals with controlled sizes and morphologies. Looking specifically at experiments related to biomineralization, surfactant phases including microemulsions have been used to prepare particles with a range of shapes and polymorphs (e.g., References [9–11]), but due to the number of experimental variables and their dynamic nature, these systems are not well suited to systematic studies of the effects of confinement. Porous single crystals of calcite have been grown within templates such as colloidal crystals^[12] and porous polymer

1. Introduction

A fundamental characteristic of biological systems is that their organization and function are based on compartmentalization. Indeed, there is an increasing realization that biological and

[*] Prof. F. C. Meldrum
School of Chemistry
University of Leeds
Leeds LS2 9JT (UK)
E-mail: f.meldrum@leeds.ac.uk

Dr. H. K. Christenson, C. J. Stephens, S. F. Ladden
School of Physics and Astronomy
University of Leeds
Leeds LS2 9JT (UK)
E-mail: h.k.christenson@leeds.ac.uk

DOI: 10.1002/adfm.201000248

membranes,^[13–15] while ice templates have been used to form porous hydroxyapatite/collagen composites.^[16] Showing that the local reaction environment can affect crystallization, CaCO_3 was precipitated within deformed collagen matrices and different crystal morphologies and polymorphs were obtained according to the extension of the matrix.^[17,18] Considering mesoscale environments, a low density of calcium phosphate (CaP) nanoparticles were precipitated within mesoporous silica.^[19] Many investigations have precipitated hydroxyapatite in association with collagen fibrils.^[20] In a classic study, Glimcher observed that hydroxyapatite could nucleate in the hole zones of collagen, producing structures resembling embryonic bone,^[7] while approaches such as crystallization during fibrillogenesis^[21] or in the presence of anionic polymers^[22] have yielded some evidence of crystallization in the hole regions. In another article, a polymer-induced liquid precursor phase (PILP) of CaP was used to infiltrate collagen fibrils. Hydroxyapatite crystals nucleated within the gap regions of the fibrils, producing a material structurally similar to bone.^[6]

Of particular relevance to the current experiments, a small number of studies have investigated how amorphous CaCO_3 (ACC) forms within constrained volumes. While traditional models of CaCO_3 biomineralization considered this to proceed by a combination of ions pumped into the mineral deposition site,^[4] it is now well established that formation of calcite and aragonite in biological systems frequently proceeds via ACC precursor phases, where the ACC precipitated within localized environments subsequently crystallizes to give either single-crystal or polycrystalline crystal phases.^[12,23] ACC was precipitated within the confines of the rod-shaped pores perforating track-etch membranes, and crystallization yielded single crystals of calcite with high aspect ratios.^[24,25] Precipitation of ACC within a mould comprising two planar substrates separated by a regular array of pillars, and subsequent controlled nucleation at a single, defined site, yielded either polycrystalline calcite at pillar separations of less than 15 μm , or millimeter-sized calcite crystals at larger separations.^[26] It was suggested that the micropattern provided a “microsump” for the release of excess water during the ACC to calcite transition, which appeared to occur by mass transport between the amorphous and crystalline phases. Both of these sets of experiments therefore suggest that confinement can strongly affect the mechanism of crystallization of ACC.

In the experiments described here we employ a simple model system that enables a systematic investigation of the effect of a restricted crystallization environment on the precipitation of CaCO_3 . CaCO_3 biominerals are extremely widespread, and much of our understanding of biomineralization processes comes from studying their formation. It therefore provides an excellent model system for study. We use gold-coated glass half-cylinders bearing self-assembled monolayers (SAMs) of mercaptohexadecanoic acid (MHA) to generate a well-defined surface on which to grow crystals. Such SAMs are known to promote oriented, face-selective growth of CaCO_3 (calcite) crystals.^[27,28] A crossed-cylinder configuration creates an annular wedge, which offers separations ranging continuously from angstroms to macroscale and enables easy assay of the effects of confinement in a single experiment. The surface separation h between crossed cylinders of equal radius of curvature R is equal to that between a sphere of radius R and a flat surface (Figure 1a–c), and is related to the radial distance x from the

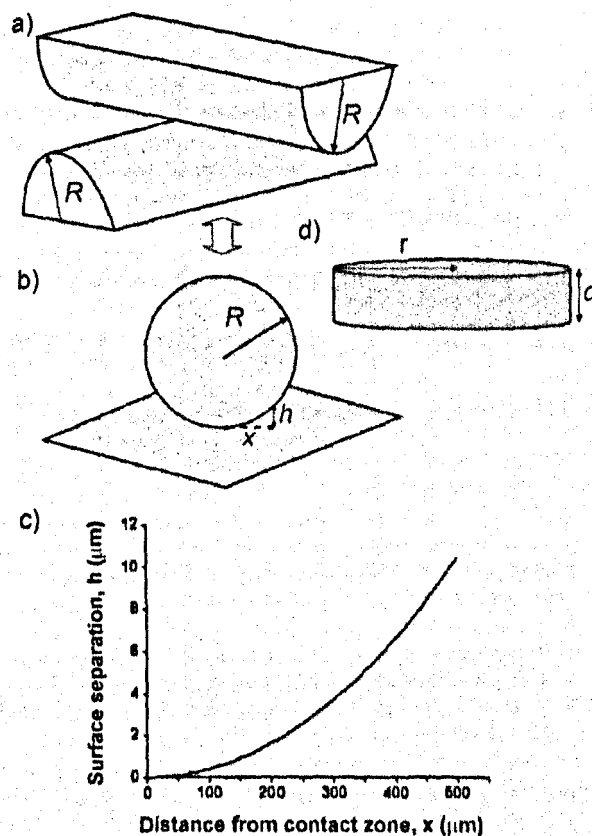


Figure 1. a) Schematic diagram of the crossed-cylinder configuration with radius of curvature R , b) the equivalent sphere-on-a-flat configuration, with the surface separation h , related to the distance from contact x , and R by Equation (1), c) the surface separation h plotted as a function of distance x to the contact point, and d) the disc of radius r and thickness d used to model the amorphous precipitates.

contact point by:

$$h = R - \sqrt{R^2 - x^2} \approx x^2/2R \quad (1)$$

Thus, h varies continuously from zero around the contact point to 2–3 mm at the vapor interface of the solution droplet, some 7–8 mm from the contact point. While the focus of most experiments mimicking biomineralization processes is on the role of soluble and insoluble organic macromolecules in modulating features such as polymorphism, crystal size, orientation, and morphology, the current experiments investigate the possibility that nature uses confinement alone as a mechanism of controlling biomineral formation.

2. Results and Discussion

CaCO_3 was precipitated by either placing a drop of a metastable solution of calcium carbonate in the wedge and allowing precipitation to occur with time, or by placing a drop of calcium chloride solution in the wedge and then exposing the set-up to ammonium carbonate vapor. Precipitation on isolated glass surfaces yielded almost identical results for both experimental

methods, with mostly randomly oriented rhombohedral calcite crystals, and the remainder aragonite and/or vaterite. In contrast, oriented calcite crystals were obtained on the MHA SAMs, in keeping with published data.^[28,29] Both precipitation methods supported the growth of calcite rhombohedra only, although the orientation control varied according to the method used. With gas diffusion, approximately 85% of the calcite crystals nucleated parallel to either the (012) or (015) planes, while only 45% of the calcite crystals were in these orientations with the double-decomposition method. This agrees with observations that the orientation of calcite on MHA SAMs is pH-dependent^[28] and

hence differs between the double-decomposition and the gas-diffusion methods.

The nucleation densities, orientations, and morphologies of the CaCO_3 crystals precipitated at surface separations greater than $10\ \mu\text{m}$ were similar to those of crystals grown on the isolated control surfaces (Figure 2a). Crystals grown using the gas-diffusion method had maximum dimensions of $5\text{--}15\ \mu\text{m}$ whereas the double-decomposition growth method yielded slightly smaller crystals of $2\text{--}10\ \mu\text{m}$, with the size dependent upon the growth period and solute concentration, yet independent of whether the crystals were grown on isolated surfaces or at large surface separations. An influence of the dimensions of the precipitation environment was observed at surface separations below $\approx 10\ \mu\text{m}$, where significant changes in the crystal habits were observed. At these separations the particles produced were typically $\approx 5\ \mu\text{m}$ in size for the gas-diffusion method (slightly smaller for the double-decomposition method) and no longer exhibited well-defined rhombohedral

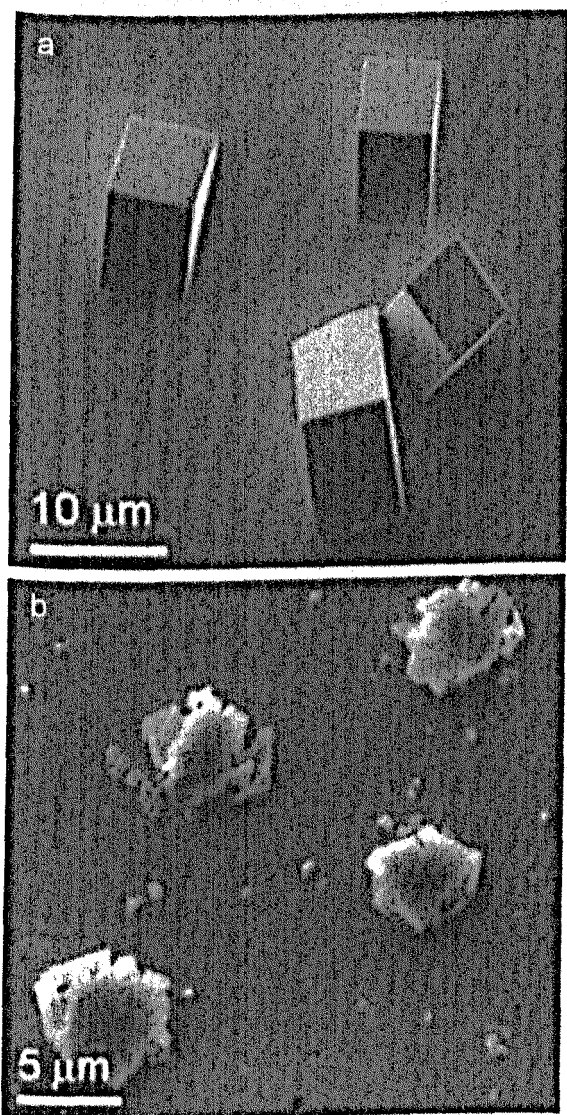


Figure 2. Representative SEM images of CaCO_3 precipitated between crossed cylinders coated with MHA using the gas-diffusion method. a) At millimeter separations the face-selective growth of well-defined calcite rhombohedra occurs as on isolated MHA surfaces ($[\text{Ca}^{2+}] = 4\ \text{mM}$ for 24 h). b) At surface separations of about $10\ \mu\text{m}$ the particles are of irregular morphology with a flattened top surface and geometric facets around the edges ($[\text{Ca}^{2+}] = 8\ \text{mM}$ for 24 h).

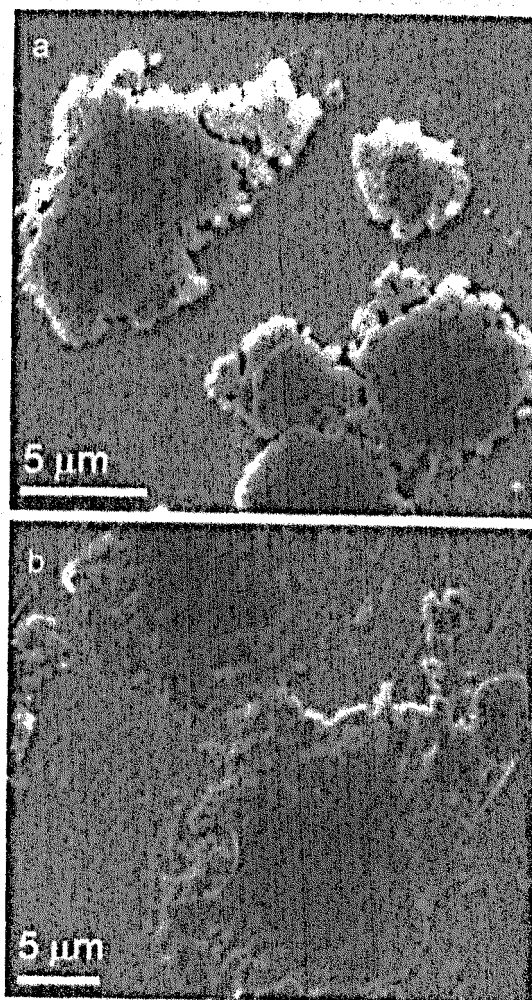


Figure 3. Representative SEM images of CaCO_3 precipitated between MHA-coated crossed cylinders using the gas-diffusion method with $[\text{Ca}^{2+}] = 8\ \text{mM}$ at approximate surface separations of a) $2\ \mu\text{m}$ and c) $0.5\ \mu\text{m}$. As the separation decreases the particles become less geometric and more amorphous in character.

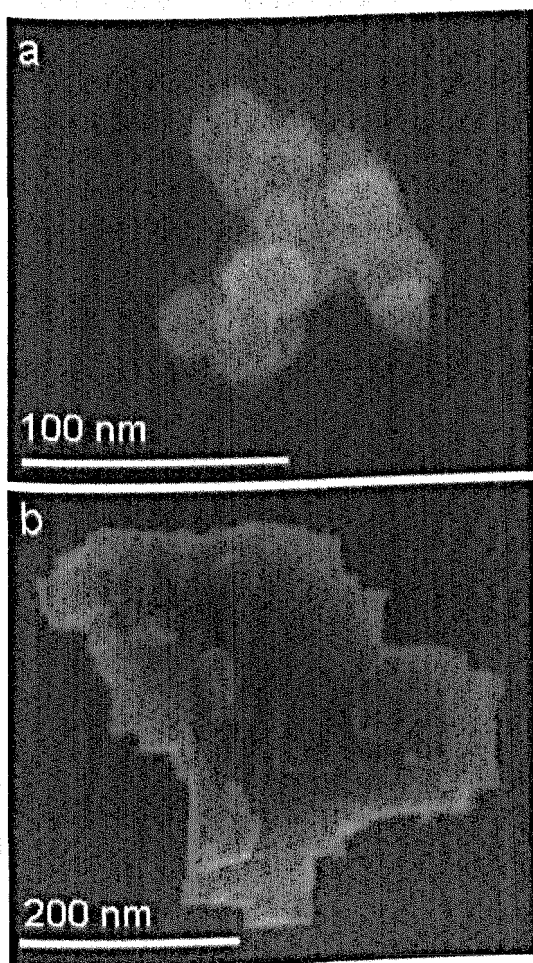


Figure 4. Representative high-resolution SEM images of smaller CaCO_3 particles found between MHA-coated crossed cylinders at a submicrometer surface separation, adjacent to the contact region, using the gas-diffusion method with $[\text{Ca}^{2+}] = 4 \text{ mM}$. a) After termination of growth with the surfaces still in contact aggregates of 10–25-nm spherical particles, morphologically consistent with ACC, are found. b) If the growth is terminated 1 h after separation of the surfaces in the depleted solution the particles exhibit planar edges and faces, consistent with a transformation to a more crystalline material.

forms, but were irregular in shape. They were bounded by many small faces morphologically indicative of calcite, but had flattened upper surfaces (Figure 2b). An effect on the particle morphology of the constraining volume was apparent in that the edges of the particles became increasingly irregular with greater confinement, and as shown in Figure 3a and b for a surface separation of $\approx 2 \mu\text{m}$ and $\approx 0.5 \mu\text{m}$, respectively. At surface separations of $< 0.5 \mu\text{m}$, that is, within $\approx 100 \mu\text{m}$ from the point of contact, the particles were about $10 \mu\text{m}$ in diameter, and roughly circular in shape. With no morphological features characteristic of a crystalline material, these suggested instead an amorphous precipitate (Figure 3b). Examination of the region close to contact at a higher resolution showed the presence of aggregates of 10–50-nm spherical particles, which are typical of ACC (Figure 4a). Accordingly, the possibility that the particles precipitated at this degree of confinement were amorphous was investigated by studying their stability in solution.

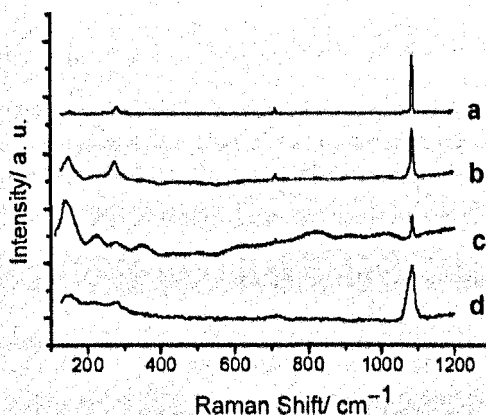


Figure 5. Raman spectra of CaCO_3 precipitated between MHA-coated crossed cylinders at different surface separations h with precipitation by the double-decomposition growth method, $[\text{Ca}^{2+}] = 5 \text{ mM}$. a) $h \approx 3 \text{ mm}$, b) $h \approx 10 \mu\text{m}$, and c) $h \approx 0.5 \mu\text{m}$. d) Synthetic ACC precipitated from high-pH solutions using the method outlined by Koga et al.^[56]

After one 24 h precipitation experiment the cylinders were separated to a distance of approximately 5 mm and the exposed particles were incubated in the (depleted) growing solution for 1 h. After this treatment the particles showed clear evidence of crystallization to calcite, as suggested by development of well-defined faces and edges (Figure 4b).

That constraining the precipitation volume resulted in stabilization of amorphous calcium carbonate with respect to calcite was also confirmed using Raman microscopy of individual particles. Calcite has five fundamental Raman-active peaks (not all visible in Figure 5a) and is easily distinguished from aragonite and vaterite by the unique position of the internal E_g modes at 711 cm^{-1} , which correspond to the in-plane bending of the carbonate ions (ν_4).^[30] Synthetic ACC was differentiated from calcite by i) the characteristic broadening of the internal A_{1g} carbonate bending mode, centered at 1086 cm^{-1} , ii) a broad peak in the range of $140\text{--}220 \text{ cm}^{-1}$, and iii) an absence of the 711 cm^{-1} ν_4 mode (Figure 5d).^[31] Raman microscopy of particles produced at surface separations $> 10 \mu\text{m}$ confirmed that these were calcite, while the spectra of the irregular particles grown at intermediate separations of $2\text{--}10 \mu\text{m}$ also corresponded to calcite (Figure 5b), albeit with a broadening of the 1086 cm^{-1} peak, as expected for a polycrystalline sample.^[32] In contrast, the Raman spectra of the CaCO_3 particles precipitated at submicrometer surface separations (Figure 5c) showed a significant reduction in the intensity of the 1086 cm^{-1} peak, and had several features in common with those of synthetic ACC (Figure 5d), that is, a broad $140\text{--}240 \text{ cm}^{-1}$ peak and the absence of an external E_g mode in the range of $700\text{--}750 \text{ cm}^{-1}$. While most of the morphological studies and the Raman spectrum in Figure 5c were for 24 h growth times, precipitates after 72 h confinement showed similar features. A comparison of the Raman spectra of the same particles before and after heating in a furnace at 180°C showed substantial conversion of ACC into calcite, as shown by an eightfold increase in the intensity of the internal A_{1g} carbonate peak 1085 cm^{-1} , and the emergence of a peak at 711 cm^{-1} , which had been previously absent (Figure 6).

The changes in the morphologies of the precipitates with surface separation convincingly illustrate that confinement in the

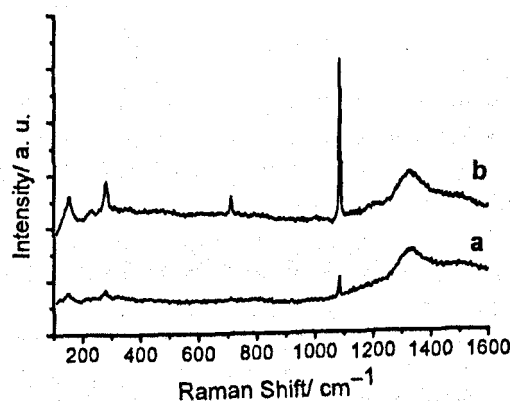


Figure 6. Raman spectra of CaCO_3 precipitated between MHA-coated crossed cylinders using the gas-diffusion method at $[\text{Ca}^{2+}] = 8 \text{ mM}$ a) before and b) after heating overnight at 180°C . The spectra are for the same particle at a surface separation of approximately $1.5 \mu\text{m}$. There was an eightfold intensity increase in the $\text{A}_{1\text{G}}$ internal carbonate bending mode centered at 1086 cm^{-1} , suggesting a significant conversion from ACC to calcite.

annular wedge has a significant influence on crystal growth. Indeed, the habits of the particles were strongly modified when confined between surfaces as far apart as $10 \mu\text{m}$, with flattened particles bounded by irregular, multifaceted edges precipitating. The typical dimensions ($5\text{--}10 \mu\text{m}$) of the calcite crystals on isolated surfaces and at large separations suggest that they could potentially grow all the way from one surface to the second surface at these separations. The flattened calcite surfaces in Figure 2b may therefore result from diffusion-limited growth as the crystals approach the second surface, or perhaps even from direct contact with the second surface.

With increasing confinement, that is, with decreasing surface separation, the modification of the crystal morphologies from the rhombohedra produced in bulk solution becomes successively more marked until all suggestion of crystallinity is lost. The Raman spectra support the picture provided by the scanning electron microscopy (SEM) images, with evidence for increasing polycrystallinity and a greater proportion of ACC in the precipitates as the separation decreases. At submicrometer separations the confined particles appear to consist primarily of amorphous CaCO_3 . That these particles crystallized as calcite, on incubation in solution or through heat treatment, is further strong evidence for their amorphous character. The very flattened appearance of the amorphous precipitates suggests that the particles have grown outwards until they come close to the second surface. When the two half-cylinders are separated at the end of the growth it would be natural to assume that the bond between the precipitate and the surface on which it nucleated is stronger than any adhesion to the second surface. The flat surface of the particles viewed by SEM therefore corresponds to the surface that has grown towards the top substrate. Whether the flattening is mainly a kinetic effect due to restrictions on ion flow between the growing precipitates and the second surface, or whether in some cases the structures have actually made contact with the second surface, is difficult to determine. Our observations also suggest that the nucleation rate is not greatly affected by moderate degrees of confinement, down to surface separations of about $10 \mu\text{m}$, although this was not

quantitatively studied. This is not surprising, as the separations are much larger than the dimensions of a critical nucleus, which would be expected to have a radius of only 1 nm at the supersaturations employed here.

The most surprising feature of our results is the size of these amorphous precipitates, and the separation between the MHA surfaces at which they remain stable. We observe a marked increase in stability of an amorphous phase compared to the crystal at surface separations from hundreds of nanometers up to as much as micrometers. These are much larger surface separations than those at which confinement effects are usually seen. The effect of confinement on the physical properties of matter is primarily due to the increasing importance of the surface free energy compared to the bulk free energy when the surface-area-to-volume ratio increases. This gives rise to phenomena such as melting- and freezing-point depression of substances in porous media, and capillary condensation – the condensation of liquid from under-saturated vapor in narrow pores and cracks. Temperature shifts in solid–solid phase transitions^[33] and the glass transition^[34,35] in confinement have also been documented, as have changes in the relative polymorph stability of crystals precipitated from solution.^[22,36,37] However, such confinement effects are usually only significant enough to be detectable when the dimension of the confining pores is of the order of 100 nm or less. In highly confined systems the normal bulk transitions become smeared out and may vanish altogether,^[8,38,39] although this usually occurs only in nanometer-sized pores, far beyond what we are considering here.

A confinement effect of some relevance to this study is the case of capillary condensation of liquid below the bulk melting point of the substance. Just as the surface free-energy terms stabilize the liquid with respect to the vapor in a pore, they also favor the liquid phase over a crystalline solid. Liquid therefore condenses from vapor in a pore even below the bulk melting point, and the quantitative relation between the amount of condensed liquid and the temperature depression below the melting point has recently been experimentally determined and correlated with theoretical predictions.^[40,41] In these experiments, condensation from saturated vapor below the bulk melting point was studied in the same geometry as here, around the contact point of two crossed cylinders of mica in a surface-force apparatus.^[8,42–45] The condensates remained liquid below the melting point but their size decreased as the temperature decreased, with the surface separation at where stable condensates were found typically in the range of $20\text{--}100 \text{ nm}$ for $1\text{--}6^\circ\text{C}$ of undercooling, in the case of water.^[41]

Phase equilibria involving crystalline phases are considerably more complex than those of fluids (liquids and vapors). The surface free energy of a crystal depends on the lattice plane of the crystal face and is affected by defects, lattice strain, and the possibility of surface rearrangements and reconstructions. However, in the absence of anisotropy, as with amorphous phases such as ACC, we may expect a situation comparable to that of a liquid-vapor system. The surface free energy of ACC would be expected to be lower than that of calcite (or vaterite and aragonite), and contact between ACC and a solid substrate should be more favorable than contact between calcite and the substrate. ACC confined between the two MHA surfaces would hence be stabilized with respect to calcite.

If we model the amorphous precipitates close to the contact zone as discs of radius r and thickness d (Figure 1d) we can estimate the thermodynamic stabilization of a disc of ACC with respect to

crystallization to calcite. We assume that the surfaces are locally flat, and that the total free-energy difference ΔG consists of a bulk term ΔG_{bulk} and a surface term ΔG_{surf} . The surface free-energy change for crystallization is given by

$$\begin{aligned}\Delta G_{\text{surf}} &= 2\pi r^2(\gamma_{\text{S/calc}} - \gamma_{\text{S/ACC}}) + 2\pi r d(\gamma_{\text{W/calc}} - \gamma_{\text{W/ACC}}) \\ &= 2\pi r(r\Delta\gamma_{\text{S}} + d\Delta\gamma_{\text{L}})\end{aligned}\quad (2)$$

where $\gamma_{\text{S/calc}}$, $\gamma_{\text{S/ACC}}$, $\gamma_{\text{W/calc}}$, and $\gamma_{\text{W/ACC}}$ are the free energies of the substrate–calcite interface, the substrate–ACC interface, the water–calcite interface, and the water–ACC interface, respectively. $\Delta\gamma_{\text{S}}$ and $\Delta\gamma_{\text{L}}$ are the differences according to Equation (2). The bulk term is

$$\Delta G_{\text{bulk}} = \pi r^2 d \frac{\Delta G_{\text{cryst}}}{V_{\text{M}}}\quad (3)$$

where ΔG_{cryst} is the free energy of crystallization of calcite per mole and V_{M} is the molar volume of calcite. At equilibrium

$$\Delta G = \Delta G_{\text{surf}} + \Delta G_{\text{bulk}} = 0\quad (4)$$

and

$$2(r\Delta\gamma_{\text{S}} + d\Delta\gamma_{\text{L}}) = -rd \frac{\Delta G_{\text{cryst}}}{V_{\text{M}}}\quad (5)$$

$$2\left(\frac{\Delta\gamma_{\text{S}}}{d} + \frac{\Delta\gamma_{\text{L}}}{r}\right) = -\frac{\Delta G_{\text{cryst}}}{V_{\text{M}}}\quad (6)$$

The value of ΔG_{cryst} for the conversion of ACC to calcite may be conveniently found from a precipitation diagram for CaCO_3 polymorphs.^[46] By subtracting the chemical potential change for the precipitation of ACC from solution from the change in chemical potential for calcite precipitation one obtains the change in chemical potential for the crystallization of ACC to calcite. Figure 1 of Reference [46] gives $\Delta\mu = -7.3kT$, or $\Delta G_{\text{cryst}} = -7.3RT = -18 \text{ kJ mol}^{-1}$ at 20°C . With $V_{\text{M}} = 3.7 \times 10^{-5} \text{ m}^3$, and estimating $\Delta\gamma_{\text{S}} \approx 10 \text{ mJ m}^{-2}$, $\Delta\gamma_{\text{L}} \approx 100 \text{ mJ m}^{-2}$, one obtains

$$\left(\frac{0.01}{d} + \frac{0.1}{r}\right) = 0.24\quad (7)$$

where d and r are in nm. Although values of $\Delta\gamma_{\text{S}}$ and $\Delta\gamma_{\text{L}}$ above are only order-of-magnitude estimates, it is clear that for r values of the order of micrometers (1000 nm) d is of the order of 0.1 nm! We therefore conclude that ACC confined between the surfaces cannot be thermodynamically stable at the micrometer-scale separations observed. The reason for the large difference compared to the capillary condensation of water^[41] may be found by comparing the bulk free-energy terms. For confined, under-cooled water $\Delta G = \Delta T\Delta S = \Delta T\Delta H/T_{\text{m}}$, where ΔT is the temperature depression below the melting point T_{m} , and this ΔG is only 132 J mol^{-1} for water at -6°C . For equal volumes the free-energy decrease on crystallization of ACC as calcite is almost 70 times larger than the free-energy gain on freezing water at -6°C ! Also, the surface free-energy terms for ACC and calcite are

most likely smaller than for ice and water, further reducing the confinement effect. The very large bulk free-energy gain on crystallization of an amorphous phase hence easily dominates over surface energy effects at all but the smallest surface separations, of the order of 1 nm or less. We note that a similar conclusion was reached in a recent model calculation of the transformation of ACC to calcite.^[47]

Clearly, thermodynamics cannot explain the presence of ACC between the surfaces in the wedge, and the answer must lie in kinetic stabilization. The rate of the conversion of ACC into calcite may be retarded by confinement, especially if the crystallization proceeds via a dissolution–reprecipitation mechanism. The similarity of the precipitates after 24 and 72 h growth times suggests that the kinetic stabilization is significant. Restricted contact between the amorphous precipitates and the solution would certainly be expected to be important in this case.

That ACC is stabilized within small volumes with respect to the crystalline polymorphs of CaCO_3 such as calcite and vaterite has implications for our understanding of biomineralization processes. It is generally accepted that organic macromolecules, acting in combination with ions such as magnesium and phosphate, are involved in the stabilization of ACC in vivo, tuning its stability such that crystallization of transient ACC can be triggered as desired.^[48,49] The work presented here suggests that in addition to soluble additives, organisms may also use confinement as a means to stabilize and control the crystallization of amorphous precursor phases. That this effect is kinetic rather than thermodynamic in origin is intriguing, as is our suggestion that this derives from the restricted contact between the ACC precipitates and solution. Synthetic ACC shows long-term stability when isolated from aqueous solution, or when precipitated from non-aqueous solvents such as ethanol^[50] (despite containing a similar quantity of structural water to ACC precipitated from aqueous solution^[51]). Sea urchin larval spicules form via a precursor ACC phase, within a membrane-bounded compartment, where the membrane is in direct contact with the surface of the spicule; no intermediate water is observed.^[52]

The role of water in the crystallization of ACC – and indeed, more generally, the mechanism of crystallization of ACC – is poorly understood. A recent study examining the formation of sea urchin larval spicules showed that these form via a hydrated ACC phase, similar in composition to synthetic ACC, which then dehydrates to give anhydrous ACC.^[53] Crystallization subsequently occurs in the absence of a well-defined crystallization front to give a single crystal of calcite, possibly via secondary nucleation, where crystalline domains trigger the crystallization of adjacent ACC domains. Aizenberg's study of ACC crystallization within an array of pillars^[26] suggested that a dissolution–reprecipitation mechanism operated in this system. Further suggestion that contact of ACC with water affects its crystallization was shown by crystallization of ACC within the cylindrical pores of track-etch membranes.^[24,25] Single crystals of calcite were obtained within small (0.2–5 μm) pores that completely filled with ACC prior to crystallization, while polycrystalline particles were obtained in larger (10 μm) pores that only partially filled prior to crystallization, thus exposing a large fraction of the surface to the solution. The results obtained here support these latter studies, suggesting that the availability of a dissolution–reprecipitation pathway can affect the stability and crystallization mechanism of ACC.

4. Conclusions

We have shown that the environment in which minerals form can have a significant effect on their stabilities and mechanisms of crystallization, and demonstrated that ACC can be stabilized with respect to the crystalline polymorphs of CaCO_3 by confinement alone. That stabilization of ACC was achieved in the current system at micrometer-scale separations clearly demonstrates the versatility of this strategy and its potential value in biological systems. This effect was readily reversed by removal of the confining surface, and as the stabilization in our model system appears to be a kinetic, rather than a thermodynamic effect, it is envisaged that crystallization in this case could also be triggered on introduction of a suitable nucleating agent or surface. Therefore, while precipitating minerals within localized environments is fundamental to biologically controlled biomineralization processes, it can be suggested that confinement – and specifically the large ratio of mineral/organic surface area to mineral volume – also provides organisms with an additional mechanism of control over mineral formation.

4. Experimental

Glass tubing with an outer diameter of 25 mm was cut to produce 25-mm-long half-cylinders. The half-cylinders were cleaned by immersing in a NaOH (10% w/v) solution for 2 h under sonication, followed by 10 min in an argon plasma cleaner, prior to rinsing with Millipore (18.2 M Ω) water. The half-cylinders were coated with a 2-nm Cr film, followed by a 50–150-nm Au layer (Goodfellow, 99.99%) using a Cressington 308R high-vacuum coating system, with a deposition rate of 0.1 nm s⁻¹. The gold surfaces were then functionalized with SAMs of MHA (Sigma–Aldrich 99%) by immersing the half-cylinders in a dichloromethane solution of MHA (0.1 mM) at 4 °C for 24 h. Subsequently, the cylinders were rinsed in dichloromethane, dried under nitrogen, and mounted with the curved surfaces facing each other with the cylinder axes orthogonal to each other. The surfaces were brought into contact by slowly increasing the force applied to the top surface.

CaCO_3 was precipitated from a 0.2–0.3 mL drop of solution (4–10 mM) held by capillary action around the crossed half-cylinders in contact, using double-decomposition or gas-diffusion methods. In the double-decomposition method, equimolar aqueous solutions of CaCl_2 and Na_2CO_3 (Sigma–Aldrich) were combined in equal volumes, and CaCO_3 precipitation occurred with time [25]. The gas-diffusion method was performed by exposing a droplet of CaCl_2 solutions to CO_2 generated on decomposition of $(\text{NH}_4)_2\text{CO}_3$ in a sealed desiccator [54]. In both cases precipitation was terminated after 24 h (72 h in the case of one experiment) by flushing the system with Milli-Q water while the surfaces were still in contact. The half-cylinders were then slowly separated and dried under a stream of nitrogen. Control experiments on isolated surfaces were carried out with bare and MHA-coated 25 × 75-mm glass microscope slides. The coating procedure was identical to that used with the half-cylinders, and crystallization was carried out using the gas-diffusion and double-decomposition methods by suspending the slides vertically in 50 mL of solution.

The precipitates were imaged with SEM and analyzed using Raman microscopy. SEM was carried out using either a Phillips XL-30 ESEM or a Leo 1530 Gemini FEG-SEM, after coating the samples with a 5-nm layer of Pt. The region around the contact point of the half-cylinders was found by identifying a region devoid of precipitates on the SEM micrographs. The approximate magnitude of x for the precipitates was then determined by estimating the distance to this contact region, and the surface separation h calculated from Equation (1). The orientations of calcite crystals were determined using the method outlined by Archibald et al. [55] by measuring the projected angles around the threefold c -axis of the calcite rhombohedron and matching these to the corresponding angles of

crystals in known orientations, as simulated with the SHAPE program. Raman spectra were acquired using a Renishaw inVia microscope equipped with a 785-nm high-performance near-IR diode laser with a 1- μm spot size.

Amorphous calcium carbonate was synthesized as a reference for Raman spectroscopy using the procedure described by Koga et al. [56]. Briefly, aqueous CaCl_2 (0.1 M) was rapidly mixed with equal amounts of Na_2CO_3 and NaOH (both 0.1 M) solutions at 4 °C, before filtering and washing with ethanol.

Acknowledgements

We acknowledge support from the EPSRC via a DTA for C.J.S. and allocation of some SEM time through the Leeds EPSRC Nanoscience and Nanotechnology Facility (LENNF). We thank Y.-Y. Kim, A. N. Kulak, R. S. K. Lam, and E. H. Noel for assistance and advice. M. R. Chisholm participated in some experiments.

Received: February 5, 2010

Revised: March 26, 2010

Published online: June 2, 2010

- [1] H. X. Zhou, G. N. Rivas, A. P. Minton, *Ann. Rev. Biophys.* 2008, 37, 375.
- [2] H. Gardeniers, *Anal. Bioanal. Chem.* 2009, 394, 385.
- [3] W. Wang, W. X. Xu, Y. Levy, E. Trizac, P. G. Wolynes, *Proc. Natl. Acad. Sci. USA* 2009, 106, 5517.
- [4] H. A. Lowenstam, S. Weiner, *On Biomineralization*, Oxford University Press, New York 1989.
- [5] F. C. Meldrum, H. Colfen, *Chem. Rev.* 2008, 108, 4332.
- [6] M. J. Olszta, X. G. Cheng, S. S. Jee, R. Kumar, Y. Y. Kim, M. J. Kaufman, E. P. Douglas, L. B. Gower, *Mater. Sci. Eng. R* 2007, 58, 77.
- [7] M. J. Glimcher, *Philos. Trans. R. Soc. B* 1984, 304, 479.
- [8] H. K. Christenson, *J. Phys. Condens. Matt.* 2001, 13, R95.
- [9] S. Thachepan, M. Li, S. A. Davis, S. Mann, *Chem. Mater.* 2006, 18, 3557.
- [10] C. E. Fowler, M. Li, S. Mann, H. C. Margolis, *J. Mater. Chem.* 2005, 15, 3317.
- [11] J. Mittal, R. B. Best, *Proc. Natl. Acad. Sci. USA* 2008, 105, 20233.
- [12] L. B. Gower, *Chem. Rev.* 2008, 108, 4551.
- [13] W. Yue, R. J. Park, A. N. Kulak, F. C. Meldrum, *J. Cryst. Growth* 2006, 294, 69.
- [14] B. Wucher, W. Yue, A. N. Kulak, F. C. Meldrum, *Chem. Mater.* 2007, 19, 1111.
- [15] A. S. Finnmore, M. R. J. Scherer, R. Langford, S. Mahajan, S. Ludwigs, F. C. Meldrum, U. Steiner, *Adv. Mater.* 2009, 21, 3928.
- [16] S. Yunoki, T. Ikoma, A. Monkawa, K. Ohta, M. Kikuchi, S. Sotome, K. Shinomiya, J. Tanaka, *Mater. Lett.* 2006, 60, 999.
- [17] G. Falini, S. Fermani, M. Gazzano, A. Ripamonti, *Chem. Eur. J.* 1997, 3, 1807.
- [18] G. Falini, S. Fermani, M. Gazzano, A. Ripamonti, *J. Chem. Soc. Dalton Trans.* 2000, 3983.
- [19] A. Diaz, T. Lopez, J. Manjarrez, E. Basaldella, J. M. Martinez-Blanes, J. A. Odriozola, *Acta Biomater.* 2006, 2, 173.
- [20] L. C. Palmer, C. J. Newcomb, S. R. Kaltz, E. D. Spoerke, S. I. Stupp, *Chem. Rev.* 2008, 108, 4754.
- [21] J. H. Bradt, M. Mertig, A. Teresiak, W. Pompe, *Chem. Mater.* 1999, 11, 2694.
- [22] J. L. Chen, C. Burger, C. V. Krishnan, B. Chu, B. S. Hsiao, M. J. Glimcher, *Macromol. Chem. Phys.* 2005, 206, 43.
- [23] L. Addadi, S. Raz, S. Weiner, *Adv. Mater.* 2003, 15, 959.
- [24] E. Loste, F. C. Meldrum, *Chem. Commun.* 2001, 901.
- [25] E. Loste, R. J. Park, J. Warren, F. C. Meldrum, *Adv. Funct. Mater.* 2004, 14, 1211.
- [26] J. Aizenberg, D. A. Muller, J. L. Grazul, D. R. Hamann, *Science* 2003, 299, 1205.
- [27] J. Aizenberg, *J. Chem. Soc. Dalton Trans.* 2000, 3963.

- [28] A. M. Travaille, J. J. M. Donners, J. W. Gerritsen, A. J. M. Sommerdijk, R. J. M. Nolte, H. V. Kempen, *Adv. Mater.* **2002**, *14*, 492.
- [29] J. Aizenberg, A. J. Black, G. M. Whitesides, *J. Am. Chem. Soc.* **1999**, *121*, 4500.
- [30] M. Prencipe, E. F. Pascale, C. M. Zicovich-Wilson, V. R. Saunders, R. Orlando, R. Dovesi, *Phys. Chem. Minerals* **2004**, *31*, 559.
- [31] S. Raz, O. Testeniere, A. Hecker, S. Weiner, G. Luquet, *Biol. Bull.* **2002**, *203*, 269.
- [32] J. Zuo, C. Xu, Y. Liu, Y. Qian, *Nanostruct. Mater.* **1998**, *10*, 1331.
- [33] H. Farman, F. M. Coveney, J. C. Dore, *Physica B* **1992**, *180*, 857.
- [34] M. Alcoutlabi, G. B. McKenna, *J. Phys. Condens. Matt.* **2005**, *17*, R461.
- [35] G. T. Rengarajan, D. Enke, M. Steinhart, M. Beiner, *J. Mater. Chem.* **2008**, *18*, 2537.
- [36] B. D. Hamilton, M. A. Hillmyer, M. D. Ward, *Cryst. Growth Des.* **2008**, *8*, 3368.
- [37] S. Tanaka, S. U. Egelhaaf, W. C. K. Poon, *Phys. Rev. Lett.* **2004**, *92*, 128102.
- [38] T. Iiyama, K. Nishikawa, T. Suzuki, K. Kaneko, *Chem. Phys. Lett.* **1997**, *274*, 152.
- [39] K. Morishige, K. Kawano, *J. Chem. Phys.* **2000**, *112*, 11023.
- [40] D. Nowak, M. Heuberger, M. Zach, H. K. Christenson, *J. Chem. Phys.* **2008**, *129*, 154509.
- [41] D. Nowak, H. K. Christenson, *Langmuir* **2009**, *25*, 9908.
- [42] H. K. Christenson, *Chem. Phys. Lett.* **1985**, *118*, 455.
- [43] J. L. Parker, H. K. Christenson, B. W. Ninham, *Rev. Sci. Instrum.* **1989**, *60*, 3135.
- [44] H. K. Christenson, *Colloids Surf. A* **1997**, *123*, 355.
- [45] S. Ohnishi, M. Hato, K. Tamada, H. K. Christenson, *Langmuir* **1999**, *15*, 3312.
- [46] J. Kawano, N. Shimobayashi, A. Miyake, M. Kitamura, *J. Phys. Condens. Matt.* **2009**, *21*, 425102.
- [47] P. Fratzl, F. D. Fischer, J. Svoboda, J. Aizenberg, *Acta Biomater.* **2009**, *6*, 1001.
- [48] J. Aizenberg, G. Lambert, S. Weiner, L. Addadi, *J. Am. Chem. Soc.* **2002**, *124*, 32.
- [49] J. Aizenberg, G. Lambert, L. Addadi, S. Weiner, *Adv. Mater.* **1996**, *8*, 222.
- [50] H. S. Lee, T. H. Ha, K. Kim, *Mater. Chem. Phys.* **2005**, *93*, 376.
- [51] N. Koga, Y. Yamane, *J. Thermal Anal. Calorim.* **2008**, *94*, 379.
- [52] E. Beniash, L. Addadi, S. Weiner, *J. Struct. Biol.* **1999**, *125*, 50.
- [53] Y. Politi, R. A. Metzler, M. Abrecht, B. Gilbert, F. H. Wilt, I. Sagi, L. Addadi, S. Weiner, P. Gilbert, *Proc. Natl. Acad. Sci. USA* **2008**, *105*, 17362.
- [54] R. S. K. Lam, J. M. Charnock, A. Lennie, F. C. Meldrum, *Cryst. Eng. Commun.* **2007**, *9*, 1226.
- [55] D. D. Archibald, S. B. Qadri, B. P. Gaber, *Langmuir* **1996**, *12*, 538.
- [56] N. Koga, Y. Z. Nakagoe, H. Tanaka, *Thermochimica Acta* **1998**, *318*, 239.

Bibliography

- [1] N. Rodriguez-Hornedo S. J. Nehm K. F. Seefeldt Y. Pagn-Torres C. J. Falkiewicz. Reaction crystallization of pharmaceutical molecular complexes. *Mol. Pharm*, 3:362-267, 2006.
- [2] W. Beckmann. Crystallization of pharmaceutical compounds - polymorphs, pseudo-polymorphs and particle formation. *Eng. Life. Sci*, 3:113-120, 2003.
- [3] I. Grzegory. High-pressure crystallization of gan for electronic applications. *J. Phys. Cond. Mater*, 14:1055-1067, 2002.
- [4] P. C. van der Wilt B. D. van Dijk G. J. Bertens R. Ishihara C. I. M. Beenakker. Formation of location-controlled crystalline islands using substrate-embedded seeds in excimer-laser crystallization of silicon films. *Appl. Phys. Lett.*, 79:1819-1822, 2001.
- [5] A. L. Briseno S. C. B. Mannsfeld M. M. Ling S. Liu R. J. Tseng C. Reese M. E. Roberts Y. Yang F. Wudl Z. Bao. Patterning organic single-crystal transistor arrays. *Nature*, 444:913-917, 2006.
- [6] Y. Morita S. Aibara H. Yemashita F. Yagi T. Suganuma K. Hiromi. Crystallization and preliminary x-ray investigation of soybean /beta-amylase. *J. Biochem*, 77:343-351, 1975.
- [7] G. Mazzanti A. G. Marangoni S. H. J. Idziak. Modeling of a two-regime crystallization in a multicomponent lipid system under shear flow. *Eur. Phys. J. E.*, 27:135-144, 27.
- [8] D. E. Parsell K. J. Anusavice. Optimization of glass-ceramic crystallization based on dta exotherm analysis. *Dent. Mater*, 10:167-171, 1994.

- [9] T. J. Headley R. E. Loehman. Crystallization of a glass-ceramic by epitaxial growth. *J. Am. Cer. Soc.*, 67:620-625, 1984.
- [10] G. Palasciano G. P. van Berge-Henegouwen K. J. van Erpecum P. Portincasa N. G. Vennemana A. Moschett A. van den Berg. Quantitation of cholesterol crystallization from supersaturated model bile. *J. Lipid Res.*, 43:604-610, 2002.
- [11] G. Zhang J. Y. Howe D. W. Coffey D. A. Blom L. F. Allard J. Cho. A biomimetic approach to the deposition of zirconium dioxide films on self-assembled nanoscale templates. *Mater. Sci. Eng.*, 26:1344-1350, 2005.
- [12] S. E. Habas H. Lee V. Radmilovic G. A. Somorjai P. Yang. Shaping binary metal nanocrystals through epitaxial seeded growth. *Nature*, 6:692-696, 2007.
- [13] F. Kim S. Connor H. Song T. Kuykendal P. Yang. Platonic gold nanocrystals. *Angew. Chem. Int. Edn.*, 43:3673-3677, 2004.
- [14] H. Song F. Kim S. Connor G. A. Somorjai P. Yang. Pt nanocrystals: Shape control and langmuir-blodgett monolayer formation. *J. Phys. Chem. B*, 109:188-193, 2005.
- [15] C. J. Murphy T. K. Sau. Room temperature, high-yield synthesis of multiple shapes of gold nanoparticles in aqueous solution. *J. Am. Chem. Soc.*, 126:8648-8649, 2004.
- [16] H. Tagaki H. Ogawa Y. Yamazaki A. Ishizaki T. Nakagiri. Quantum size effectson photoluminescence in ultrafine. *Appl. Phys. Lett.*, 56:2379-2380, 1990.
- [17] M. A. Hines P. Guyot-Sionnest. Synthesis and characterization of strongly luminescing zns-capped cdse nanocrystals. *J. Phus. Chem.*, 100:468-471, 1996.
- [18] M. V. Kovalenko B. Spokoyny J-S. Lee M. Scheele A. Weber S. Perera D. Landry D. V. Talapin. Semiconductor nanocrystals functionalized with anti-mony telluride zintl ions for nanostructured thermoelectrics. *J. Am. Chem. Soc.*, 132:6686-6695, 2010.

- [19] K. Naka, editor. *Biom mineralization II: Mineralization Using Synthetic Polymers and Templates*. Springer, 2007.
- [20] W. A. Tiller. *The Science of Crystallization*. Cambridge University Press, 1991.
- [21] M. Andr Meyers P-Y Chena A. Yu-Min Lin Y. Seki. Biological materials: Structure and mechanical properties. *Prog. Mater. Sci*, 53:pp1-206, 2007.
- [22] L. A. Estroff. Introduction: Biom mineralization. *Chem. Rev.*, 108:3429-3431, 2008.
- [23] H. A. Lowenstam S. Weiner. *On Biom mineralization*. Oxford University Press, 1989.
- [24] S. Weiner P. M. Dove. An overview of biom mineralization processes and the problem of the vital effect. *Reviews in Mineralogy and Geochemistry*, 54:pp 1-29, 3003.
- [25] J. Webb D. J. Macey W. Chua anusorn T. G. St. Pierre L .R. Brooker I. Rahman B. Noller. Iron biom minerals in medicine and the environment. *Co. Chem. Rev.*, 190-192:1199-1215, 1999.
- [26] F. C. Meldrum H. Colfen. Controlling mineral morphologies and structures in biological and synthetic systems. *Chem. Rev. Mineral Geochem*, 108: 4332-4432, 2008.
- [27] S. Raz O. Testeniere A. Hecker S. Weiner G. Luquet. Stable amorphous calcium carbonate is the main component of the calcium storage structures of the crustacean *orchestia cavimana*. *Biol. Bull.*, 203:269-274, 2002.
- [28] B. Wucher W. Yue A. N. Kulak F. C. Meldrum. Designer crystals: Single crystals with complex morphologies. *Chem. Mater.*, 19:1111-1119, 2007.
- [29] S. Weiner L. Addadi. Design strategies in mineralized biological materials. *J. Mater. Chem.*, 7:689-702, 1997.
- [30] F. C. Meldrum W. Yue, A. N. Kulak. Growth of single crystals in structured templates. *J. Mater. Chem.*, 16:408-416, 2006.

- [31] Y. Oaki H. Imai. Nanoengineering in echinoderms: The emergence of morphology from nanobricks. *Small*, 2:66–70, 2006.
- [32] H. Elfil H. Roques. Role of hydrate phases of calcium carbonate and the scaling phenonemon. *Desalination*, 137:177–186, 2001.
- [33] E. Beniash J. Aizenberg L. Addadi S. Weiner. Amorphous calcium carbonate transforms into calcite during sea urchin larval spicule growth. *Proceedings of the Royal Society of London*, 264:461–465, 1997.
- [34] B. Pokroy J. Aizenberg. Calcite shape modulation through the lattice mismatch between the self-assembled monolayer template and the nucleated crystal face. *CrystEngComm*, 9:1219–1225, 2007.
- [35] H. Teng P. M. Dove C. A. Orme J. J. De Yoreo. Thermodynamics of calcite growth: Baseline for understanding biomineral formation. *Science*, 282:724–727, 1998.
- [36] X. Zhao H. Bala Z. Wang C. Wang J. Zhao. Synthesis of nanosized calcium carbonate (aragonite) via a polyacrylamide inducing process. *Powder Technology*, 163:134–138, 2006.
- [37] J. L. Grazul D. R. Hamann J. Aizenberg D. A. Muller. Direct fabrication of large micropatterned single crystals. *Science*, 299:1205–1208, 2003.
- [38] E. A. Minchin. Sponge-spicules. a summary of present knowledge. *Ergeb. Fortschr. Zool*, 2:177–274, 1909.
- [39] L. Addadi S. Raz S. Weiner. Taking advantage of disorder: Amorphous calcium carbonate and its role in biomineralization. *Advanced Materials*, 15: 959–970, 2003.
- [40] M. Prenant. The types of calcium mineral in living beings and the problem of their determination. *Biological Reviews and Biological Proceedings of the Cambridge Philosophical Society*, 2:365–393, 1927.
- [41] A-W. Xu Q. Yu-Min W-F. Dong M. Antonietti H. Colfen. Stable amorphous calcium carbonate microparticles with hollow spherical superstructures stabilized by phytic acid. *Advanced Materials*, 17:2217–2221, 2005.

- [42] J-Y. Gali J-C. Bollinger H. Tolosa N. Gache. Calcium carbonate solubility: a reappraisal of scale formation and inhibition. *Talanta*, 43:1497-1509, 1996.
- [43] J. J. J. M. Donners B. R. Heywood E. W. Meijer R. J. M. Nolte C. Roman A. P. H. J. Schenning N. A. J. M. Sommerdijk. Amorphous calcium carbonate stabilised by poly(propylene imine) dendrimers. *Chem. Commun*, 19:1937-1938, 2000.
- [44] J. T. Lowitz. Bemerkungen uber das krystallisiren der salze, und anzeige eines sicheren mittels, regelmassige krystallen zu erhalten. *Crell's Chem. Ann.*, 1:3-11, 1795.
- [45] S. M. Kathmann. Understanding the chemical physics of nucleation. *Theoretical Chemistry Accounts*, 116:169-182, 2006.
- [46] A. S. Myerson A. F. Izamialov. *Handbook of Crystal Growth Volume 1. Fundamentals Part 5. The structure of supersaturated solutions.* Elsevier Science Publishers, 1993.
- [47] J. W. Gibbs. On the equilibrium of heterogeneous substances. *Trans. Connect. Acad. Sci*, 3:108-248, 1876.
- [48] J. W. Gibbs. On the equilibrium of heterogeneous substances. *Trans. Connect. Acad. Sci*, 16:343-524, 1878.
- [49] J. J. De Yoreo P. G. Vekilov. Principles of crystal nucleation and growth. *Rev. Mineral Geochem*, 54:57-93, 2003.
- [50] C. Y. Tai W-C Chien J-P Hsu C-C Lee. Supersaturation, induction period and metastable zone width of calcium chloride- ammonium carbonate-hydrochloric acid system. *Comm. Eng. Comm*, 188:243-263, 2001.
- [51] J. Bohm. The history of crystal growth. *Acta Physica Hugarica*, 57(3-4): 161-178, 1985.
- [52] J. W. Cahn. Phase separation by spinodal decomposition in isotropic systems. *The Journal of Chemical Physics*, 42:93-99, 1965.
- [53] K-J Kim A. Mersmann. Estimation of metastable zone width in different nucleation processes. *Chemical Engineering Science*, 56:2315-2324, 2001.

- [54] D. Kashchiev D. Verdoes G. M. van Rosmalen. Induction time and metastability limit in new phase formation. *Journal of Crystal Growth*, 110:373-380, 1991.
- [55] J. Nyvlt. Kinetics of nucleation in solution. *Journal of Crystal Growth*, 3: 377-383, 1968.
- [56] D. Turnbull J. C. Fisher. Rate of nucleation in condensed systems. *Journal of Chemical Physics*, 1:71-73, 1949.
- [57] J. C. Fisher J. H. Holloman D. Turnbull. Nucleation. *Journal of Applied Physics*, 19:775-784, 1948.
- [58] P. G. Debenedetti. Thermodynamics: When a phase is born. *Nature*, 441: 168-169, 2006.
- [59] M. Volmer A. Weber. Germ-formation in oversaturated figures. *ZEITSCHRIFT FUR PHYSIKALISCHE CHEMIE-STOCHIOMETRIE UND VERWANDTSCHAFTSLEHRE*, 119:277-301, 1926.
- [60] P. G. Debenedetti. *Metastable Liquids Concepts and Principles*. Princeton University Press, 1996.
- [61] R. Bahadur R. B. McClurg. Comparison of cluster definitions in homogeneous nucleation rate calculations. *Journal of Physical Chemistry B*, 105: 11893-11900, 2001.
- [62] H-J. Butt K. Graf M. Kappl. *Physics and Chemistry of Interfaces*. Wiley-VCH, 2006.
- [63] R. Becker. . *Ann. Physik*, 32:1, 1938.
- [64] J. K. Lee F. F. Abraham G. M. Pound. On the validity of the capillarity approximation in the rate theory of homogeneous nucleation. *Surface Science*, 34:745-758, 1973.
- [65] A. Laaksonen I. Napari. Breakdown of the capillarity approximation in binary nucleation. a density functional study. *Journal of Physical Chemistry B*, 105:11678-11682, 2001.

- [66] B. Lewis. Bond energy formulations of heterogeneous nucleation theory. *Thin Solid Films*, 1:85-107, 1967.
- [67] A. G. Walton. *The Formation and Properties of Precipitates*. Robert E. Krieger Publishing Company, Huntington, New York, 1979.
- [68] T. Young. An essay on the cohesion of fluids. *Philosophical Transactions of the Royal Society of London*, 95:65-87, 1805.
- [69] J. D. Gunton. Homogeneous nucleation. *Journal of Statistical Physics*, 95: 904-923, 1999.
- [70] D. W. Oxtoby. Nucleations of first-order phase transitions. *Acc. Chem. Res.*, 31:91-97, 1998.
- [71] G. Kahl H. Lowen. Classical density functional theory: An ideal tool to study heterogeneous crystal nucleation. *Journal of Physics: Condensed Matter*, 21: 464101, 2009.
- [72] D. W. Oxtoby R. Evans. Non-classical nucleation theory for the gas-liquid transition. *J. Chem. Phys*, 89:7521, 1988.
- [73] W. Kossel. Uber krystallwachstum. *Die Naturwissenschaften*, 44:901-910, 1930.
- [74] H. J. Scheel. Historical aspects of crystal growth technology. *Journal of Crystal Growth*, 211:1-12, 2000.
- [75] S. Mann. *Biomineralization - Principles and Concepts in Bioinorganic Materials Chemistry*. Oxford University Press, 2001.
- [76] F. C. Frank J. H. van der Merwe. One-dimensional dislocations. *Proceedings of the Royal Society of London. Series A, Mathematical and Physical*, 198: 205-216, 1949.
- [77] W. K. Burton N. Cabrera F. C. Frank. The growth of crystals and the equilibrium structures of their surfaces. *Philosophical Transactions of the Royal Society of London*, 243:299-358, 1951.

- [78] W. K. Burton N. Cabrera F. C. Frank. Role of dislocations in crystal growth. *Nature*, 163:393–399, 1949.
- [79] F. Lippmann. *Sedimentary Carbonate Minerals*. Springer-Verlag: Berlin, 1973.
- [80] S. Hassuhl. *Physical properties of Crystals*. Wiley VCH, 2007.
- [81] A. Kelly G. W. Groves P. Kidd. *Crystallography and Crystal Defects*. Wiley, 2000.
- [82] C. Gervais J. Hulliger. Impact of surface symmetry on growth-induced properties. *Crystal Growth & Design*, 7:1925–1935, 2007.
- [83] H. D. Keith F. J. Padden. Spherulitic crystallization from the melt. i. fractionation and impurity segregation and their influence on crystalline morphology. *Journal of Applied Physics*, 35:1270–1285, 1964.
- [84] O. A. Jurchescu J. Bass T. T. M. Palstra. Effect of impurities on the mobility of single crystal pentacene. *Applied Physics Letters*, 84:3061–3063, 2004.
- [85] H. Kodera. Diffusion coefficients of impurities in silicon melt. *Japanese Journal of Applied Physics*, 2:212–219, 1963.
- [86] P. J. Brown J. B. Forsyth. *The Crystal Structure of Solids*. Crane Russak, 1973.
- [87] P. Gay. *The Crystalline State*. Oliver and Boyd, 1972.
- [88] F. F. C. Hessel. Krystallometrie oder krystallonomie und krystallographie; *Gehler's Physikalisches Worterbuch*, 5:1062, 1830.
- [89] R. Steadman. *Crystallography*. Van Nostrand Reinhold (UK), 1982.
- [90] A. Bravais. Mmoire sur les systmes forms par les points distribus rgulirement sur un plan ou dans l'espace. *J. Ecole Polytech*, 19:1–128, 1850.
- [91] M. I. Aroyo U. Muller H. Wondratschek. The fundamental laws of crystallography. *International Tables for Crystallography*, A1:2–3, 2006.

- [92] T. Hahn. *International Tables for Crystallography Volume A: Space Group Symmetry*. Springer Netherlands, 2007.
- [93] Jr. C. Klein C. S. Hurlburt. *Manual of Mineralogy*. Wiley, 1999.
- [94] R. J. Reeder. *Crystal Chemistry in the Rhombohedral Carbonates*. Reviews of Mineralogy and Geochemistry, Mineral Soc America, 1983.
- [95] H. Effenberger K. Mereiter J. Zemann. Crystal structure refinements of magnesite, calcite, rhodochrosite, siderite, smithonite, and dolomite with discussion of some aspects of the stereochemistry of calcite-type carbonates. *Zeitschrift für Kristallographie*, 156:233-243, 1981.
- [96] M. S. Vasnev E. K. Zhukov. Technical strontium carbonate - a useful substitute for scarce raw materials. *Translated from Steklo i Keramika*, 18:33-44, 1961.
- [97] A. J. Skinner J. P. LaFemina H. J. F. Jansen. Structure and bonding of calcite: A theoretical study. *American Mineralogist*, 79:205-214, 1994.
- [98] E. C. Keene J. S. Evans L. A. Estroff. Matrix interactions in biomineralization: Aragonite nucleation by an intrinsically disordered nacre polypeptide, n16n, associated with a beta-chitin substrate. *Crystal Growth and Design*, published online:00, 2010.
- [99] J. P. R. De Villiers. Crystal structures of aragonite, strontianite and witherite. *American Mineralogist*, 56:758-762, 1971.
- [100] R. W. G. Wyckoff. Orthorhombic space group criteria and their application to aragonite. *American Journal of Science*, 9:145-175, 1925.
- [101] W. L. Bragg. The structure of aragonite. *Proceedings of the Royal Society of London*, A105:16-37, 1924.
- [102] M. E. Tucker V. P. Wright. *Carbonate Sedimentology*. Blackwell Science, 1990.
- [103] B. Pokroy J. S. Fieramosca R. B. Von Dreele A. N. Fitch E. N. Caspi E. Zolotoyabko. Atomic structure of biogenic aragonite. *Chem. Mater.*, 19: 3244-3251, 2007.

- [104] E. N. Caspi B. Pokroy P. L. Lee J. P. Quintana E. Zolotoyabko. On the structure of aragonite. *Acta Crystallographica*, B61:129-132, 2005.
- [105] L. Qiao Q. L. Feng Y. Liu. A novel bio-vaterite in freshwater pearls with high thermal stability and low dissolubility. *Materials Letters*, 62:1793-1796, 2008.
- [106] S. E. Grasby. Naturally precipitating vaterite spheres: Unusual carbonate formed in an extreme environment. *Geochim. Cosmochim. Acta*, 67:1659-1666, 2003.
- [107] T. Ogino T. Suzuki K. Sawada. The formation and transformation mechanism of calcium carbonate in water. *Geochimica et Cosmochimica Acta*, 51: 2757-2767, 1987.
- [108] N. A. Palchik T. N. Moroz. Polymorph modifications of calcium carbonate in gallstones. *Journal of Crystal Growth*, 283:450-456, 2005.
- [109] A. M. Oliveira. Vaterite, calcite and aragonite in the otholiths of three species of piranha. *Naturwissenschaften*, 83:133-135, 1996.
- [110] V. R. Meenakashi P. L. Blackwelder N. Watabe. Studies on the formation of calcified egg-capsules of ampullarid snails. *Calcif. Tiss. Res.*, 16:283-291, 1974.
- [111] A. Sigel H. Sigel R. K. O. Sigel, editor. *Biom mineralization: From Nature to Application*. Wiley, 2008.
- [112] W. Seng Ang S. Lee M. Elimelech. Chemical and physical aspects of cleaning of organic-fouled reverse osmosis membranes. *Journal of Membrane Science*, 272:198-210, 2005.
- [113] J. Kang P. A. Rowntree. Gold film surface preparation for self-assembled monolayer studies. *Langmuir*, 23:509-516, 2007.
- [114] R. H. Stokes R. A. Robinson. *Electrolyte Solutions*. Butterworth and Co., 1959.
- [115] F. Schreiber. Structure and growth of self-assembling monolayers. *Progress in Surface Science*, 65:151-256, 2000.

- [116] R. J. Needs M. Mansfield. Calculations of the surface stress tensor and surface energy of the (111) surfaces of iridium, platinum and gold. *J. Phys. Condens. Matter*, 1:7555-7563, 1989.
- [117] K. Critchley L. Zhang H. Fukushima M. Ishida T. Shimoda R. J. Bushby S. D. Evans. Soft-uv photolithography using self-assembled monolayers. *J. Phys Chem B*, 110:17161-17167, 2006.
- [118] K. Critchley S. D. Evans G. J. Leggett N. J. Brewer, S. Janusz. Photooxidation of self-assembled monolayers by exposure to light of wavelength 254 nm. a static sims study. *J. Phys. Chem. B*, 109:11247-11256, 2005.
- [119] C. S. Dulcey J. H. Georger Jr. M-S Chen S. W. McElvany C. E. OFerrall V. I. Benezra J. M. Calvert. Photochemistry and patterning of self-assembled monolayer films containing aromatic hydrocarbon functional groups. *Langmuir*, 12:1638-1650, 1996.
- [120] R. S. K. Lam J. M. Charnock A. Lennie F. C. Meldrum. Synthesis-dependant structural variations in amorphous calcium carbonate. *CrystEngComm*, 9: 1226-1236, 2007.
- [121] Jr. J. E. House. Decomposition of ammonium carbonate and ammonium bicarbonate and proton affinities of the anions. *Inorg. Nucl. Chem. Letters*, 16:185-187, 1980.
- [122] H. Cho, editor. *Opto-Mechatronic Systems Handbook - Techniques and Applications*. CRC Press, 2003.
- [123] M. J. Dykstra L. E. Reuss. *Biological Electron Microscopy*. Kluwer Academic, 2003.
- [124] J. J. Bozzola L. D. Russell. *Electron Microscopy: Second Edition*. Jones and Bartlett, 1992.
- [125] J. Goldstein D. Newbury D. Joy C. Lyman P. Echlin E. Lifshin L. Sawyer J. Michael. *Scanning Electron Microscopy and X-Ray Microanalysis*. Springer, 2003.

- [126] W. L. Bragg. The diffraction of short electromagnetic waves by a crystal. *Proceedings of the Cambridge Philosophical Society*, 17:43-57, 1913.
- [127] G. Turrell J. Corset, editor. *Raman Microscopy*. Elsevier, 1996.
- [128] D. D. Archibald S. B. Qadri B. P. Gaber. Modified calcite deposition due to ultrathin organic films on silicon substrates. *Langmuir*, 12:538-546, 1996.
- [129] M. Royer. -. *Bull. Soc. Fr. Miner.*, 50:684-690, 1928.
- [130] J. H. van der Merwe. Misfitting monolayers and oriented overgrowth. *Discussions of the Faraday Society*, 5:201-214, 1949.
- [131] L. G. Schultz. Growth of alkali halide crystals from the vapor phase and from solution onto substrates of mica. *Acta Crystallographia*, 4:483-486, 1951.
- [132] L. G. Schultz. Growth of alkali halides from the vapor on single-crystal substrates of alkali halides. *Acta Crystallographia*, 5:130-132, 1952.
- [133] N. D. Lisgarten. Oriented overgrowths of alkali halides on mica. *Transactions of the Faraday Society*, 50:684-690, 1954.
- [134] J. Aizenberg A. J. Black G. M. Whitesides. Oriented growth of calcite controlled by self-assembled monolayers of functionalized alkanethiols supported on gold and silver. *J. Am. Chem. Soc.*, 121:1500-1509, 1999.
- [135] J. Aizenberg A. J. Black G. M. Whitesides. Control of crystal nucleation on self-assembled monolayers. *Nature*, 398:495-498, 1999.
- [136] A. M. Travaille J. J. J. M. Donners J. W. Gerritsen N. A. J. M. Sommerdijk R. J. M. Nolte H. van Kempen. Aligned growth of calcite crystals on a self-assembled monolayer. *Advanced Functional Materials*, 14:492-495, 2002.
- [137] S. Kewalramani K. Kim B. Stripe G. Evmenenko G. H. B. Dommett P. Dutta. Observation of an organic-inorganic lattice match during biomimetic growth of (001)-oriented calcite crystals under floating sulfate monolayers. *Langmuir*, 24:10579-10582, 2008.
- [138] A. Berman D. J. Ahn A. Lio M. Salmeron A. Reichert D. Charych. Total alignment of calcite at acidic polydiacetylene films. *Science*, 269:515-518, 1995.

- [139] B. Pokroy E. Zolotoyabko. Aragonite growth on single-crystal substrates displaying a threefold axis. *Chem. Commun.*, 1:2140-2142, 2005.
- [140] E. Garcia P. Alfonso E. Tauler S. Gali. Surface alteration of dolomite in dedolomitization reaction in alkaline media. *Cement and Concrete Research*, 33:1449-1456, 2002.
- [141] L. Pastero D. Aquilano. Calcite zabuyelite anomalous mixed crystals. sector zoning and growth mechanisms. *Crystal Growth and Design*, 8:3451-3460, 2008.
- [142] K. Lida J-I Inagaki K. Shinohara Y. Suemor M. Ogawa T. Dewa M. Nango. Near-ir absorption and fluorescence spectra and afm observation of the light-harvesting 1 complex on a mica substrate refolded from the subunit light-harvesting 1 complexes of photosynthetic bacteria rhodospirillum rubrum. *Langmuir*, 21:3069-3075, 2005.
- [143] P. A. Ciullo. *Industrial Minerals and their Uses: a Handbook and Formulary*. Noyes Publication, 1996.
- [144] K. Muller C. C. Chang. Electric dipoles on clean mica surfaces. *Surf. Sci*, 14:39, 1969.
- [145] H. Poppa A. G. Elliot. The surface composition of mica substrates. *Surface Science*, 24:149-163, 1971.
- [146] H. K. Christenson. Adhesion and surface energy of mica in air and water. *J. Phys. Chem*, 97:12034-12041, 1993.
- [147] F. Ostendorf C. Schmitz S. Hirth A. Kuhnle J. J. Kolodziej M. Reichling. How flat is an air cleaved mica surface? *Nanotechnology*, 19:No 305705, 2008.
- [148] H. K. Christenson J. N. Isrealachvili. Growth of ionic crystallites on exposed surfaces. *Journal of Colloid and Interface Science*, 117:576-577, 1987.
- [149] F. Ostendorf C. Schmitz S. Hirth J. J. Kolodziej M. Reichling. Evidence for potassium carbonate crystallites on air-cleaved mica surfaces. *Langmuir*, 25: 10764-10767, 2009.

- [150] R. T. Downs. The ruff project: an integrated study of the chemistry, crystallography, raman and infrared spectroscopy of minerals. *Program and Abstracts of the 19th General Meeting of the International Mineralogical Association in Kobe, Japan.*, -:03-13, 2009.
- [151] Downs r t (2006) the ruff project: an integrated study of the chemistry, crystallography, raman and infrared spectroscopy of minerals. program and abstracts of the 19th general meeting of the international mineralogical association in kobe, japan. o03-13.
- [152] J. N. Isrealachvili R. R. Pashley. Molecular layering of water at surfaces and origin of repulsive hydration forces. *Nature*, 306:249-251, 1983.
- [153] M. C. Upreti A. G. Walton. Heterogeneous nucleation of alkali halide crystals from solution. *Journal of Chemical Physics*, 44:1936-1939, 1966.
- [154] P. Conrad G. E. Ewing R. L. Karlinsey V. Sadtschenko. Ice nucleation on barium fluoride (111). *Journal of Chemical Physics*, 122:no 064709, 2005.
- [155] H. Colfen M. Antoniette. Mesocrystals: Inorganic superstructures made by highly parallel crystallization and controlled alignment. *Angewandte Chemie*, 44:5576-5591, 2005.
- [156] S. Yamanaka N. Ito A. Shimosaka Y. Shirakawa J. Hidaka. Afm investigation for the initial growth processes of calcium carbonate on hydrophilic and hydrophobic substrate. *Crystal Growth and Design*, 9:3245-3250, 2009.
- [157] J. Kawanoa N. Shimobayashia M. Kitamuraa K. Shinodab N. Aikawa. Formation process of calcium carbonate from highly supersaturated solution. *Journal of Crystal Growth*, 237:419-423, 2002.
- [158] J. Kuther W. Tremel. Template induced crystallization of biominerals on self-assembled monolayers of alkylthiols. *Thin Solid Films*, 327-329:554-558, 1998.
- [159] D. B. Wurm S. T. Britten Y-T. Kim. Controlled nucleation of inorganic crystals on self-assembled monolayers. *Journal of Materials Science Letters*, 15:1285-1287, 1996.

- [160] K. Naka Y. Chujo. Control of crystal nucleation and growth of calcium carbonate by synthetic substrates. *Chem. Mater*, 13:3245-3259, 2001.
- [161] J. Aizenberg. Patterned crystallization of calcite in vivo and in vitro. *Journal of Crystal Growth*, 211:143-148, 2000.
- [162] J. Aizenberg. A bio-inspired approach to controlled crystallization at the nanoscale. *Bell Labs Technical Journal of Applied Crystallography*, 10:129-141, 2005.
- [163] A. Kumar H. A. Biebuyck G. M. Whitesides. Patterning self-assembled monolayers: Applications to materials science. *Langmuir*, 10:1498-1511, 1994.
- [164] E. Kim H. A. Biebuyck G. M. Whitesides A. Kumar, N. L. Abbot. Patterned self-assembled monolayers and meso-scale phenomena. *Acc. Chem. Res*, 28: 219-226, 1995.
- [165] J. Sagiv. Organized monolayers by adsorption, i . formation and structure of oleophobic mixed monolayers on solid surfaces. *J. Am. Chem. Soc.*, 102: 92-98, 1980.
- [166] J. Gun J. Sagiv. On the formation and structure of self-assembling monolayers : Iii. time of formation, solvent retention, and release. *Journal of Colloid and Interface Science*, 112:457-472, 1986.
- [167] H. Ogawa T. Chihara K. Taya. Selective monomethyl esterification of dicarboxylic acids by use of monocarboxylate chemisorption on alumina. *J. Am. Chem. Soc*, 107:1365-1369, 1985.
- [168] N. E. Schlotter M. D. Porter T. B. Bright D. L. Allara. Formation and structure of a spontaneously adsorbed monolayer of arachidic on silver. *Chemical Physical Letters*, 132:93-98, 1986.
- [169] H. Sellers A. Ulman Y. Shnidman J. E. Eilers. Structure and binding of alkanethiolates on gold and silver surfaces: Implications for self-assembled monolayers. *J. Am. Chem. Soc*, 115:9389-9401, 1993.

- [170] A. Ulman. Formation and structure of self-assembled monolayers. *Chem. Rev.*, 96:1533-1554, 1996.
- [171] R. G. Nuzzo D. L. Allara. Adsorption of bifunctional organic disulfides on gold surfaces. *J. Am. Chem. Soc.*, 105:4481-4483, 1983.
- [172] G. A. Somorjai. *Chemistry in Two Dimensions: Surfaces*. Cornell University Press, 1982.
- [173] D. E. King. Oxidation of gold by ultraviolet light and ozone at 25 c. *J. Vac. Science*, 13:1247-1253, 1995.
- [174] R. H. Tredgold. *Order in Thin Organic Films*. Cambridge University Press, 1994.
- [175] J. Kuther G. Nelles R. Seshadri M. Schaub H-J. Butt W. Tremel. Templated crystallisation of calcium and strontium carbonates on centred rectangular self-assembled monolayer substrates. *Chem. Eur. J.*, 4:1834-1842, 1998.
- [176] A. N. Parikh D. L. Allara. Quantitative determination of molecular structure in multilayered thin films of biaxial and lower symmetry from photon spectroscopies. i. reflection infrared vibrational spectroscopy. *J. Chem. Phys.*, 96:927-945, 1992.
- [177] R. G. Nuzzo E. M. Korenic L. H. Dubois. Studies of the temperature-dependent phase behavior of long chain n-alkyl thiol monolayers on gold. *J. Chem. Phys.*, 93:767-773, 1990.
- [178] A. Ulman J. E. Eilers N. Tillman. Packing and molecular orientation of alkanethiol monolayers on gold surfaces. *Langmuir*, 5:1147-1152, 1989.
- [179] R. K. Smith P. A. Lewis P. S. Weiss. Patterning of self assembled monolayers. *Progress in Surface Science*, 75:1-68, 2004.
- [180] M. Himmelhaus F. Eisert M. Buck M. Grunze. Self-assembly of n-alkanethiol monolayers. a study by ir-visible sum frequency spectroscopy (sfg). *J. Phys. Chem. B.*, 104:576-584, 2000.
- [181] H. J. Kreuzer. Sticking of rare gases: The effect of lateral interactions. *Surface Science*, 344:1264-1270, 1995.

- [182] R. Rioux. *Model Systems in Catalysis - Single Crystals to Supported Enzyme Mimics*. Springer, 2010.
- [183] A. P. Henderson L. N. Seetohul A. K. Dean P. Russell S. Pruneanu Z. Ali. A novel isotherm, modeling self-assembled monolayer adsorption and structural changes. *Langmuir*, 25:931-938, 2009.
- [184] K. A. Peterlinz R. Georgiadis. In situ kinetics of self-assembly by surface plasmon resonance spectroscopy. *Langmuir*, 12:4731-4740, 1996.
- [185] C. D. Bain E. B. Troughton Y-T Tao J. Evall G. M. Whitesides R. G. Nuzzo. Formation of monolayer films by the spontaneous assembly of organic thiols from solution onto gold. *J. Am. Chem. Soc.*, 111:321-335, 1989.
- [186] Y. Zhang R. H. Terrill T. A. Tanzer P. W. Bohn. Ozonolysis is the primary cause of uv photooxidation of alkanethiolate monolayers at low irradiance. *J. Am. Chem. Soc.*, 120:2654-2655, 1998.
- [187] C. Zhou A. V. Walker. Dependence of patterned binary alkanethiolate self-assembled monolayers on uv-photopatterning conditions and evolution with time, terminal group, and methylene chain length. *Langmuir*, 22:11420-11425, 2006.
- [188] P. Prompinit A. S. Achalkumar X. Han R. J. Bushby C. Walti S. D. Evans. Improved photoreaction yields for soft ultraviolet photolithography in organothiol self-assembled monolayers. *J. Phys. Chem. C*, 113:21642-21647, 2009.
- [189] Y. Li K-S. Moon C. P. Wong. Adherence of self-assembled monolayers on gold and their effects for high performance anisotropic conductive adhesives. *J. Elec. Mater.*, 34:266-271, 2005.
- [190] A. Amirfazli A. Keshavarz L. Zhang A. W. Neumann. Determination of line tension for systems near wetting. *Journal of Colloid and Interface Science*, 265:152-160, 2003.
- [191] M. S. Wang L. B. Palmertz A. Razatos. Evaluating protein attraction and adhesion to biomaterials with the atomic force microscope. *Langmuir*, 20:7753-7759, 2004.

- [192] M. E. Schrader. Ultrahigh-vacuum techniques in the measurement of contact angles. *J. Phys. Chem.*, 74:2313–2317, 1970.
- [193] P. E. Laibinis M. A. Fox J. P. Folkers G. M. Whitesides. Comparisons of self-assembled monolayers on silver and gold. *Langmuir*, 7:3167–3173, 1991.
- [194] T. Ishida S. Tsuneda N. Nishida M. Hara H. Sasabe W. Knoll. Surface-conditioning effect of gold substrates on octadecanethiol self-assembled monolayer growth. *Langmuir*, 13:4638–4643, 1997.
- [195] S-Y. Kwak E. DiMasi Y-J. Han J. Aizenberg. Orientation and mg incorporation of calcite grown on functionalized self-assembled monolayers: A synchrotron x-ray study. *Crystal Growth & Design*, 5:2139–2145, 2005.
- [196] C. Lu L. Qi J. Ma H. Cheng M. Zhang W. Cao. Controlled growth of micropatterned, oriented calcite films on a self-assembled multilayer film. *Langmuir*, 20:7378–7380, 2004.
- [197] A. M. Travaille E. G. A. Steijven H. Meekes H. van Kempen. Thermodynamics of epitaxial calcite nucleation on self-assembled monolayers. *J. Phys. Chem. B*, 109:5618–5626, 2005.
- [198] P. Jensen A-L. Barabasi H. Larralde S. Havlin H. E. Stanley. Deposition, diffusion and aggregation of atoms on surfaces: A model for nanostructure growth. *Phys. Rev. B*, 50:326–330, 1994.
- [199] C. L. Freeman J. H. Harding D. M. Duffy. Simulations of calcite crystallization on self-assembled monolayers. *Langmuir*, 24:9607–9615, 2008.
- [200] D. M. Duffy J. H. Harding. The crystallisation of calcite clusters on self-assembled monolayers. *Surf. Sci*, 595:151–156, 2005.
- [201] E. DiMasi S-Y. Kwak B. P. Pichon N. A. J. M. Sommerdijk. Structural adaptability in an organic template for calcium carbonate mineralization. *Cryst. Eng. Comm.*, 9:1192–1204, 2007.
- [202] C. J. Stephens S. F. Ladden F. C. Meldrum H. K. Christenson. Amorphous calcium carbonate is stabilized in confinement. *Advanced Functional Materials*, 20:1–8, 2010.

- [203] V. Balsamo N. Urdaneta L. Perez P. Carrizales V. Abetz A.J. Muller. Effect of the polyethylene confinement and topology on its crystallisation within semicrystalline abc triblock copolymers. *European Polymer Journal*, 40: 1033-1049, 2004.
- [204] M. J. Olszta X. Cheng S-J Sang R. Kumar Y-Y. Kim M. J. Kaufman E. P. Douglas L. B. Gower. Bone structure and formation: A new perspective. *Mater. Sci. Eng.*, 2007:77-116, 2007.
- [205] L. G. Camara F. Bresme. Molecular dynamics simulations of crystallization under confinement at triple point conditions. *Journal of Chemical Physics*, 5:2792-2800, 2003.
- [206] H. K. Christenson. Confinement effects on freezing and melting. *Journal of Physics. Condensed Matter*, 13:R95-R133, 2001.
- [207] C. J.H. Jacobsen C. Madsen T. V.W. Janssens H. J. Jakobsen J. Skibsted. Zeolites by confined space synthesis -. *Microporous and Mesoporous Materials*, 39:393-401, 2000.
- [208] S. Thachepan M. Li S. Mann. Mesoscale crystallization of calcium phosphate nanostructures in protein (casein) micelles. *Nanoscale*, DOI: 10.1039:00158a, 2010.
- [209] E. Loste F. C. Meldrum. Control of calcium carbonate morphology by transformation of an amorphous precursor in a constrained volume. *Chem. Commun*, 1:901-902, 2001.
- [210] Y-Y. Kim N. Hetherington A. P. Ramaros F. C. Meldrum. Templating calcium carbonate rods and cylinders: Role of amorphous precursor, confinement and surface chemistry. *In preparation*, --, 2010.
- [211] E. Loste R. J. Park J. Warren F. C. Meldrum. Precipitation of calcium carbonate in confinement. *Advanced Functional Materials*, 14:1211-1220, 2004.
- [212] J. Aizenberg D. A. Muller J. L. Grazul D. R. Hamann. Direct fabrication of large micropatterned single crystals. *Science*, 299:1205-1208, 2003.

- [213] N. Koga Y. Nakagoe H. Tanaka. Crystallization of amorphous calcium carbonate. *Thermochimica Acta*, 318:239–244, 1998.
- [214] H. N. Rutt J. H. Nicola. Raman spectra of carbonates of calcite structure. *J. Phys C: Solid State Phys.*, 7:4522–4528, 1974.
- [215] W. G. Fately N. T. McDevitt F. F. Betley. Infrared and raman selection rules for lattice vibrations: The correlation method. *Applied Spectroscopy*, 25:155–173, 1971.
- [216] D. Krishnamurti. The raman spectra of aragonite, strontianite and witherite. *D. Krishnamurti*, 121:285–295, 1960.
- [217] S. Martinez-Ramireza S. Sanchez-Cortesa J.V. Garcia-Ramosa C. Domingoa C. Fortes M.T. Blanco-Varela. Micro-raman spectroscopy applied to depth profiles of carbonates formed in lime mortar. *Cement and Concrete Research*, 33:2063–2068, 2003.
- [218] J. Urmos S. K. Sharma F. T. Mackenzie. Characterization of some biogenic carbonates with raman spectroscopy. *American Mineralogist*, 76:641–646, 1991.
- [219] D. E. Jacob T. Hagera W. Hofmeister U. Wehrmeister, A. L. Soldati. Raman spectroscopy of synthetic, geological and biological vaterite: a raman spectroscopic study. *Journal of Raman Spectroscopy*, 41:193–201, 2010.
- [220] J. Zuo C. Xu Y. Liu Y. Qian. Crystallite size effects on the raman spectra of hausmannite. *Nanostructured Materials*, 10:1331–1335, 1998.
- [221] E. M. Pouget P. H. H. Bomans J. A. C. M. Goos P. M. Frederik G. de With N. A. J. M. Sommerdijk. The initial stages of template-controlled calcium carbonate formation revealed by cryo-tem. *Science*, 323:1455–1458, 1999.
- [222] P. Baber T. Asakawa H. K. Christenson. What determines the size of liquid capillary condensates below the bulk melting point? *J. Phys. Chem. C*, 111: 2141–2148, 2007.
- [223] H. Farman F. M. Coveney J. C. Dore. Structural features of the liquid/plastic crystal phase transition for cyclohexane in bulk and confined geometry. *Physica B*, 180:857–860, 1992.

- [224] M. Alcoutlabi G. B. McKenna. Effects of confinement on material behavior at the nanometer size scale. *Journal of Physics: Condensed Matter*, 17: R464-R524, 2005.
- [225] J. Chen C. Burger C. V. Krishnan B. Chu B. S. Hsiao M. J. Glimcher. In vitro mineralization of collagen in demineralized fish bone. *Macromolecular Chemistry and Physics*, 206:43-51, 2004.
- [226] S. Tanaka S.U. Egelhaaf W.C. K. Poon. Crystallization of a globular protein in lipid cubic phase. *Physical Review Letters*, 92:128102, 2004.
- [227] B. D. Hamilton M. A. Hillmyer M. D. Ward. Glycine polymorphism in nanoscale crystallization chambers. *Crystal Growth and Design*, 8:3368-3375, 2008.
- [228] J. Kawano A. Miyake N. Shimobayashi M. Kitamura. Molecular dynamics simulation of the rotational order-disorder phase transition in calcite. *Journal of Physics: Condensed Matter*, 095406:11pp, 2009.
- [229] H-S. Lee T. H. Ha K. Kim. Fabrication of unusually stable amorphous calcium carbonate in an ethanol medium. *Materials Chemistry and Physics*, 93:376-382, 2005.
- [230] P. J. Heaney E. P. Vicenzi L. A. Giannuzzi K. J. T. Livi. Focused ion beam milling: A method of site-specific sample extraction for microanalysis of earth and planetary materials. *American Mineralogist*, 86:1094-1099, 2001.
- [231] H-D. Yu D. Yang D. Wang M-Y. Han. Top-down fabrication of calcite nanoshoot arrays by crystal dissolution. *Advanced Materials*, xx:pp1-4, 2010.
- [232] J. M. Baumann B. Affolter U. Caprez D. Lauper F. Maier H. P. Siegrist T. Zysset. Nucleation and aggregation of calcium oxalate in whole urine; spectrophotometric sedimentation analysis: A new approach to study the aggregation of calcium oxalate dihydrate. *Urol. Res.*, 28:147-154, 2000.
- [233] M. I. H. Wakita I. Masuda. Analyses of precipitation processes of bis(dimethylglyoximate)ni(ii) and related complexes. *Journal of Crystal Growth*, 61:377-382, 1983.

- [234] P. A. Carosso E. Pelizzetti. A stopped-flow technique in fast precipitation kinetics - the case of barium sulphate. *Journal of Crystal Growth*, 68:532-536, 1984.
- [235] D. J. Gunn M. S. Murthy. Kinetics and mechanisms of precipitations. *Chemical Engineering Science*, 27:1293-1313, 1972.
- [236] D. J. Gunn. Mechanism for the formation and growth of ionic precipitates from aqueous solution. *Faraday Disc. Chem. Soc.*, 61:133, 1976.
- [237] M. Faatz F. Grohn G. Wegner. Amorphous calcium carbonate: Synthesis and potential intermediate in biomineralization. *Advanced Materials Letters*, 16:996-1000, 2004.
- [238] J. Liu J. Rieger K. Huber. Analysis of the nucleation and growth of amorphous calcium carbonate by means of time-resolved static light scattering. *Langmuir*, 24:8262-8271, 2008.
- [239] W. G. Zijlstra A. Buursma O. W. van Assendelft. *Visible and Near Infrared Spectra of Human and animal Haemoglobin*. VSP, 2000.
- [240] B. Guillement M. Faatz F. Grohn G. Wegner Y Gnanou. Nanosized amorphous calcium carbonate stabilized by poly(ethylene oxide)-b-poly(acrylic acid) block copolymers. *Langmuir*, 22:1875-1879, 2006.
- [241] E. Loste R. M. Wilson R. Seshadri F. C. Meldrum. The role of magnesium in stabilising amorphous calcium carbonate and controlling calcite morphologies. *Journal of Crystal Growth*, 254:206-218, 2003.
- [242] K. Sawada. The mechanisms of crystallization and transformation of calcium carbonates. *Pure and Applied Chemistry*, 69:921-928, 1997.
- [243] J. Xiao Z. Wang Y. Tang S. Yang. Biomimetic mineralization of calcium carbonate on a phospholipid monolayer: From an amorphous calcium carbonate precursor to calcite via vaterite. *Langmuir*, 26:4977-4983, 2009.
- [244] J. Bolze D. Pontoni M. Ballauff T. Narayanan H. Colfen. Time-resolved saxs study of the effect of a double hydrophilic block-copolymer on the formation of caco3 from a supersaturated salt solution. *Journal of Colloid and Interface Science*, 277:88-94, 2004.

- [245] J. Bolze B. Peng N. Dingenouts P. Panine T. Narayanan M. Ballauff. Formation and growth of amorphous colloidal CaCO_3 precursor particles as detected by time-resolved SAXS. *Langmuir*, 18:8364–8369, 2002.
- [246] H. Colfen Volkel. Application of the density variation method on calcium carbonate nanoparticles. *Progr. Colloid. Polym. Sci.*, 131:126–128, 2006.
- [247] N. E. Chayen P. D. Shaw Stewart D. M. Blow. Microbatch crystallization under oil a new technique allowing many small-volume crystallization trials. *Journal of Crystal Growth*, 122:176–180, 1992.
- [248] S. K. Chang E. H. Trinh. Containerless protein crystal growth in rotating levitated droplets. *Journal of Crystal Growth*, 194:384–397, 1998.
- [249] D. Knezic J. Zaccaro A. S. Myerson. Nucleation induction time in levitated droplets. *J. Phys. Chem. B*, 108:10672–10677, 2004.
- [250] S. E. Wolf J. Leiterer M. Kappl F. Emmerling W. Tremel. Early homogenous amorphous precursor stages of calcium carbonate and subsequent crystal growth in levitated droplets. *Journal of the American Chemical Society*, 130:12342–12347, 2008.
- [251] A. Y. Lee I. S. Lee S. S. Dette J. Boerner A. S. Myerson. Crystallization on confined engineered surfaces: A method to control crystal size and generate different polymorphs. *Journal of the American Chemical Society*, 127:14982–14983, 2005.
- [252] D. Qin Y. Xiao B. Xu H. Yang C. Zhu G. M. Whitesides. Fabrication of ordered two-dimensional arrays of micro- and nano-particles using patterned self-assembled monolayers as templates. *Advanced Materials*, 11:1433–1437, 1999.
- [253] Y. Masuda K. Koumoto. Low dimensional particle patterning. *Journal of Dispersion Science and Technology*, 25:503–511, 2004.
- [254] W. R. Barchet. The validity of the spherical cap approximation in heterogeneous nucleation. *J. Atmos. Sci.*, 26:112–114, 1969.

- [255] K. S. Birdi D. T. Vu A. Winter. A study of the evaporation rates of small water drops placed on a solid surface. *Journal of Physical Chemistry*, 93: 3702-3703, 1989.
- [256] Calcium chloride handbook-a guide to properties, forms, storage and handling. dow chemical company.